Mathematical models of cellular decisions: investigating immune response and apoptosis

A thesis presented for the degree of

Doctor of Philosophy of Imperial College London

by

Heather Anne Harrington

Department of Mathematics

Imperial College London

180 Queen's Gate, London SW7 2AZ

SEPTEMBER 6, 2010

I certify that this thesis, and the research to which it refers, are the product of my own work, and that any ideas or quotations from the work of other people, published or otherwise, are fully acknowledged in accordance with the standard referencing practices of the discipline.

Signed:

Copyright

To Jaroslav...

and his legacy.

Abstract

The main objective of this thesis is to develop and analyze mathematical models of cellular decisions. This work focuses on understanding the mechanisms involved in specific cellular processes such as immune response in the vascular system, and those involved in apoptosis, or programmed cellular death.

A series of simple ordinary differential equation (ODE) models are constructed describing the macrophage response to hemoglobin:haptoglobin (Hb:Hp) complexes that may be present in vascular inflammation. The models proposed a positive feedback loop between the CD163 macrophage receptor and anti-inflammatory cytokine interleukin-10 (IL-10) and bifurcation analysis predicted the existence of a cellular phenotypic switch which was experimentally verified. Moreover, these models are extended to include the intracellular mediator heme oxygenase-1 (HO-1). Analysis of the proposed models find a positive feedback mechanism between IL-10 and HO-1. This model also predicts cellular response of heme and IL-10 stimuli.

For the apoptotic (cell suicide) system, a modularized model is constructed encompassing the extrinsic and intrinsic signaling pathways. Model reduction is performed by abstracting the dynamics of complexes (oligomers) at a steady-state. This simplified model is analyzed, revealing different kinetic properties between type I and type II cells, and reduced models verify results. The second model of apoptosis proposes a novel mechanism of apoptosis activation through receptor-ligand clustering, yielding robust bistability and hysteresis. Using techniques from algebraic geometry, a model selection criterion is provided between the proposed and existing model as experimental data becomes available to verify the mechanism.

The models developed throughout this thesis reveal important and relevant mechanisms specific to cellular response; specifically, interactions necessary for an organism to maintain homeostasis are identified. This work enables a deeper understanding of the biological interactions and dynamics of vascular inflammation and apoptosis. The results of these models provide predictions which may motivate further experimental work and theoretical study.

Acknowledgements

First and foremost, I would like to thank the people who have helped me academically during my PhD. I acknowledge my debt of gratitude to my Supervisor, the late Jarsolav Stark for providing me excellent advice and teaching me invaluable lessons. I am deeply saddened he will not read the final thesis and that we will not share any future scientific experiences. I would like to thank Piers Ingram for stepping up as acting supervisor during the end of my PhD and for helping me throughout the write-up period. I am indebted to Dorothy Buck, who has provided excellent mathematical, career and life advice as well as supervision. Special thanks to Panayotis Kevrekidis and Nathaniel Whitaker, for their continued support, advice and collaboration throughout the PhD. Many thanks to Joe Boyle for helpful discussions and providing me with data for modeling in Chapters 4 and 5. I would like to thank Michael Stumpf and Tina Toni for discussions about ABC-SMC. Special thanks to Chris Barnes who helped me with the parameter inference and model selection in Chapter 5. I would also like to thank the members of Jaroslav's group, BioMaths and CISBIC who shared their work at seminars and group meetings, as well as those that were generous with their time to discuss science. Many thanks go to Coralie Simmons for helping to make everything run smoothly in the office and I would like to acknowledge my PG tutor John Gibbons. Finally, I would like to thank Ken Ho, who has been an incredible friend and collaborator throughout my PhD. He has made an enormous difference to the work in Chapters 6 and 7.

I am grateful for the Imperial College Deputy Rector's Award, Imperial College Mathematics Department as well as the National Science Foundation Graduate Research Fellowship. This financial support enabled me to come to London to study. I would also like to thank Avner Friedman and MBI for hosting the 2007 summer school and Leslie Greengard who hosted and facilitated my work at the Courant Institute.

I would also like to thank my family and friends who have personally supported me throughout the PhD. Mom and Dad, thank you for your guidance, support and always believing in me. Adriane, Melissa and Brietta, thanks for always being there, supporting me in more ways than I can express, and for making me laugh. I would like to acknowledge my close friends: Jackie, Katie, Tejas, Inna, Kody, Anneli and Erin, thank you. Sincere thanks go to the rowers, runners and EDGErs who have been great friends, despite distance and time. Many thanks to Adele Peel and Matthew Fleming for their interest in my work and for proof reading this entire thesis. I would also like to thank Natalja, Deborah, Diana, Gerardo, Sylvain, Owen, and Andy for coffee/lunch interventions and for stimulating discussions. Many thanks go to Susan Whitbourne who introduced me to the fellowships available to study in London and then remaining enthusiastic about my academic endeavors. Lastly, special thanks to Mariano for sharing the ups and downs of the PhD and challenging me to be better, especially during the write-up. I look forward to doing the same when he writes up next year.

Table of contents

List of Figures

List of Tables

List of Abbreviations

ABC-SMC	Approximate Bayesian computation based on sequential Monte Carlo sampling, page 82
AP-1	Activator protein 1, page 26
Apaf-1	Apoptotic protease activation factor-1, page 31
ATP	Adenosine triphosphated, page 31
Bach1	Basic leucine zipper transcription factor 1, page 25
BAR	Bifunctional apoptosis inhibitor, page 31
c-FLIP	Cellular FADD-like IL-1b-converting enzyme inhibitory protein, page 31
CD163	Cluster of differentiation 163, page 24
CO	Carbon monoxide, page 26
CVD	Cardiovascular disease, page 23
dATP	Deoxyadenosine triphosphated, page 31
DISC	Death inducing signaling complex, page 30
ELISA	Enzyme-linked immunosorbent assay, page 28
ERK	Extracellular signal regulated kinase, page 26
FADD	Fas-associating proteins with death domain, page 30
FAST	Fourier amplitude sensitivity test, page 50
Hb	Hemoglobin, page 25
Hb:Hp	Hemoglobin-haptoglobin, page 24

HCP-1	Heme carrier protein-1, page 25
HO-1	Heme oxygenase-1, page 25
Hp	Haptoglobin, page 25
IL-10	Interleukin-10, page 25
IL-6	Interleukin-6, page 26
LDL	Low-density lipoproteins, page 23
MAC	Mitochondrial apoptosis-induced channel, page 30
MAPK	Mitogen-activated protein kinase, page 26
MPSA	Multi-parametric sensitivity analysis, page 50
mRNA	messenger RNA, page 23
NF-κB	Nuclear factor κ B, page 26
NNLS	Nonnegative least squares, page 146
ODEs	Ordinary differential equations, page 34
PBMC	Peripheral blood mononuclear cell, page 27
PC	Principal component, page 87
PCR	Polymerase chain reaction, page 28
PDEs	Partial differential equations, page 34
PI-3K	Phosphatidylinositol-3 kinase, page 26
PRCC	Partial rank correlation coefficient, page 50
QSSA	Quasi-steady-state assumption, page 41
Smac/DIABLO	Second mitochondria-derived activator of caspases/Direct IAP binding protein with low PI, page 31
STAT	Signal transducer and activator of transcription, page 26
TNFR1	Tumor necrosis factor receptor family, page 30

List of publications and submissions

Some of the research presented in this thesis can also be found in the following list of publications and submissions:[1]

1. H. A. Harrington, M. Maier, L. Naidoo, N. Whitaker and P. G. Kevrekidis. A hybrid model for tumor-induced angiogenesis in the cornea in the presence of inhibitors. *Mathematical and Computer Modelling* Volume 46, Issues 3-4, August 2007, Pages 513-524.

2. H. A. Harrington, K. L. Ho, S. Ghosh, and K. C. Tung. Construction and analysis of a modular model of caspase activation in apoptosis. *Theoretical Biology and Medical Modelling*. Volume 5, Issue 1, December 2008, Page 26.

3. J. J. Boyle, H. A. Harrington, E. Piper, K. Elderfield, J. Stark, R. C. Landis and D. O. Haskard. Coronary intraplaque hemorrhage evokes a novel atheroprotective macrophage phenotype. *American Journal of Pathology*. Volume 174, Issue 3, March 2009, Pages 1097-1108.

4. K. L. Ho and H. A. Harrington. The fas trimer hysteron model: bistability in apoptosis from receptor clustering. *PLoS Computational Biology*. Accepted 2010.

5. H. A. Harrington, C. Barnes, P. J. Ingram, J. J. Boyle and J. Stark A mechanistic study of anti-inflammatory response by macropahges after stimulation with Hb:Hp complexes/heme. *In preparation for submission*.

   Most of the author's own research can be found after Chapter 3 of this thesis.

[1]The first paper revision and acceptance of the manuscript occurred during the PhD period.

Chapter 1

Introduction

This work presents a variety of mathematical approaches to model cellular decision-making. Through the construction and analysis of mathematical models, the aim of this research is to give quantitative and mechanistic insights to medically relevant questions in areas such as immune response in the vascular system and apoptosis, a type of programmed-cell death. This research involves designing mathematical relationships and methods to identify intra-cellular switches from a variety of available biological information and data. To achieve this, dynamical models are built, validated and analyzed; moreover, model results provide insights to the general principles underlying the interaction and dynamical behavior of cellular biological switches. In this work, continuum techniques are employed to depict the behavior of complex systems, and standard numerical techniques are used to solve the models and compare model predictions to data.

In this thesis, two complex systems are studied: vascular inflammation and apoptosis. In these systems, the intra- and inter-cellular interactions may be difficult to explain biologically or where intuition alone does not work. To gain a better insight of the complicated interactions that occur among several agents requires a quantitative approach. Therefore, mathematical models of cellular decision-making are developed and analyzed to gain a better understanding of the underlying biology of these two topics. Inflammation in vascular plaques for this specific system have not previously been mathematically modeled, and it is only recently that a better understanding of the network of components has begun to emerge. While many models exist of the components of the apoptotic signaling pathway, this work is one of the first simple full system models. In addition to this work, a novel mechanism between the death receptor and ligand is hypothesized. For both systems, the incorporation of biological knowledge and data of cellular mechanisms motivated the construction of models with results that may provide hypotheses

and predictions. Overall, this work may have implications for future models of cellular switching and provide mechanistic insights to the systems of interest.

The first set of models presented focus on immune response specific to an inflammatory disease called atherosclerosis. Atherosclerosis is a precursor to many acute cardiovascular diseases that is characterized by the formation of plaque in the arterial wall. When immune cells located in ruptured plaque are introduced to certain stimuli, these cells may participate in a switch like transition in cellular phenotype. This switch is characterized by the release of anti-inflammatory mediators, important for immune response. In collaboration with Dr. Joseph J. Boyle and co-workers from the Imperial College London Faculty of Medicine, a simplified model is developed based on these findings using a pharmacological/systems biology approach. This effort resulted in a published paper in a peer-reviewed journal with experimental and modeling results (Boyle *et al*., 2009) and is presented in Chapter 4. Furthermore, this model is extended in Chapter 5 to describe the intra-cellular mechanisms governing the anti-inflammatory response using experimental data. These results are currently in preparation for submission.

The second focus of this thesis reproduces, extends and develops models of apoptosis, or programmed-cell death, a regulatory process employed by the cell that is necessary for homeostasis, or internal maintenance, of an organism. Apoptosis is characterized by a series of molecular interactions which must behave appropriately to ensure homeostasis. When dysregulation of apoptosis occurs, these interactions fail to respond properly and this may result in cancer or neurodegenerative diseases. A modularized model is constructed and analyzed of the activation and signaling pathways involved in the apoptosis process to highlight the key apoptotic mechanisms involved in different cell types and lineages. This research was conducted in collaboration with participants from the 2007 Mathematical Biosciences Institute Summer School at Ohio State University, Columbus, OH, USA, resulting in a first author published paper in a peer-reviewed journal (Harrington *et al*., 2008) and is presented in Chapter 6. Subsequently, in collaboration with co-author Kenneth L. Ho from Courant Institute of Mathematical Sciences at New York University, New York, NY, USA, a novel mathematical model was developed of receptor-ligand trimerization mechanisms in apoptosis, as presented in Chapter 7 and has been accepted by *PLoS Comput Biol* for publication.

The thesis is organized as follows: relevant biology is introduced in Chapter 2 followed by an introduction of the necessary mathematical modeling techniques in Chapter 3. The results chapters of this thesis (Chapters 4 - 7) are split into two themes: the first theme, models of immune cell response in vascular plaque, is presented in Chapters 4 and 5. Simple models of vascular inflammation are presented in Chapter 4. These

models are extended in Chapter 5 to investigate intracellular mechanisms, various signals, and parameter fitting. The second theme (contained in Chapters 6 and 7) encompasses models of apoptosis. A modularized model of apoptosis is developed and analyzed in Chapter 6, and Chapter 7 presents a novel model of death ligand-receptor interaction. Chapter 8 provides general conclusions and suggests further work.

Chapter 2

Biological background

2.1 Introduction

How a cell comes to a coordinated decision is a complicated process; the internal environment in the cell must decide how to appropriately respond to its external environment. A pioneer in the field of cellular response, Earl W. Sutherland, revealed the complexity and rich structure of signaling (Sutherland, 1972). Sutherland and colleagues found that a cell's surface is important for a stimulus, such as epinephrine, to trigger signal transmission; following this, Sutherland and co-workers discovered that when liver and skeletal muscle cells are stimulated by epinephrine, intermediate steps are required for glycogen breakdown. Since this work, the study of the cellular decision processes remains an active area of research (Campbell and Reece, 2002).

Many signals in the body are mediated by one of two ways: direct cell-cell contact or by small signaling proteins such as cytokines and hormones which convey information from one cell to another. When a cytokine binds to the receptor of its target cell, as shown in Fig. 2.1, it triggers an intra-cellular signaling cascade, which may result in gene expression or other responses (Campbell and Reece, 2002). Such interactions allow a collection of cells to come to a coordinated decision and change of physiological state (Alberts *et al*., 2002).

Signal reception is the process by which cells sense the extracellular environment. This may be initiated by cell-cell contact or through small signaling molecules (Perkins and Swain, 2009; Saez-Rodríguez *et al*., 2004). Cell-cell interaction may occur through structures such as gap junctions, enabling chemical communication between cells, or a cell may present a protein, which binds to a receptor, usually a transmembrane protein, of its target cell. Receptors, often large molecules that are highly specific, bind to ligands which are small signaling molecules, such as hormones, cytokines, or growth

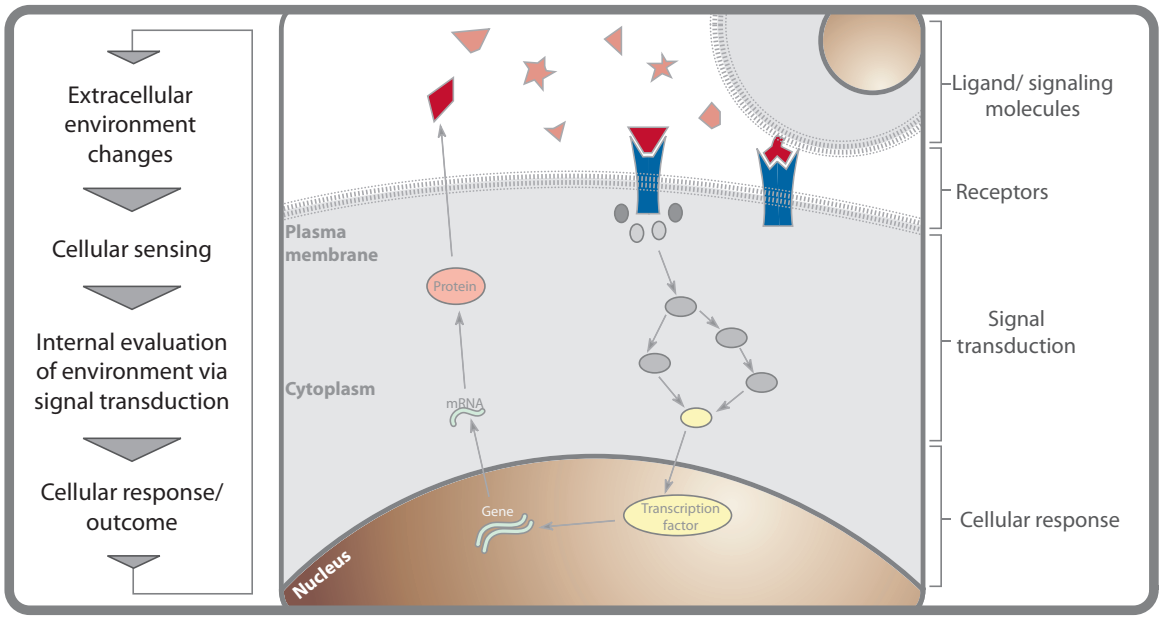

Figure 2.1: Cellular signaling. Consider a cell in the presence an environment of signaling molecules such as cytokines. Specific receptors on the cellular plasma membrane may detect a specific ligand and bind to it. If the receptor-ligand binding has high affinity in the concentration range of this ligand then an intracellular response is communicated via a complex signal pathway. A signal transduction pathway consists of many proteins which may interact through different mechanisms, mediating the expression of genes and synthesis of proteins. This schematic was inspired by Saez-Rodríguez *et al.*, 2004.

factors. Following receptor-ligand binding, the ligand may remain in the extracellular environment or enter the cell by a process called endocytosis, and the receptor undergoes a change in its conformational shape. This enables the receptor to interact with an intracellular molecule and initiate a signaling cascade within the cell.

The initial signal is converted into a cellular response by signal transduction pathways, a multistep sequence of intracellular signaling and communication between molecules. Most of these molecules are proteins, such as enzymes that catalyze a reaction, and perform a crucial role in relaying information. Special enzymes called kinases bind and add a phosphate group, resulting in activation or inactivation of a protein. If the protein is activated, it transfers information downstream and may engage multiple signaling cascades by chemical reactions. Sometimes these chemical interactions occur in a linear fashion, that is, the input of the interaction is proportional to the output (Stark and Hardy, 2003); however, many interactions are not linear, or nonlinear, and amplification of the signal may occur via positive feedback loops, or inhibition may exist via negative feedback. Specifically, the repertoire of upstream dynamics, such as interactions between signaling molecules and signaling pathways, may control enzymatic activity, and/or activate or inhibit regulatory proteins called transcription factors.

Transcription factors regulate gene expression: to turn a gene on, an activated transcription factor translocates from the cytoplasm into the nucleus, binds to the enhancer or promoter region of DNA, and RNA polymerase transcribes the DNA template to synthesize RNA. Then a type of RNA, messenger RNA (mRNA), leaves the nucleus and enters the cytoplasm where ribosomes translate mRNA into a protein (Alberts *et al.*, 2002). Conversely, transcription factors may also turn a gene off by repressing the recruitment of RNA polymerase. These two possible responses regulate proteins synthesis, whereby proteins may be released out of the cell, modify the cellular environment, and act as signaling molecules which restart the cellular sensing and signaling process.

2.2 Vascular inflammation

Immune response is highly dependent on how immune cells, such as mononuclear phagocytes, respond to their external environment (Gordon, 2003; Gordon and Taylor, 2005; Mosser, 2003; Mosser and Edwards, 2008). This is particularly the case in atherosclerosis, an inflammatory disease of the arteries, which is the formation of plaque along the arterial wall and is a precursor to many cardiovascular diseases (CVDs). CVD risk factors increase oxidative stress via highly reactive oxygen species, leading to the modification of the inner lining of the blood vessel wall (endothelium), cholesterol in blood plasma and erythrocytes (Kolodgie *et al.*, 2003; Virmani *et al.*, 2005). Subsequently, atherogenic substances composed of mononuclear phagocytes (i.e., blood monocytes that may differentiate into different subsets of macrophages after entering the subendothelium (Gordon and Taylor, 2005; Hansson and Libby, 2006; Weber *et al.*, 2008)), endothelial cells, and smooth muscle cells may ingest low-density lipoproteins (LDL), which may transform into foam cells, accumulate and calcify in the endothelium; thus, narrowing the arterial passage ways and triggering an inflammatory response (Glass and Witztum, 2001; Hansson *et al.*, 2002; Heinecke, 2006; Lee *et al.*, 2004; Morita, 2005). Vascular inflammation, metabolic factors and neovessels invading the arterial plaque may cause exceptionally developed plaques to rupture, known as intraplaque hemorrhage; this event accelerates the progression of atherosclerosis, and may implicate highly fatal conditions such as thrombosis, stroke and coronary heart disease (Davies and Thomas, 1985; Kolodgie *et al.*, 2003; Levy and Moreno, 2006; Takaya *et al.*, 2006; Virmani *et al.*, 2005). Recent work has revealed an anti-inflammatory response within plaque macrophages (Boyle *et al.*, 2009; Lee and Chau, 2002; Moestrup and Moller, 2004; Otterbein and Zuckerbraun, 2005; Ugocsai *et al.*, 2006; Van den Heuvel *et al.*, 1999); hence, it is important to understand how blood monocytes differentiate into different subsets of macrophages. Much

effort is still needed to unveil the cellular players, signaling pathways and mechanisms involved in this disease; specifically, the interactions governing an anti-inflammatory macrophage response remain unresolved.

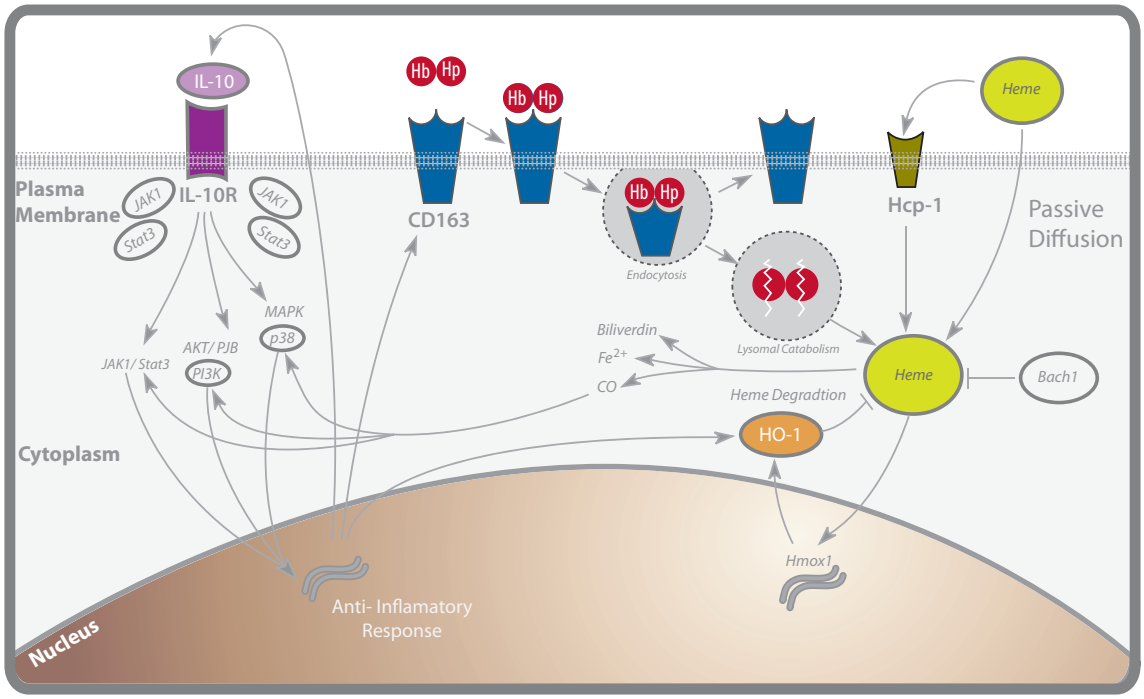

Figure 2.2: Vascular inflammation signaling pathway. The cluster of differentiation 163 (CD163) receptor, binds with the hemoglobin-haptoglobin (Hb:Hp) complex which undergoes endocytosis, recycles CD163 back to the cell surface and acts as a heme transporter. Alternatively, extracellular heme may be transported via heme carrier protein (HCP)-1 or diffuse passively into the cell. Intracellular heme is negatively regulated by Bach1. Heme serves as a signaling molecule, by synthesizing its enzyme, heme oxygenase-1 (HO-1), which thereby degrades heme into its metabolites. Following heme degradation, the metabolites activate a signaling cascade resulting in an anti-inflammatory response. Original schematic courtesy of Dr. Boyle and extended using pathway information from BioCarta, 2010; Latunde-Dada *et al.*, 2006; Otterbein and Zuckerbraun, 2005; Philippidis *et al.*, 2004; Sabosciences, 2010; Sulahian *et al.*, 2000.

Key players in vascular inflammation are mononuclear phagocytes, specific types of cells of the innate immune system. As the name would suggest, mononuclear phagocytes are single nucleus "eating" cells, such as monocytes and macrophages. As shown in Fig. 2.2, a large number of molecular components within monocytes/macrophages are involved in complicated interactions which may result in an anti-inflammatory response. The cluster of differentiation 163 (CD163) receptor on macrophages, known to be involved in the regulation of inflammatory processes, mediates endocytosis of hemoglobin-haptoglobin (Hb:Hp), a molecular complex found in the blood; subsequently, the complex undergoes lysosomal catabolism reducing to heme (Takami, 1993; Van den Heuvel *et al.*, 1999). Heme may also enter the cell by other means; however, intracellular heme is regulated by many mediators (Ogawa *et al.*, 2002; Tsiftsoglou *et al.*, 2006). Intra-

cellular heme activates signal transduction by contributing to the synthesis of its rate limiting enzyme heme oxygenase-1 (HO-1) (Hoekstra *et al*., 2004; Siow *et al*., 1999), which degrades heme into its metabolites (Morita, 2005; Otterbein *et al*., 2003). This signaling cascade induces interleukin-10 (IL-10), an anti-inflammatory cytokine (Boyle *et al*., 2009; Lee and Chau, 2002; Moestrup and Moller, 2004; Otterbein and Zuckerbraun, 2005; Ugocsai *et al*., 2006), which contributes to the synthesis of HO-1 (Abraham and Drummond, 2006; Lee and Chau, 2002) and induces a high expression of CD163 (Sulahian *et al*., 2000). Therefore, Hb:Hp is responsible for activating signal transduction resulting in an anti-inflammatory and atheroprotective cell response.

Heme, the molecule found in hemoglobin (Hb), is responsible for oxygen binding, electron transport, and chemical catalysis (Gunsalus *et al*., 1977; Mense and Zhang, 2006). When erythrocytes undergo hemolysis such as in intraplaque hemorrhage, the potentially harmful free extracellular Hb quickly binds with a molecule common in blood plasma, haptoglobin (Hp) forming a hemoglobin-haptoglobin (Hb:Hp) complex (Ascenzi *et al*., 2005; Levy and Moreno, 2006; Nielsen and Moestrup, 2009). This complex, while less harmful, may still catalyze LDL oxidation; therefore, immune cells such as monocytes or macrophages are recruited to the atherosclerotic lesion where the free pro-oxidative Hb:Hp are endocytosed by the CD163 scavenger receptor (Kristiansen *et al*., 2001). CD163, a transmembrane glycoprotein, is exclusively expressed on monocyte cells and acts as a heme transporter (Buechler *et al*., 2000; Philippidis *et al*., 2004). Endocytosed Hb:Hp then undergoes lysosomal catabolysis, and intracellular heme may then be degraded; conversely, if free heme, not Hb:Hp, is present extracellularly, heme may be transported into the macrophage by heme carrier protein (HCP)-1 (Latunde-Dada *et al*., 2006; Schaer *et al*., 2008) and/or may enter the cell via passive diffusion (Schaer *et al*., 2008; Tsiftsoglou *et al*., 2006). In order for the cell to regulate heme import, Hb:Hp-CD163 mediated scavenging saturates (Nielsen and Moestrup, 2009); and heme and Hb somewhat suppress HCP-1 (Schaer *et al*., 2008).

To protect macrophages expressing CD163 from heme's critically pro-oxidative and cytotoxic effects, intracellular levels of heme are regulated by synthesis and degradation rates. Another two mediators of intracellular heme levels are HO-1 (Immenschuh and Ramadori, 2000; Otterbein and Zuckerbraun, 2005; Pae *et al*., 2008) and basic leucine zipper transcription factor 1 (Bach1) (Kitamuro *et al*., 2003; Ogawa *et al*., 2002; Sun *et al*., 2002, 2004). Unlike erythrocytes that rely on reactive oxygen species for non-enzymatic heme degradation (Nagababu and Rifkind, 2004), non-erythroid cells such as monocytes and macrophages degrade heme via the inducible form of the rate limiting enzyme, heme oxygenase (HO-1) (Schaer *et al*., 2006). HO-1 is upregulated by many factors such as

CVD risk factors, cytokines (i.e., IL-10), endotoxin, growth factors, highly reactive oxygen species and transcriptionally by pro-inflammatory mediators, such as transcription factor nuclear factor κ B (NF-κB), activator protein 1 (AP-1) and interleukin-6 (IL-6), as well as heme (Idriss *et al*., 2008; Morita, 2005; Philippidis *et al*., 2004; Schaer *et al*., 2006; Takaya *et al*., 2005). Subsequently, HO-1 plays an important role in modulating intracellular heme levels by catabolyzing heme into equimolar amounts of its putative anti-oxidative and vasoprotective metabolites bilirubin, ferrous iron (Fe^{2+}) and carbon monoxide (CO) (Morita, 2005; Otterbein *et al*., 2003; Ryter *et al*., 2002; Takami, 1993). In addition to degrading heme, HO-1 is cytoprotective and mediates anti-inflammatory, anti-proliferatory, and anti-apoptotic functions (Cheng *et al*., 2009; Otterbein *et al*., 2003; Pae *et al*., 2008). When HO-1 levels decrease, intraceullar heme levels may bind to hemoprotein Bach1, a negative regulator of HO-1 transcription and promote HO-1 expression (Otterbein and Zuckerbraun, 2005; Sun *et al*., 2002, 2004). Hence, heme modulates the level of its intracellular heme by feedback mediated by transport (HCP-1), enzymatic degradation (HO-1), and repression of its degradation enzyme (Bach1).

Mononuclear phagocytes stimulated with heme molecules play a significant role in the anti-inflammatory response (Boyle *et al*., 2009; Lee and Chau, 2002; Moestrup and Moller, 2004; Otterbein and Zuckerbraun, 2005; Ugocsai *et al*., 2006). The products of heme degradation by HO-1, that is, CO may upregulate the expression of HO-1 (Sawle *et al*., 2005) as well as IL-10, via mitogen-activated protein kinase (MAPK) family members:[1] p38 MAPK, MAPK 3/6 and extracellular signal regulated kinase (ERK) (Morita, 2005; Pae *et al*., 2008). Experimental agreement shows IL-10 induces HO-1 (Abraham and Drummond, 2006; Lee and Chau, 2002; Ricchetti *et al*., 2004; Schaer *et al*., 2006); however, there is disagreement between the responsible signaling pathway. Lee and Chau, 2002 find HO-1 upregulation by IL-10 requires p38 MAPK; whereas, Ricchetti *et al*., 2004 observe HO-1 expression is induced by IL-10 via signal transducer and activator of transcription (STAT)-3 and phosphatidylinositol-3 kinase (PI-3K), not p38 MAPK. This conflict extends to the existence of an anti-inflammatory feedback loop between IL-10 and HO-1. Moreover, previous findings show that CD163 ligation by Hb:Hp is linked to secretion of IL-10 (Philippidis *et al*., 2004; Sulahian *et al*., 2000), resulting in

[1]The mitogen-activated protein kinases are a large family of kinases involved in a regulator of cellular activities such as proliferation, differentiation and apoptosis. The MAPKs are characterized by the presence of a Thr-Xxx-Tyr activation motif and often these kinases require the phosphorylation of both threonine and tyrosine in this motif. There are three main sub-families: the extracellular signal regulated kinases (ERKs, encoded by two genes where the amino acid Xxx is glutamic acid), cJun N-terminal kinases (JNKs, encoded by three genes where Xxx is proline), and the p38 MPAKs (encoded by four genes where Xxx is glycine).

the upregulation of CD163 (Sulahian *et al*., 2000; Williams *et al*., 2002) and facilitating atheroprotective function against plaque hemorrhage (Mallat *et al*., 1999; Potteaux *et al*., 2004).

The roles of cellular mediators in vascular inflammation are only now becoming better characterized; therefore, a better understanding of the mechanisms and interactions leading to an anti-inflammatory response may provide future treatments to the classically observed pro-inflammatory response in atherosclerosis.

Data

In the past ten years, significant advances have revealed the cellular components and their functions that govern the monocyte/macrophage response to Hb:Hp, Hb and heme. Published time-course data and dose-response curves of inflammatory markers in response to human peripheral blood mononuclear cell (PBMC) stimulated with Hb:Hp are given in Fig. 2.3 and Fig. 2.4; these are normalized to represent fold change according to the baseline level of initial marker obtained from Schaer *et al*., 2006 and Philippidis *et al*., 2004, respectively. This work shows induction of HO-1 and IL-10, respectively, by macrophages in response to Hb:Hp; furthermore, both indicate at approximately 10 μg/mL Hb:Hp, there is a four-fold increase in expression. As previously discussed (not shown), Sulahian *et al*., 2000 observed that monocytes incubated with increasing concentration levels of IL-10 result in increased expression of CD163.

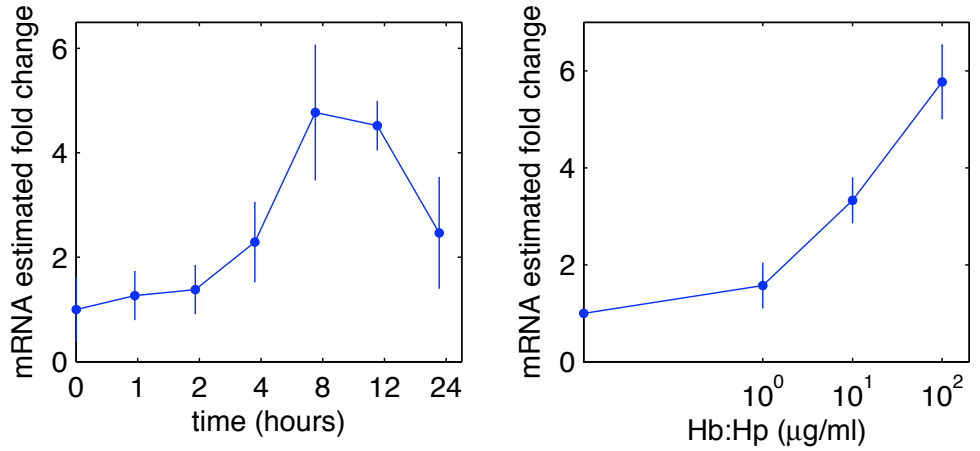

Figure 2.3: HO-1 mRNA expression by Hb:Hp complexes (Schaer *et al*., 2006). HO-1 mRNA expression of CD163 positive-HEK macrophages stimulated with Hb:Hp complex. Assays were determined by LightCycler-polymerase chain reaction (PCR), an experimental technique which provides a quantitative measure of mRNA, where each data point is the estimated mean ($\pm$ standard deviation) fold change from n$=$ 3 experiments. Time course of CD163-mediated IL-10 protein induction by macrophages stimulated with Hb:Hp complexes (100 μg/mL). Dose response of HO-1 mRNA expression after 8 hours incubation of Hb:Hp complex (increasing concentration).

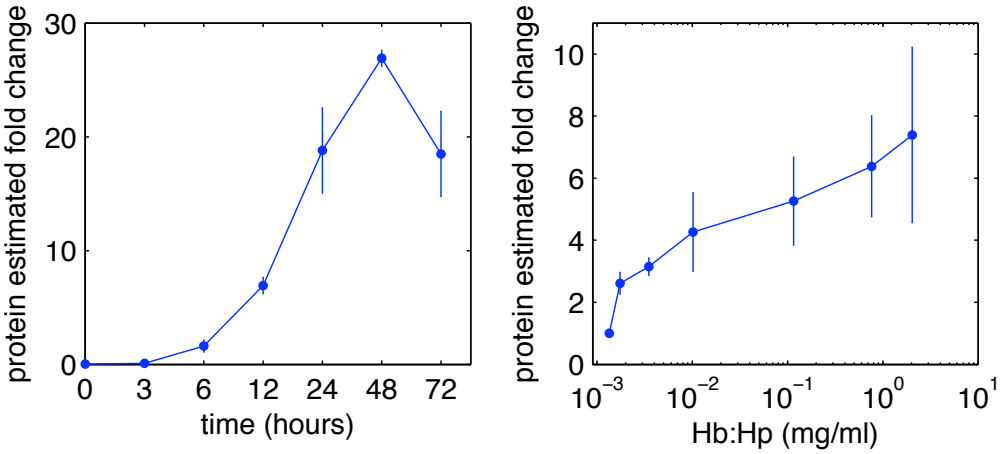

Figure 2.4: IL-10 induction by Hb:Hp complexes (Philippidis *et al*., 2004). IL-10 protein expression of CD163 positive in vitro differentiated human macrophages (day 7) stimulated with Hb:Hp complex. Assays were carried out in duplicate and determined by enzyme-linked immunosorbent assay (ELISA) PCR, an experimental technique which provides a quantitative measure of protein, such as IL-10 expression, where each data point is the estimated mean ($\pm$ standard deviation) fold change from n$=$ 3 experiments. Time course of CD163-mediated IL-10 protein induction of macrophages incubated with Hb:Hp complexes (1mg/mL). Dose response of IL-10 protein after 24 hours of incubation of Hb:Hp complex (increasing concentration).

2.3 Apoptosis

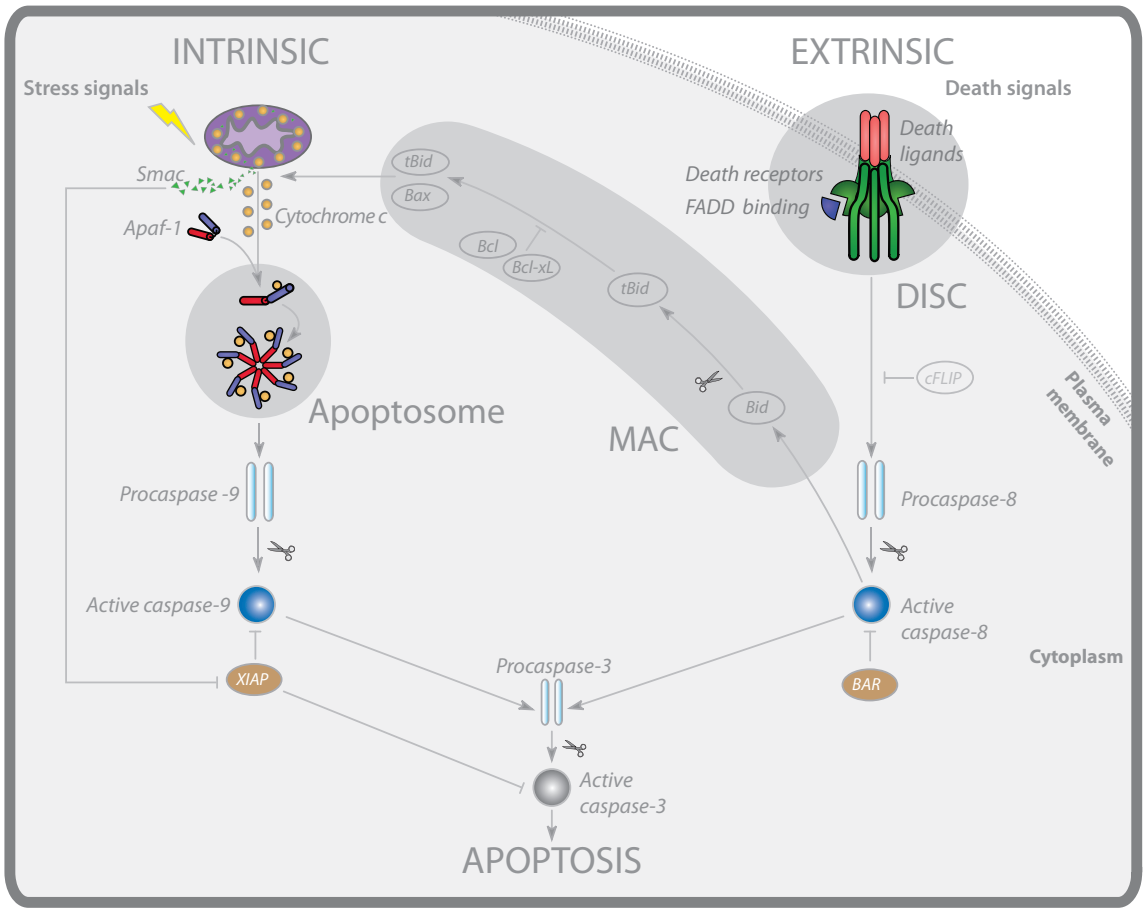

Figure 2.5: Apoptosis signaling pathways. Apoptosis is triggered by the activation of caspases in response to both extracellular (extrinsic) and intracellular (intrinsic) signals. The extrinsic and intrinsic pathways are characterized by the formation of the death-inducing signaling complex (DISC) and the apoptosome, respectively; both the DISC and the apoptosome are oligomers with complex formation dynamics. Once the oligomers are formed, procaspases may be cleaved (illustrated as scissors) to activate corresponding caspases of both pathways. Additionally, the extrinsic and intrinsic pathways are coupled through the mitochondrial apoptosis-induced channel (MAC) via the Bcl-2 family of proteins. Schematic inspired by Zheng and Flavell, 2000.

Apoptosis, or programmed cell death, is a highly regulated cell death mechanism involved in many physiological processes. Normal function of apoptosis is critical for development, tissue homeostasis, cell termination, and immune response (Hengartner, 2000; Hutchins and Barger, 1998; Jacobson *et al.*, 1997; Leist and Jäättelä, 2001; Lockshin and Zakeri, 2001; Meier *et al.*, 2000; Oppenheim, 1991; Raff, 1998; Zuzarte-Luis and Hurle, 2002). Dysregulation of apoptosis is associated with pathological conditions such as developmental defects, neurodegenerative disorders, autoimmune disorders, and tumorigenesis (Chang and Yang, 2000; Fadeel *et al.*, 1999; Haass, 1999; Johnstone *et al.*,

2002; Pritchard and Hickman, 1994; Thompson, 1995; Thornberry and Lazebnik, 1998). As shown in Fig. 2.5, the apoptotic pathway is characterized by complex interactions of a large number of molecular components which are involved in the induction and execution of apoptosis. Due to its fundamental importance, apoptosis is the subject of intense active research, and key characteristics have been identified which motivate further study of this cellular process.

Apoptosis is a cell suicide mechanism in which cell death is mediated by apoptotic complexes along one of two pathways: the extrinsic pathway (receptor mediated) via the death inducing signaling complex (DISC), or the intrinsic pathway (mitochondrial) via the apoptosome (Ashkenazi and Dixit, 1998; Budihardjo *et al*., 1999; Cain *et al*., 1999, 2000, 2002; Fumarola and Guidotti, 2004; Hengartner, 2000; Jiang and Wang, 2004). The extrinsic initiator caspase (caspase-8) couples the two pathways by initiating the mitochondrial apoptosis-induced channel (MAC), leading to activation of the intrinsic pathway (Li *et al*., 1998). The subsequent cell death for either pathway is executed through a cascade activation of effector caspases (e.g., caspase-3) by initiator caspases (e.g., caspase-8 and -9) and the amplification of death signals implemented by several positive feedback loops and inhibitors in the network (Arends and Wyllie, 1991; Budihardjo *et al*., 1999; Nunez *et al*., 1998; Oppenheim, 1991; Takahashi and Earnshaw, 1996; Thornberry and Lazebnik, 1998; Zimmermann *et al*., 2001). While apoptosis can be activated by either pathway, some cell lines are pathway specific. Cells requiring death receptors (and caspase-8) but not needing help from mitochondria organelles for apoptosis are classified as type I, such as T cells and thymocytes (Barnhart *et al*., 2003); conversely type II cells, for example, hepatocytes of Bcl-2 transgenic mice (Barnhart *et al*., 2003), have a reduced DISC formation and predominantly depend on the mitochondria pathway (formation of apoptosome and caspase-9) to undergo cell death (Barnhart *et al*., 2003; Fulda *et al*., 2001; Scaffidi *et al*., 1998; Schmitz *et al*., 2000).

The extrinsic pathway is initiated by the assembly of the DISC, which is formed by the ligation of transmembrane death receptors with extracellular death ligands (Ashkenazi and Dixit, 1998). One of the most easily characterized death receptors is Fas, a member of Tumor necrosis factor receptor family TNFR1 also called CD95 or Apo1, (Marsden and Strasser, 2003; Strasser *et al*., 1995) with corresponding ligand FasL. FasL is a homotrimer, a molecule with three identical polypeptides, that serves as an extracellular signal of apoptosis and induces the trimerization of Fas (Gruss and Dower, 1995; Nagata, 1997; Smith *et al*., 1994). This binding clusters the intracellular death domains of each Fas (Ashkenazi and Dixit, 1998; Nagata, 1997; Tartaglia *et al*., 1993), allowing adaptor proteins called FADD (Fas-associating proteins with death domain) to attach

(Boldin *et al*., 1995; Chinnaiyan *et al*., 1995). Recent structural data by Scott *et al*., 2009 found Fas to exist in both closed and open forms, only the latter of which allows FADD binding and hence transduction of the apoptotic signal. Moreover, open Fas were shown to be capable of self-stabilization through stem helix and globular interactions, suggesting that perhaps FasL is not necessary for Fas clustering. The full complex then recruits initiator caspase zymogens, such as, procaspase-8, through death effector domain interactions, and catalyzes their activation to, its corresponding, caspase-8. Initiator caspases then activate effector caspases, e.g., procaspase-3/caspase-3, which ultimately execute cell death by direct cleavage of cellular targets (Nicholson, 1999; Nicholson and Thornberry, 1997; Nunez *et al*., 1998; Thornberry and Lazebnik, 1998).

The intrinsic pathway is activated by stimuli (such as cellular stress or extrinsic pathway signals) inducing mitochondrial membrane permeabilization, followed by the formation of the apoptosome (Eskes *et al*., 2000; Green, 2000). The apoptosome is a large caspase-activating complex (Cain *et al*., 1999, 2000, 2002) that assembles in response to cytochrome c released from mitochondria due to physical or chemical stress (Fumarola and Guidotti, 2004; Jiang and Wang, 2004). Cytosolic cytochrome c activates the protein Apoptotic protease activation factor-1 (Apaf-1) by inducing a conformational change that allows the binding of deoxyadenosine triphosphated/adenosine triphosphate (dATP/ATP) (Jiang and Wang, 2000; Kim *et al*., 2005). Activated Apaf-1 then oligomerize to form the apoptosome, a wheel-like heptamer with angular symmetry (Acehan *et al*., 2002; Cain *et al*., 2000), which recruits and activates procaspase-9 through proteolytic cleavage (Cain *et al*., 2002). Caspase-9 then induces the apoptotic cascade through catalytic activation of procaspase-3 (Li *et al*., 1997; Rodriguez and Lazebnik, 1999).

These apoptotic pathways also include essential positive and negative regulators. Negative regulators such as bifunctional apoptosis inhibitor (BAR), cellular FADD-like IL-1b-converting enzyme inhibitory protein (c-FLIP) or X-linked inhibitor of apoptosis (XIAP) prevent caspase activation. Conversely, Smac/DIABLO (Second mitochondria-derived activator of caspases/Direct IAP binding protein with low PI), which is a protein released with cytochrome c from the mitochondria, interacts with inhibitors of apoptosis to promote caspase activation (Du *et al*., 2000; Li *et al*., 2004; Madesh *et al*., 2002; Srinivasula *et al*., 2000).

Both the extrinsic and intrinsic pathways may converge at the destruction of the mitochondrial membrane. The extrinsic pathway may activate the intrinsic pathway through a mitochondrial apoptosis-induced channel (MAC) of intracellular signals involving the Bcl-2 protein family, which includes both pro-apoptotic members such as Bid, tBid, Bax, Bad, Bcl-xs, and anti-apoptotic members, including Bcl-2, Bcl-xL (Adams and Cory,

1998; Danial and Korsmeyer, 2004). Specifically, mitochondrial release of cytochrome c is enhanced by truncated Bid (Sprick and Walczak, 2004; Werner *et al.*, 2002a,b); upon cleavage by caspase-8, Bid translocates to the outer mitochondrial membrane. The MAC formation requires truncated Bid interaction with Bax, leading to membrane pore formation by Bax oligomerization (Antonsson *et al.*, 2000; Bagci *et al.*, 2006; Danial and Korsmeyer, 2004; Li *et al.*, 1998; Schlesinger and Saito, 2006; Suzuki *et al.*, 2000). The sequence of activated pro and anti-apoptotic signaling may result in cytochrome c release and caspase activation; therefore, the particular cell undergoes apoptosis.

Corresponding to the two apoptotic signaling pathways are two principal classes of cells: type I and type II (Barnhart *et al.*, 2003; Schmitz *et al.*, 2000). In response to death ligand, cells that require the mitochondrial release of apoptogenic factors for apoptosis are type II (e.g., hepatocytes of Bcl-2 transgenic mice), whereas cells that do not are type I (e.g., T cells and thymocytes). Thus, type I and II cells rely primarily on the extrinsic and intrinsic pathways, respectively (Barnhart *et al.*, 2003; Fulda *et al.*, 2001; Scaffidi *et al.*, 1998; Schmitz *et al.*, 2000).

2.4 Conclusion

The biology of decision making can be divided into three phases. The *cellular sensing phase*, in this context, is the receptor-ligand interaction, i.e., CD163-Hb:Hp or Fas-FasL. In both of the biological systems of interest, vascular inflammation and apoptosis, the *signal transduction phase*, or communication within the cell plays a determinant role in the outcome. While many of the intracellular signaling molecules and pathways are known, the interactions and mechanisms by which positive and negative feedbacks occur remains elusive. The *response phase* occurs as a result of the upstream dynamics, and often, the outcome is the only experimentally testable information, in this context, protein expression of caspase-3, CD163, and IL-10. Despite scientific advances in the aforementioned biological systems, further theoretical and quantitative study is required to understand the mechanisms responsible for a particular cellular response.

Chapter 3

Mathematical modeling background

3.1 Introduction

A given behavior in a biological system is often governed by many cellular interactions, which in aggregate, ultimately translate into a full system decision or outcome (Bhalla and Iyengar, 1999; Weng *et al*., 1999). In the last few decades, scientific and medical technology has provided significantly more information and data about biological systems and their behavior, for example consider the genomic/proteomic technologies which have enhanced the knowledge of gene/protein function and network structure. However, these governing dynamics and mechanisms may be difficult to interpret and understand qualitatively (Hashimoto *et al*., 1999; Hooper *et al*., 2001; Stark *et al*., 2003b), thus, mathematical models may be developed to explain observations that arise from seemingly simple biological components and that may be difficult to reconcile biologically, such as intra/inter-cellular interactions (Stark *et al*., 2003b).

Mathematical models are often constructed in a conceptual, theoretical, and quantitative framework using known information to describe a system. These models may provide hypotheses and/or an explanation of the inner workings of a system; however, the model findings must also be validated by experimental results. Models may be numerically simulated as computational experiments, which are often less expensive in resources than biological experiments, and may enable a deeper insight to the biology, such as predicting how physiology and phenotype emerge via cellular decisions and switches (Alon, 2007; Lodhi and Muggleton, 2009). Another benefit of creating models is the ability to motivate new experiments and then test the real biological system which can either validate a model or identify an incorrect one. While many experimentalists take into account the numerous variables and complexity within a biological system, theoreticians attempt to create a simplified representation of the system, whilst including key

components and attempting to capture the behavior of the system. For example, consider some of the first mathematical representations of a biological system, such as Alan Turing's work on morphogenesis, the process of different chemicals reacting and diffusing throughout a tissue (Turing, 1952), or Hodgkin and Huxley's mathematical model, that explained the ionic mechanisms in the giant axon of a squid responsible for initiation and propagation of an action potential along a nerve (Hodgkin and Huxley, 1952). These scientists started a trend of modeling using mathematical approaches to predict biological mechanisms. Since then, the science of modeling has evolved and presented new challenges; often, these include investigating the importance of model components such as interactions and rates of these interactions, and parameters using existing data and optimization routines.

This chapter overviews the theoretical framework and methods of analysis used for modeling biological processes specific to this thesis. Other texts are more comprehensive, see: Britton, 2003; de Vries *et al*., 2006; Edelstein-Keshet, 2004; Keener and Sneyd, 1998; Murray, 2002; Rubinow, 1975; Segel, 1980, and the following publications: Albeck *et al*., 2006; Aldridge *et al*., 2006; Alon, 2007; Angeli *et al*., 2004; Callard *et al*., 1999; Ferrell, 1996; Higham, 2008; Janes and Yaffe, 2006; Kholodenko, 2006; Lodhi and Muggleton, 2009; Stark *et al*., 2003a; Tyson *et al*., 2003.

3.2 Approach

3.2.1 Type of model

Systems encompassing complicated interactions, for example, signaling pathways and biochemical reactions, can be translated into different types of quantitative representations (Murray, 2002). Dynamical approaches, such as ordinary differential equations (ODEs) and partial differential equations (PDEs), may be employed for most reactions in signal transduction since these consider the temporal deterministic evolution of the system, and may provide mechanistic information about pathways, components and kinetics. Conversely, non-dynamic approaches i.e., statistical/clustering, may be appropriate for systems with an overwhelming amount of data and relatively little prior knowledge. In a system exhibiting homogeneous mixing, the reactions or interactions between species can be written into a system of ODEs; whereas, in systems that have spacial constraints, for example diffusion, PDEs may be more appropriate. Molecular biological systems that exhibit intrinsic noise and cell variability may be modeled by using a stochastic approach, such as stochastic simulation algorithms or stochastic differential equations;

however, these techniques are often used for populations of species with a small number of molecules. For the systems of interest, the mathematics of nonlinear ODEs are well developed and enable suitable analysis of a model to be performed; therefore, this is the chosen approach (Callard *et al*., 1999; Howison, 2005; Stark and Hardy, 2003; Stark *et al*., 2003a, 2007; Yates *et al*., 2001).

3.2.2 Level of model

While there is not a unique way to formulate a mathematical model, certain factors, such as the level of the model, must be considered. Previous models have almost exclusively focused on decision making by a single cell. There is now considerable biological information on the transcription factors, such as T-bet and GATA-3, which determine the decision made by a single cell in the immune system. The intra-cellular behavior of these has been modeled using systems of ordinary differential equations (Höfer *et al*., 2002; Yates *et al*., 2004), revealing switch-like behavior in each transcription factor, with the whole system acting as a pair of coupled switches (Yates *et al*., 2004). Models have also previously been constructed at the cell-population level, for example Yates *et al*., 2000; in practice, however, the behavior of switches within individual cells is modulated by a rich repertoire of cell-cell signals. A preliminary multi-level model, combining the intracellular switches with cell-cell signaling via cytokines was constructed in Yates *et al*., 2004, using a state-structured framework. Since signaling occurs within an individual cell as well as coupled cells, the development, solution and analysis of such models is a major challenge, for example consider the work of Diekmann *et al*., 2003, where even basic questions regarding existence and stability of solutions require sophisticated mathematical techniques. This is in marked contrast to the rich variety of standard mathematical tools that exist to analyze the behavior of ODE models at either the intra-cellular, or cell population levels. Formulating multi-scale models that range from the cellular to the population level is currently an active area of research since it provides the potential to develop new mathematical techniques as well as model complicated biological problems whose outcome may depend on decisions made at both the cellular and system level.

3.2.3 Level of complexity

Models of biological systems have been developed at differing levels, ranging from models with minimal interactions, which have few components and parameters, to comprehensive models that include the entire network of interactions, for example, consider

models of mitogen activated kinase pathway (MAPK) (Aksan and Kurnaz, 2003; Angeli *et al*., 2004; Brightman and Fell, 2000; Ferrell and Machleder, 1998; Ferrell and Xiong, 2001; Hatakeyama *et al*., 2003; Huang and Ferrell, 1996; Kholodenko *et al*., 1999; Markevich *et al*., 2004; Schoeberl *et al*., 2002; Yamada *et al*., 2004) or cell cycle oscillator (see Figure 1 of Ingolia and Murray, 2004). The level of complexity of models may be constrained by the known network of interactions, and often, a model does not require the inclusion of the entire network in order to analyze a specific feature or behavior of the system, as reviewed in Schlitt and Brazma, 2005 and Sauro and Kholodenko, 2004. In some cases, models may be developed and analyzed in a modularized fashion (Saez-Rodríguez *et al*., 2004), whereby the network is divided into disjoint sub-networks or modules with each module defined by an independent function or process, for example consider the integrative model of yeast's response to osmotic shock by Klipp *et al*., 2005. This approach may create connectedness within a large system and determine dependencies between functions.

Therefore, the scale and complexity of the system must be considered when developing a model.

3.3 Theoretical framework

3.3.1 Reaction kinetic models

Chemical reactions are necessary to drive changes in any organism. For reactions in the context of this thesis, consider a protein molecule binding to another molecule called a ligand. This binding forms weak chemical bonds which often require a good physical fit, such as a lock and key between the two molecules. These two molecules or reactants may be represented by A and B and their interaction produces a product C at a speed or rate of k, which can be described by the following forward reaction:

$$A + B \xrightarrow{k} C. \tag{3.1}$$

Valuable information may be obtained from describing reactions in an ODE framework, such as exact or approximate solutions, quantitative or qualitative behavior, from the powerful theories of dynamical systems (Stark *et al*., 2003b). Consider a simple

ordinary differential equation for n variables

$$\frac{d\mathbf{x}}{dt} = f(\mathbf{x}, t, \boldsymbol{\alpha}), \tag{3.2}$$

where $\mathbf{x} \in \mathbb{R}^n$ is an n length vector of state variables (such as species, concentrations, or reactants), $\boldsymbol{\alpha} \in \mathbb{R}^m$ is a set of m parameters (relationship of interactions between variables such as binding or reaction rates), t is time, and $f : \mathbb{R}^n \to \mathbb{R}^n$ is the rate function that describes the balance between production and consumption of each x_i for $i = 1, \ldots, n$. When a system of ODEs, $\frac{d\mathbf{x}}{dt}$, and an initial condition of the system, $\mathbf{x}(0)$, is given, then the behavior of the system can be fully determined. Note, for convenience, bold face notation is used throughout this thesis to denote both vectors and sets interchangeably as appropriate.

Mass action

Define $[A] = a$, $[B] = b$, and $[C] = c$, where $[-]$ denotes concentration and $\mathbf{x} = [a, b, c]^T$. Then this forward reaction (Eq. 3.1), can be written as an ODE, where we solve for the product $\left(\frac{dc}{dt}\right)$ and conservation is maintained, that is, $a + b + c =$ constant. Conceptually, this means the change of product over time is equal to the number of times A and B collide times the probability that enough collisions occur for kinetic energy to initiate a reaction. Thus, the equation

$$\frac{dc}{dt} = kab,$$

where k is the same rate as in Eq. 3.1 is called law of mass action. This is the simplest reaction model, and in this case, only describes the forward direction. The reversible reaction,

$$A + B \underset{k_r}{\overset{k_f}{\rightleftharpoons}} C, \tag{3.3}$$

where k_f and k_r are the forward and reverse reaction rates, respectively, and $\boldsymbol{\alpha} = [k_f, k_r]^T$. The bidirectional reaction can be written as:

$$\frac{da}{dt} = k_r c - k_f ab, \tag{3.4}$$

$$\frac{db}{dt} = k_r c - k_f ab, \tag{3.5}$$

$$\frac{dc}{dt} = k_f ab - k_r c, \tag{3.6}$$

where a, b, and c are modified by both directions of the reaction. By formulating mathematical equations from these reactions, the behavior of the dynamical system may be analyzed.

A useful method for understanding and analyzing molecular dynamical systems is investigating the long-term or steady-state behavior of the system. From Eq. 3.2, the long-term or asymptotic behavior of the solutions of the vector field f are considered. As $t \to \infty$, there are a number of possibilities: f goes to plus or minus infinity, f converges to a steady-state (or equilibrium point) of the system $\mathbf{x}^*$, such that $f(\mathbf{x}^*, t, \boldsymbol{\alpha}) = 0$, or there is no convergence. If there is convergence, as in the second case, then the solution may give points $\mathbf{x}^*$, which provide information about the stability of the system. Conversely, as in the latter case, the solution may not converge; consider $f(x, t) = \sin t$, which yields an oscillating solution. Many systems of equations given a starting point or initial condition, $f(0, \boldsymbol{\alpha}) = f_0(\mathbf{x}, \boldsymbol{\alpha})$ converge to a steady-state, an attractor (a point, curve or manifold) and have a basin of attraction, such that solution of the system for certain initial conditions follow a path to the attractor. If small perturbations are made to a state near a stable attractor, then it remains in the neighborhood of the basin of attraction. Other attractors may be, for example, a periodic orbit, such as circadian rhythms or clocks, or even more complex attractors, exhibiting behavior difficult to predict, known as chaos. In most cases, applying mathematical techniques such as linearization and eigenvalue calculations of the Jacobian matrix may determine connectivity and stability at steady-state. In this case, the system of kinetic equations (Eqs. 3.4-3.6) may be solved to determine the steady-state concentrations, that is, $\frac{d\mathbf{x}}{dt} = 0$. From Eq. 3.4, then $c_{eq} = \frac{k_f}{k_r} a_{eq} b_{eq}$ (see Fig. 3.1). If there are no other reactions, then it is clear for initial a, denoted a_0, and assuming $a + c = a_0$, then

$$c_{eq} = \frac{a_0 b}{K_{eq} + b},$$

where $K_{eq} = k_r/k_f$ is the equilibrium constant and indicates the affinity between a and

b. Note that for $B = K_{eq}$, then exactly half of A is in the bound state.

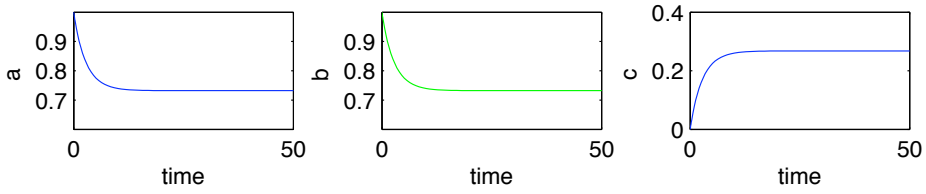

Figure 3.1: Time course of simplest reaction model. The simplest reaction model given in Eq. 3.1 may be written as a system of ODEs (Eqs. 3.4-3.6) and solved given initial conditions and reaction rates (in arbitrary units). These steady-states are solved for $a(0) = b(0) = 1, k_f = 0.1$ and $k_r = 0.2$.

Michaelis-Menten

When an enzyme, such as a protein, binds to a substrate, such as a ligand, the enzyme may catalyze the reaction; however, there may not be an equal or abundant number of reactants as assumed in the conventional chemical mass-action kinetics (Keener and Sneyd, 1998; Segel and Slemrod, 1989). In 1913, Michaelis and Menten derived the standard enzymatic reaction scheme to describe the process where an enzyme is saturated by the substrate (Edelstein-Keshet, 2004; Murray, 2002), causing the substrate to be a bottleneck (rate-limiting) for the entire reaction (Keener and Sneyd, 1998). In this reaction, there are four variables: enzyme (E), substrate (S), enzyme-substrate complex (C) and product (P). Here, the enzyme catalyzes the reaction such that an intermediate step occurs and the product is created in a two-step process: one describing the reversible substrate binding, followed by an irreversible catalytic step.

$$E + S \underset{k_r}{\overset{k_f}{\rightleftharpoons}} C \xrightarrow{k_{\text{cat}}} P + E. \tag{3.7}$$

Define $s = [S], e = [E], c = [C]$ and $p = [P]$, then it follows that the ODEs are

$$\begin{aligned}
\frac{ds}{dt} &= k_r c - k_f s e, \\
\frac{de}{dt} &= (k_r + k_{\text{cat}})c - k_f s e, \\
\frac{dc}{dt} &= k_f s e - (k_{\text{cat}} + k_r)c, \\
\frac{dp}{dt} &= k_{\text{cat}} c.
\end{aligned}$$

At steady-state, as shown in Fig. 3.2, these equations can be analyzed as before. Given that p can be found by integration and $\frac{de}{dt} + \frac{dc}{dt} = 0$, then by conservation $e + c = e_0$,

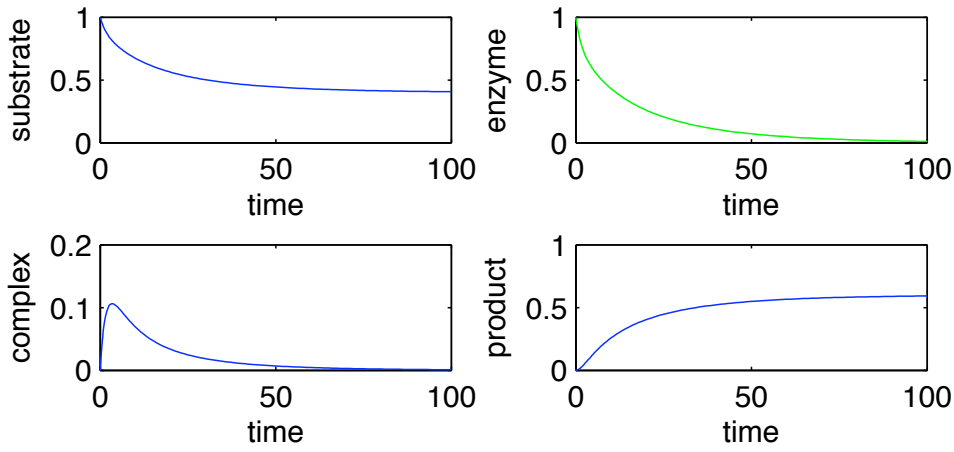

Figure 3.2: Time course of standard enzymatic reaction system. The standard enzymatic reaction given in Eq. 3.7 may be written as a system of ordinary differential equations (ODEs) and solved given initial conditions and reaction rates (in arbitrary units). These steady-states are solved for $s(0) = e(0) = 1$ and $k_f = 0.1$, $k_r = 0.2$, and $k_{cat} = 0.3$.

where e_0 is total available enzyme. One method to derive the Michaelis-Menten reaction rate expression requires the assumption that the substrate and complex are in equilibrium because one assumes that some reactions are fast, this yields

$$k_f s e = k_r c.$$

Given that $e + c = e_0$, substituting $e_0 - c$ for the enzyme, then,

$$c = \frac{e_0 s}{K_s + s}, \tag{3.8}$$

where $K_s = k_r/k_f$. It then follows that the rate, or velocity, V, at which the product is formed, is

$$V = \frac{dp}{dt} = k_{\text{cat}} c = \frac{k_{\text{cat}} e_0 s}{K_s + s} = \frac{V_{max} s}{K_s + s},$$

where $V_{max} = k_{\text{cat}} e_0$ is the maximum velocity; and the dissociation rate constant, k_{cat}, is the limiting rate in this reaction. For $s = K_s$, the reaction rate is half the maximum reaction rate.

An alternative way to analyze the enzymatic reaction is possible by quasi-steady-state assumption (QSSA) (Fowler, 1997; Segel, 1993), which assumes the concentration of the substrate-bound enzyme changes slower than that of the substrate or product and allows the dynamics of species C to be neglected, $\frac{dc}{dt} = 0$. It follows that the forward and reverse

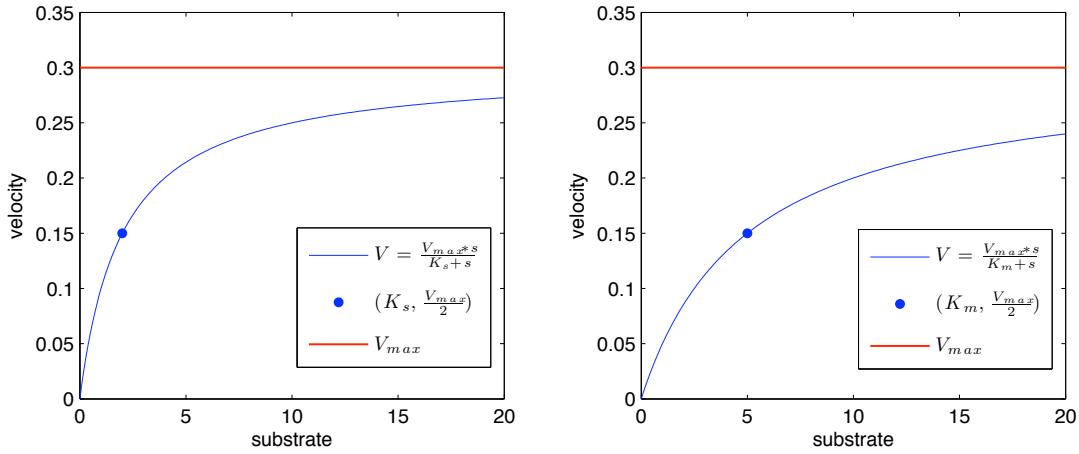

(a) Michaelis-Menten plot (equilibrium assumption) (b) Michaelis-Menten plot (QSSA assumption)

Figure 3.3: Saturation curves of standard enzymatic reaction system. The blue curve describes the relationship between the substrate concentration and the reaction rate at which the product is formed using $e(0) = 1$ and $k_f = 0.1$, $k_r = 0.2$, and $k_{\text{cat}} = 0.3$; whereas, the maximum velocity, V_{max}, is the red horizontal asymptote. Although clear from the derivation, the blue curve here is precisely that shown in Fig. 3.2d. (a) The blue marker represents the point at which $s = K_s = k_r/k_f$ or the reaction rate is half of its maximum. (b) The K_m, as used in the quasi-steady-state assumption (QSSA), also indicates the half maximal velocity; however, this relationship also includes the catalytic rate k_{cat}. As a result, the blue marker maintains the same vertical coordinate as (a); whereas, the horizontal coordinate changes due to the different properties of the kinetic rate constant $K_m = \frac{k_r + k_{\text{cat}}}{k_f}$.

reaction rates are equal, and the velocity may be determined

$$V = \frac{dp}{dt} = -\frac{ds}{dt} = \frac{k_{\text{cat}} e_0 s}{K_m + s} = \frac{V_{max} s}{K_m + s},$$

where $K_m = \frac{k_r + k_{\text{cat}}}{k_f}$, and the concentration of the complex is

$$c = \frac{e_0 s}{s + K_m}. \tag{3.9}$$

Note the similarity between Eqs. 3.8 and 3.9. These reaction equations are slightly different due to the kinetic rate constants; however, the derivation of the Michaelis-Menten reaction rate equation using the equilibrium or the QSSA assumption gives the same form. Based on the equilibrium or QSSA assumption, the Michaelis-Menten constant K_M is essentially three parameters; however, only one must be determined which allows a reduction of parameters and variables. There are, however, certain conditions that must be satisfied in order to assume QSSA, such as separation of time-scales and the assumption that inermediate reactions are short lived in relation to other reactants (Segel

and Slemrod, 1989). Conversely, for larger kinetic models, analytical investigation may be more difficult using Michaelis-Menten than mass action, despite the reduction in parameters. For more details on kinetic models, see Keener and Sneyd, 1998 and Segel, 1993.

Cooperativity

The Michaelis-Menten equation does not reflect reactants that exhibit cooperative kinetics such as when a ligand may have a higher affinity to bind to a molecule if there are already other ligands bound to that molecule or it has multiple binding sites, both of which are circumstances that relate the nature of cooperative binding. Originally, the reaction velocity of cooperative binding was discovered by Hill, 1910 to understand the dissociation curve of the enzyme, hemoglobin to its substrate, oxygen, which can be described by the general Hill equation,

$$V = \frac{V_{max} s^n}{K_m^n + s^n}, \tag{3.10}$$

where n, a Hill coefficient, also known as an "interaction" coefficient, denotes cooperative binding and provides a global measure of the response, such as ultrasensitivity (Hill, 1910; Huang and Ferrell, 1996; Weiss, 1997). The Michaelis-Menten formulation, a subcase of the Hill equation, reflects independent binding, that is, $n = 1$ (see Murray, 2002 for derivation). Positive cooperative binding is reflected in Eq. 3.10 where $n > 1$; conversely, $n < 1$ suggests negative cooperativity. Hill equations may provide many benefits such as superseding more complicated rate equations when exact mechanisms are unknown and data is insufficient (Westermark *et al.*, 2004). Often Hill coefficients $n > 1$ may increase ultrasensitivity or amplify the response to a stimulus, resulting in a sharp switch transition between states. In fact, if a Hill coefficient is equivalent to n at one level of a signaling cascade and m at another level, then the response is multiplicative, that is $n \cdot m$, and the response becomes more switch-like (Ferrell, 1997). Since equations including Hill functions are nonlinear in nature, solutions may not be determined analytically as explained in detail by Polynikis *et al.*, 2009. Cooperativity alone, giving rise to ultrasensitivity, while significant to capturing biological behavior, is not the only feature of complicated system interactions.

3.3.2 Feedback mechanisms

The universal motifs of cell-signaling networks often include feedback loops, where a cell will regulate biological products via activation or inhibition, corresponding to positive or negative feedback loops, respectively (Kholodenko, 2006; Sauro and Kholodenko, 2004; Tyson *et al*., 2003). If X and Y denote two species interacting, where species may be cells or molecules. As shown in Fig. 3.4, there are three nondegenerate feedback

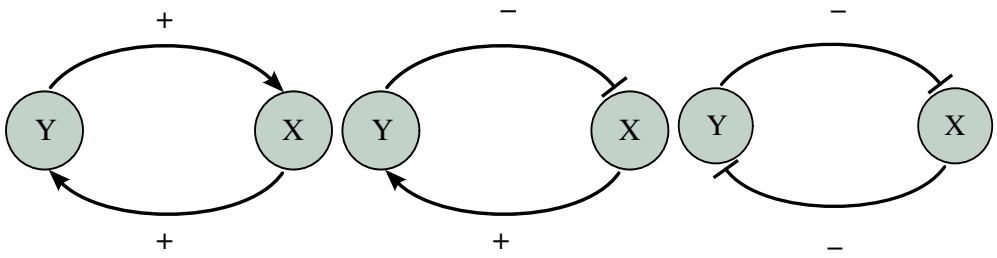

Figure 3.4: Schematic of feedback interactions. Feedback loops corresponding to biological behavior in species X and Y (a) Both species contribute to the production of the other resulting in a positive feedback loop (b) Species X activates the production of Y which inhibits the production of X resulting in a negative feedback loop (c) Species X and Y mutually inhibit one another and create a double negative feedback loop.

scenarios:

1. mutual activation giving rise to a positive feedback loop
   (X activates Y and Y activates X);

2. mutual inhibition resulting in a negative feedback loop
   (X activates Y and Y inhibits X, or X inhibits Y and Y activates X) ;

3. mutual inhibition creating a double negative feedback loop
   (X inhibits Y and Y inhibits X).

Interestingly, the behavior of double feedbacks is of particular interest to cells switching between two courses of action, such as a phenotypic switch or cell fate (Angeli *et al*., 2004; Balaban *et al*., 2004; Kussell and Leibler, 2005; Laurent and Kellershohn, 1999; Pomerening *et al*., 2003; Xiong and Ferrell, 2003). Negative feedback may provide robustness to noise, increase resistance to disturbances inside a feedback loop, and create oscillatory behavior (Ma *et al*., 2009). Examples of models displaying oscillatory behavior in the immune system, as reviewed by Stark *et al*., 2007, have focused on transcription factor nuclear factor κ B (NF-κB) (Hayot and Jayaprakash, 2006; Hoffmann *et al*., 2002;

Krishna *et al*., 2006; Monk, 2003; Nelson *et al*., 2004), and transcription factor Hes1 (Hirata *et al*., 2002; Momiji and Monk, 2008; Monk, 2003). Conversely, positive feedback may increase sensitivity of the target to the signal and lead to multiple possible outcomes (Bagowski and Ferrell, 2001; Kholodenko, 2006; Pomerening *et al*., 2003). If feedback loops are interlinked and signal at different speeds, then this may result in switches (such as turning a gene on or off) that regulate vital cellular decisions (Brandman *et al*., 2005). There are many well-known examples where theoretical models and their predicted behavior have improved the knowledge of complicated biological systems; for example, consider multistability of the mitogen-activated protein kinase (MAPK) cascade (Angeli *et al*., 2004; Ferrell and Machleder, 1998; Ferrell and Xiong, 2001; Hornberg *et al*., 2005; Markevich *et al*., 2004) or switches in the cell-cycle (Angeli *et al*., 2004; Ingolia and Murray, 2004; Kholodenko, 2006; Tyson *et al*., 2003).

Reaction kinetic models that were previously discussed only described specific chemical reactants; however, these concepts may be extended to describe general molecules interacting in cell signaling. These interactions can be translated into mathematical models which describe temporal dynamics of signaling cascades, such as cellular and intracellular communication between cells. Consider, for example, a simple two-variable system demonstrating switching in the G2/M component (entry into mitosis) of the cell cycle from Angeli *et al*. (2004) and Tyson *et al*. (2003). This model describes the mutual inhibition between Cdc2-cyclin B complex (which was previously called M-phase promoting factor) and Wee1 protein (the activated kinase that favors the G2 or interphase state). The relationship between these two variables is a double-negative feedback mechanism which my be represented by substituting the complex and protein into the X and Y of Fig. 3.4(c). Furthermore, the Cdc2-cyclin B complex and Wee1 kinase may be in either the active (on) form x_1 and y_1, or inactive (off) form x_2 and y_2, respectively. Thus, the interactions of the active and inactive forms of the species can be written as equations:

$$\frac{dx_1}{dt} = \alpha_1 x_2 - \frac{\beta_1 x_1 \cdot (\omega \cdot y_1)^{\gamma_1}}{K_1 + (\omega \cdot y_1)^{\gamma_1}}, \quad \frac{dx_2}{dt} = -\alpha_1 x_2 + \frac{\beta_1 x_1 \cdot (\omega \cdot y_1)^{\gamma_1}}{K_1 + (\omega \cdot y)^{\gamma_1}},$$
$$\frac{dy_1}{dt} = \alpha_2 y_2 - \frac{\beta_2 y_1 \cdot x_1^{\gamma_2}}{K_2 + x_1^{\gamma_2}}, \qquad \frac{dy_2}{dt} = -\alpha_2 y_2 + \frac{\beta_2 y_1 \cdot x_1^{\gamma_2}}{K_2 + x_1^{\gamma^2}},$$

where αs and βs are rate constants, Ks are Michaelis (saturation) constants, γs are Hill coefficients and ω is the coefficient reflecting the strength that Wee1 influences Cdc2-cyclin B. If conservation is assumed (total concentrations of Wee1 and Cdc2-cyclin B are unchanging), then it follows $x_2 = 1 - x_1$ and $y_2 = 1 - y_1$. For convenience, the active forms x_1 and y_1 are denoted as x and y, which yields a simpler system of coupled

differential equations:

$$\frac{dx}{dt} = \alpha_1(1-x) - \frac{\beta_1 x \cdot (\omega \cdot y)^{\gamma_1}}{K_1 + (\omega \cdot y)^{\gamma_1}}, \tag{3.11}$$

$$\frac{dy}{dt} = \alpha_2(1-y) - \frac{\beta_2 y \cdot x^{\gamma_2}}{K_2 + x^{\gamma_2}}, \tag{3.12}$$

where $\mathbf{x} = [x, y]^T$ represent active Cdc2-cyclin B and Wee1, respectively; and $\boldsymbol{\alpha} = [\alpha_1, \alpha_2, \beta_1, \beta_2, \gamma_1, \gamma_2, K_1, K_2]$ are parameter values from Angeli *et al*. (2004). For the remainder of the chapter as mathematical techniques are introduced, we will refer to this cell cycle example.

The cell cycle system (Eqs. 3.11 and 3.12) includes Hill coefficients (γ_1, γ_2) to describe the interactions between Cdc2-cyclin B complex and Wee1 protein, which makes the analytical solution not easily understood; therefore, numerics are used to calculate the steady-state. As shown in the Fig. 3.5, a time course of the system may be numerically solved and simulated given initial conditions and parameter values. When analyzing this

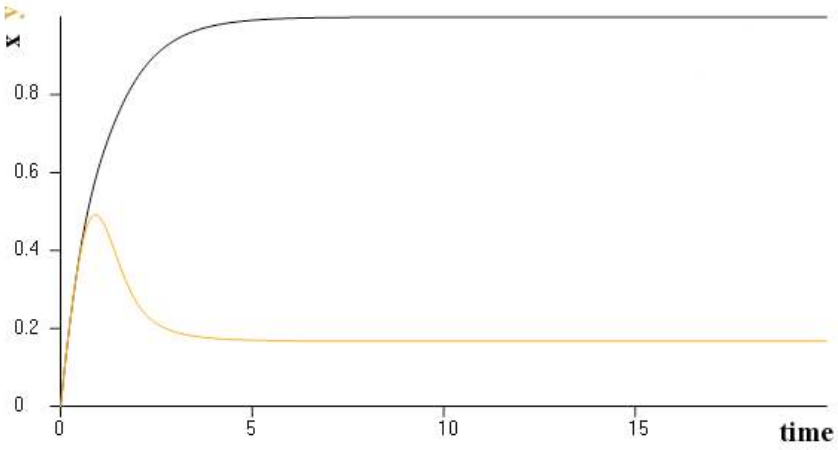

Figure 3.5: Time course for Cdc2-cyclin B complex/Wee1 system. The steady-state of the switch example system from Eqs. 3.11 and 3.12 for parameter values $\alpha_1 = \alpha_2 = 1$, $\beta_1 = 200$, $\beta_2 = 10$, $\gamma_1 = \gamma_2 = 4$, $K_1 = 30$, $K_2 = 1$, and $\omega = 1$ (Angeli *et al*., 2004) show Wee1 (yellow) approaches a low steady-state whereas Cdc2-cyclin B complex (black) approaches a high steady-state. The Wee1^{low}Cdc2-cyclin $\text{B}^{\text{high}} \sim$ Wee1^{off}Cdc2-cyclin B^{on} state, suggesting that for the given parameters and initial conditions, the cell favors the M phase of the cell cycle.

two-dimensional system, nullclines, curves that are horizontal or vertical in the vector field, may be determined by setting either $\frac{dx}{dt} = 0$ or $\frac{dy}{dt} = 0$ and can provide a graphical representation of the dynamical system that is especially helpful when the analytical solution is not available. The nullclines can be graphically shown in the state space (space of variables) or phase plane and these curves divide the $\frac{dx}{dt}$ and $\frac{dy}{dt}$ into regions where

the sign changes and the intersection of nullclines, that is, $\frac{dx}{dt} = \frac{dy}{dt} = 0$, is an equilibrium point. This system is monostable at low or high levels of Wee1, dependent on the parameter value of the input signal ω, as shown in Fig. 3.6(a) and Fig. 3.6(b).

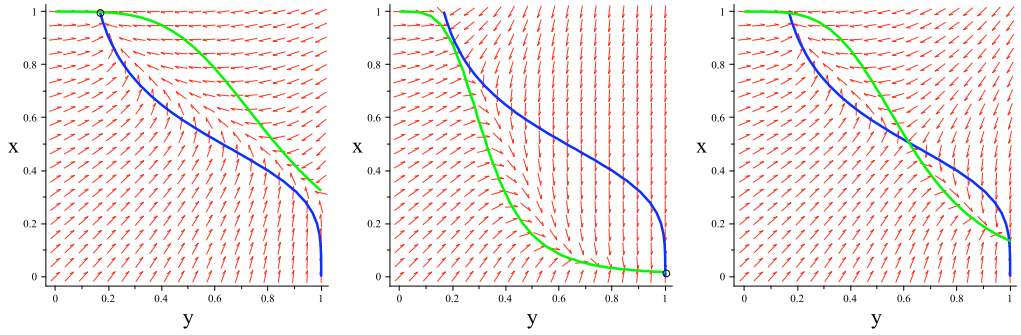

(a) $\omega = 0.75$ (b) $\omega = 1.9$ (c) $\omega = 1$

Figure 3.6: Nullclines of Cdc2-cyclin B complex/Wee1 system. Nullclines in phase plane of the Cdc2-cyclin B complex (x) and Wee1 (y) system from Eqs. 3.11 and 3.12. The vector fields represent the state space where red arrows denote the basin of attraction for each system, and nullclines (y and x nullclines are green and blue, respectively) indicate fixed points at intersections.

Biological systems may have many attractors for a given set of initial conditions and parameter values giving rise to multiple states, called multistability. Many dynamic cellular systems are bistable, that is, the system has three attractors, where two are stable states and one unstable. This is easily observed in the nullcline intersections of the cell cycle example (Eqs. 3.11 and 3.12) where Fig. 3.6(c) graphically displays the three fixed points for a value of ω that yields the two possible stable states or outcomes. The unstable state, as shown where the nullclines intersect in Fig. 3.6(c), is not observed in a biological system since even a small perturbation or noise to this initial value will destabilize it and the other two states dictate the two outcomes, such as an on or off switch. Recall positive feedbacks may lead to this switching, often bistability, and a hysteresis loop can occur representing the switches between states. A hysteresis loop occurs in a bistable system where the switching between states depends on the initial state (or condition) of the system, meaning that the system has memory and may be reversible; however, for systems with strong feedback and exhibiting irreversible bistability, the system cannot switch between states even after the parameter is changed (stimulus turned off) (Ferrell, 2002; Ferrell and Xiong, 2001; Pomerening *et al.*, 2003). The bistable properties of the cell cycle example exhibit a switch between two states as demonstrated in Fig. 3.6. The concept of stability is vital in modeling biological systems, since stable states are robust to noise. When considering the asymptotic behavior of systems, a change in parameters can:

1. slightly alter the steady-states of a system;

2. create or destroy a fixed point; or

3. change the state dramatically.

In the context of the biological systems in this thesis, a change in parameters, such as the strength of an activation or inhibition signal, initial concentration or rate of a reaction, can all change the state of the system, often rendering a different cellular phenotype. To study this behavior, we use bifurcation analysis techniques. A bifurcation occurs when a change in parameter causes significant qualitative changes in system output (Strogatz, 1994). The parameter responsible for the change in system behavior is called a bifurcation parameter and the point at which a system changes is called a bifurcation point. When drastic changes occur to the behavior of a system based on a variation in parameter, then bifurcation analysis may lead to classifying the system and the properties it holds. A bifurcation can be shown visually in a bifurcation diagram, also known as a dose-response curve in biology (see the corresponding cell cycle bifurcation diagram in Fig. 3.7). For full ODE and dynamical systems treatment, see texts such as Bender and

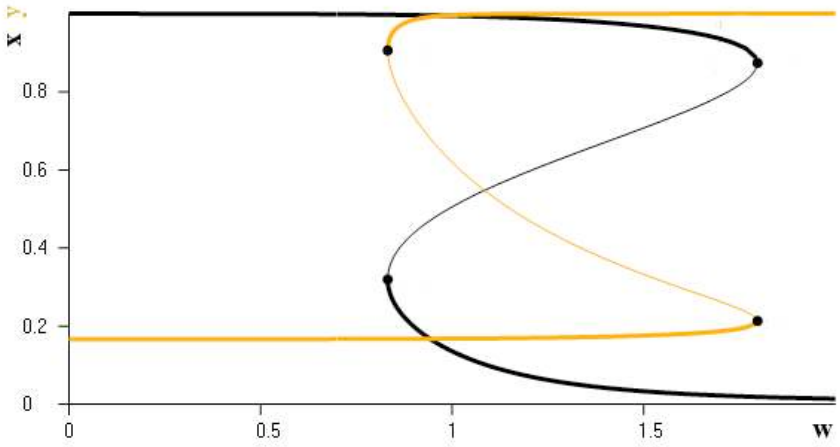

Figure 3.7: Bifurcation diagram of Cdc2-cyclin B complex/Wee1 system. The switch in the cell cycle example (see Eqs. 3.11 and 3.12) occurs as ω is varied. The cellular decision or behavior of the system under bistable conditions, that is for $\omega = 1$, is dependent on the initial condition ($x = y = 0$).

Orszag, 1999; Ellner and Guckenheimer, 2006; Glendinning, 1995; Heinrich and Schuster, 1996; Keener and Sneyd, 1998; Lodhi and Muggleton, 2009; Murray, 2002; Strogatz, 1994; Tenenbaum and Pollard, 1963.

3.3.3 Parameter analyses

The selection of parameters, such as their meaning and value in a model, is especially important; therefore, parameter analysis examines the response of the system to changes in parameters. Many methods for estimating parameters depend on time series, known in experimental biology, as time course data. These data generally give a quantitative measure of the variable level, such as mRNA or protein concentration level, at different time points. Testing a model against experimental data is a good way to identify an incorrect model; however, experimental data is often too expensive to determine all parameter values and overfitting (describing noise instead of the relationship) is a risk. Parameter estimation and model identifiability is so crucial in this field that once estimates of parameter values are calculated the next challenge is to determine which mechanisms and interactions are most significant. A good way to test the model is by exploring the sensitivity of model parameters, which is the evaluation of a qualitative or quantitative relationship between parameters and their effect on the system outcome (Saltelli *et al*., 2005).

Parameter estimation

The output and prediction of mechanistic models is often verified by inferring interactions and parameters from experimental data, which may be unknown (Brewer *et al*., 2008; Crampin *et al*., 2004). To estimate parameters, as explained in Brewer *et al*. (2008), the model is compared to the data and the difference between the two values for a given set of parameters at different points in time is calculated. This difference is the error as a function of parameters, $E_D(\boldsymbol{\alpha})$, and the goal is to minimize $E_D(\boldsymbol{\alpha})$ which may be performed in an iterative fashion (Brewer *et al*., 2008; Gershenfeld, 1999).

To implement any of these iterative minimization techniques, an approximate numerical solution $\mathbf{u}(t) \approx \mathbf{x}(t)$ from Eq. 3.2 must be found by solving

$$\frac{d\mathbf{u}}{dt} = \mathbf{f}(\mathbf{u}, t, \boldsymbol{\alpha}), \tag{3.13}$$

with parameters α_i, using Runge-Kutta (Atkinson, 1988) or a similar numerical method whenever an analytical solution is not available; otherwise, regression analysis or nonlinear fitting is implemented. The values of $\mathbf{u}(t_i)$ should be close to the data points of

$\hat{\mathbf{x}}(t_i)$ which motivates quantifying the error function $E_D(\boldsymbol{\alpha})$ using sum of squared errors

$$E_D(\boldsymbol{\alpha}) = \sum_{i=1}^{n} ||\mathbf{u}(t_i) - \hat{\mathbf{x}}(t_i)||^2. \tag{3.14}$$

As described in Eq. 3.14, the sum of squared errors, a common regression technique, is the same as the maximum likelihood where the error is minimized through an optimization routine (Jaqaman and Danuser, 2006). Here, direct search algorithms instead of other faster techniques are used when the analytical form of the function is not available. Common iterative methods include Nelder-Mead Simplex, Levenberg-Marquart, simulated annealing and Markov Chain Monte Carlo, as described by Brewer *et al*., 2008 and Ray *et al*., 2008. Furthermore, Brewer *et al*., 2008 highlight the benefit of treating the initial conditions as parameters of the model, such that the error is then defined as $E_D(\boldsymbol{\alpha}, \mathbf{x}(t_0))$ and other methods may be employed.

Sensitivity analyses

Once parameters values are estimated for a given model, either from data or existing literature, the robustness of the model must be investigated. A robust system is one where perturbations of the parameters or initial conditions, will still result in the same outcome; however, there are many trade-offs (see Blüthgen and Herzel, 2003; Kitano and Oda, 2006; Stelling *et al*., 2004). Much research has focused on stability and robustness, for example, metabolic states (Grimbs *et al*., 2007) or MAPK-cascade (Blüthgen and Herzel, 2003); however, certain properties of a biological system must also be able to withstand variations in environment. There are specific techniques for computing total parameter variation (TPV), see Barkai and Leibler, 1997 and this may be achieved by analyzing the effects of the parameters on the system by conducting sensitivity analysis (Gutenkunst *et al*., 2007).

Local sensitivity analysis determines how a perturbation to a parameter affects the output of a system. The output of $d\mathbf{x}/dt = f(\mathbf{x}, t, \boldsymbol{\alpha})$ (previously introduced as Eq. 3.2) can be approximated by the first-order Taylor series around the baseline or reference input values, thus, the local sensitivity coefficient, $s_{i,j}$ is the partial derivative of the ith state to the jth parameter

$$s_{i,j}(t) = \frac{\partial x_i(t)}{\partial \alpha_j},$$

where $j = 1, \ldots m$ and $i = 1 \ldots n$. The $s_{i,j}$ elements form the sensitivity matrix

$S = \partial \mathbf{x}/\partial \boldsymbol{\alpha}$, which may be calculated by determining the the column sensitivity vector $S_j = \partial \mathbf{x}/\partial \alpha_j$ at each jth parameter by simultaneously solving the states:

$$\frac{dS_j}{dt} = \mathbf{J}(t) \cdot S_j + F_j, \tag{3.15}$$

where $\mathbf{J} = \partial \mathbf{f}/\partial \mathbf{x}$ is the Jacobian matrix, $F_j = \partial \mathbf{f}(t)/\partial \alpha_j$ is the parametric Jacobian matrix, $\mathbf{x}(t_0) = \mathbf{x_0}$ and $S_j(t_0)$ is a zero vector (Yue *et al*., 2008). This local deterministic method should be used for systems of ODEs with a known range of parameter values.

Global sensitivity analyses; conversely, use statistical approaches to investigate how all the parameters, globally, affect the model output (Saltelli *et al*., 2000). Methods employed include partial rank correlation coefficient analysis (PRCC), Sobol's method, multi-parametric sensitivity analysis (MPSA), weighted average of local sensitivities (WALS), and the Fourier amplitude sensitivity test (FAST). Briefly, PRCC is based on multiple linear regression and uses latin hypercube sampling scheme, Sobol and FAST are variance-decomposition methods (Sobol uses Monte Carlo integrations and FAST uses Fourier analysis), MPSA uses a classifier-based discrimination scheme, and WALS extends local sensitivity analysis; for details, see Bentele *et al*., 2004; Chan *et al*., 1997; Marino *et al*., 2008; Saltelli *et al*., 2005; Sobol', 2001; Turányi, 1990; Zheng and Rundell, 2006; Zi *et al*., 2005. As shown in Fig. 3.8, local and global sensitivity analysis of the cell cycle model of Eqs. 3.11 and 3.12 has been performed. The sensitivities are each calculated using a different approach and these results may used for different purposes; however, overall, the parameters ω and γs are globally significant to the steady-state Wee1 response. This is clearly the case for ω which was shown in the bifurcation diagram to be responsible for changes in the steady-state; similarly, since the Hill coefficient may describe the cooperativity, changes in this value often translate into a more sensitive response of the steady-state behavior. Therefore, as demonstrated in the example, performing sensitivity analysis can identify key parameters that influence the overall response of the model system behavior.

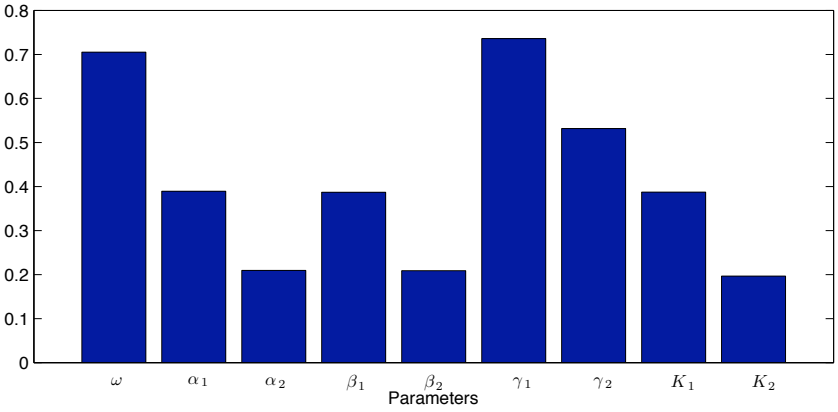

(a) Local sensitivity analysis of Wee1

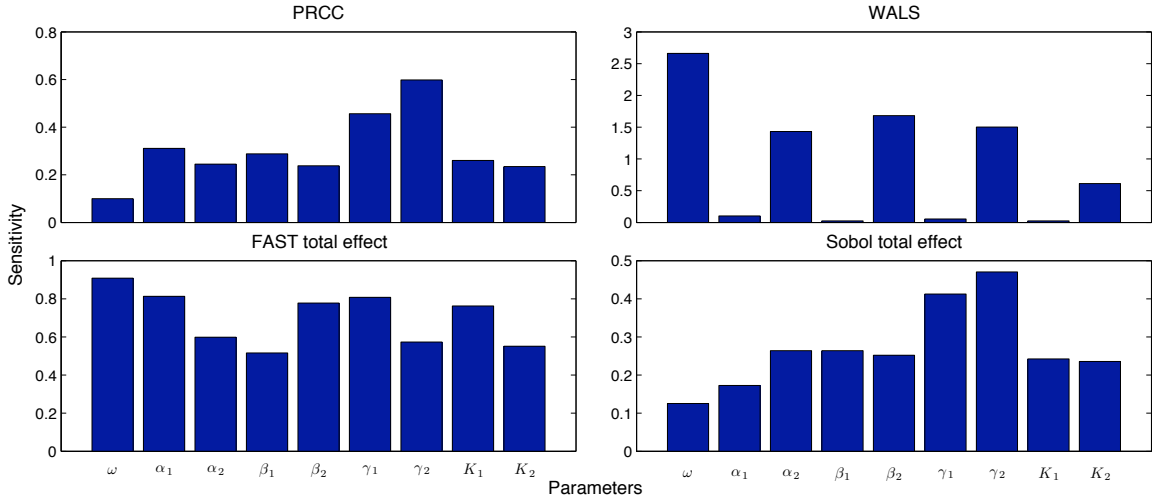

(b) Global sensitivity analysis of Wee1

Figure 3.8: Sensitivity of Cdc2-cyclin B complex/Wee1 system. Sensitivity of Wee1 (y) in the Cdc2-cyclin B / Wee1 system from Eqs. 3.11 and 3.12. Local sensitivity analysis was conducted with a perturbation coefficient of 0.01 about parameters, whereas parameters are perturbed by one order of magnitude and 10^3 simulations in the global analyses. The global analyses identify ω and γs as most significant to the steady-state of Wee1. Note that certain global analyses may be used for different purposes, such as PRCC and FAST (sampling versus variance), which offer measures of particular model properties.

3.4 Model selection

When constructing a mathematical representation of a complex system, often more than one model is developed to describe a particular system; however, steady-state and parameter analysis may not be sufficient for determining the most appropriate model. This may happen for a variety of reasons including unknown mechanisms, parameter values or initial conditions of variables within the network. A cross-disciplinary principle, known as Occam's razor or parsimony, that is, the simplest explanation is often correct, may be used for developing and selecting mathematical models. For example, if two models accurately describe a system where one model is simple (few unknown parameters and variables) and the other is more complicated, then by Occam's razor, the simpler model is chosen and this principle may serve as a model selection tool. However, discrimination between models is often not straight forward which has necessitated the development of more sophisticated techniques (Dzeroski and Todorovski, 2008; Ingram *et al*., 2008; Manrai and Gunawardena, 2008; Toni *et al*., 2009; Xu *et al*., 2010). Often, model selection may be performed using likelihood ratio tests, Akaike information criterion or Bayesian information criterion; however, recently, approximate Bayesian computation (ABC) has become favored since the method employs a simulation procedure that evades the likelihood calculation. Toni *et al*., 2009 developed an ABC method based on sequential Monte Carlo (SMC) to enable both model selection and parameter fitting by inferring a posterior distribution of values. Dzeroski and Todorovski, 2008 have developed a machine learning method which only seems appropriate when the model structure is completely unknown; however, it is computationally intensive. When the structure of models is known, for example, mechanisms of multisite phosphorylation following Manrai and Gunawardena, 2008, then steady-state invariants derived using tools from algebraic geometry may be used to distinguish between models. Model discrimination may be performed using model selection tools, and therefore, may enable important model components to be identified.

3.5 Computational tools

All calculations in this thesis were performed using Maple 12 (Maplesoft, Waterloo, Ontario, Canada), or MATLAB (and toolboxes therein) versions 7.4.0, R2008bSV, and R2009b (The MathWorks, Inc., Natick, MA, USA). MATLAB add on toolboxes used include SBTOOLBOX2 (Schmidt and Jirstrand, 2006) for sensitivity analysis and SBML export, SBML-SAT (Zi *et al*., 2008) for sensitivity and robustness analysis, CL_MATCONT

(Dhooge *et al*., 2003) for bifurcation analysis. Additional bifurcation analysis tools include XPPAUT (Ermentrout, 2009) and Oscill8 (Conrad). The approximate Bayesian computation scheme based on sequential Monte Carlo (ABC-SysBio package in Python with GPU support) (Liepe *et al*., In press) was used for parameter fitting and model selection in Chapter 5. The final work in Chapter 7 was performed using Sage 4.2.1 (http://www.sagemath.org/), supplemented with NumPy/SciPy (http://www.scipy.org/; Oliphant, 2007) for numerical computation and matplotlib (Hunter, 2007) for data visualization. The Sage worksheet containing all computations described in Chapter 7 can be downloaded from http://www.sagenb.org/home/pub/1224/.

3.6 Conclusion

Complex biological systems necessitate a quantitative study. The chosen framework is highly dependent on available information. Certain mathematical approaches favor specific methods for studying a system; in the context of understanding systems with reactions and feedback mechanisms, dynamical models offer valuable information. To construct such a model, many factors must first be considered, such as scalability of the model (cell, population or multi-scale), and complexity of the model (the number of variables/parameters which is often dependent on the desired scope of the model). Cellular decisions, specifically the mechanisms of how cells switch between different states may be modeled using a chemical reaction approach and these interactions can be expressed as ordinary differential equations. An essential foundation in reaction-based ODE models requires a basic understanding of the kinetics between reactants or species of a process, which may be described via mass action or Michaelis-Menten kinetics. While Michaelis-Menten has its limitations, it is often used to reduce the number of parameters in the model by eliminating complex formation dynamics. These reaction kinetic models may use dynamical systems approaches to describe how a system with many variables (such as species or concentrations) evolves over time, provided that certain information is known, such as interactions between species. Analysis of ODEs may be conducted to determine the long-term or steady-state behavior, such as the outcome of a system and the number of steady-states; furthermore, bifurcation analysis complements this by studying the qualitative changes within a dynamical system as parameter values are varied. Since the behavior of the system can be highly dependent on parameters values, techniques have been developed to estimate parameter values from existing information/data and identify the parameters most sensitive to altering the outcome of a system. Dynamical models also allow the inclusion of complicated interactions such as feedback loops, to describe

the behavior of a system; however, discriminating between proposed models presents many challenges and requires tools for model selection.

Clearly, dynamical systems is a powerful tool to describe a biological system which may enable a deeper understanding of the inner workings and behavior that might escape intuition; thus, the focus of the work hereafter is a dynamical systems approach to analyzing and selecting the models developed.

Chapter 4

Models of Hb:Hp induced macrophage response

4.1 Overview

The focus of this work is the development of models of the macrophage scavenger receptor cluster of differentiation 163 (CD163) and the inflammatory response induced by hemoglobin : haptoglobin (Hb:Hp) complexes. In collaboration with experimentalists, this is investigated through the construction of a coupled systems of ODEs. The first model presented identifies a positive feedback loop between CD163 and interleukin-10 (IL-10), to be responsible for the observed anti-inflammatory response; furthermore, steady-state and bifurcation analysis predict an anti-inflammatory phenotypic switch in the macrophage cell. This model is in agreement with flow cytometric measurements of plaque macrophages that exhibit a switch-like behavior, from a lipid-laden and pro-inflammatory phenotype to an anti-inflammatory and atheroprotective (HA-mac) cell phenotype. This first model is extended to incorporate additional interactions, such as feedback and cooperativity, that may enable a bistable response. While these models are not as simple as the former; and therefore, not as easy to analytically investigate, numerical solutions of the extended models reveal that the inclusion of additional factors are qualitatively better models when compared to data. The proposed models improve the understanding of the macrophage differentiation in this system by including a switching mechanism within the macrophage from a pro-inflammatory to anti-inflammatory response.

This research was conducted in collaboration with Dr. Joseph J. Boyle and co-workers from the Imperial College London Faculty of Medicine and published (Boyle *et al.*,

2009).

4.2 Introduction

Recall from Chapter 2 that immune response is highly dependent on how mononuclear phagocytes respond to their external environment (Gordon, 2003; Gordon and Taylor, 2005; Mosser, 2003; Mosser and Edwards, 2008). The inflammatory disease, atherosclerosis, characterized by plaque formation along the inner lining of the arterial wall, recruits monocytes to the arterial plaque. Under certain conditions, these monocytes may differentiate into macrophages with scavenger receptor CD163 surface expression (Buechler *et al*., 2000; Philippidis *et al*., 2004), which acts as a vehicle to import free pro-oxidative stress hemoglobin-haptoglobin (Hb:Hp) complexes (Kristiansen *et al*., 2001). Internalized Hb:Hp has been found to induce a response in inflammatory plaques; specifically, the Hb:Hp-CD163 binding has been found to induce an anti-inflammatory response of IL-10 (Boyle *et al*., 2009; Lee and Chau, 2002; Moestrup and Moller, 2004; Otterbein and Zuckerbraun, 2005; Ugocsai *et al*., 2006; Van den Heuvel *et al*., 1999). Recent studies have also found interactions between HO-1 and IL-10 suggesting the existence of a positive feedback loop (Abraham and Drummond, 2006; Lee and Chau, 2002; Ricchetti *et al*., 2004; Schaer *et al*., 2006). It has also been found that macrophages stimulated with IL-10 can induce a high expression of CD163 (Sulahian *et al*., 2000; Williams *et al*., 2002).

It was hypothesized by Dr. Boyle that macrophages originating from hemorrhaging plaques exposed to Hb:Hp participate in a switch-like transition from a $CD163^{low}$ HLA-DR^{high} lipid-laden and proatherogenic phenotype to a $CD163^{high}$ HLA-DR^{low} (see Fig. 4.1(a)) (Glass and Witztum, 2001; Hansson *et al*., 2002). The $CD163^{high}$ HLA-DR^{low} cell is referred to as the HA-mac lineage, characteristic of an increase in IL-10. We investigate the anti-inflammatory and antioxidant phenotype of *in vitro* differentiated $CD163^{high}$HLA-DR^{low} macrophages.

4.3 Materials and methods

4.3.1 Model formulation

As introduced in Chapter 3, many molecular interactions may be represented as ordinary differential equations (ODEs) in the form of mass action or Michaelis-Menten kinetics. The first approximation, from a standard pharmacological modeling approach, is given

by

$$\text{Effect} = \frac{R[\text{Ligand}]}{[\text{Ligand}] + K_d},$$

where R is a constant reflecting total receptor number (how strong the signal produces the effect), [Ligand] is the concentration of cytokine or stimulant and K_d is the dissociation constant. This ligand-receptor model resembles Michaelis-Menten kinetic equations described in Chapter 3, rather than mass action since in this case, the ligand concentration may limit the effect. Specific to the models developed, the variables are $[\mathrm{CD163}]$ and $[\mathrm{IL}-10]$ which describe the time course of the concentrations of the two species. The rate of change of each species is determined by the production and degradation of each. As a general relation using standard modeling approaches (Kholodenko, 2006; Tyson *et al*., 2003), coupled ordinary differential equations, Eq. 4.1 describe the evolution of the X_i concentration,

$$\frac{d[X_i]}{dt} = [X_i] \text{ production} - [X_i] \text{ degradation}, \tag{4.1}$$

where i denotes the number of variables or species within the system.

4.3.2 Experimental data

Experimental work was conducted specific to the HA-mac and anti-inflammatory response induced by Hb:Hp complexes.[1] Immunohistochemistry and flow cytometry data were obtained in conjunction with the model results presented (see Figs. 4.1, 4.2 and 4.7).

4.4 Results and discussion

To investigate the stable regulation into the two macrophage lineages, a positive feedback loop is hypothesized in which Hb:Hp binding to CD163 leads to IL-10 secretion, in turn up-regulating CD163. Positive feedback loops have recently been shown to generate sta-

[1]Erythrocytes were obtained from monocyte purification, subjected to hypotonic lysis in 50mL sterile endotoxin-free water (Invitrogen, tissue culture grade water). Cells were centrifuged at 3000rpm to remove debris (sterile tissue culture 50mL centrifuge tubes), and the supernatant was collected. Hb concentration was determined by Soret peak spectrophometry, endotoxin-free status by Limulus amebocyte assay and purity by SDS-PAGE and Coomassie staining. Hb:Hp complexes were prepared and added at culture outset as for commercial Hb, after which the macrophages were cultured as before. Flow cytometry staining was (CD163-FITC, HLA-DR-PE and isotype controls), but without dual-staining to obviate cytometer signal compensation.

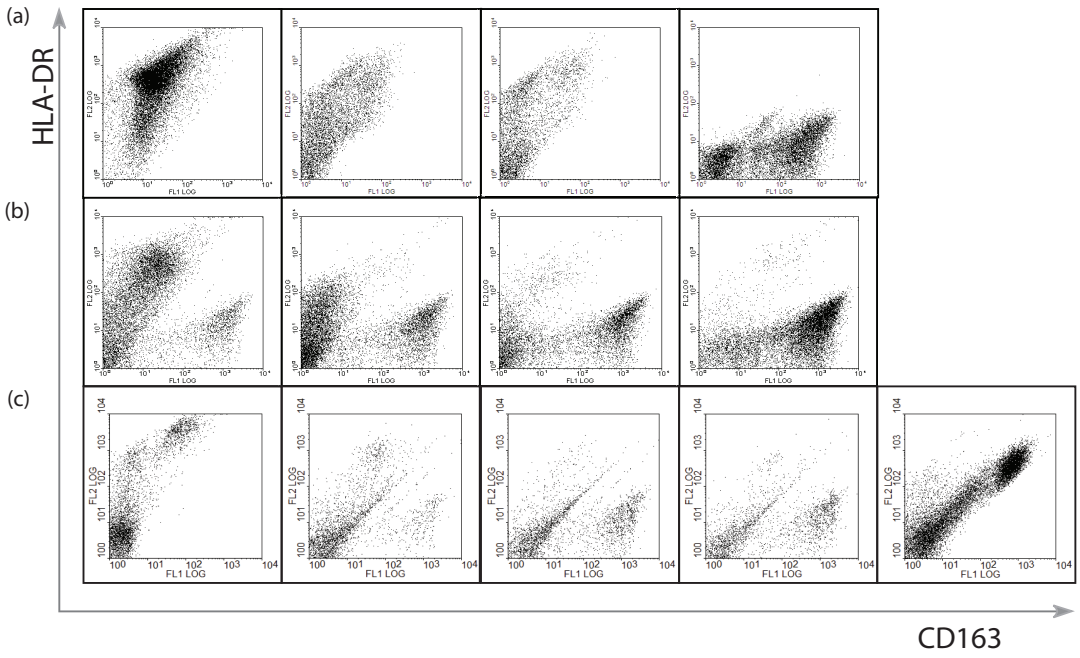

Figure 4.1: Flow cytometry data (Boyle). Mechanisms causally linking Hb:Hp to HA-mac phenotype. Human peripheral blood monocytes were incubated in the presence of Hb, Hp, Hb:Hp complexes, and cytokines, at the indicated concentrations. After 8 days of culture, macrophages were detached and dual stained for CD163 (FITC) and HLA-DR (PE). Representative flow cytometric dot plots, a technique used to count and examine the effects of Hb:Hp complexes versus control on the assays. For each, the x axis is CD163 and the y axis is HLA-DR (isotype controls were in the first quadrant, not shown). (a) Stimulus effect on HA-mac phenotype. From left to right: unstimulated culture of day 8 macrophages, incubated with Hb at 100 nM, incubated with Hp at 100 nM, incubated with Hb:Hp complexes at 100 nM. (b) Concentration-effect curves for IL-10. From left to right: incubated with 50 pM IL-10 from outset of culture, 500 pM, 5 nM, 50 nM. (c) Concentration-effect curves for Hb:Hp complexes. All are macrophages culture day 6 cultured in the presence or absence of Hb:Hp complexes at the indicated concentrations from outset of culture to analysis. From left to right: untreated, 1 nM, 10 nM, 100 nM, 1 μM.

ble divergence and commitment to two steady-states in T-helper cells (Yates *et al.*, 2000) and in monocytes vs neutrophils (Laslo *et al.*, 2006). More generally, similar regulatory architectures are being observed in a variety of systems biology contexts (Tyson *et al.*, 2003).

The feedback loop between CD163 and IL-10 in response to Hb:Hp is shown diagrammatically in Fig. 4.3. Simple conceptual models of this loop are developed using two coupled ordinary differential equations. This is intended to demonstrate the feasibility of this feedback loop yielding a threshold value of Hb:Hp that differentiates between $CD163^{high}HLA\text{-}DR^{low}$ phenotype (a lipid-laden macrophage that functions to increase atherogenicity) (Glass and Witztum, 2001; Hansson *et al.*, 2002) and $CD163^{low}HLA\text{-}DR^{high}$ phenotypes. These models are therefore deliberately kept as simple as possible and are not meant to provide a complete quantitative description of the regulatory system.

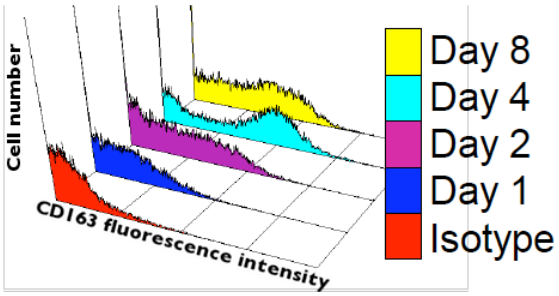

Figure 4.2: Time course of CD163 fluorescence induced by Hb:Hp. Macrophages treated with Hb:Hp complexes at $10^{-7} mol/L$. CD163 expression (x-axis) and cell number (y-axis) are measured at days 1, 2, 4, and 8.

Since none of the required parameter values have been experimentally determined, the variables, $[\mathrm{CD163}]$ and $[\mathrm{IL}-10]$ and time, are described in arbitrary units and parameters assigned illustrative values. This enables a theoretical exploration of a particular network topology with given dynamics; furthermore, as described later, it is possible to verify these arbitrary parameter choices do not affect the conclusions.

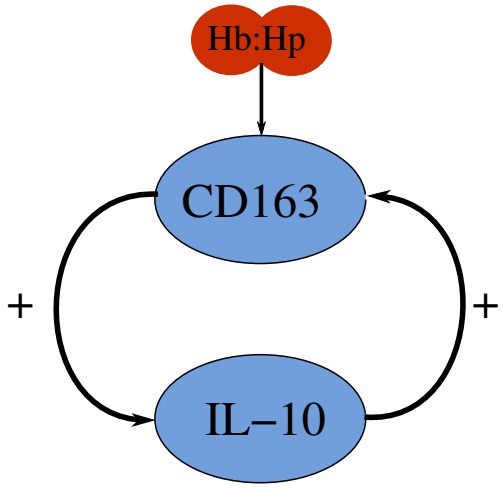

Figure 4.3: Diagram of CD163/IL-10 feedback loop. Hb:Hp complex (red) initiates CD163 (blue) to produce IL-10 (blue) which creates a positive feedback loop.

A positive feedback loop between CD163 and IL-10 could generate runaway growth of both species. To confirm that it could generate a stable switch governed by [Hb:Hp] levels, conceptual models were constructed with the intention to test the principle that a threshold level of Hb:Hp could switch the system between two lineages rather than providing a complete quantitative description.

The motivation, construction, analysis and discussion of each developed model is presented in this section; the model variables, parameters and dynamical equations are summarized in Tables 4.2 and 4.1. Models are qualitatively compared to experimental

Model	Equations
4.1	$\frac{d[\mathrm{CD163}]}{dt} = \frac{p_1[\mathrm{IL-10}]}{[\mathrm{IL-10}]+K_{d1}} - k_1[\mathrm{CD163}]$ $\frac{d[\mathrm{IL-10}]}{dt} = \frac{[\mathrm{CD163}][Hb{:}Hp]}{[Hb{:}Hp]+K_{d2}} - k_2[\mathrm{IL}-10]$
4.2	$\frac{d[\mathrm{IL-10}]}{dt} = \frac{[\mathrm{CD163}][Hb{:}Hp]}{[Hb{:}Hp]+K_{d2}} - k_2[\mathrm{IL}-10] = 0$
4.3	$\frac{d[\mathrm{CD163}]}{dt} = \alpha + \frac{p_1[\mathrm{IL-10}]}{[\mathrm{IL-10}]+K_{d1}} - k_1[\mathrm{CD163}]$ $\frac{d[\mathrm{IL-10}]}{dt} = \frac{[\mathrm{CD163}][Hb{:}Hp]}{[Hb{:}Hp]+K_{d2}} - k_2[\mathrm{IL}-10]$
4.4	$\frac{d[\mathrm{CD163}]}{dt} = \alpha + \frac{p_1[\mathrm{IL-10}]}{[\mathrm{IL-10}]+K_{d1}} - k_1[\mathrm{CD163}]$ $\frac{d[\mathrm{IL-10}]}{dt} = \frac{[\mathrm{CD163}][Hb{:}Hp]}{[Hb{:}Hp]+K_{d2}} + \frac{p_1[\mathrm{IL-10}][\mathrm{CD163}]}{[\mathrm{IL-10}]+K_{d3}} - k_2[\mathrm{IL}-10]$
4.5	$\frac{d[\mathrm{CD163}]}{dt} = \alpha + \frac{p_1[\mathrm{IL-10}]^n}{[\mathrm{IL-10}]^n+K_{d1}} - k_1[\mathrm{CD163}]$ $\frac{d[\mathrm{IL-10}]}{dt} = \frac{[\mathrm{CD163}][Hb{:}Hp]}{[Hb{:}Hp]+K_{d2}} - k_2[\mathrm{IL}-10]$

Table 4.1: Dynamical equations for the models with species $[\mathrm{CD163}]$ and $[\mathrm{IL}-10]$.

data, after the construction of the models and comparison of the data to model results are discussed.

4.4.1 Model 4.1: Simple first model

Motivation and dynamical equations

The intention of constructing this simple model was to test whether a threshold level of Hb:Hp could be responsible for switching the system between two lineages, rather than providing a complete quantitative description of the system. The model is described by a coupled system of differential equations:

$$\frac{d[\mathrm{CD163}]}{dt} = \frac{p_1[\mathrm{IL}-10]}{[\mathrm{IL}-10]+K_{d1}} - k_1[\mathrm{CD163}], \tag{4.2}$$

$$\frac{d[\mathrm{IL}-10]}{dt} = \frac{[\mathrm{CD163}][Hb:Hp]}{[\mathrm{Hb{:}Hp}]+K_{d2}} - k_2[\mathrm{IL}-10]. \tag{4.3}$$

Here [Hb:Hp] is a parameter indicating the strength of the Hb:Hp input (in arbitrary units) and p_1 is a parameter that determines the sensitivity of [CD163] upregulation to [IL-10] levels. Degradation is modeled using simple exponential decay with rates k_1 and k_2, while the parameters K_{d1} and K_{d2} determine the saturation of the production rates of [IL-10] and [CD163] respectively.

Three different limiting factors were considered for the saturation of [IL-10]:

Variable	Description	Initial condition
$[\mathrm{CD163}]$	CD163 macrophage scavenger receptor	0.1
$[\mathrm{IL}-10]$	Interleukin-10 anti-inflammatory cytokine	1
Parameter	**Description**	**Baseline value**
p_1	rate at which IL-10 upregulates CD163	10
K_{d1}	saturation of CD163 production rate	12
k_1	degradation rate of CD163	1
[Hb:Hp]	hemoglobin:haptoglobin	$10^{-6} - 10^{0}$
K_{d2}	saturation of IL-10 production rate	10^{-5}
k_2	degradation rate of IL-10	0.75
α	basal production rate of CD163	0.01
p_2	strength of IL-10 autoactivation	1
K_{d3}	saturation of IL-10 autoactivation rate	10^{-3}
n	hill coefficient	2

Table 4.2: Description of model variables and parameters, where [-] denotes concentration, p_i are synthesis rates, k_i are degradation rates, K_{di} denotes saturation constant of variable production.

1. CD163 receptor concentration;

2. CD163-Hb:Hp binding;

3. Hb:Hp only.

From a biological perspective, Dr. Boyle noted that assumption 1 (CD163 acts as the only limitation) seemed incorrect suggesting Hb:Hp is required to saturate IL-10; therefore, the remaining assumptions include Hb:Hp. The second case assumes saturation of IL-10 occurs downstream of the CD163-Hb:Hp binding and there are excess free CD163 receptors. This saturation is most likely to occur upstream, not downstream; consequently, Hb:Hp and not the CD163-Hb:Hp complex may be the limiting factor (where the formation of IL-10 is linear with respect to CD163 but saturates based on available Hb:Hp). A biological interpretation is that Hb:Hp may bind to an upstream receptor and therefore limit its binding to CD163. This in turn, effects the transcription of IL-10. Eq. 4.2 assumes that IL-10 binds to a receptor, with downstream signaling to CD163 transcription; therefore, a plausible biological interpretation is that the first term of Eq. 4.2 represents the concentration of IL-10 receptors available for CD163 binding on the cell surface. Similarly, Eq. 4.3 corresponds to the signal saturating to a limited number of CD163 receptors on the surface but a linear effect on the IL-10 transcription.

Hb:Hp acts as bifurcation parameter in transcritical bifurcation

An advantage to formulating this simplified model is that the steady-state values can be derived analytically and it is possible to verify that these arbitrary choices do not affect conclusions. Conducting steady-state analysis of this system, there are two stationary points (equilibrium concentrations), one always at the origin, $[\mathrm{CD163}]^* = [\mathrm{IL}-10]^* = 0$, which corresponds to a low CD163 concentration and the other explicitly solved for

$$[\mathrm{CD163}]^* = \frac{p_1[\text{Hb:Hp}] - k_1k_2K_{d1}[\text{Hb:Hp}] - k_1k_2K_{d1}K_{d2}}{k_1[\text{Hb:Hp}]},$$
$$[\mathrm{IL}-10]^* = \frac{p_1[\text{Hb:Hp}] - k_1k_2K_{d1}[\text{Hb:Hp}] - k_1k_2K_{d1}K_{d2}}{k_1k_2([\text{Hb:Hp}] + K_{d2}),}$$

corresponding to a high [CD163] steady-state. Since only non-negative states are of biological relevance, the above expressions must satisfy $p > k_1k_2K_{d1}$ and [Hb:Hp] $\geq H^*$, where H^* is a threshold value,

$$H^* = \frac{k_1k_2K_{d1}K_{d2}}{p_1 - k_1k_2K_{d1}}, \tag{4.4}$$

which determines whether the system will reach the low or high CD163 state. For [Hb:Hp] $= H^*$, the threshold Eq. 4.4, denotes clearly when the stability of the system switches: for [Hb:Hp] $<$ H* (Fig. 4.4(a)), the origin is stable and globally attracting (corresponding to the low CD163 phenotype); conversely, if [Hb:Hp] $>$ H* (Fig. 4.4(b)) then the origin is unstable and the positive fixed point attracts all positive solutions. In fact, it is easily observable that there is a transcritical bifurcation at the origin (see Fig. 4.8(a)).

Phenotypic switch prediction

In simulations, for high Hb:Hp concentrations, CD163 rose to a stable plateau (Fig. 4.5(a), red curves); however, for low Hb:Hp concentrations, CD163 and IL-10 (not shown) fell to negligible levels at low levels of Hb:Hp irrespective of starting concentrations (Fig. 4.5(a), blue curves). Final CD163 was independent of initial CD163. Thus the model predicts that the CD163-IL-10 positive feedback leads to two binary CD163 high or CD163 low phenotypes depending on [Hb:Hp] input. The model is sufficiently simple to analytically determine the final steady-state levels of CD163 and IL-10 (Eqs. 4.2 and 4.3) and hence show that there is a threshold level of Hb:Hp, H^*, given by Eq. 4.4, below which [CD163] drops to negligible levels (e.g., blue curves in Fig. 4.5(a)) and above which they rise to a stable plateau (e.g., red curves in Fig. 4.5(a)). This threshold is illus-

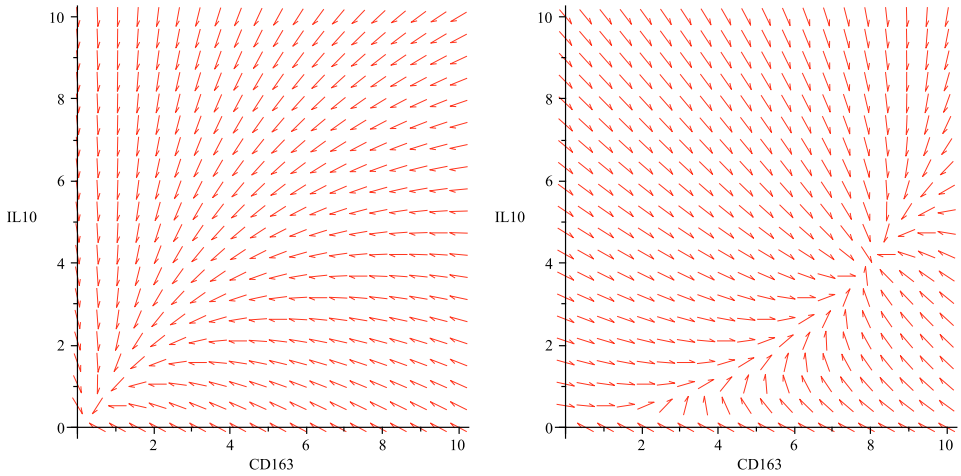

(a) CD163^{low} state (b) CD163^{high} state

Figure 4.4: Phase diagram of CD163-Hb:Hp-IL-10 system. The phase diagram re-iterates the transcritical bifurcation. The graphs show the solutions approaching the equilibrium state. All parameter values equal one unless otherwise specified. (a) Low steady-state (corresponding to fixed point at origin) where $p_1 = 2$, satisfying the biological constraint and exhibiting the state below threshold. (b) High steady-state, where $p_1 = 10$ and exceeds the given threshold (see Eq. 4.4).

trated in Fig. 4.5(b) which shows that the final steady-state level of [CD163] rises rapidly as Hb:Hp concentration reaches the threshold, before saturating to a fixed level.

The construction of the first simple model provided some insight into how the Hb-initated CD163-gated macrophage phenotypic switch may become polarized to either a high or low CD163 state; however, there were significant simplifications and assumptions which are addressed in the remaining models.

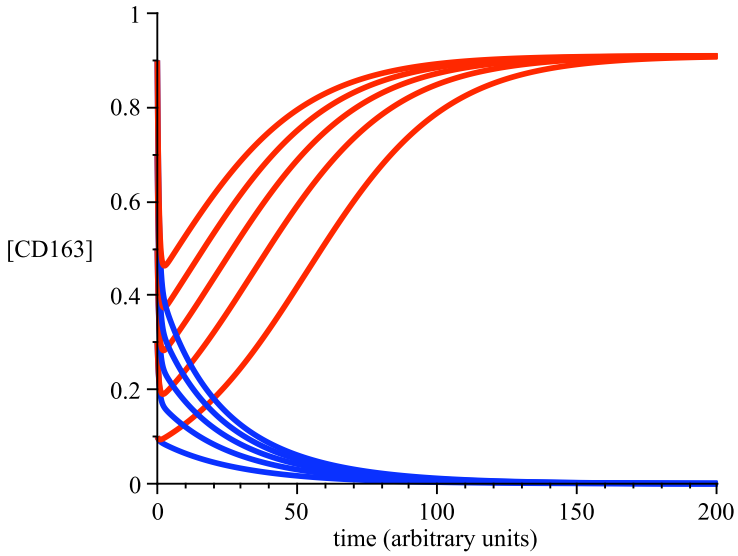

(a) Phenotypic CD163 switch

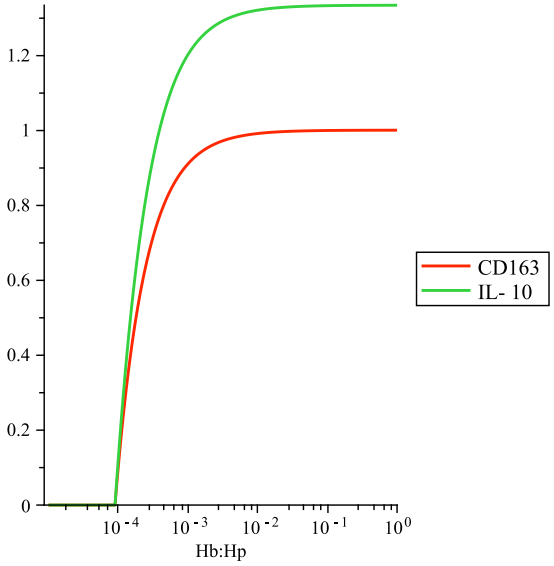

(b) Bifurcation Diagram

Figure 4.5: Phenotypic CD163 switch of CD163-Hb:Hp-IL-10 system (a) Representative simulated time course of CD163 levels in a simple mathematical model describing the positive feedback loop between CD163 and IL-10 given by Eqs. 4.2 and 4.3. Both axes are in arbitrary units. Blue curves show the behavior of CD163 for a low [Hb:Hp] input ([Hb:Hp] = 0.01 in arbitrary units) for a number of starting values ([CD163] = $0, 2, ..., 8$). Red curves show behavior for a high [Hb:Hp] input ([Hb:Hp] = 1) with the same starting levels. Other parameter values are $p_1 = 10$, $k_1 = 1$, $k_2 = 1$, $K_{d1} = 1$, $K_{d2} = 1$ (arbitrary units) and the initial level of IL-10 is 0.5 in all cases. The qualitative behavior is independent of this choice, and similar threshold behavior can be observed for all choices of k_1 , k_2 , K_{d1} and K_{d2} as long as the sensitivity of $[\mathrm{CD163}]$ to $[\mathrm{IL}-10]$ is sufficiently high ($p_1 > k1\ k2\ K_{d1}$). (b) Variation of final steady-state values of CD163 and IL-10 with Hb:Hp input (all given in arbitrary units). Parameter values are $p_1 = 10$, $k_1 = 1$, $k_2 = 12$, K_{d1} = 0.75, K_{d2} = 10^{-5}. The steady-states were obtained and clearly illustrate the threshold which for these parameter values occurs at $H^* = 9$ x 10^{-5}. Similar qualitative behavior is seen for all other parameter values as long as $p_1 > k1\ k2\ K_{d1}$.

4.4.2 Model 4.2: Non-feedback

Motivation and dynamical equations

The importance of CD163 on the production of IL-10 and the relationship between this anti-inflamatory mediator and constant CD163 is important to understand; therefore, the previous model has been modified in order to explore the IL-10 dynamics without feedback from CD163. To implement this,

$$\frac{d[\mathrm{IL}-10]}{dt} = \frac{[\mathrm{CD163}][\mathrm{Hb{:}Hp}]}{[\mathrm{Hb{:}Hp}]+K_{d2}} - k_2[\mathrm{IL}-10]$$

is set to zero and solved

$$k_2[\mathrm{IL}-10]([\mathrm{Hb{:}Hp}]) = \frac{[\mathrm{CD163}][\mathrm{Hb{:}Hp}]}{\mathrm{Hb{:}Hp}+K_{d2}}, \tag{4.5}$$

which gives the relationship of IL-10 to Hb:Hp stimulus and concentration of CD163.

Non-feedback condition alters threshold

As shown in Fig. 4.6, the production of IL-10 concentration described by Eq. 4.5 is heavily dependent on CD163; leading to IL-10 taking on a range of values. Notice that the IL-10 steady-state levels start rising at much lower levels of Hb:Hp input, suggesting there is not the same threshold H^*. This seems reasonable since the system input is taking higher levels of CD163 than those in the equilibrium CD163 feedback case previously discussed. Experimental findings also support the functional dependence of IL-10 to Hb:Hp (see Fig. 4.7(b) obtained from Dr. Boyle and Fig. 2.4 as published by Philippidis *et al*. (2004)).

4.4.3 Model 4.3: Inclusion of basal production rate

Motivation and dynamical equations

One of the notable criticisms of the coupled system (Eqs. 4.2 and 4.3) is that the first equilibrium solution is at the origin, suggesting that both IL-10 and CD163 are absent, which was an over-simplification of the aforementioned models. The inclusion of a small basal production rate term, α, to the system (see Eqs. 4.6 and 4.7) introduces a non-zero low CD163 state.

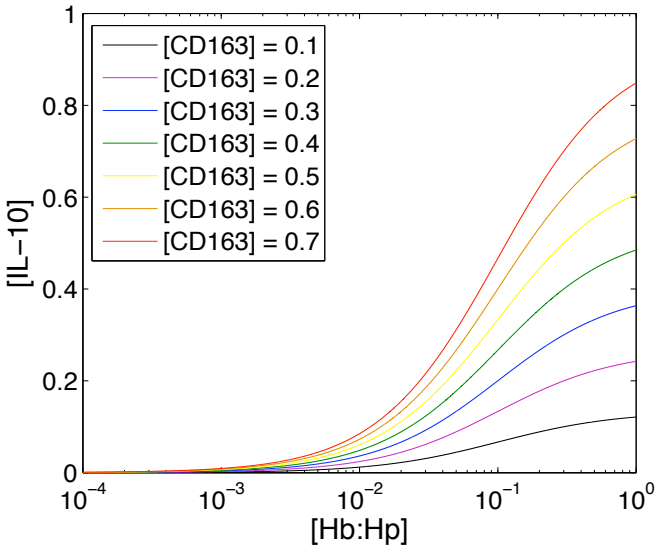

Figure 4.6: Simulated dose response of IL-10 under non-feedback conditions. Incremented every 0.1, [CD163] (arbitrary concentration) input ranges from 0.1,..., 0.7 at baseline parameter values (Table 4.2).

$$\frac{d[\text{CD163}]}{dt} = \alpha + \frac{p_1[\text{IL}-10]}{[\text{IL}-10]+K_{d1}} - k_1[\text{CD163}], \tag{4.6}$$

$$\frac{d[\text{IL}-10]}{dt} = \frac{[\text{CD163}][\text{Hb:Hp}]}{[\text{Hb:Hp}]+K_{d2}} - k_2[\text{IL}-10]. \tag{4.7}$$

Inclusion of basal rate reveals unfolding transcritical bifurcation

While this parameter addition does not affect any of the subsequent qualitative conclusions (Fig. 4.9), this minor modification complicates the model, and gives the following analytic expression for the equilibrium points

$$([\text{CD163}]^*, [\text{IL}-10]^*) = \left(\frac{1}{2k_1[\text{Hb:Hp}]}(\beta \pm \sqrt{\gamma-\delta}), \frac{1}{2k_1k_2([\text{Hb:Hp}]+K_{d2})}(\beta \pm \sqrt{\gamma-\delta})\right) \tag{4.8}$$

where

$$\begin{aligned}
\beta &= [\text{Hb:Hp}]\left(\alpha + p_1 - k_1k_2K_{d1}\right) - k_1k_2K_{d1}K_{d2},\\
\gamma &= [\text{Hb:Hp}]^2\left(\alpha^2 + 2\alpha p_1 + 2\alpha k_1k_2K_{d1}p_1^2 - 2p_1k_1k_2K_{d1}\right) + 2\alpha[\text{Hb:Hp}]k_1k_2K_{d1}K_{d2}, \text{ and}\\
\delta &= 2p_1[\text{Hb:Hp}]k_1k_2K_{d1}K_{d2} + k_1^2k_2^2K_{d1}^2[\text{Hb:Hp}]^2 + 2k_1^2k_2^2K_{d1}^2[\text{Hb:Hp}]K_{d2} + k_1^2k_2^2K_{d1}^2K_{d2}^2.
\end{aligned}$$

The solution is difficult to analytically investigate with arbitrary parameter values; furthermore, it is not possible to write an expression of the threshold in [Hb:Hp].

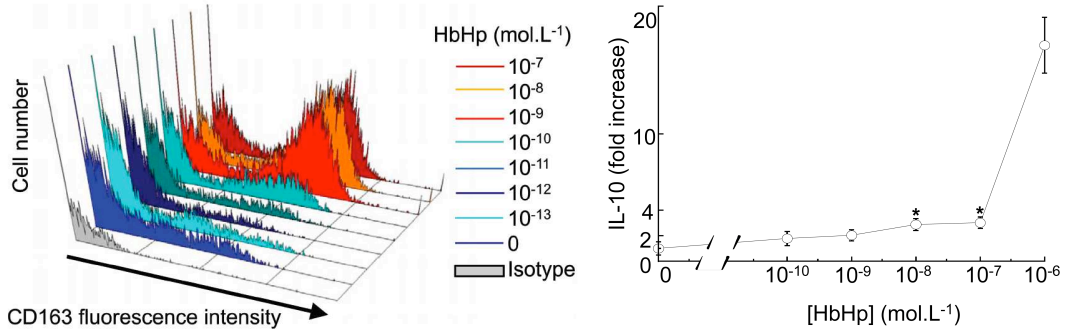

(a) Dose response of CD163 by Hb:Hp (b) Dose response of IL-10 by Hb:Hp

Figure 4.7: Dose response of CD163 and IL-10 expression by Hb:Hp. (a) Flow cytometry of CD163 florescence intensity. For low levels of Hb:Hp ($0 - 10^{-10}$ mol/L) low expression of CD163 is observed, whereas, values of Hb:Hp above 10^{-9} mol/L yield high expression of CD163. (b) Concentration-effect curves for Hb:Hp complexes on macrophage IL-10 production. Supernatant IL-10 levels (y-axis) from macrophage cultures at 24 hours, adding Hb:Hp (x-axis, concentration log molar) at culture onset. Levels are normalized by ratio to control wells, for n=5 donors (Boyle *et al*. (2009)).

In fact, the introduction of this term α causes the transcritical bifurcation to disappear in a generic way and leave an unavoided crossing. According to Glendinning, 1995, an unfolding degenerate singularity occurs when adding a parameter, such as α, acts as a perturbation to the system and breaks the degeneracy and the threshold value H^* is no longer explicitly defined. This yields all the possible behaviors in nearby families (see symmetry breaking bifurcations in Figs. 4.8(b) and 4.8(c)). To satisfy the biological scenario (and in order to maintain a small positive basal level of transcription), $\alpha > 0$ is used. When comparing the positive solution set of the numerical bifurcation diagram of the system for $\alpha > 0$ (Fig. 4.9) compared to the $\alpha = 0$ case (Fig. 4.5(b)), the different families of bifurcations are clear. As expected, the case for $\alpha < 0$ is biologically implausible since this suggests negative basal production; moreover, the bifurcation diagram in Fig. 4.8(c) exhibits a range of [Hb:Hp] for which there is no solution.

As the biological interpretation and motivation for this model has been discussed, experimental data from Dr. Boyle (Fig. 4.7(a)) demonstrates quite clearly the necessity for the basal production. As confirmed qualitatively by this data, this model's bifurcation predicts a low non-zero steady-state and also highlights that the threshold or critical point is not a definitive value.

4.4.4 Model 4.4: IL-10 autoactivation in the absence of Hb:Hp

Previously proposed models depended in some manner on the amount of [Hb:Hp] present in the system and this served as the mechanism to determine whether the CD163 phe-

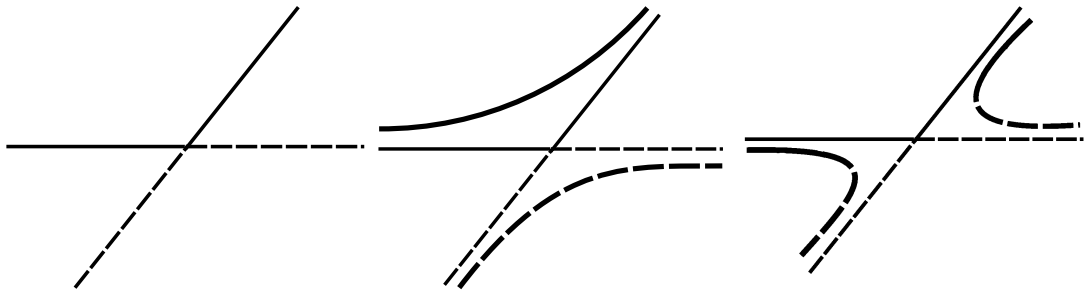

(a) Bifurcation, $\alpha = 0$ (b) Unfolding bifurcation, $\alpha > 0$ (c) Unfolding bifurcation, $\alpha < 0$

Figure 4.8: Family of transcritical bifurcation diagrams. Family of transcritical bifurcation diagrams (based on those from Glendinning, 1995 page 278). Solid lines and dashed lines denote stable and unstable solution curves, respectively. (a) Standard transcritical bifurcation where the solution curves intersect and change stability, symmetry exists ($\alpha = 0$); (b) Bifurcation with symmetry-breaking $\alpha > 0$; (c) Bifurcation with symmetry-breaking $\alpha < 0$.

notypic switch occurred. However, as Dr. Boyle (Fig. 4.1(b)) and others (Sulahian *et al*., 2000; Williams *et al*., 2002) have found, IL-10 may instigate the synthesis of CD163; therefore, this model must be tested to validate if this condition holds. Consider Model 4.3 (Eqs. 4.6 and 4.7) when the parameter $[\text{Hb:Hp}] = 0$, there is a transient increase in CD163 concentration; however, the steady-state tends to a low value (Fig. 4.10(a)).

To account for the absence of the Hb:Hp complex and a possible mechanism for a high CD163 state, the coupled differential equations are modified. A feedback term by CD163 on IL-10 $\left(\frac{[\text{CD163}][\text{IL}-10]p_2}{[\text{IL}-10]+K_{d3}}\right)$ is added, as a possible [Hb:Hp] independent interaction in the system

$$\frac{d[\text{CD163}]}{dt} = \alpha + \frac{p_1[\text{IL}-10]}{[\text{IL}-10]+K_{d1}} - k_1[\text{CD163}], \tag{4.9}$$

$$\frac{d[\text{IL}-10]}{dt} = \frac{[\text{CD163}][\textbf{Hb:Hp}]}{[\textbf{Hb:Hp}]+K_{d2}} + \frac{p_2[\text{IL}-10][\text{CD163}]}{[\text{IL}-10]+K_{d3}} - k_2[\text{IL}-10], \tag{4.10}$$

and

$$[\text{CD163}](0) = [\text{CD163}]_0 \quad \text{and} \quad [\text{IL}-10](0) = [\text{IL}-10]_0,$$

where p_2 is a parameter that determines the strength of autoactivation by CD163 and IL-10 interaction on IL-10 and K_{d3} is a parameter that determines the saturation of the autoactivation rates of this IL-10 term.

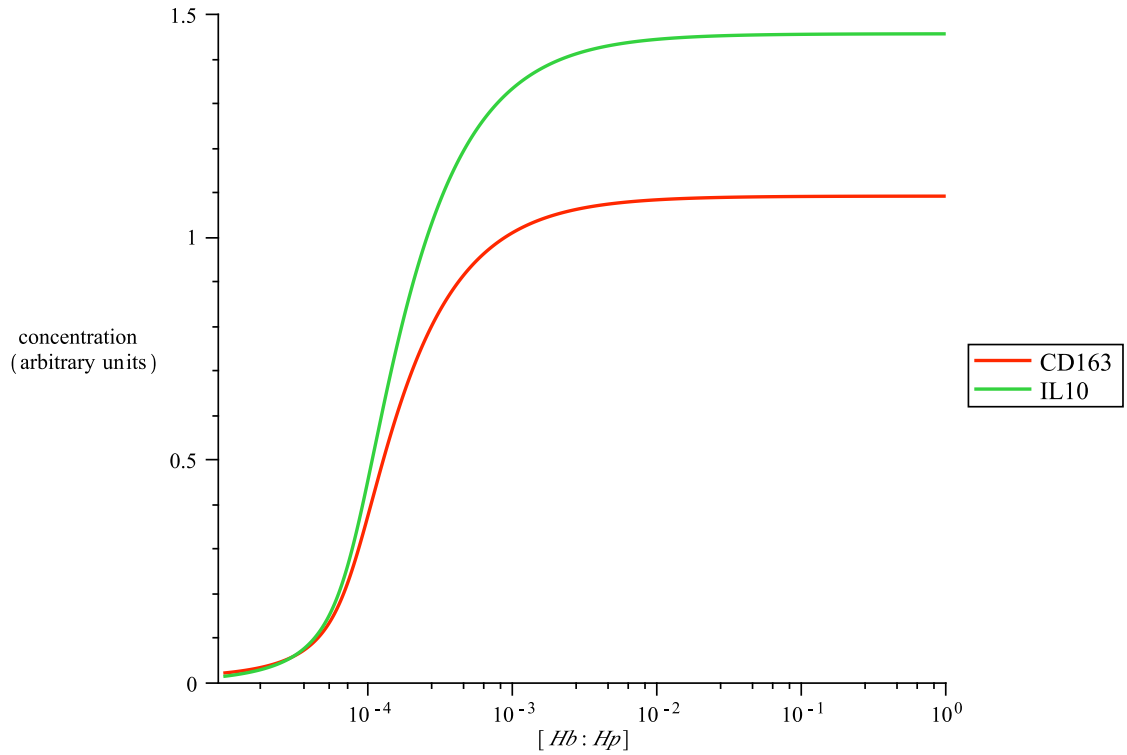

Figure 4.9: Bifurcation diagram of system with CD163 basal production. Bifurcation diagram of system with added basal term. This transcritical bifurcation unfolds when the system is perturbed by the addition of α; therefore, the solution can only be obtained numerically. The solution is qualitatively similar to Fig. 4.5(b), except that the CD163 low phenotype value now slightly above the zero y-axis and the behavior of the switch can no longer be calculated for a threshold value H^*. The positive quadrant (i.e., biologically relevant) solution of IL-10 and CD163 concentration (arbitrary units) is shown. In this simulation, $\alpha = .01$, $p_1 = 10, k_1 = 1, k_2 = 0.75, K_{d1} = 12$, and $K_{d2} = 1\text{x}10^{-5}$ (arbitrary units).

Bistability by IL-10 autoactivation is not robust in presence of Hb:Hp

Recall that when exogenous IL-10 is added to CD163, the system behaves in a similar fashion as to when the [Hb:Hp] complexes activate the macrophage switch (Fig. 4.1). Analytical expressions of the steady-states are not simple; therefore, exploration of steady-states is performed by considering the model without basal transcription or Hb:Hp stimulus, i.e., $\alpha = Hb = 0$. This reveals a similar structure to the original simple Model 4.1 displaying a high and low level of CD163 determined by the IL-10 interaction parameter p_2, not Hb:Hp (Fig. 4.10(b)). Solving $\frac{d[\text{CD163}]}{dt} = 0$ and $\frac{d[\text{IL}-10]}{dt} = 0$ simultaneously, the trivial states where both concentrations are zero are found, i.e., $[\text{CD163}]^* = [\text{IL}-10]^* = 0$. To classify the trivial state and analyze its dynamics, the Jacobian is computed:

$$J = \left.\begin{pmatrix} \frac{\partial[\dot{\text{CD163}}]}{\partial[\text{CD163}]} & \frac{\partial[\dot{\text{CD163}}]}{\partial[\text{IL}-10]} \\ \frac{\partial[\dot{\text{IL}-10}]}{\partial[\text{CD163}]} & \frac{\partial[\dot{\text{IL}-10}]}{\partial[\text{IL}-10]} \end{pmatrix}\right|_{([\text{CD163}]^*,[\text{IL}-10]^*)} = \begin{pmatrix} -k_1 & \frac{p_1}{k_{d1}} \\ 0 & -k_2, \end{pmatrix}$$

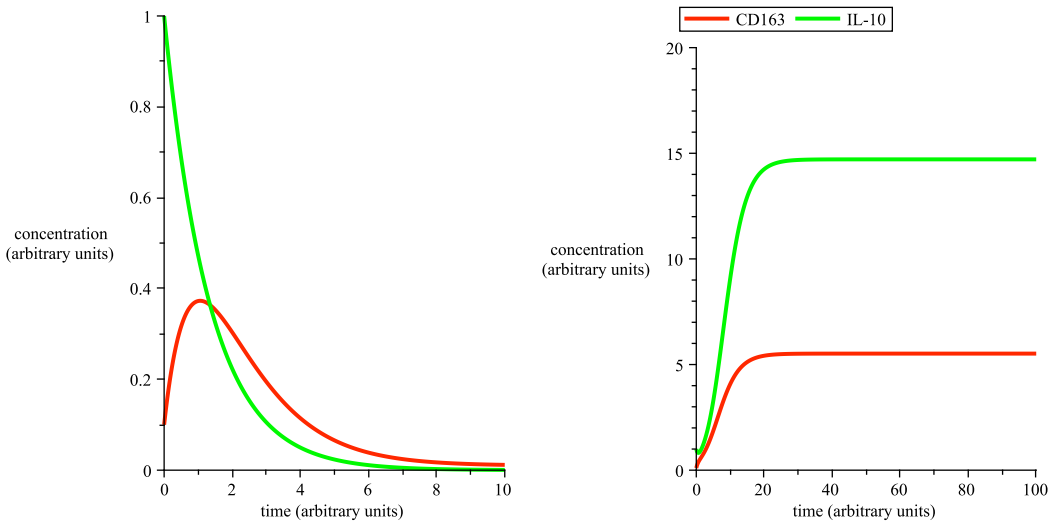

(a) Model 4.3, Hb:Hp= 0 (b) Model 4.4, Hb:Hp= 0

Figure 4.10: Time course of Models 4.3 and 4.4 with no Hb:Hp (parameter [Hb:Hp] set to zero). The solution of IL-10 and CD163 concentration is shown. In these simulations, [Hb:Hp] $= 0$, $\alpha = .01$, $p_1 = 10$, $k_1 = 1$, $k_2 = 0.75$, $K_{d1} = 12$, $K_{d2} = 10^{-5}$, $p_2 = 2$ and $K_{d3} = 0.001$. (a) Time course of Model 4.3. (b) Time course of Model 4.4.

which has the characteristic polynomial

$$p(\lambda) = \lambda^2 + (k_1 + k_2)\lambda + k_1 k_2,$$

and solving for eigenvalues,

$$\lambda_{1,2} = -k_1, -k_2,$$

where parameters k_1 and k_2 must be positive; therefore, the trivial state is *always* a locally stable state. An intuitive explanation for the stability of the trivial state (independent of parameter values) may be that for no initial [IL-10], [CD163] will remain at zero.

Depending on the choice of parameters, two, positive, non-trivial steady-states exist:

$$\begin{aligned}
[\text{CD163}]^* &= -\frac{1}{2}\Big(- p_1 p_2 + k_2 k_1 K_{d1} - k_2 K_{d3} k_1 \\
&\quad \pm \frac{\left(p_1^2 p_2^2 - 2p_1 p_2 k_2 k_1 K_{d1} - 2p_2 k_1 k_2 K_{d3} p_1 + k_2^2 k_1^2 K_{d1}^2 - 2k_2^2 k_1^2 K_{d1} K_{d3} + k_2^2 K_{d3}^2 k_1^2\right)^{1/2}\Big)}{p_2 k_1}, \\
[\text{IL}-10]^* &= -\frac{1}{2}\Big(k_1 k_2 K_{d1} + k_1 k_2 K_{d3} - p_2 p_1 \\
&\quad \pm \frac{\left(k_1^2 k_2^2 K_{d1}^2 - 2k_1^2 k_2^2 K_{d3} K_{d1} - 2k_1 k_2 K_{d1} p_2 p_1 + k_1^2 k_2^2 K_{d3}^2 - 2k_1 k_2 K_{d3} p_2 p_1 + p_2^2 p_1^2\right)^{1/2}\Big)}{k_1 k_2};
\end{aligned}$$

which yield bistable dynamics, that is, three non-negative steady-states, *ceteris paribus*[2] of the baseline parameter values (Table 4.2) and the autoactivation strength parameter $p_2 > p^*$ where $p^* = 0.92$. By numerically calculating the steady-states and investigating the nullclines, the smaller of the two states is found to be a saddle (i.e., corresponding to $det|\text{Jacobian}| < 0$ or eigenvalues are real and have opposite signs), whereas the larger steady-state is stable (i.e., corresponding to $det|\text{Jacobian}| > 0$ and $tr(\text{Jacobian}) < 0$ or eigenvalues are negative), thus, this system exhibits a switch as shown in Fig. 4.11. However, since the combination of parameters yields an unstable state close to the CD163$^{\text{low}}$ state, Fig. 4.11(b) does not clearly elicit the dependence on initial conditions that exists. To visually explain the two possible outcomes, a bifurcation diagram is presented as the autoactivation rate parameter p_2 is varied (Fig. 4.12). It is clear that the dynamics of the model change from monostable to bistable behavior and hence, switching for the case when IL-10 acts as the stimulus, that is, $[\text{IL} - 10]_0 \neq 0$, for a critical strength of IL-10 feedback with dependence on CD163 interaction, enables both a high IL-10 and CD163 state.

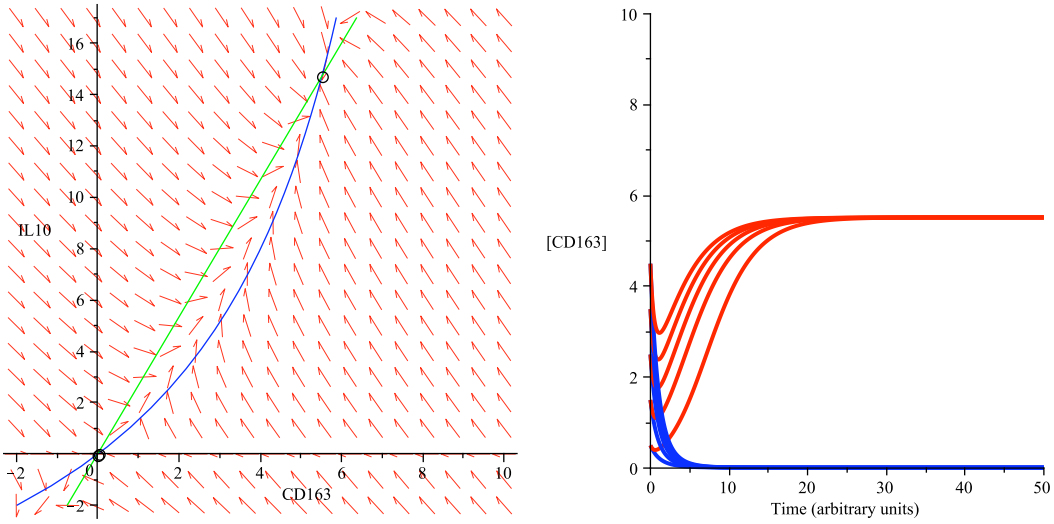

(a) CD163 switching (b) CD163 time course state

Figure 4.11: Dynamics of CD163-IL-10 Model 4.4 (Eqs. 4.9 and 4.10) in the absence of Hb:Hp. Unless specified, baseline values and initial conditions are those given in Table 4.2. (a) Phase diagram and nullclines of CD163-IL-10 bistable dynamics where $[\text{Hb:Hp}] = 2$ and $p_2 = 2$. (b) Time course of CD163 exhibiting switching for low and high feedback strengths where the low and high states correspond to $p_1 = 0.1$ and $p_2 = 2$, respectively.

Next, the Hb:Hp stimulus contribution term is included (with continued absence of α) and analytically solved for three steady-states. Sampling values of [Hb:Hp] and p_2

[2]"all other factors held constant"

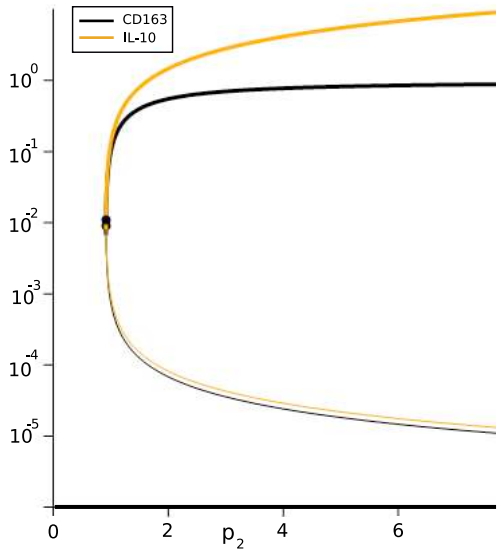

Figure 4.12: Bifurcation diagram of IL-10 autoactivation strength on CD163. Parameter value denoting strength of IL-10 positive feedback (with CD163 dependence) is varied from 0 to 7 and the vertical log axis represents the expression of CD163 (black line) and IL-10 (gold line). Low values reveal the only non-negative real equilibrium point is (0,0). At approximately $p_2 = 0.92$, two equilibrium points emerge, corresponding to a CD163$^{\text{high}}$ phenotype (solid line). The other equilibrium point (thin line) is an unstable equilibrium point. Default parameter values Table 4.2 and $\alpha = [\text{Hb:Hp}] = 0$.

provide only two biologically admissible states for large values of [Hb:Hp] ([Hb:Hp] $>$ 0.0001) or small values of p_2 ($p_2 < 0.40$ where $[\text{Hb:Hp}] = 10^{-5}$). For small values of [Hb:Hp] or large p_2, three non-negative states exist: the trivial and two positive states; interestingly, for any values of [Hb:Hp], the trivial state, under this parameter combination is so close to the unstable positive state that the dynamics do not yield the desired bistability hypothesized, such as a solution curve approaching either a low and high stable state depending on initial condition. Instead, a switch is observed from the trivial stable state for Hb:Hp absent to a stable CD163 high state, depending only on the parameter values, not the initial conditions, which is a limitation to the parameter set constructed thus far.

One should also note that this model assumes the feedback mechanism of IL-10 is dependent on some initial CD163 present. This may not be biologically faithful, as cells stimulated with Hb:Hp have been observed to have an increase of IL-10 prior to an elevation of CD163 expression; therefore, this suggests that the mechanism involved for IL-10 autocatalytic activation (positive feedback) may be independent of CD163. Modifying the feedback term in Model 4.4 $\left(\frac{[\text{IL}-10][\text{CD163}]p_2}{[\text{IL}-10]+K_{d3}}\right)$ to $\frac{[\text{IL}-10]p_2}{[\text{IL}-10]+K_{d3}}$ enables IL-10 autoactivation independent of CD163 levels. First, a simplified case with no basal or Hb:Hp stimulus is examined, $\alpha = [\text{Hb:Hp}] = 0$. There are two admissible steady-states, indi-

cating the existence of $\text{CD163}^{\text{low}} = 0$ and $\text{CD163}^{\text{high}}$ states (Fig. 4.11(b)). Inclusion of [Hb:Hp] maintains the $\text{CD163}^{\text{low}} = 0$ and $\text{CD163}^{\text{high}}$ states, and introduces a negative state despite exploration of parameter values. Analysis of the Jacobian reveals that the trivial steady-state is stable when

$$k_1 + k_2 < \frac{k_3}{K_{d3}} \quad \text{and} \quad k_1 k_2 > \frac{p_1[\text{Hb:Hp}]}{k_{d1}([\text{Hb:Hp}] + K_{d2})} + \frac{k_1 k_3}{K_{d3}}.$$

At the baseline parameters the trivial state is unstable, even for small values of [Hb:Hp] (order of 10^{-8}), therefore $K_{d3} = 50$ is used to satisfy the above conditions. Moreover, numericaly, it is found that when [Hb:Hp] is small ($[\text{Hb:Hp}] \leq 10^{-5}$), the trivial state is the only non-negative that satisfies the stability condition; for larger values of [Hb:Hp], two non-negative states exist and the positive is stable whereas the trivial state is unstable. This model has a similar transcritical behavior as Model 4.1 and lacks the bistability often necessary for cells initialized at different variable concentrations; therefore, the additional term merely adds complexity to the system.

The original feedback model (Model 4.4) exhibits bistability for the case when IL-10 is the driver for CD163 expression and Hb:Hp is absent; furthermore, the models enable a method by which IL-10 may induce expression of itself as well as CD163. The model in the absence of Hb:Hp also provides a simplification of the mechanism of IL-10 binding to its receptor, initiating signal transduction pathways, upregulating its own synthesis, and resulting in an anti-inflammatory cell phenotype. Through the analysis presented, the models may not robustly capture the bistability dynamics of elevated IL-10 when incorporating both IL-10 and Hb:Hp stimuli. Moreover, as experimental data that finds maintained elevation of stimulus IL-10 by mononuclear phagocytes stimulated with IL-10 is lacking, the models are unable to provide an explanation for both IL-10 and Hb:Hp stimuli. While feedback of IL-10 by IL-10 may exist, the model may require other interactions, such as additional variables included in the model by Figueiredo *et al.*, 2009), biological evidence is not conclusive to support the specific hypothesis, and our models, despite parameter variation, do not suggest this a robust simplification of the mechanism; thus, different method for bistability are considered.

4.4.5 Model 4.5: Cooperativity in IL-10

Previous mathematical models of biological switches and bistable systems often include cooperative binding (Angeli *et al.*, 2004; Bagowski and Ferrell, 2001; Callard *et al.*, 1999; Ferrell, 2002; Laurent and Kellershohn, 1999; Tyson *et al.*, 2003). In this context, con-

sider cooperative binding of IL-10 to activate CD163. This minor change to Model 4.3 (Eqs. 4.6 and 4.7) gives the system

$$\frac{d[\mathrm{CD163}]}{dt} = \alpha + \frac{p_1[\mathrm{IL}-10]^n}{[\mathrm{IL}-10]^n + K_{d1}^n} - k_1[\mathrm{CD163}], \tag{4.11}$$

$$\frac{d[\mathrm{IL}-10]}{dt} = \frac{[\mathrm{CD163}][\mathrm{Hb{:}Hp}]}{[\mathrm{Hb{:}Hp}] + K_{d2}} - k_2[\mathrm{IL}-10], \tag{4.12}$$

where n is a parameter denoting cooperativity, a Hill coefficient. In developing this model, cooperativity between Hb:Hp and CD163 was also considered, however, data obtained later from Dr. Boyle confirmed a linear relationship, or a Hill coefficient equivalent to one. Therefore, only cooperativity between CD163 and IL-10 is considered.

Cooperativity in IL-10 yields bistable system

Steady-state analysis of this system reveals the addition of a positive hill coefficient $n > 1$ creates the desirable bistability, i.e., two steady-states representing a CD163^{low} and CD163$^{\text{high}}$ phenotype and one unstable middle state. Visualization of nullclines aids the switching of stability (Fig. 4.13); furthermore, bifurcation analysis improves our understanding of the model dynamics and how the parameters [Hb:Hp] and K_{d1} affect the outcome (Fig. 4.15). Interestingly, the range of parameter values ([Hb:Hp], K_{d1}) yielding the region of CD163 bistability results in a cusp catastrophe, an elementary object of catastrophe theory, which studies how small perturbations in certain parameters can lead to large and sudden changes in the behavior of a nonlinear system (Arnol'd, 1992). A more instructive view of the dependence of the $[\mathrm{CD163}]$ state on [Hb:Hp] and K_{d1} is shown in Fig. 4.15. In comparison with the previous models, this model remains simple in structure while encompassing bistability, cooperativity and a biologically feasible interpretation.

4.5 Conclusion

Mathematical models were developed with the central aim to explore and predict behavior of macrophages in atherosclerotic intraplaque hemorrhages in response to various stimuli. Immunohistochemistry and flow cytometry data of plaque macrophages stimulated with hemoglobin - haptoglobin (Hb:Hp) complex and interleukin-10 indicated strong evidence for Hb:Hp induced macrophage differentiation from CD163$^{\text{low}}$ and CD163$^{\text{high}}$ phenotypes. This collaboration enabled the development, analysis and

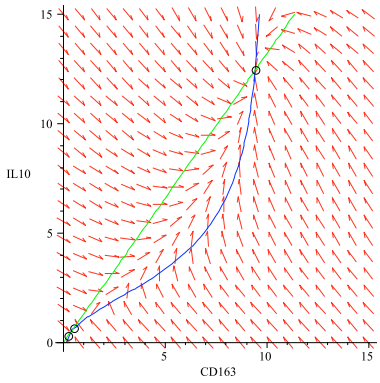

Figure 4.13: Nullclines of bistable cooperative CD163 system. Nullclines and phase diagram with two stable equilibrium points representing low and high CD163 phenotypes and one unstable fixed point. The parameter are baseline values as stated in Table 4.2, except that $\alpha = 0.15$, $k_2 = 12$, and the stimulus is [Hb:Hp]=10^-3 (arbitrary units).

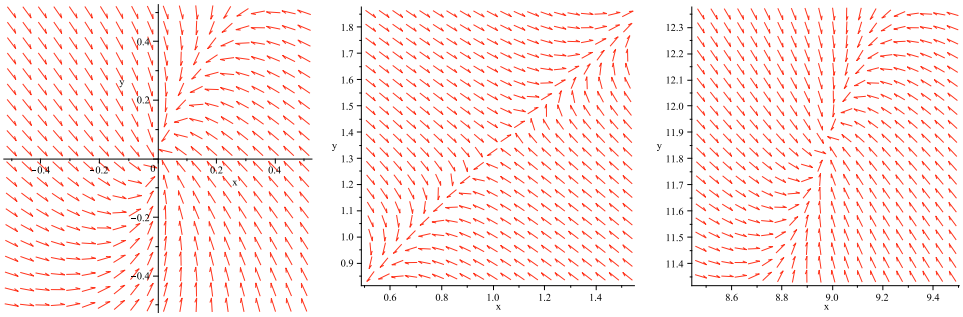

(a) Stable trivial state (b) Unstable state (saddle) (c) Stable high state

Figure 4.14: Phase field diagram of Model 4.5 steady-states, with baseline parameter values and $\alpha = 0$ (a) Stability of trivial state (b) Saddle point of middle state (c) Stability of CD163^{high} state.

comparison of ODE models based on measured data. Through the iterative process of constructing and revising each model, a deeper insight was gained about the underlying biology, all the while acknowledging the limitations of each model.

The first model (Model 4.1), a simple coupled ODE, predicted a switch-like behavior, from a lipid-laden and pro-inflammatory phenotype to an anti-inflammatory and athero-protective (HA-mac) cell phenotype. This model hypothesized that stable regulation into these two lineages could be determined by the observed positive feedback loop in which Hb:Hp binding to CD163 leads to IL-10 secretion, in turn up-regulating CD163. The data validation of this conceptual model motivated further investigation of the interactions.

A simplification of Model 4.1, the second model (Model 4.2) was formulated to understand the effect of constant CD163 amount on IL-10. We found that IL-10 levels were highly dependent on CD163 initially present in the cell, confirming the importance of the feedback loop. After considering the unlikeliness of monocytes/macrophages existing

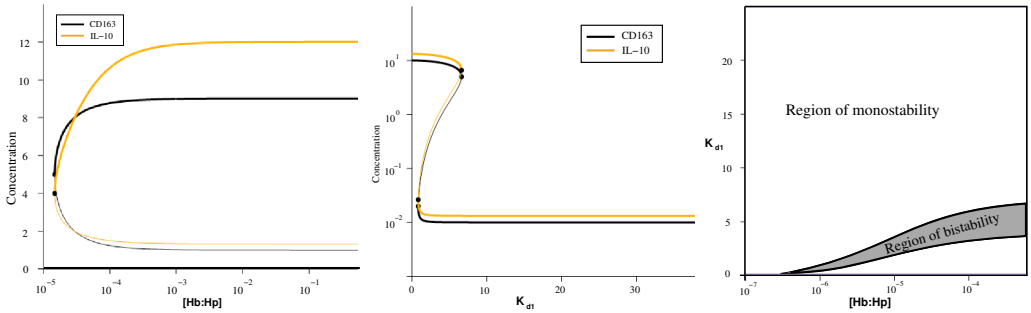

(a) Hb:Hp bifurcation (b) K_{d1} bifurcation (c) Region of bistability

Figure 4.15: Bifurcation diagrams for Model 4.5 and surface of cusp catastrophe. (a) Bifurcation diagram of [Hb:Hp]; (b) Bifurcation diagram of K_{d1}; (c) surface of cusp catastrophe in ([Hb:Hp],K_{d1}) plane.

with absolutely no initial CD163, a basal transcription rate (Model 4.3) was introduced. This model was intriguing, mathematically, with the observation that this parameter induced an unfolding to the bifurcation structure of the first model (Model 4.1).

The next model (Model 4.4) investigated the role of IL-10 as a stimulus when Hb:Hp is not present in the system. Two variations of this model were considered, both including an autoactivation term on IL-10. It was determined that this feedback could yield to bistable behavior; moreover, the feedback loop initiated by IL-10 (promoting its own synthesis) facilitated the phenotypic switch of CD163 from low to high states. It was found however, that many parameter combinations did not yield bistable behavior; thus, the increased complexity of the model did not warrant the benefits without further parameter investigation. Another bistable scheme that was considered was cooperativity between CD163 and IL-10, which was hypothesized to be possible given that many interactions must occur between IL-10 synthesis and CD163 activation.

The models presented in this chapter are conceptual and mechanistic in nature and proved useful; however, they have limitations. Extending the conceptual models to a population of heterogeneous macrophages, wherein methods and techniques from Chávez-Ross *et al.*, 1997; Hofbauer, 1988, analogous to Lacker type models (Lacker, 1988), may render more light on the phenotypic switch and interesting results may come from such an approach. Another future direction is to include intercellular mediators as data become available to provide additional insight to the pro-inflammatory/anti-inflammatory balance; thus, models investigating the cellular switching mechanisms and mediators may lead to an increased understanding and may point to improve medical therapies for vascular inflammatory diseases.

Chapter 5

A mechanistic study of anti-inflammatory response by macrophages after stimulation with Hb:Hp complexes/heme

5.1 Overview

The primary focus of this work is motivated by extending the simple extracelluar model of CD163/IL-10 upregulation driven by Hb:Hp complexes by Boyle *et al*. (2009) to include the intracellular mediator heme oxygenase-1. The aim is to gain further insights into the responsible mechanisms for HA-mac differentiation of this system. To accomplish this, four models are presented, which test specific components in the signaling network and corroborate experimental evidence through data-fitting, sensitivity analysis and model selection techniques. The selected model's predictions are compared to experimental data of the response of a different stimulus, heme, on monocytes. Moreover, the model result predicts that an anti-inflammatory stimulus, such as IL-10 also induces an anti-inflammatory macrophage phenotype. Therefore, this work identifies a model which describes mechanisms responsible for anti-inflammatory response in monocytes/macrophages under a number of stimuli. Finally, this work provides a mechanistic insight to the anti-inflammatory response and suggests future experiments to test the predictions.

This research was conducted in collaboration with Dr. Joseph J. Boyle and co-workers from the Imperial College London Faculty of Medicine and Dr. Christopher Barnes from

the department of Bioinformatics. This work is in preparation for submission.

5.2 Introduction

Recall from Chapters 2 and 4 that monocytes and macrophages, present at the site of the inflammatory disease, atherosclerosis, respond to stimuli to invoke either a pro- or anti-inflammatory response. Under certain conditions, these monocytes may differentiate into macrophages with scavenger receptor CD163 surface expression (Buechler *et al*., 2000; Philippidis *et al*., 2004), which acts as a vehicle to import free pro-oxidative stress hemoglobin-haptoglobin (Hb:Hp) complexes (Kristiansen *et al*., 2001). Internalized Hb:Hp undergoes lysosomal catabolysis into intracellular heme which may synthesize its rate limiting enzyme HO-1, resulting in heme degradation and inducing a response (Idriss *et al*., 2008; Immenschuh and Ramadori, 2000; Morita, 2005; Otterbein and Zuckerbraun, 2005; Pae *et al*., 2008; Philippidis *et al*., 2004; Sawle *et al*., 2005; Schaer *et al*., 2006; Takaya *et al*., 2005). Specifically, the Hb:Hp-CD163 binding has been found to induce an anti-inflammatory response of IL-10 (Boyle *et al*., 2009; Lee and Chau, 2002; Moestrup and Moller, 2004; Otterbein and Zuckerbraun, 2005; Ugocsai *et al*., 2006; Van den Heuvel *et al*., 1999). Recent studies have also found interactions between HO-1 and IL-10 suggesting the existence of a positive feedback loop (Abraham and Drummond, 2006; Lee and Chau, 2002; Ricchetti *et al*., 2004; Schaer *et al*., 2006). Additionally, autoactivation of IL-10 via Stat-3 may occur through a positive feedback loop (Sanjabi *et al*., 2009). It has also been found that macrophages stimulated with IL-10 can induce a high expression of CD163 (Sulahian *et al*., 2000; Williams *et al*., 2002).

Recently, construction of a mathematical model of the stable regulation into the two lineages ($CD163^{low}$ $HLA\text{-}DR^{high}$ and $CD163^{high}$ $HLA\text{-}DR^{low}$) observed positive feedback in which Hb:Hp binding to CD163 leads to IL-10 secretion, in turn up-regulating CD163 Boyle *et al*. (2009). A coupled ordinary differential equation (ODE) model was constructed and a positive feedback hypothesizing the phenotypic switch was validated by experimental evidence; however, the model did not include other possible transport mechanisms, such as free heme, incorporate additional intracellular players, nor did it accurately match elevation time of species expression levels. As highlighted previously, the biological evidence requires a model which includes observed intracellular feedbacks and incorporation of different possible transport mechanisms to give testable predictions. Positive feedback loops have been shown to generate stable divergence and commitment to two steady-states in T-helper cells (Yates *et al*., 2000) and in monocytes vs neutrophils (Laslo *et al*., 2006). Furthermore, identifying specific species in biological positive feed-

back systems have been shown to govern cell fate, for instance, models of caspase feedbacks control cell death (Eissing *et al*., 2004; Legewie *et al*., 2006). More generally, similar regulatory architectures are being observed in a variety of systems biology contexts (Tyson *et al*., 2003).

5.3 Results and Discussion

5.3.1 Model formulation

Four models (5.1, 5.2, 5.3 and 5.4) were developed of macrophage response by Hb:Hp complexes. These models assume a positive feedback loop between species [CD163] and [IL-10] (see Chapter 4) and the models include the intermediate [HO-1], where [-] denotes concentration. The stimulus, Hb:Hp complex, is endocytosed by CD163, upregulating HO-1, which instigates the synthesis of IL-10. One difference between the stimulus in these models than in previous is that Hb:Hp is assumed to degrade exponentially rather than remain constant. This may be a more realistic assumption in the model since in actually, the stimulus does not remain constant externally as it is internalized by the cell, and thus is no longer available to initiate a signal for all time. Furthermore, as Hb:Hp is internalized, HO-1 degrades Hb:Hp, and thus serves as another interpretation of the decrease in levels of Hb:Hp. For simplicity, Hb:Hp is kept a model parameter rather than a model variable. As diagrammatically shown in Fig. 5.1, models consider the intracellular mechanisms that describe the baseline model: Hb:Hp degrades exponentially either naturally or by HO-1; Hb:Hp binds to CD163 and upregulates HO-1; HO-1 initiates the synthesis of IL-10; and IL-10 induces expression of CD163 with cooperativity. Although this complex system includes other regulators and possible feedback mechanisms, the interactions between these three species are investigated using literature hypotheses of mechanisms: Model 5.2 extends the baseline model to include an auto-activation IL-10 positive feedback loop (via Stat-3 (Sanjabi *et al*., 2009)), whereas Model 5.3 extends the baseline model to investigate the effects of IL-10 inducing HO-1 expression, creating an HO-1/IL-10 positive feedback loop (Lee and Chau, 2002) and Model 5.4 is the composite of both mechanisms.

As summarized in Table 5.1, Model 5.1 is the baseline, Model 5.2 includes an autoactivation feedback loop by IL-10, Model 5.3 includes a feedback loop by IL-10 on HO-1 and Model 5.4 is the composite of Models 5.2 and 5.3. Model variables and parameters are described in Table 5.2.

Model	Equations
5.1	$\frac{d[\text{CD163}]}{dt} = \alpha + v_1 - v_2$
	$\frac{d[\text{IL}-10]}{dt} = v_3 - v_4$
	$\frac{d[\text{HO}-1]}{dt} = v_5 - v_6$
5.2	$\frac{d[\text{CD163}]}{dt} = \alpha + v_1 - v_2$
	$\frac{d[\text{IL}-10]}{dt} = v_3 - v_4 + v_7$
	$\frac{d[\text{HO}-1]}{dt} = v_5 - v_6$
5.3	$\frac{d[\text{CD163}]}{dt} = \alpha + v_1 - v_2$
	$\frac{d[\text{IL}-10]}{dt} = v_3 - v_4$
	$\frac{d[\text{HO}-1]}{dt} = v_5 - v_6 + v_8$
5.4	$\frac{d[\text{CD163}]}{dt} = \alpha + v_1 - v_2$
	$\frac{d[\text{IL}-10]}{dt} = v_3 - v_4 + v_7$
	$\frac{d[\text{HO}-1]}{dt} = v_5 - v_6 + v_8$
	Reaction velocities
	$v_1 = \frac{p_1[\text{IL}-10]^n}{[\text{IL}-10]^n + K_{d1}^n}$
	$v_2 = k_1[\text{CD163}]$
	$v_3 = \frac{p_3[\text{HO}-1]}{[\text{HO}-1]+K_{d4}}$
	$v_4 = k_2[\text{IL}-10]$
	$v_5 = \frac{[\text{CD163}][\text{Hb:Hp}]}{[\text{Hb:Hp}]+K_{d2}}$
	$v_6 = k_3[\text{HO}-1]$
	$v_7 = \frac{p_2[\text{IL}-10]}{[\text{IL}-10]+K_{d3}}$
	$v_8 = \frac{p_4[\text{IL}-10]}{[\text{IL}-10]+K_{d5}}$

Table 5.1: Dynamical equations for models. Model 5.1 is the baseline; Model 5.2 includes v_7, an autoactivation feedback loop by IL-10; Model 5.3 includes v_8, a feedback loop by IL-10 on HO-1; and Model 5.4 is the composite of Models 5.2 and 5.3. The reaction in v_5 corresponds to an exponential decaying stimulus: $[\text{Hb:Hp}] = H \cdot e^{-\lambda \cdot t}$ where H is the original stimulus concentration.

Variable	Description
$[\mathrm{HO}-1]$	Heme oxygenase-1
$[\mathrm{IL}-10]$	Interleukin-10 anti-inflammatory cytokine
$[\mathrm{CD163}]$	CD163 macrophage scavenger receptor
Parameter	**Description**
p_1	rate at which IL-10 upregulates CD163
K_{d1}	saturation of CD163 production rate
k_1	degradation rate of CD163
[Hb:Hp]	hemoglobin-haptoglobin complex
K_{d2}	saturation of HO-1 production rate by Hb:Hp-CD163 binding
K_{d4}	saturation of IL-10 production rate by HO-1
k_2	degradation rate of IL-10
α	basal production rate of CD163
p_2	strength of IL-10 autoactivation
K_{d5}	saturation of HO-1 production rate by IL-10
K_{d3}	saturation of IL-10 autoactivation rate
k_3	degradation rate of HO-1
p_3	rate at which HO-1 upregulates IL-10
p_4	rate at which IL-10 synthesizes HO-1
n	hill coefficient
λ	degradation rate of Hb:Hp complexes

Table 5.2: Description of variables and parameters of models, where [-] denotes concentration, and p_i, k_i, K_{di} are parameters representing synthesis, degradation and saturation rates, respectively.

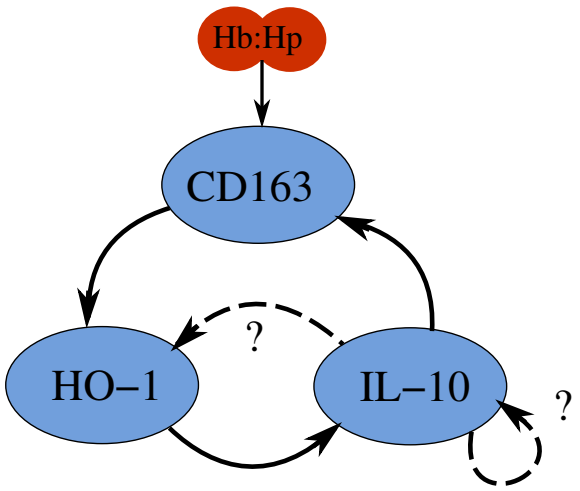

Figure 5.1: Diagram of CD163/HO-1/IL-10 feedback loop. Hb:Hp complex initiates CD163 to upregulate HO-1, which initiates the synthesis of IL-10. Solid arrows represent the known biological behavior that is incorporated in all models, whereas the dashed arrows represent mechanisms that in included in select models.

5.3.2 Parameter fitting and model selection

Developing a model capable of exhibiting bistable behavior is often dependent on model structure, parameters and initial conditions. As investigated in Chapter 4, the structure of the models (positive feedback with Hill functions) may give rise to multistability. This switching objective between states is highly dependent on parameter values and initial conditions. Model parameters k_2 and k_3 are estimated degradation rates of IL-10 and HO-1 from the literature and stimulus levels are taken from experimentation (see Materials and Methods). Remaining parameters are estimated using approximate Bayesian computation (ABC) based on sequential Monte Carlo (SMC) sampling. This statistical approach uses an initial prior range which was estimated using many Nelder-Meads (see Materials and Methods) given in Table 5.3. ABC-SMC provides a posterior distribution of inferred parameter values. ABC-SMC is also used to estimate initial conditions of the models, which previously, had been achieved, but not implemented in the ABC-SysBio package. Simultaneous to inferring parameters, the model selection is performed to discriminate the most appropriate model when compared to published time course data of monocyte/macrophage response to Hb:Hp complexes (see Materials and Methods). Each iteration of the algorithm reduces the acceptance tolerance of parameters/models, which increases the accuracy of the fit and model selection. This gives an output of a population of particles (accepted sampled algorithm inputs) with a given acceptance rate at each iteration (see Fig. 5.2) which selects Model 5.3 after all remaining models have zero probability. Please note acceptance rates from one population to the next depends on the

epsilon schedule. If the next step is small compared to previous step then it can increase. Ideally the acceptance rate should be fixed between populations so that it is approximately constant though this is rarely achieved in practice. It does not have to monotonically decrease though usually it does. As the model selection runs for the given priors, Model 5.3

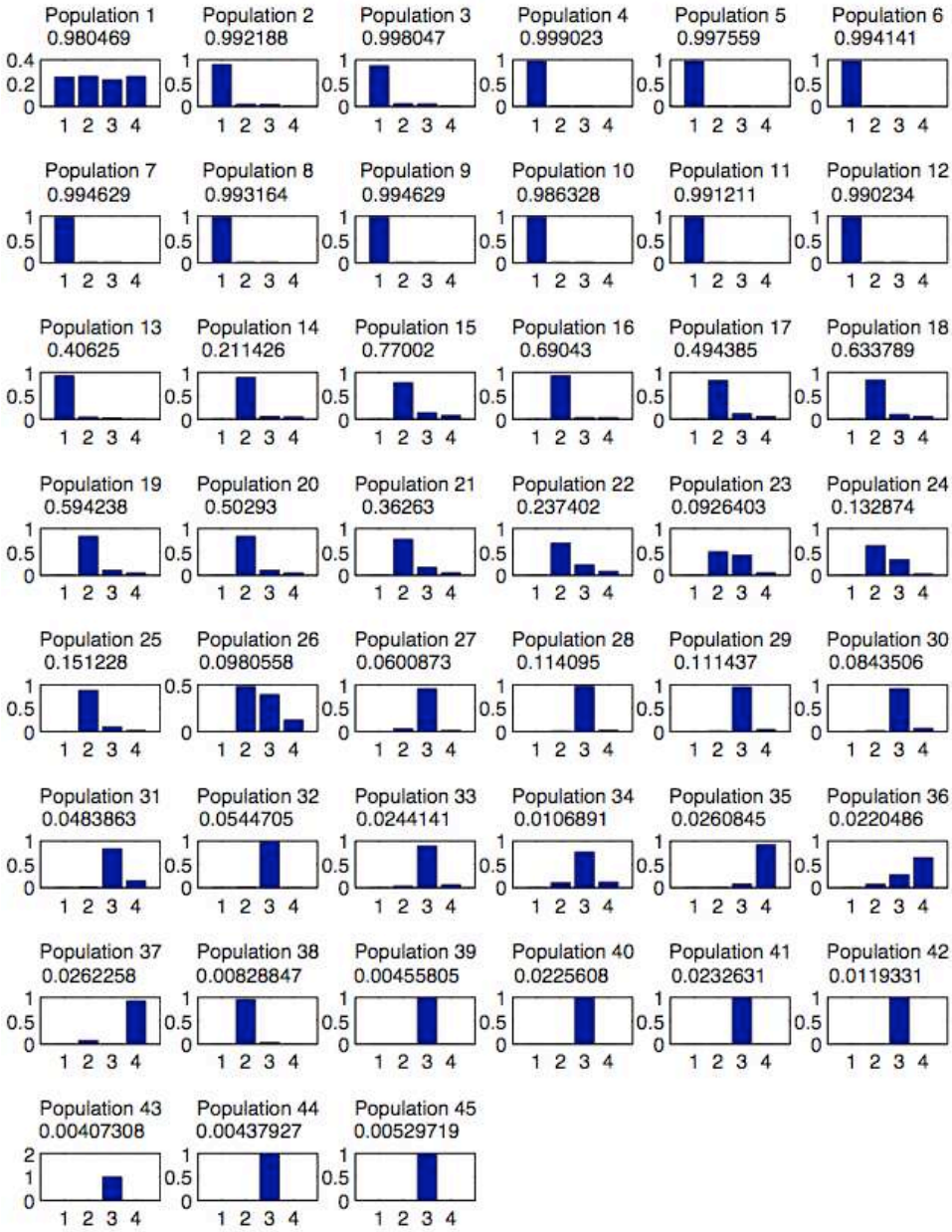

Figure 5.2: Model probability as ABC-SysBio algorithm progresses. Order is Model 5.1, 5.2, 5.3, and 5.4. The final population (45) shows Model 5.3 represents the data best. Each iteration of the algorithm reduces the distance between simulations and observed data, which increases the accuracy of the fit and model selection, resulting in a population of particles (accepted sampled algorithm inputs) that approximates the marginal posterior probability. The small numbers correspond to acceptance rate for each iteration.

is found to most accurately describe the data (see Fig. 5.2). This result corroborates the hypothesis by Lee and Chau, 2002 of positive feedback mechanisms between IL-10 and HO-1. The Model 5.3 time trajectory of the species at the inferred parameter values and initial conditions which was numerically solved and it fits the IL-10 and CD163 time course data reasonably well (Fig. 5.3). The curve representing the HO-1 behavior approaches a higher steady-state than the obtained HO-1 data. This may occur since the simplicity of the model does not include regulators, rather, the focus is to explore the specific interactions between IL-10 and HO-1 species. Inspection of the model structure suggests that elevated IL-10 may only occur if HO-1 levels remain high since the production terms of IL-10 and HO-1 are highly dependent on each other. The ABC-SMC result

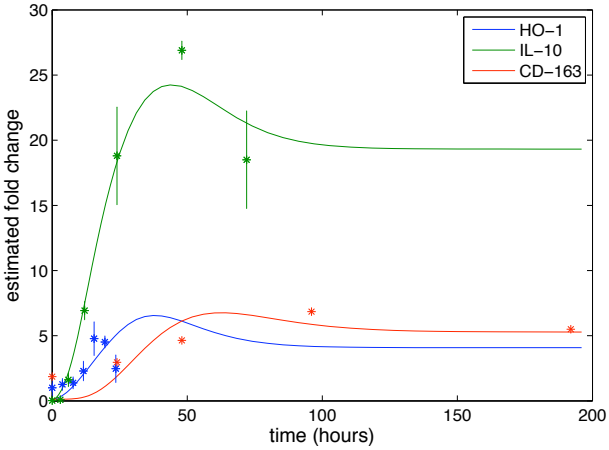

Figure 5.3: Model 5.3 time course at inferred parameter values (see Table 5.3). The time course data (stars and error bars) obtained from Philippidis *et al*., 2004; Schaer *et al*., 2006 and Boyle *et al*., 2009 (see Materials and Methods) and simulated time course of Model 5.3 (solid lines) of HO-1 mRNA (blue), IL-10 protein (green) and CD163 protein (red) .

provides a posterior distribution over parameters and models (Fig. 5.4). While many parameters are inferred well, some are not identifiable, such as the initial conditions, as well as p_4, p_1, and λ. The identifiability of parameters may be shown by the interquantile ranges of the posterior, i.e., identifiable parameters converge whereas non-identifiable which jump around, such as the IL-10 initial condition, α, k_1 and λ (Fig. 5.5). However, the identifiability of parameters may occur as an artifact of insufficient sampling, i.e., the chosen perturbation kernel may not fully cover the space (see Materials and Methods). It should be noted that this inference was performed multiple times with different seeds, which resulted in the same conclusions. With the posterior of inferred parameters and initial conditions, the model system may be studied in more detail.

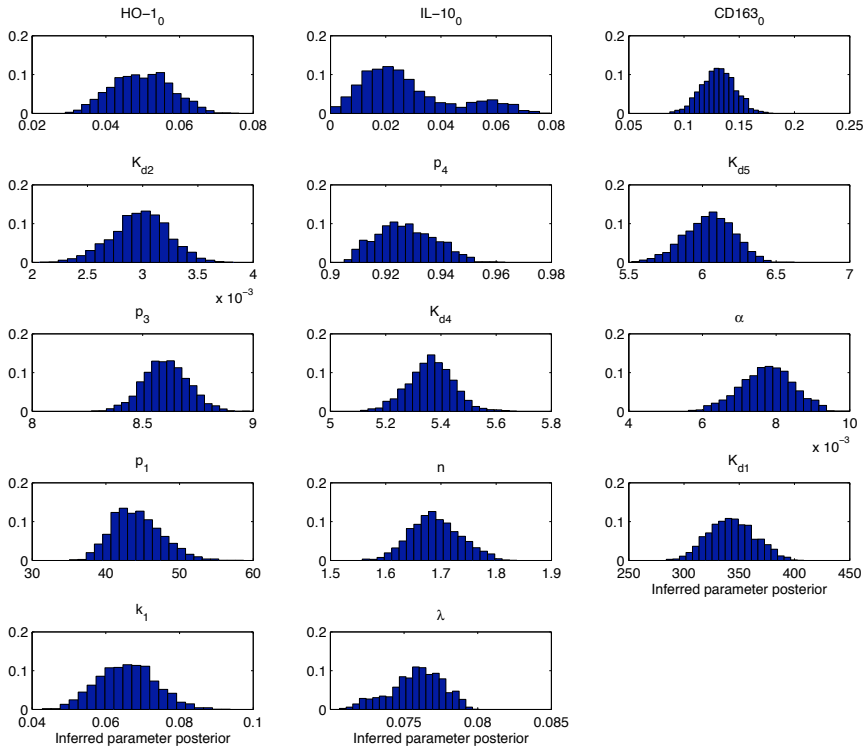

Figure 5.4: Weighted posterior parameter distribution of final Model 5.3 fit at final population for N=2000 particles.

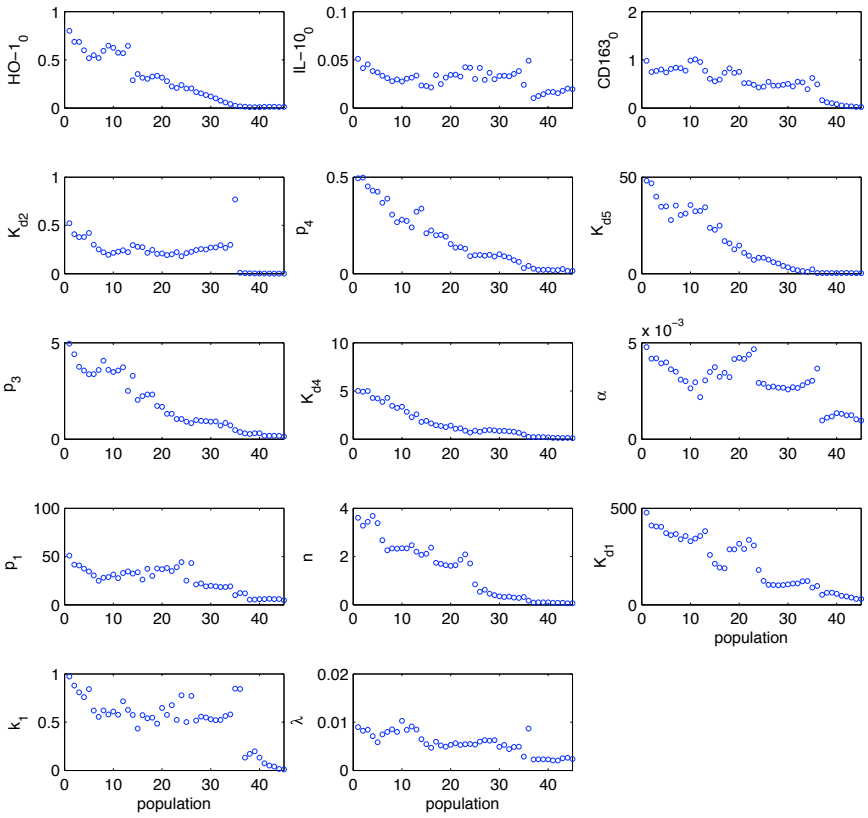

Figure 5.5: Interquantile ranges of each population. This displays the interquantile ranges of the posterior as the algorithm passes through the 45 populations. Generally, identifiable parameters will reduce until the true posterior is reached; however ranges that jump around may indicate non-identifiable parameters or this output may occur an artifact of insufficient sampling.

5.3.3 Sensitivity analysis of Model 5.3 parameters

Performing principal component (PC) analysis on the posterior of final population gives a similar sensitivity as calculating the Hessian (Secrier *et al*., 2009). The principal component coefficients provide a method to measure the sloppiness and sensitivity of the inferred parameters: the largest PC gives sloppy parameters that have the least information whereas the smallest PC gives sensitive parameters which correspond to stiff combinations (see Material and Methods). Briefly, the eigenvectors ν_i corresponding to eigenvalues λ_i of the corresponding PC (for $i = 1, ..., m$ where m is the number of eigen-parameters) are ranked and the PC variance (Fig. 5.6(a)) may be used to determine the most sloppy and sensitive parameters. The PC numbers that explain less than one percent of the total variance (last two PCs) are taken to correspond to stiff parameter combinations. As shown in Fig. 5.6(b), the sensitivity of model parameters is shown by calculating the eigen-parameter projection ($p_{a,b}$), which represents the square of the eigenvalue associated with parameter a pointing in the direction of raw parameter b, taken to be $p_{a,b} = \nu_{a,b}^2 / \sum \nu_{ai}^2$ of the final PC. The pie chart describing the eigen-projection of the fourteenth PC identifies combinations of parameters n and K_{d1}, which are most constrained to the data and these parameters do not explain much of the total variance of the posterior distribution. Performing global sensitivity analysis (Fig. 5.7) also is in agreement that parameter n is most sensitive. Additionally, the global sensitivity analysis suggests that the degradation rate k_1 which is the third smallest PC in Fig. 5.6(b) and the interaction parameters p_1 and p_3 are found to affect the model steady-states. The sloppy parameters may be determined by examining the largest projections of the largest PC. As shown in Fig. 5.6(b), the first PC, primarily shades of blue, identifies the initial conditions to have the least amount of information.

Numerical investigation of Model 5.3 at the inferred parameters for constant Hb:Hp stimulus has only one real steady-state, corresponding to a (CD163, IL-10, HO-1)$^{\text{high}}$ state, thus the model trajectory will always approach this anti-inflammatory state. Further exploration of the parameter values motivated by the principal component analysis reveals that for the inferred value $n = 1.68$ at small initial CD163, IL-10, and HO-1, the other fixed points are complex, which explains why all biologically relevant trajectories approach the (CD163, IL-10, HO-1)$^{\text{high}}$ state. For instance, increasing the value of the Hill coefficient to $n = 2$ changes the steady-state classification to three real fixed points. However, inspection of the steady-states which are numerically calculated using initial conditions ranging from 0 to 20 for all species. This permits only one non-negative fixed point corresponding to the high anti-inflammatory state. However, as the last PC

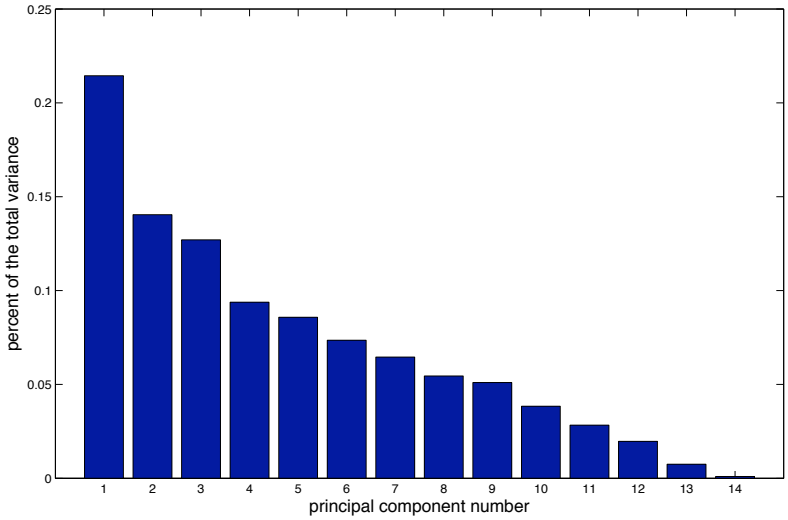

(a) Principal component variance

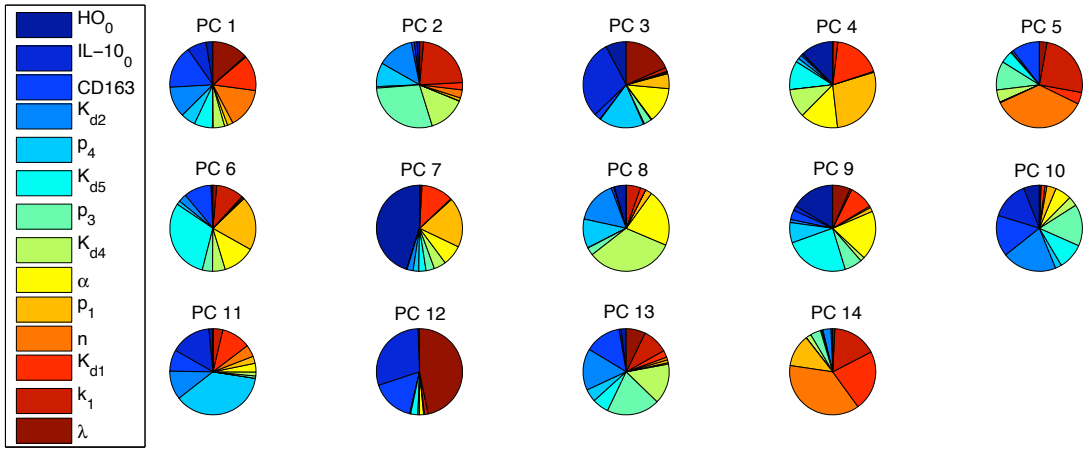

(b) Projection of eigen-parameters

Figure 5.6: Principal component analysis of Model 5.3. The first PC describes 21% of the total variance with each subsequent PC describing 14%, 12%, 9%, 8.5%, 7.3%, 6.4%, 5.4%, 4%, 3.8%, 2.8%, 1.9%, 0.7%, and 0.1%) of the total posterior variance, respectively. The projections of eigen-parameters onto the raw parameters gives an account of which parameter combinations may be 'sloppy' or 'stiff' corresponding to the largest and smallest PCs, respectively. As a heuristic, the number of 'sloppy' parameters may equate to the PC numbers that explain $< 1\%$ of total variance, taken as the last two. The eigen-parameter projections determined by the eigen-direction in the final PC suggest n, and K_{d1} are the most stiff parameter combinations.

suggests, the stiff parameter combinations occur for n and K_{d1}. While the Nelder-Mead method restricted many prior choices, the range for K_{d1} was not easily determined (recall $K_{d1} \sim$ U(0,1000)); therefore, the values for K_{d1} were varied within the prior range for different initial conditions. As an example, it was found that if $K_{d1} = 0.3$ and $n = 2$,

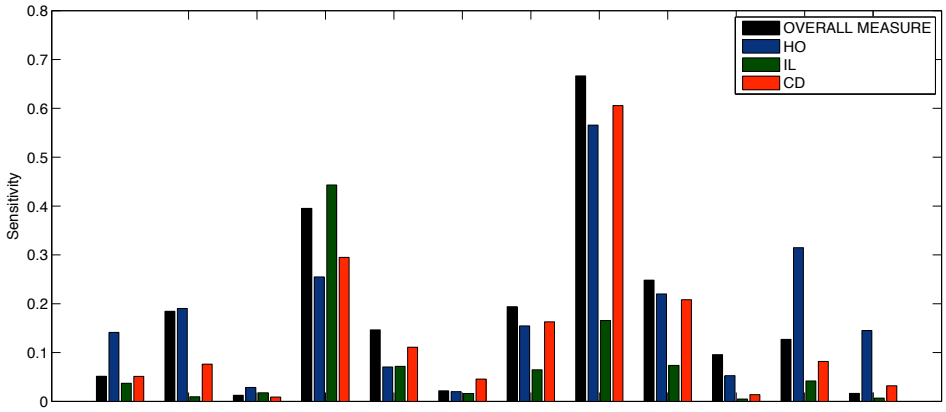

(a) PRCC

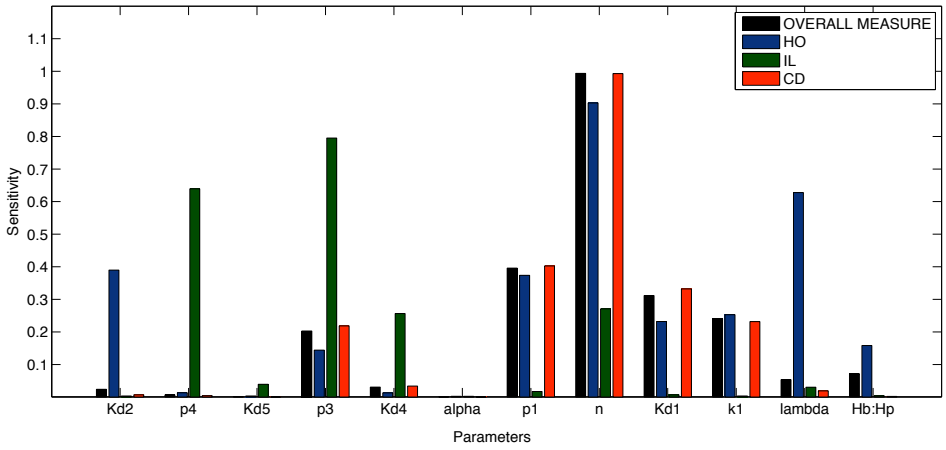

(b) FAST total effect

Figure 5.7: Global sensitivity analysis results of Model 5.3. Paremeters are perturbed by half an order of magnitude and 10^3 simulations for each analysis.

there exists a (CD163, IL-10, HO-1)$^{\text{low}}$ and (CD163, IL-10, HO-1)$^{\text{high}}$ state. Inspection suggests for the inferred parameter values that this bistability is not robust; however, here, principal component analysis provides a method for determining stiff parameters and facilitating the exploration of parameter combinations that ultimately lead to multi-stability. Further experimentation with additional time points performed under the same experimental conditions would perhaps improve parameter estimation and may provide the means for developing a more complex model.

Also inspired by the sensitivity analysis, the model, at baseline parameter values and the inferred initial conditions (as well as at the adjusted parameters n and K_{d1}), is found to be somewhat insensitive to changes in the Hb:Hp stimulus (for both constant and

exponential decay), meaning that if [Hb:Hp] $= 0$, the steady-state still approaches the (CD163, IL-10, HO-1)$^{\text{high}}$ state and does not afford the same switching effect as observed previously in Chapter 4 or by Model 5.1. This may suggest that if cells initially have low levels of CD163, IL-10 and HO-1, then the response, nonetheless, may result in an anti-inflammatory cellular phenotype despite the absence of Hb:Hp stimulus. Interestingly, when there is no stimulus [Hb:Hp] $= 0$ and absence of initial anti-inflammatory mediators (CD163, IL-10, HO-1)$_0 = (0, 0, 0)$, such as, for example, for cells that are pro-inflammatory, then the cell remains at a (CD163, IL-10, HO-1)$^{\text{low}}$ state. This model, in fact, predicts that for cells with no initial predisposition to an anti-infammatory phenotype that Hb:Hp is necessary to initiate a change in phenotype whereas cells that already have an anti-inflammatory predilection may not require the additional stimulus.

5.3.4 Comparison of model results to other stimuli

Much research suggests that the heme component of the Hb:Hp complex is responsible for both the cytotoxic effects (leading to the oxidation of molecules) and the anti-inflammatory response (Boyle *et al*., 2009; Kristiansen *et al*., 2001; Lee and Chau, 2002; Moestrup and Moller, 2004; Otterbein and Zuckerbraun, 2005; Sawle *et al*., 2005; Ugocsai *et al*., 2006). To test the anti-inflammatory effects, experimental time course data of HO-1, IL-10 and CD163 mRNA transcript expression after stimulation by 10 μM heme was obtained (see Materials and Methods). The heme stimulus was approximated to be $\sim 9.176 \times 10^{-4}$ g/mL Hb:Hp, which was used as the model stimulus (see Materials and Methods).

The obtained mRNA time course data of monocytes stimulated with heme is qualitatively compared to the simulated model results for the equivalent heme stimulus and Hb:Hp stimulus (Fig. 5.8). The Hb:Hp simulated time course (solid line) peaks and then falls to the steady-state level whereas the simulated heme time course (dotted line) does not have the same peaking behavior. The peaking behavior may indicate that the larger stimulus concentration (Hb:Hp) overshoots the steady-state before reaching the same state as the simulated heme model. In comparison to the experimental data (top row), the peaking behavior also occurs and then the mRNA levels decrease. In the first instance, the experimental stimulus of heme and simulated Hb:Hp levels may be too large and the species may initially over-respond before reaching the intended steady-state. Interestingly, the steady-state level of the experimental HO-1 mRNA fold change approaches a low steady-state after an initial peak ~ 12 fold change, whereas the Hb:Hp model simulation reaches a peak of ~ 7 fold change and both simulated models remain at an elevated

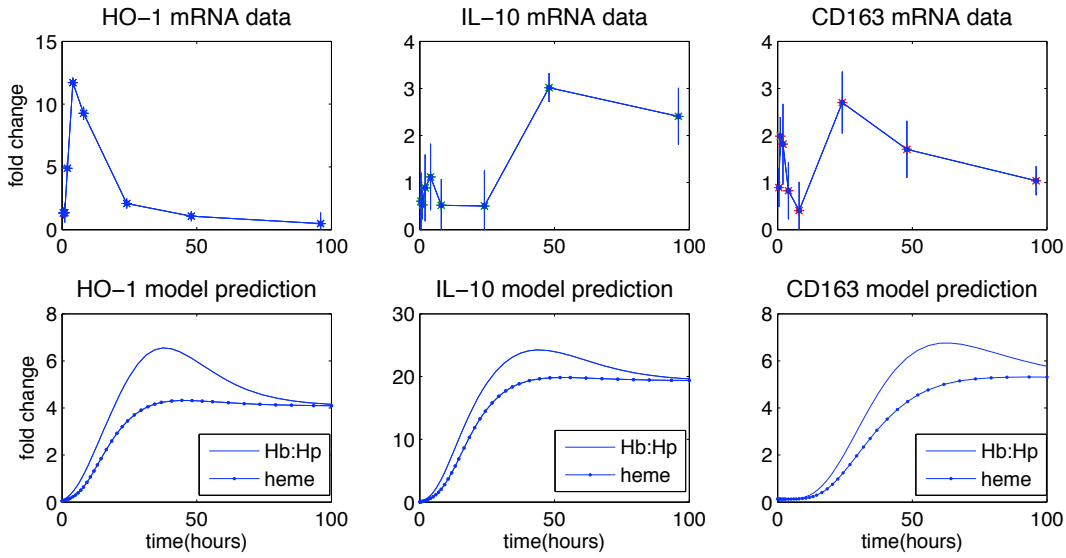

Figure 5.8: Time course (mRNA data) of monocyte response to heme stimulus. Time course of HO-1, IL-10, and CD163 induction by macrophages stimulated with heme (10 μM). Assay was determined by real-time reverse-transcription polymerase chain reaction (qRT-PCR), an experimental technique which provides a quantitative measure of mRNA, gene transcription expression, where the each data point is the mean fold change from $n = 3$ experiments. Data is qualitatively compared to model predictions

steady-state of approximately 4 fold change. Investigation of the model indicates that the HO-1 prolonged expression is necessary for prolonged IL-10 activation due to the positive feedback structure of the model. The IL-10 mRNA response for the heme stimuli suggests that the larger (Hb:Hp) stimulus gives a better qualitative representation; however both simulations predict that the fold change is approximately 20. The synthesis rates (p_i), determined to be sensitive parameters by the global sensitivity analysis, may require adjustment for a heme stimulus as the cellular mechanisms, such as lysosome catabolism and perhaps signaling to initiate IL-10 differs. Finally, the CD163 mRNA response peaks and then decays to a low level whereas the simulated model predicts the steady-state to remain elevated. Perhaps, since the simulation parameters were estimated using CD163 fluorescence expression rather than mRNA (known to synthesize before translation), the protein level may eventually reach a low state which was not taken into account in the parameter estimation.

Interestingly, the activation time of the heme simulation also occurs later than the Hb:Hp simulation. An explanation may be that a larger stimulus induces a quicker response compared to a smaller stimulus that results in a slower response. Contrasting the activation time of the experimental data to the simulated data shows an earlier activation peak. This may occur as a result of the initial parameter estimation; specifically, that the IL-10 and CD163 experimental measurement was protein expression whereas the exper-

imental set-up of heme recorded mRNA transcript response. Hence, fitting parameters to protein time course data and then comparing these results to mRNA would cause such a difference in activation time. This difference may also be extended to deactivation time, which, could not be taken into account from the protein expression data, and therefore, the end behavior could not be included in the parameter inference. The difference in the time scale may also be improved by obtaining both mRNA and protein data of Hb:Hp anti-inflammatory response performed under the same experimental conditions. Nevertheless, since protein synthesis is translated from mRNA, it can be assumed that the experimental results of protein expression for the heme system would occur at some time τ later after the given experimental mRNA fold change. Taking this into account as well as the fact that heme may enter cells by other means such as passive diffusion and heme carrier protein-1 (Latunde-Dada *et al.*, 2006; Schaer *et al.*, 2008; Tsiftsoglou *et al.*, 2006), the degradation of heme resulting in anti-inflammatory response may occur on a slightly quicker time scale; therefore, more comprehensive experimentation would be welcomed and serve to better identify the difference between different stimuli provoking an anti-inflammatory cellular phenotype.

Another possible stimulus of the system, as identified in the sensitivity analysis discussion, is interleukin-10. This cytokine has previously been found to increase CD163 expression (Boyle *et al.*, 2009; Sulahian *et al.*, 2000; Williams *et al.*, 2002). To test if this model could, in the absence of Hb:Hp stimulus, initiate an anti-inflammatory response, the trajectory of the system was numerically solved at the initial condition (CD163, IL-10, HO-1)$_0 = (0, 1, 0)$ and baseline parameter values. As shown in Fig. 5.9, the model does reproduce this finding and the system reaches the anti-inflammatory steady-state. In comparison to when the system is initiated at (CD163, IL-10, HO-1)$_0 = (0, 0, 0)$, the steady-state of both IL-10 and HO-1 remain at zero. Thus, the initial state of the cell and the IL-10 stimulus play an important role in the anti-inflammatory response.

5.4 Materials and Methods

5.4.1 Estimation of parameters

Values of model parameters were estimated from the literature and remaining parameters were fit to published data. A literature search was conducted of the variables: CD163, IL-10 and HO-1 as well as the stimuli, Hb:Hp complex and heme. The half-life of IL-10 is 3.6 ± 0.9 hours (Huhn *et al.*, 1997; Marino and Kirschner, 2004), the average of these values yields the degradation rate 0.193 hours^{-1}. The half-life of HO-1 in RAW 264.7

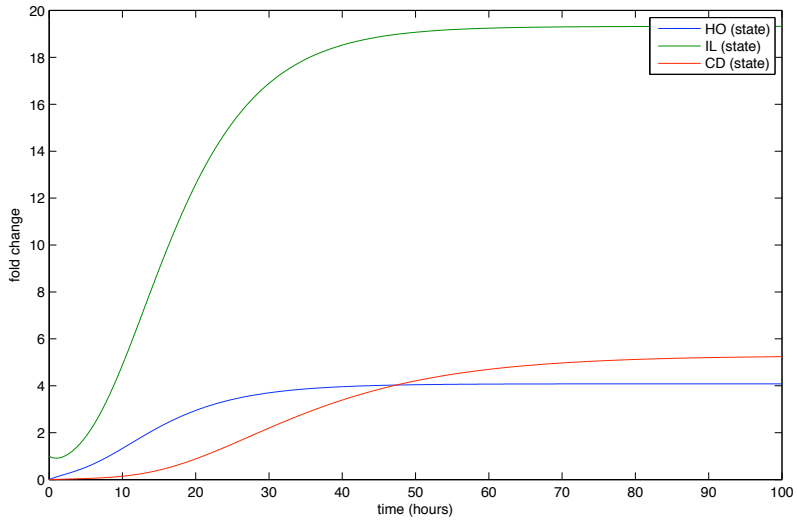

Figure 5.9: Time course of IL-10 stimulus prediction

macrophages is 3.41 ± 0.81 hours (Alcaraz *et al.*, 2001); giving an estimated degradation rate of 0.173 hours^{-1}. The half-life of Hb:Hp was determined to be 20 minutes (Garby and Noyes, 1959; Van Vlierberghe *et al.*, 2004) giving a degradation rate of 2.079 hours^{-1} and Hb has been reported to have an extracellular half-life of approximately 30 minutes, equivalent to a degradation rate of 1.385 hours^{-1}. The stimulus degradation rates were not used since it was assumed that the stimulus remained for a much longer time within the cell, thus the a smaller range between 0 and 1 for the degradation of Hb:Hp and heme, here, taken to be $\sim$ 0.08 hours^{-1}. In fact, since Hb:Hp may remain longer in the cells until degraded, an exponentially decaying stimulus is used, $[\text{Hb:Hp}] = H \cdot e^{-\lambda \cdot t}$ where H is the original stimulus concentration.

All simulations for stimuli were assumed as follows: the most common stoichometry of Hb:Hp is 1:1, where Hp is type 1-1, known to have anti-inflammatory effects (Guetta *et al.*, 2007), and each Hb includes four heme subunits. The Hb:Hp stimulus used by Schaer *et al.*, 2006, Philippidis *et al.*, 2004 and Boyle *et al.*, 2009 were 100 μg/mL, 1 mg/mL and 10^{-7} mol/L, all of which upregulated HO-1, IL-10 and CD163, respectively. Since the molecular weight of Hb:Hp is $\sim 1.504 \times 10^5$ g/mol (Odegaard and Atassi, 1984), then the Hb:Hp stimulus of 10^{-7} mol/L is approximately 1.5×10^{-5} g/mL. Therefore, the stimulus for simulations was set to $[\text{Hb:Hp}] \sim 5 \times 10^{-3}$ g/mL, where intuitively, this value is large enough to induce an anti-inflammatory response for all species. In order to compare the effects of heme using these models, an equivalent amount of Hb:Hp was calculated for a given heme dose: Given there are four heme subunits in each

Hb, and Heme b has a chemical formula $C_{34}H_{32}O_4N_4Fe$ with molecular weight of 616.5 g/mol (PubChem, 2009), then a heme dose of 10 μmol/L is equivalent to 9.176×10^{-4} g/mL Hb:Hp.

5.4.2 Data fitting and model selection

The ranges of initial conditions and remaining parameters (priors) were determined using the Nelder-Mead method. Recall from Chapter 3, direct search algorithms for fitting a model to data, such as the simplex method developed by Nelder and Mead, 1965, must be implemented when the derivative of the error function, ($E_D(\boldsymbol{\alpha})$ where $\boldsymbol{\alpha} \in \mathbb{R}^m$ is a set of m parameters) cannot be analytically determined. This nonlinear optimization technique for multidimensional unconstrained minimization, constructs a simplex S which is iteratively reflected, expanded, contracted and reduced. The simplex $S = \{s_1, \ldots, s_m, s_{m+1}\}$, is the convex hull of $m+1$ vertices such that $s_i \in \mathbb{R}^m$ and is sorted, $E_D(s_1) \leq \cdots \leq E_D(s_m) \leq E_D(s_{m+1})$. The centroid, or average of the lowest, or best m points is

$$\bar{s} = \frac{1}{m} \sum_{i=1}^{m} s_i,$$

and the simplex contracts towards s_1 by substituting s_i for $\frac{s_1+s_i}{2}$ to shrink the simplex (Nocedal and Wright, 2006). The fitting routine convergence is constrained (Lagarias *et al*., 1998) for the estimated set of parameters $\boldsymbol{\alpha}$, which include initial conditions.

This method also requires a range of values to search. The data are presented in fold change units, similar to that used of IL-10 in Figueiredo *et al*., 2009; therefore, the same parameter range is searched for

$$\boldsymbol{\alpha} = [[\mathrm{HO}-1_0], [\mathrm{IL}-10_0], [\mathrm{CD163}_0], K_{d2}, p_4, K_{d5}, p_3, K_{d4}, \alpha, p_1, n, K_{d1}, k_1],$$

between 10^{-3} and 100. For each of the four models, 2000 Nelder-Mead simulations were performed, with initial conditions randomly selected from the logarithmic interval $[-3, 2]$ and the degradation rate of the exponential stimulus was set to be 0.08 hours^{-1} since the stimulus is assumed to remain in the cell much longer than the *in vitro* rate ranging between 1.38 - 2.08 hours^{-1} (Garby and Noyes, 1959; Van Vlierberghe *et al*., 2004). The five fits of each model with the lowest error were taken as the initial prior range and given in Table 5.3.

Fitting of the parameters and initial conditions was performed using approximate Bayesian computation (ABC) based on sequential Monte Carlo (SMC) sampling, a method

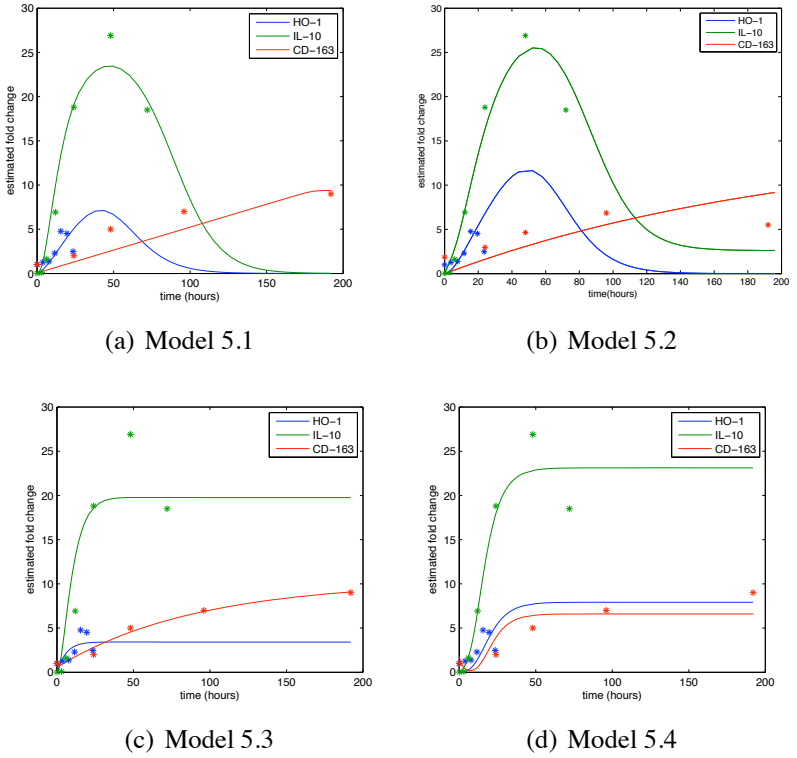

(a) Model 5.1 (b) Model 5.2

(c) Model 5.3 (d) Model 5.4

Figure 5.10: Data fitting from Nelder Mead results. Parameters and initial conditions fit to estimated fold change published data (Boyle *et al.*, 2009; Philippidis *et al.*, 2004; Schaer *et al.*, 2006). Hb:Hp is initialized at 5×10^{-3} g/mL (recall experimental results determine the phenotypic switch has been observed to occur for values as small as [Hb:Hp] $> 10^{-6}$ for CD163 and 10^{-4} for HO-1); therefore, the system is stimulated with initial Hb:Hp concentration comparable to the actual experiments. The fitting of these four models determined the range of initial condition and parameter priors for the ABC-SysBio model selection implementation.

developed by (Secrier *et al.*, 2009; Toni and Stumpf, 2010; Toni *et al.*, 2009), and available using the ABC-SysBio algorithm (Liepe *et al.*, In press). This statistical approach can infer parameters from experimental data given priors and simultaneously, this approach can perform model selection. Given the prior range obtained from the Nelder-Mead optimization and distribution $P(\boldsymbol{\alpha})$ found in Table 5.3 of parameters:

$$\boldsymbol{\alpha} = [[\mathrm{HO}-1_0], [\mathrm{IL}-10_0], [\mathrm{CD163}_0], K_{d2}, p_4, K_{d5}, p_3, K_{d4}, \alpha, p_1, n, K_{d1}, k_1, \lambda]\,,$$

the method provides an approximation of the posterior distribution $P(\boldsymbol{\alpha}|\hat{\mathbf{x}}) \propto f(\hat{\mathbf{x}}|\boldsymbol{\alpha})P(\boldsymbol{\alpha})$ where $f(\hat{\mathbf{x}}|\boldsymbol{\alpha})$ is the likelihood of $\boldsymbol{\alpha}$ given the experimental data $\hat{\mathbf{x}}$. ABC algorithms sample a parameter vector $\boldsymbol{\alpha}^*$ from a prior distribution $P(\boldsymbol{\alpha})$, then simulate a dataset $\mathbf{x}^*$ from the mechanistic model. If the distance between the experimental and simulated dataset, $d(\hat{\mathbf{x}}, \mathbf{x}^*)$, is less than a specified tolerance, ϵ, then $\boldsymbol{\alpha}^*$ is accepted. The ABC-SMC param-

eter inference samples a number of particles from the prior distribution. As the inference runs, the tolerance of acceptance ϵ is iteratively decreased such that $\epsilon_1 > \ldots > \epsilon_F \geq 0$ where F is the number of tolerances, and each tolerance ϵ_i determines an intermediate posterior distribution. The sampling from one iteration to the next is determined by the perturbation kernel, taken here to be a standard adaptive uniform kernel.

The ABC-SMC may be extended to parameter inference and model selection simultaneously using a joint space approach. This may be performed for M models where $M = [M_1, \ldots, M_4]$, by assigning each model (and parameters therein) a prior distribution and perturbation kernel that designates weights for model transition. The algorithm accepts N particles at the ϵ_F tolerance, which forms the joint posterior distribution $P(\boldsymbol{\alpha}, M|\hat{\mathbf{x}})$ and upon marginalizing over parameters, the marginal posterior distribution $P(M|\hat{\mathbf{x}})$ is approximated, providing a measurement for model selection. Bayes model selection, similar to other approaches including the likelihood ratio test or Akaike Information Criteria (AIC), also penalizes overparameterization. For example, as the ABC-SMC algorithm is searching through a larger parameter space for Model 5.4 than Model 5.3 (a submodel of Model 5.4 with less parameters), then it is more difficult to"hit" good parameters for Model 5.4 and thus penalizes models with more parameters. This ABC-SMC approach serves useful for simultaneous model discrimination and parameter inference.

5.4.3 Experimental data

Published data of HO-1 mRNA, IL-10 protein and CD163 fluoresence expression by Schaer *et al*., 2006, Philippidis *et al*., 2004 and Boyle *et al*., 2009, respectively, as shown in Figs. 2.3, 2.4, and 4.2, were used for the development, and refinement of intracellular mechanistic models presented. Additionally, Dr. Boyle provided time courses of HO-1, IL-10 and CD163 mRNA transcript expression after stimulation by 10 μM heme (see Fig. 5.8) to compare the model predictions of the intracellular models developed in the latter part of the chapter.

5.4.4 Sensitivity analysis

A sensitivity analysis on the estimated posterior of the final population was performed using principal component analysis (PCA), an approach that provides similar sensitivity results as computing the Hessian around the mode of the posterior distribution (Secrier *et al*., 2009). The posterior of inferred parameter values for the N particles may be described in a covariance or correlation matrix Σ of rank m where m is the number of

Initial Conditions	Prior Range	Estimated Value
$[\mathrm{HO}-1]$	$U(0, 1.5)$	4.96×10^{-2}
$[\mathrm{IL}-10]$	$U(0, 0.1)$	2.77×10^{-2}
$[\mathrm{CD163}]$	$U(0, 2)$	1.31×10^{-1}
Parameters	**Prior range**	**Estimated Value**
K_{d2}	$U(0, 1)$	3.0×10^{-2}
p_4	$U(0, 1)$	9.27×10^{-1} hours^{-1}
K_{d5}	$U(0, 100)$	6.047
p_3	$U(0, 10)$	8.607 hours^{-1}
K_{d4}	$U(0, 10)$	5.365
α	$U(0, 0.01)$	7.7×10^{-3} hours^{-1}
p_1	$U(0, 100)$	44.231 hours^{-1}
n	$U(1, 8)$	1.689
K_{d1}	$U(0, 1000)$	343.48
k_1	$U(0, 2)$	6.57×10^{-2} hours^{-1}
λ	$U(0.07, 0.09)$	7.58×10^{-2} hours^{-1}
K_{d3}	$U(0, 10)$	Not included in Model 5.3
p_2	$U(0, 10)$	Not included in Model 5.3
k_2		0.193 hours^{-1} hours^{-1}
k_3		0.173 hours^{-1} hours^{-1}
[Hb:Hp]		5×10^{-3} g/mL
heme		9.176×10^{-4} g/mL

Table 5.3: Initial condition and parameter priors and values for models. Prior distributions taken to be uniform (U) and interval of values taken from Nelder-Mead method (see Materials and Methods). ABC-SMC parameter inference and model selection gives parameter values relevant to the selected model. Remaining parameter values taken from the literature and described in text. The measure of species concentration have no units since these are nondimensional fold change and parameter units correspond.

inferred parameters. It follows that the set of eigen-parameters $\mathrm{X}_i = \nu_{i1}\alpha_1 + \cdots + \nu_{im}\alpha_m$ may be determined where ν_i is the normalized eigenvector of Σ, corresponding to its eigenvalue λ_i. The eigenvectors ν_is corresponding to their eigenvalues λ_is are the principle components of the posterior and the value of λ_i gives the variance of the ith principal component, which can be described a proportion of the total variance of all PCs, $\lambda_i/\mathrm{trace}(\Sigma)$, where $\sum_{i=1}^{m}\lambda_i = \mathrm{trace}(\Sigma)$ is the total variance of all PCs. Often, the largest principal component, corresponding to the dominant eigenvalue λ_1 is most important; however, in this case, the dominant eigenvalues (and first few PCs) represent the 'sloppy' parameters, that is, parameters that have the least information. The final or smallest PCs, equivalent to the leading eigenvalues of the Hessian, represent the most sensitive parameters, corresponding to stiff parameter combinations. The sensitivity of the parameters described by the smallest PC may be taken as projections of the eigen-parameters X_i onto the raw parameters α_i by computing the eigen-directions which have the largest value (Secrier *et al*., 2009). Therefore, in this context, performing PCA may give useful information about the sensitivity and stiff parameter combinations. For further treatment on PCA used for ABC-SMC results, see Toni *et al*., 2009 and Secrier *et al*., 2009.

Additionally, a global sensitivity analysis is performed of inferred parameter values using Partial rank correlation coefficient analysis (PRCC) and Fourier amplitude sensitivity test (FAST) methods as described previously in Chapter 3.

5.4.5 SBML implementation

For standards compliance, the Models 5.1 - 5.4 were implemented using the Systems Biology Markup Language (SBML) Level 2 Version 1 (Finney and Hucka, 2003; Hucka *et al*., 2003). The models are named `model1.xml`, `model2.xml`, `model3.xml` and `model4.xml`.

5.5 Conclusion

This work presented different models describing intracellular mechanisms between HO-1, IL-10 and CD163. In these models, cooperativity between IL-10 and CD163 was assumed, and different hypotheses of the interactions were tested. By using the ABC-SMC method, the posterior distribution of the estimated parameters was obtained, providing useful information about the identifiability of inferred parameters and thus serves as a tool for model discrimination. The results of data fitting and model selec-

tion predicted that IL-10/HO-1 feedback loop plays a key role to anti-inflammatory response, supporting the hypothesis by Lee and Chau, 2002. Interestingly, the principal component analysis also provided a procedure to pinpoint parameter combinations that are most sensitive to perturbations. Adjusting the value of the two parameters selected by this analysis facilitated a natural manner to construct a slightly different parameter space capable of multiple permissible steady-states for the selected model. Furthermore, parameter estimation determined the system exhibits cooperativity (value of the Hill coefficient greater than one) between IL-10 and CD163. The model selection and parameter inference, model selection and sensitivity analysis provided a first step in identifying the anti-inflammatory mechanisms associated with the CD163 macrophage phenotype. This model also demonstrates that additional biological work is necessary to determine the signaling pathways and the regulation of transcription factors that govern the anti-inflammatory response driven by Hb:Hp/heme stimuli.

The model was then extended to study the effects of heme, the molecule within the Hb:Hp complex thought to be responsible for initiating an anti-inflammatory response. Comparing the model results to these data revealed that a higher stimulus effects the peak behavior and increases the activation time. Taking into account the difference between data obtained (mRNA expression) compared to the model measurements (protein CD163 and IL-10), the model results gave a relatively good qualitative representation of the data, suggesting that the mechanisms responsible for heme initiated anti-inflammatory response are indeed similar to Hb:Hp complexes. Therefore, this work presents a novel mechanistic model approach of the macrophage response to heme/Hb:Hp complexes. More sophisticated models may better differentiate the effects of these two stimuli; however, further experimental work must first be obtained to compare these, such as, for example mRNA and protein expression time courses of both heme and Hb:Hp stimulated macrophages. As new experimental information becomes available, Model 5.5 may include the intracellular mediators/regulators of the model species (such as negative regulator, Bach1), intracellular heme products (such as carbon monoxide, responsible for activating known anti-inflammatory pathways p38, PI-3K or STAT3) (Lee and Chau, 2002; Ricchetti *et al*., 2004) as well as the including the upstream signaling MAPK cascade and the downstream anti-inflammatory transcription factors. Looking forward, future models of macrophage inflammatory response may include the interactions between heme and the MAPK pathway (Mense and Zhang, 2006) and incorporating the recent model of the IL-10/ERK/p38 MAPK interactions in nematodes Figueiredo *et al*., 2009, suggesting negative regulation of MAPK by IL-10. In addition to the heme/Hb:Hp characterization, this model also provided a mechanistic explanation of how an anti-inflammatory stimu-

lus, such as IL-10, affects the phenotype of a neutral cell (such as a monotcyte) that has neither pro- or anti-inflammatory predisposition.

This work enabled a quantitative study of the effects of Hb:Hp complexes, interleukin-10 and free heme on macrophage differentiation and response in vascular plaques; hence, this study may provide insight for future research and medical therapies for vascular inflammatory diseases.

Chapter 6

Modularized model of apoptosis

6.1 Overview

The primary focus of the work in this chapter is to construct a simple model of caspase-3 activation featuring the oligomerization kinetics of the DISC, mitochondrial apoptosis-induced channel (MAC) and the apoptosome; the dynamics of the extrinsic and intrinsic caspase subnetworks, as well as the coupling between the extrinsic and intrinsic pathways. To accomplish this, three independent functional modules are constructed (Hartwell *et al*., 1999; Klipp *et al*., 2005; Ortega *et al*., 2008; Watson and Pollack, 2005). These are implemented for the abstraction of oligomerization kinetics that simplify the full system. Multiple linear regression analysis is applied to investigate the role of each module and reduced models are constructed to identify key contributions of the extrinsic and intrinsic pathways in triggering apoptosis for different cell lines. Through linear regression techniques, feedbacks, dissociation of complexes, and negative regulators are identified as the key components in apoptosis. The analysis and reduced models for the model formulation reveal that the chosen cell lines predominately exhibit strong extrinsic caspase, typical of type I cell, behavior. Furthermore, under the simplified model framework, the selected cell lines exhibit different modes by which caspase activation may occur. Finally, the proposed modularized model of apoptosis may generalize behavior for additional cells and tissues, specifically identifying and predicting components responsible for the transition from type I to type II cell behavior.

This research was conducted in collaboration with Kenneth L. Ho. The inception of this work commenced at the 2007 Mathematical Biosciences Institute (MBI) Summer School at Ohio State University, Columbus, OH, USA with workshop participants Samik Ghosh, and K.C. Tung. Baltzar Aguda and Chiu-Yen Kao supervised the work, and co-authors gratefully acknowledge the financial support from MBI. In collaboration with

Kenneth L. Ho, the research was designed and conducted, model analysis (including the code), manuscript writing, and revisions, with equal contributions of intellectual content. This work was published (Harrington *et al*., 2008).

6.2 Introduction

Recall from Chapter 2, apoptosis, or programmed cell death, is a physiological process critical for development, tissue homeostasis, cell termination and immune response (Hengartner, 2000; Hutchins and Barger, 1998; Jacobson *et al*., 1997; Leist and Jäättelä, 2001; Lockshin and Zakeri, 2001; Meier *et al*., 2000; Oppenheim, 1991; Raff, 1998; Zuzarte-Luis and Hurle, 2002). Dysregulation of apoptosis may result in a myriad of conditions such as autoimmunity, cancer or neurological conditions (Chang and Yang, 2000; Fadeel *et al*., 1999; Haass, 1999; Johnstone *et al*., 2002; Pritchard and Hickman, 1994; Thompson, 1995; Thornberry and Lazebnik, 1998). As shown previously in Fig. 2.5, apoptosis is mediated by apoptotic complexes along one of two pathways: the extrinsic pathway (receptor mediated) via the death inducing signaling complex (DISC), or the intrinsic pathway (mitochondrial) via the apoptosome (Ashkenazi and Dixit, 1998; Budihardjo *et al*., 1999; Cain *et al*., 1999, 2000, 2002; Fumarola and Guidotti, 2004; Hengartner, 2000; Jiang and Wang, 2004). The extrinsic initiator caspase (caspase-8) couples the two pathways by initiating the mitochondrial apoptosis-induced channel (MAC), leading to the activation of the intrinsic pathway (Li *et al*., 1998). The subsequent cell death for either pathway is executed through a cascade activation of effector caspases (e.g., caspase-3) by initiator caspases (e.g., caspase-8 and -9) and the amplification of death signals implemented by several positive feedback loops and inhibitors in the network (Arends and Wyllie, 1991; Budihardjo *et al*., 1999; Nunez *et al*., 1998; Oppenheim, 1991; Takahashi and Earnshaw, 1996; Thornberry and Lazebnik, 1998; Zimmermann *et al*., 2001). While apoptosis can be activated by either pathway, some cell lines are pathway specific. Cells requiring death receptors (and caspase-8) but not needing help from mitochondria organelles for apoptosis are classified as type I (such as T cells and thymocytes (Barnhart *et al*., 2003)). Conversely, type II cells (i.e., hepatocytes of Bcl-2 transgenic mice (Barnhart *et al*., 2003)) have a reduced DISC formation and predominantly depend on the mitochondria pathway (formation of apoptosome and caspase-9) to undergo cell death (Barnhart *et al*., 2003; Fulda *et al*., 2001; Scaffidi *et al*., 1998; Schmitz *et al*., 2000).

Apoptosis is typically thought of as a bistable system, ideally irreversibly bistable, with attracting life and death states, and a sharp all-or-none switch in between. This bistability is important for conferring biological robustness (Kitano, 2004). Consequently,

researchers have used computational models to identify and study potential sources of bistability in apoptosis, including positive caspase feedback (Eissing *et al*., 2004), inhibition of DISC by cFLIP (Bentele *et al*., 2004), cooperativity in apoptosome formation (Bagci *et al*., 2006), double-negative caspase feedback through XIAP (Legewie *et al*., 2006), and double-negative feedback in Bcl-2 protein interactions (Cui *et al*., 2008). The maturity of the field has enabled the proliferation of mathematical models, both mechanistic and integrative, which have, in aggregate, contributed significantly to the theoretical analysis and understanding of the underlying molecular interactions (Albeck *et al*., 2008a,b; Bagci *et al*., 2006; Cui *et al*., 2008; Eissing *et al*., 2004, 2005; Fussenegger *et al*., 2000; Harrington *et al*., 2008; Hua *et al*., 2005, 2006; Janes *et al*., 2005; Lai and Jackson, 2004; Legewie *et al*., 2006; Nakabayashi and Sasaki, 2006; Okazaki *et al*., 2008; Rangamani and Sirovich, 2007; Ryu *et al*., 2008; Stucki and Simon, 2005).

Most of these models focus on specific components of the full apoptotic machinery. Models by Eissing *et al*., 2004 and Legewie *et al*., 2006 emphasized either the extrinsic or intrinsic caspase pathways, respectively. Both of these models identify inhibitors and feedback mechanisms of caspase-8, or -9, respectively, and caspase-3 to mediate bistability. The model developed by Fussenegger *et al*., 2000 implemented both pathways but did not consider the coupling between them; however, Bagci *et al*., 2006, Albeck *et al*., 2008a and Cui *et al*., 2008 modeled the mitochondrial apoptosis-induced channel (MAC). Stucki and Simon, 2005 modeled only the caspase-3 activation and degradation but none of the aforementioned models closely track the upstream formation dynamics of the DISC and the apoptosome, which have since been modeled in detail by Lai and Jackson, 2004, and by Nakabayashi and Sasaki, 2006, respectively. Hua *et al*., 2005, 2006 formulated complete system models that incorporate the differences in type I and II signaling as well as include additional species, such as Smac; however not all dynamics, e.g., feedbacks, are included from previous component models (Eissing *et al*., 2004; Lai and Jackson, 2004; Legewie *et al*., 2006; Nakabayashi and Sasaki, 2006). More recently, Okazaki *et al*., 2008 formulated a model based on Hua *et al*., 2005, 2006 of the phenotypic switch from type I and type II apoptotic death, but their model does not incorporate protein synthesis or degradation.

6.2.1 Models of oligomeric complex formation

The mechanism responsible for initiating apoptosis, oligomerization, is a process of complex formation to activate the apoptotic pathway (Chang *et al*., 2003). Recall the three oligomerizations: DISC, apoptosome and MAC, each of which have corresponding

mathematical ordinary differential equation models describing the oligomerization kinetics (Albeck *et al*., 2008a; Bagci *et al*., 2006; Cui *et al*., 2008; Lai and Jackson, 2004; Nakabayashi and Sasaki, 2006).

The Lai and Jackson, 2004 model studies the formation of the Fas/FasL complex, which feeds directly into the formation of DISC and hence is crucial to its understanding. The formation dynamics are modeled using a system of ordinary differential equations that reflects the cross-linking nature of the complex assembly, which are solved to obtain equilibrium concentrations of the complex and its intermediates. Of particular interest is that for a given receptor concentration, Lai and Jackson, 2004 predicts the existence of an optimal ligand concentration for maximum complex production (reproduced in Fig. 6.1); intuitively, this may be explained by considering a simple combinatorial argument on the rate of formation of intermediate species. Moreover, their work is the only model that exists with an explanation Fas trimerization, the complex of three Fas necessary form the DISC. Experimental methods are unable to elucidate why Fas is a trimer, thus this mathematical model offers a hypothesis of the interactions.

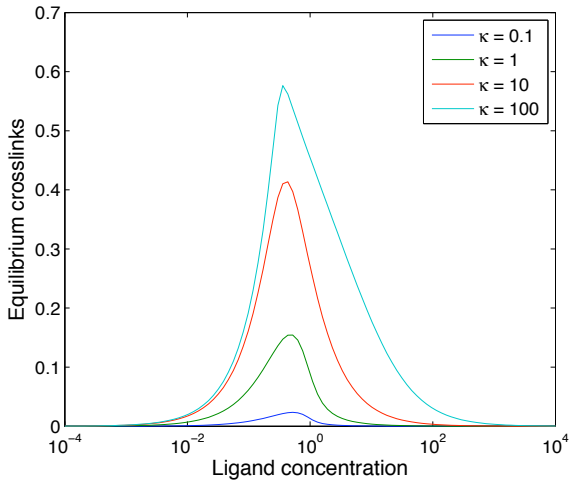

Figure 6.1: Optimal ligand (FasL) concentration for DISC formation. Reproduction of Lai and Jackson, 2004 results, optimal ligand concentration for equilibrium crosslinks (representative of the DISC formation and activation of the apoptotic pathway) for different production rate constants (κ). The model equations are described in detail in Subsec. 6.3.2.

The model developed by Nakabayashi and Sasaki, 2006 explicitly models the formation of the apoptosome. Cytochrome c binds and activates Apaf-1, which oligomerize to form heptamers with 7-fold symmetry; thereafter, the heptamers are activated by a nucleotide exchange to form apoptosomes. The novelty of this work lies in the identification of an optimal one-to-one ratio of cytochrome c and inactive Apaf-1 for the rate of apoptosome formation (reproduced in Fig. 6.2). Similar to Lai and Jackson, 2004, this model

focuses only on the complex formation without considering downstream activation of the caspase cascade.

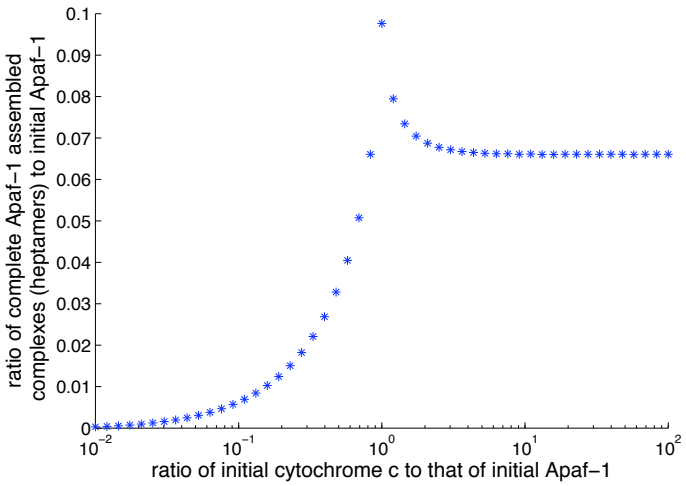

Figure 6.2: Optimal cytochrome c/Apaf-1 ratio. Reproduction of Nakabayashi and Sasaki, 2006 equilibrium results (as data) exhibiting a one-to-one ratio of cytochrome c and innative Apaf-1 for the rate of apoptosome formation and activation of the apoptotic pathway. Horizontal axis demonstrates the ratio of initial cytochrome c to that of initial Apaf-1. Vertical axis denotes the ratio of complete Apaf-1 assembled complexes (heptamers) to initial Apaf-1. The model equations are described in detail in Subsec. 6.3.2.

The Bid-induced Bax oligomerization models of, Albeck *et al.*, 2008a; Bagci *et al.*, 2006; Cui *et al.*, 2008 study the role of Bax, Bid and Bcl-2 switching mechanisms as regulators that ensure bistability in the mitochondrial apoptosis-induced channel (MAC). This work focuses solely on the mitochondrial mediated apoptotic pathway and does not include the dynamics of other signaling pathway components.

6.2.2 Caspase feedback models

In the Eissing *et al.*, 2004 model, a representation of the extrinsic caspase pathway is developed based on mass action kinetics; however, the authors do not consider the dynamics of the activating stimulus, i.e., the formation of DISC. This work also identifies the inhibitors of caspase-3 (XIAP and its degradation) to be primarily controlling the bistable behavior of the death signal rather than the positive feedback between caspase-3 and caspase-8. This bistability finding suggests the important role of the downstream apoptotic interactions.

The model developed by Legewie *et al.*, 2006 represents the intrinsic pathway behavior through a system of biochemical equations (28 equations and 33 parameters). While this model also identifies inhibitors that mediate bistability and feedback mechanisms of

caspase-3 and caspase-9, the model does not include the oligomerization of apoptosome (from Apaf-1 triggered by cytochrome c).

6.3 Methods

6.3.1 Model formulation

The full reaction network of the model is built from three component subnetworks (see Fig. 6.3): the extrinsic, coupling, and intrinsic subnetworks; and three oligomerization modules (represented by gray areas in Fig. 6.3): the DISC, MAC, and apoptosome modules. Each subnetwork captures a vital part of the full apoptotic reaction network and borrows heavily from previous work (Bagci *et al*., 2006; Eissing *et al*., 2004; Hua *et al*., 2005; Legewie *et al*., 2006; Okazaki *et al*., 2008), while each module abstracts the oligomerization kinetics of an apoptotic complex to give a simplified net synthesis function using steady-state results (Lai and Jackson, 2004; Nakabayashi and Sasaki, 2006).

The extrinsic subnetwork follows Eissing *et al*., 2004 and captures the dynamics of the extrinsic pathway. The subnetwork contains the species FasL, FasR, DISC, procaspase-8 ($\mathrm{Casp8}$), caspase-8 ($\mathrm{Casp8^*}$), procaspase-3 ($\mathrm{Casp3}$), caspase-3 ($\mathrm{Casp3^*}$), XIAP, and BAR. The subnetwork is driven by DISC, whose formation dynamics from FasL and FasR are encapsulated by the DISC module using the results of Lai and Jackson, 2004. DISC induces the cleavage of $\mathrm{Casp8}$ to $\mathrm{Casp8^*}$, which then activates $\mathrm{Casp3}$ to produce $\mathrm{Casp3^*}$. Positive feedback between $\mathrm{Casp8^*}$ and $\mathrm{Casp3^*}$ is provided by the activation of $\mathrm{Casp8}$ by $\mathrm{Casp3^*}$. XIAP and BAR act as regulators by binding to $\mathrm{Casp3^*}$ and $\mathrm{Casp8^*}$, respectively. Furthermore, degradation of XIAP is enhanced by $\mathrm{Casp3^*}$.

The extrinsic subnetwork can drive the intrinsic pathway through the coupling subnetwork, which describes the role of $\mathrm{Casp8^*}$ in inducing mitochondrial membrane permeabilization and triggering the release of cytochrome c and Smac. The coupling subnetwork is inspired by a combination of Bagci *et al*., 2006; Hua *et al*., 2005; Okazaki *et al*., 2008, and contains the additional species Bid, tBid, Bax, cytochrome c (mitochondrial, $\mathrm{Cyt}c$; cytosolic $\mathrm{Cyt}c^*$), and Smac (mitochondrial, Smac; cytosolic, $\mathrm{Smac^*}$). The subnetwork receives input from $\mathrm{Casp8^*}$, which cleaves Bid to produce tBid. Bax then dimerizes with tBid to form $\mathrm{tBid\text{-}Bax_2}$, which is taken as a representation of the MAC that controls the release of $\mathrm{Cyt}c$ and Smac from the mitochondria to produce $\mathrm{Cyt}c^*$ and $\mathrm{Smac^*}$, respectively; the formation dynamics of $\mathrm{tBid\text{-}Bax_2}$ are abstracted in the MAC module using similar methods as for the DISC module. Morever, $\mathrm{Smac^*}$ acts as a regulator by binding to XIAP.

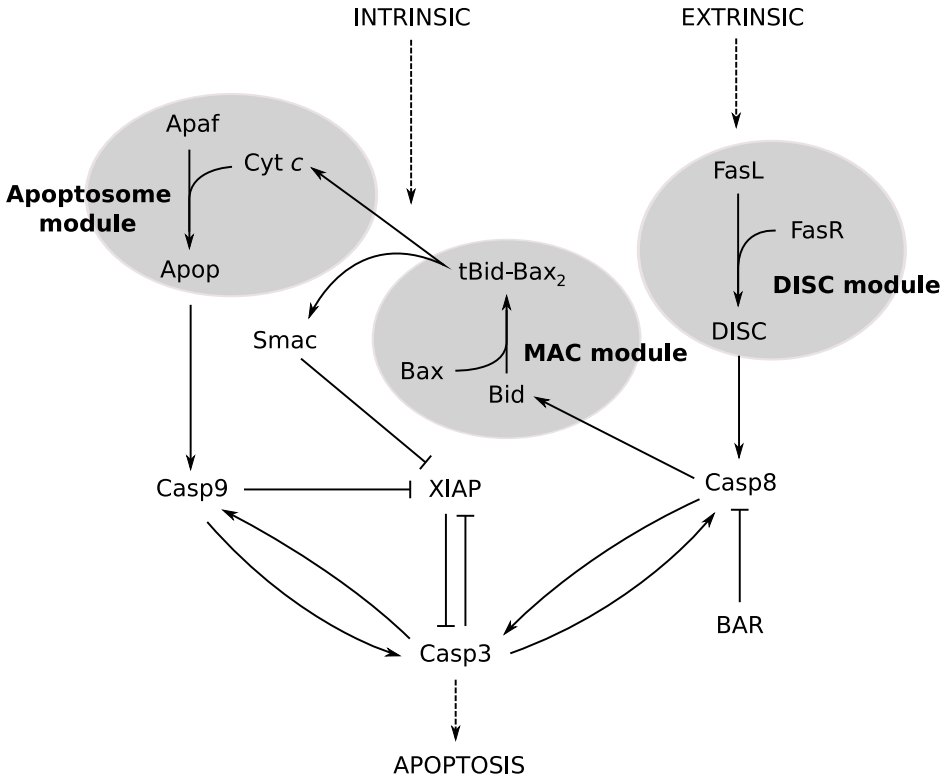

Figure 6.3: Extrinsic and intrinsic pathways to caspase-3 activation. Overview of pathways to caspase-3 activation. Each separate gray region represent the three modules: DISC (death-inducing signaling complex), MAC (mitochondrial apoptosis-induced channel) and apoptosome. Species and their symbols are: FasL (FasL), FasR (FasR), DISC (DISC), procaspase-8 and caspase-8 (Casp8), bifunctional apoptosis inhibitor (BAR), procaspase-3 and caspase-3 (Casp3), XIAP (XIAP), Bid and truncated Bid (Bid), Bax (Bax), $tBid - Bax_2$ complex ($tBid - Bax_2$), Smac (Smac), Apaf-1 (Apaf), cytochrome c (Cyt$c$), apoptosome (Apop), procaspase-9 and caspase-9 (Casp9). Arrows denote chemical conversions or catalyzed reactions while hammerheads represent inhibition.

The intrinsic subnetwork follows the intrinsic pathway from the assembly of the apoptosome to the resulting caspase interactions. The oligomerization of the apoptosome is abstracted in the apoptosome module using the results of Nakabayashi and Sasaki (2006), while the remainder of the subnetwork is simplified from Legewie *et al*. (2006). Additional species contained in the subnetwork include Apaf-1 (Apaf), apoptosome (Apop), procaspase-9 (Casp9), and caspase-9 (Casp9*). The subnetwork is driven by Cytc^*, which binds to Apaf; activated Apaf then oligomerizes to form Apop, which cleaves Casp9 to produce Casp9*. As in the extrinsic subnetwork, positive feedback exists between Casp9* and Casp3*. Furthermore, Casp9* binds XIAP.

Constitutive synthesis and degradation rates are assumed for all appropriate species.

6.3.2 Steady-state abstraction of oligomerization kinetics

The oligomerization kinetics of the DISC, MAC, and the apoptosome are abstracted using steady-state results; this abstraction is a demonstration of a simple technique for modularization and model reduction. For an oligomer X with intermediate structures $X_1, \ldots, X_n$ and dynamics

$$\frac{d[X]}{dt} = f\left([X], [X]_1, \ldots, [X]_n\right) - \mu[X],$$

where f is the oligomerization rate function and μ the degradation rate, use the steady-state approximation $f \approx f_{\mathrm{ss}} \propto [X]_{\mathrm{ss}}$. This allows the modeling of only the final complex and hence significant simplification of the dynamical equations. Although the time dependence of the oligomerization rate is neglected, information regarding the long-term behavior is retained. For the present application, $f = [X]_{\mathrm{ss}}$ with proportionality constant μ.

The abstractions for each of the DISC, MAC, and apoptosome modules are described below, where the notation is understood to apply only within each module.

DISC module

The DISC oligomerization kinetics are simplified from the crosslinking model (Delisi, 1980; Perelson, 1984, 1981) of Lai and Jackson, 2004 and follow the reactions

$$\begin{aligned}
\mathrm{FasL} + \mathrm{FasR} &\underset{k_r}{\overset{3k_f}{\rightleftharpoons}} \mathrm{FasL\text{-}FasR}, \\
\mathrm{FasL\text{-}FasR} + \mathrm{FasR} &\underset{2k_r}{\overset{2k_f}{\rightleftharpoons}} \mathrm{FasL\text{-}FasR_2}, \\
\mathrm{FasL\text{-}FasR_2} + \mathrm{FasR} &\underset{3k_r}{\overset{k_f}{\rightleftharpoons}} \mathrm{FasL\text{-}FasR_3},
\end{aligned}$$

describing the trimerization of FasR to FasL. With $l \equiv [\mathrm{FasL}]$, $r \equiv [\mathrm{FasR}]$, and $c_i \equiv [\mathrm{FasL\text{-}FasR}_i]$, the corresponding dynamics are

$$\begin{cases} dl/dt = -v_1, \\ dr/dt = -v_1 - v_2 - v_3, \\ dc_1/dt = v_1 - v_2, \\ dc_2/dt = v_2 - v_3, \\ dc_3/dt = v_3, \end{cases} \qquad \begin{cases} v_1 = 3k_f lr - k_r c_1, \\ v_2 = 2k_f c_1 r - 2k_r c_2, \\ v_3 = k_f c_2 r - 3k_r c_3, \end{cases}$$

which reduces at steady-state to,

$$c_{1,\mathrm{ss}} = 3l_{\mathrm{ss}} \left(\frac{r_{\mathrm{ss}}}{K_D} \right), \quad c_{2,\mathrm{ss}} = 3l_{\mathrm{ss}} \left(\frac{r_{\mathrm{ss}}}{K_D} \right)^2, \quad c_{3,\mathrm{ss}} = l_{\mathrm{ss}} \left(\frac{r_{\mathrm{ss}}}{K_D} \right)^3,$$

where $K_D = k_r/k_f$. Applying the conservation relations,

$$l_0 = l + c_1 + c_2 + c_2, \quad r_0 = r + c_1 + 2c_2 + 3c_3$$

to obtain

$$l_{\mathrm{ss}} = \frac{l_0}{1 + 3\left(r_{\mathrm{ss}}/K_D\right) + 3\left(r_{\mathrm{ss}}/K_D\right)^2 + \left(r_{\mathrm{ss}}/K_D\right)^3},$$

where r_{ss} is given by solving

$$r_{\mathrm{ss}}^4 + \alpha r_{\mathrm{ss}}^3 + \beta r_{\mathrm{ss}}^2 + \gamma r_{\mathrm{ss}} - K_D^3 r_0 = 0, \quad \begin{cases} \alpha = 3l_0 - r_0 + 3K_D, \\ \beta = 3K_D\left(2l_0 - r_0 + K_D\right), \\ \gamma = K_D^2\left(3l_0 - 3r_0 + K_D\right), \end{cases}$$

which has at most one positive root. Assume now that FADD is in excess (see, e.g., Hua *et al*., 2005; Okazaki *et al*., 2008) to obtain

$$[\mathrm{DISC}]_{\mathrm{ss}} = c_{2,\mathrm{ss}} + c_{3,\mathrm{ss}} \equiv f\left(l_0, r_0; K_D\right),$$

where it is assumed that both $\mathrm{FasL\text{-}FasR}_2$ and $\mathrm{FasL\text{-}FasR}_3$ can propagate the death signal (Lai and Jackson, 2004). Externally, in the full reaction network, the oligomerization rate function will be called $f_{\mathrm{DISC}}\left([\mathrm{FasL}]_0, [\mathrm{FasR}]_0; K_{\mathrm{DISC}}\right)$. This abstraction reduces the order of the system by four.

MAC module

The oligomerization kinetics of the MAC module are assumed to follow a similar crosslinking model and therefore obey the reactions

$$\mathrm{tBid} + \mathrm{Bax} \underset{k_r}{\overset{2k_f}{\rightleftharpoons}} \mathrm{tBid\text{-}Bax}, \quad \mathrm{tBid\text{-}Bax} + \mathrm{Bax} \underset{2k_r}{\overset{k_f}{\rightleftharpoons}} \mathrm{tBid\text{-}Bax_2}.$$

With analogous notation $l \equiv [\mathrm{tBid}]$, $r \equiv [\mathrm{Bax}]$, and $c_i \equiv [\mathrm{tBid\text{-}Bax}_i]$, the dynamics are

$$\begin{cases} dl/dt = -v_1, \\ dr/dt = -v_1 - v_2, \\ dc_1/dt = v_1 - v_2, \\ dc_2/dt = v_2, \end{cases} \qquad \begin{cases} v_1 = 2k_f lr - k_r c_1, \\ v_2 = k_f c_1 r - 2k_r c_2, \end{cases}$$

so

$$c_{1,\mathrm{ss}} = 2l_{\mathrm{ss}} \left(\frac{r_{\mathrm{ss}}}{K_D} \right), \quad c_{2,\mathrm{ss}} = l_{\mathrm{ss}} \left(\frac{r_{\mathrm{ss}}}{K_D} \right)^2.$$

Similar conservation relations then give

$$l_{\mathrm{ss}} = \frac{l_0}{(1 + r_{\mathrm{ss}}/K_D)^2}$$

with

$$r_{\mathrm{ss}}^3 + \alpha r_{\mathrm{ss}}^2 + \beta r_{\mathrm{ss}} - K_D^2 r_0 = 0, \quad \begin{cases} \alpha = 2l_0 - r_0 + 2K_D, \\ \beta = K_D \left(2l_0 - 2r_0 + K_D \right), \end{cases}$$

which again has at most one positive root. Therefore,

$$[\mathrm{tBid\text{-}Bax_2}]_{\mathrm{ss}} = c_{2,\mathrm{ss}} \equiv f\left(l_0, r_0; K_D \right),$$

and externally this will be denoted by $f_{\mathrm{tBid\text{-}Bax_2}}([\mathrm{tBid}], [\mathrm{Bax}]_0; K_{\mathrm{tBid\text{-}Bax_2}})$, where the dynamical concentration of tBid is used as input. This abstraction reduces the order of the system by three.

Apoptosome module

The oligomerization kinetics of the apoptosome follow the model of Nakabayashi and Sasaki, 2006 with no dissociation, which considers bimolecular interactions of the form

$$\begin{aligned} \text{Apaf} + \text{Cyt}c^* &\xrightarrow{k_1} \text{Apaf-Cyt}c^*, \\ \left(\text{Apaf-Cyt}c^*\right)_i + \left(\text{Apaf-Cyt}c^*\right)_j &\xrightarrow{k_2} \left(\text{Apaf-Cyt}c^*\right)_k, \quad i+j=k\leq 7, \end{aligned}$$

where $\text{Apop} \equiv \left(\text{Apaf-Cyt}c^*\right)_7$. With the nondimensionalizations

$$c \equiv \frac{[\text{Cyt}c^*]}{[\text{Apaf}]_0}, \quad a \equiv \frac{[\text{Apaf}]}{[\text{Apaf}]_0}, \quad x_i \equiv \frac{[\left(\text{Apaf-Cyt}c^*\right)_i]}{[\text{Apaf}]_0},$$

the dynamics are

$$\begin{aligned} \frac{da}{d\tau} &= \frac{dc}{d\tau} = -ac, \\ \frac{dx_1}{d\tau} &= ac - \lambda x_1 \left(2x_1 + x_2 + \cdots + x_6\right), \\ \frac{dx_i}{d\tau} &= \lambda \left[\sum_{j=1}^{\lfloor i/2 \rfloor} x_j x_{i-j} - x_i \sum_{j=1}^{7-i} \left(1+\delta_{ij}\right) x_j\right], \quad i = 2,\ldots,7, \end{aligned}$$

where $\tau = \alpha a_0 t$, $\lambda = k_2/k_1$, and δ is the Kronecker delta. Integration of this system until steady-state over a range of c_0 generates a curve for x_7 that may accurately fit with a piecewise exponential function

$$g\left(c_0\right) = \begin{cases} g_1\left(c_0\right), & c_0 \leq 1, \\ g_2\left(c_0\right), & c_0 > 1, \end{cases} \qquad g_i\left(c_0\right) = \alpha_i e^{\beta_i c_0} + \gamma_i.$$

Continuity at $c_0 = 1$ and boundary conditions at $c_0 = 0$ and ∞ give

$$g_1\left(c_0\right) = \left(\frac{e^{\beta_1 c_0} - 1}{e^{\beta_1} - 1}\right) x_{7,\text{ss}}\left(1\right), \quad g_2\left(c_0\right) = \left[x_{7,\text{ss}}\left(1\right) - x_{7,\text{ss}}\left(\infty\right)\right] e^{\beta_2\left(c_0 - 1\right)} + x_{7,\text{ss}}\left(\infty\right),$$

where β_1 and β_2 may be fitted for any prescribed λ. The apoptosome oligomerzation rate function is then $f(c_0;\lambda) = a_0 g(c_0;\lambda)$, and externally this is $f_{\text{Apop}}([\text{Cyt}c^*] \,/\, [\text{Apaf}]_0\,;\lambda_{\text{Apop}})$. This abstraction reduces the order of the system by eight.

Remarks on modularization

The steady-state profiles of the oligomerization kinetics (as shown in Fig. 6.4) are supported by the models that motivated this simplification (Lai and Jackson, 2004; Nakabayashi and Sasaki, 2006) and experimentally for tBid inducing a switch (Madesh *et al.*, 2002). The abstraction enables these module simplifications to operate as inputs into the full dynamical system of apoptosis.

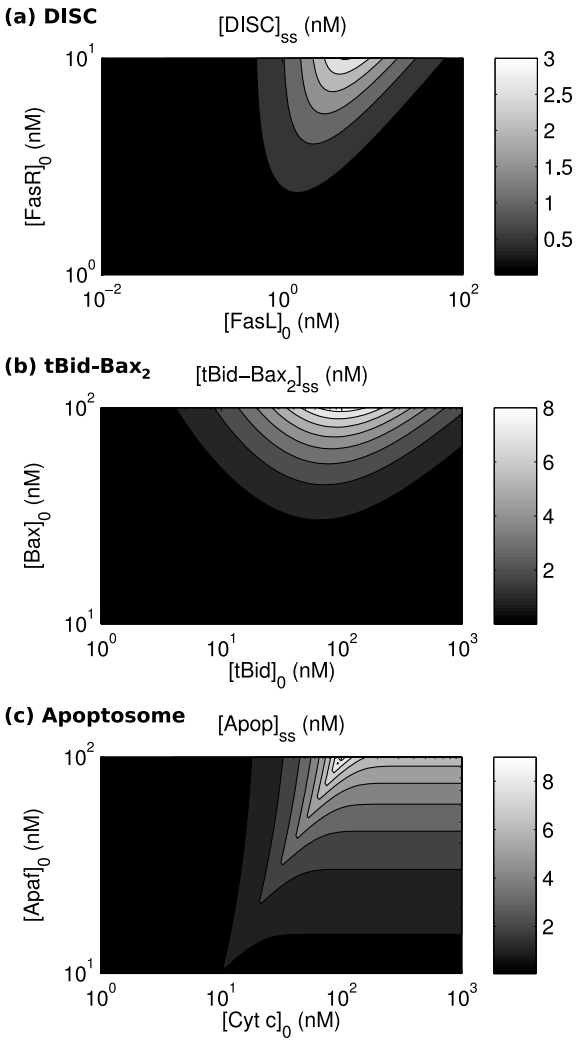

Figure 6.4: Steady-state concentrations of DISC, $\mathrm{tBid\text{-}Bax_2}$, and apoptosome, used for modularization of the DISC, MAC, and apoptosome modules, respectively. (a) The steady-state DISC concentration $[\mathrm{DISC}]_{\mathrm{ss}}$ as a function of the initial death ligand ($[\mathrm{FasL}]_0$) and receptor ($[\mathrm{FasR}]_0$) concentrations. (b) The steady-state $\mathrm{tBid\text{-}Bax_2}$ concentration $[\mathrm{tBid\text{-}Bax_2}]_{\mathrm{ss}}$ as a function of the initial Bax ($[\mathrm{Bax}]_0$) and tBid ($[\mathrm{tBid}]_0$) concentrations. (c) The steady-state apoptosome concentration $[\mathrm{Apop}]_{\mathrm{ss}}$ as a function of the initial Apaf-1 ($[\mathrm{Apaf}]_0$) and cytochrome c ($[\mathrm{Cyt}c]_0$) concentrations.

6.3.3 Model dynamical equations

The model species and reactions are summarized in Tables 6.1 and 6.2. Reaction kinetics are described by mass action, with the corresponding ordinary differential equation (ODE) system given in Table 6.3. Initial conditions to solve the ODEs for HeLa cells (from Eissing *et al*., 2004) and Jurkat T cells (based on Hua *et al*., 2005; Okazaki *et al*., 2008), as well as steady-state abstraction parameters, are given in Table 6.4, where in particular the baseline value of $[\mathrm{FasL}]_0 = 2$ nM corresponds to a dose which has been used to experimentally induce apoptosis (see Hua *et al*., 2005. Table 6.5 summarizes all model parameters (forward and reverse reactions, synthesis and degradation rates and parameters for the steady-state abstractions). Additionally, a variant of the Jurkat T cell, denoted Jurkat T*, is considered, which has the the same parameter values as Jurkat T but with $k_2 = k_5 = k_{12} = 0$ following Hua *et al*., 2005; Okazaki *et al*., 2008.

Species	Description	Synthesis rate (nM/s)	Degradation rate (s^{-1})
DISC	DISC		8.807×10^{-3}
Casp8	procaspase-8	adjusted	6.5×10^{-5} (Eissing *et al*., 2004)
Casp8*	caspase-8		9.667×10^{-5} (Eissing *et al*., 2004)
Casp3	procaspase-3	adjusted	6.5×10^{-5} (Eissing *et al*., 2004)
Casp3*	caspase-3		9.667×10^{-5} (Eissing *et al*., 2004)
XIAP	XIAP	adjusted	1.933×10^{-4} (Eissing *et al*., 2004)
Casp3*-XIAP	Casp3*-XIAP complex		2.883×10^{-4} (Eissing *et al*., 2004)
BAR	BAR	1.111×10^{-3} ($[\mathrm{BAR}]_0 = 66.67$ nM (Eissing *et al*., 2004))	1.667×10^{-5} (Eissing *et al*., 2004)
Casp8*-BAR	Casp8*-BAR complex		1.933×10^{-4} (Eissing *et al*., 2004)
Bid	Bid	4.168×10^{-4} ($[\mathrm{Bid}]_0 = 25$ nM (Hua *et al*., 2005; Okazaki *et al*., 2008))	1.667×10^{-5} (μ_{BAR})
tBid	truncated Bid		1.667×10^{-5} (μ_{Bid})
tBid-Bax_2	tBid-Bax_2 complex		0.0264
Cyt$c$	cytochrome *c* (mitochondrial)	10^{-3} ($[\mathrm{Cyt}c]_0 = 100$ nM (Hua *et al*., 2005; Okazaki *et al*., 2008))	10^{-5}
Cyt$c$*	cytochrome *c* (cytosolic)		10^{-5}
Smac	Smac (mitochondrial)	0.0167 ($[\mathrm{Smac}]_0 = 100$ nM (Hua *et al*., 2005; Okazaki *et al*., 2008))	1.667×10^{-5} (μ_{BAR})
Smac*	Smac (cytosolic)		1.667×10^{-5} (μ_{Smac})
Smac*-XIAP	Smac-XIAP complex		1.933×10^{-4} ($\mu_{\mathrm{Casp8^*\text{-}BAR}}$)
Apop	apoptosome		1.487×10^{-5}
Casp9	procaspase-9	1.3×10^{-3} ($[\mathrm{Casp9}]_0 = 20$ nM (Hua *et al*., 2005; Okazaki *et al*., 2008))	6.5×10^{-5} (μ_{Casp8})
Casp9*	caspase-9		9.667×10^{-5} ($\mu_{\mathrm{Casp8^*}}$)
Casp9*-XIAP	Casp9*-XIAP complex		2.883×10^{-4} ($\mu_{\mathrm{Casp3^*\text{-}XIAP}}$)

Table 6.1: Species description, synthesis and degradation rates for the model equations. Model species and description are given. In the model, synthesis and degradation rates are given for the model system and labeled α and μ, respectively.

Number	Reaction	Forward rate ($\mathrm{nM}^{-1}\ \mathrm{s}^{-1}$)	Reverse rate (s^{-1})
DISC	$(\mathrm{FasL}, \mathrm{FasR}) \longrightarrow \mathrm{DISC}$	f_{DISC}	
1	$\mathrm{DISC} + \mathrm{Casp8} \longrightarrow \mathrm{DISC} + \mathrm{Casp8}^*$	10^{-4} (k_2)	
2	$\mathrm{Casp3}^* + \mathrm{Casp8} \longrightarrow \mathrm{Casp3}^* + \mathrm{Casp8}^*$	10^{-4} (Eissing *et al*., 2004)	
3	$\mathrm{Casp8}^* + \mathrm{Casp3} \longrightarrow \mathrm{Casp8}^* + \mathrm{Casp3}^*$	5.8×10^{-4} (Eissing *et al*., 2004)	
4	$\mathrm{Casp3}^* + \mathrm{XIAP} \rightleftharpoons \mathrm{Casp3}^*\text{-XIAP}$	3×10^{-3} (Eissing *et al*., 2004)	0.035 (Eissing *et al*., 2004)
5	$\mathrm{Casp3}^* + \mathrm{XIAP} \longrightarrow \mathrm{Casp3}^*$	3×10^{-3} (Eissing *et al*., 2004)	
6	$\mathrm{Casp8}^* + \mathrm{BAR} \rightleftharpoons \mathrm{Casp8}^*\text{-BAR}$	5×10^{-3} (Eissing *et al*., 2004)	0.035 (Eissing *et al*., 2004)
7	$\mathrm{Casp8}^* + \mathrm{Bid} \longrightarrow \mathrm{Casp8}^* + \mathrm{tBid}$	5×10^{-4} (est. (Hua *et al*., 2005; Okazaki *et al*., 2008))	
$\mathrm{tBid\text{-}Bax_2}$	$(\mathrm{tBid}, \mathrm{Bax}) \longrightarrow \mathrm{tBid\text{-}Bax_2}$	$f_{\mathrm{tBid\text{-}Bax_2}}$	
8	$\mathrm{tBid\text{-}Bax_2} + \mathrm{Cyt}c \longrightarrow \mathrm{tBid\text{-}Bax_2} + \mathrm{Cyt}c^*$	10^{-3} (Hua *et al*., 2005; Okazaki *et al*., 2008)	
9	$\mathrm{tBid\text{-}Bax_2} + \mathrm{Smac} \longrightarrow \mathrm{tBid\text{-}Bax_2} + \mathrm{Smac}^*$	10^{-3} (Hua *et al*., 2005; Okazaki *et al*., 2008)	
10	$\mathrm{Smac}^* + \mathrm{XIAP} \rightleftharpoons \mathrm{Smac}^*\text{-XIAP}$	7×10^{-3} (Hua *et al*., 2005; Okazaki *et al*., 2008)	2.21×10^{-3} (Hua *et al*., 2005; Okazaki *et al*., 2008)
Apop	$(\mathrm{Cyt}c^*, \mathrm{Apaf}) \longrightarrow \mathrm{Apop}$	f_{Apop}	
11	$\mathrm{Apop} + \mathrm{Casp9} \longrightarrow \mathrm{Apop} + \mathrm{Casp9}^*$	2×10^{-4} (est. (Legewie *et al*., 2006))	
12	$\mathrm{Casp3}^* + \mathrm{Casp9} \longrightarrow \mathrm{Casp3}^* + \mathrm{Casp9}^*$	2×10^{-4} (Legewie *et al*., 2006)	
13	$\mathrm{Casp9}^* + \mathrm{Casp3} \longrightarrow \mathrm{Casp9}^* + \mathrm{Casp3}^*$	5×10^{-5} (Legewie *et al*., 2006)	
14	$\mathrm{Casp9}^* + \mathrm{XIAP} \rightleftharpoons \mathrm{Casp9}^*\text{-XIAP}$	1.06×10^{-4} (Hua *et al*., 2005; Okazaki *et al*., 2008)	10^{-3} (Hua *et al*., 2005; Okazaki *et al*., 2008)

Table 6.2: Reactions for the model equations. Each reaction described highlights whether the reaction is a forward or reversible reaction by the arrows. The rates are provided from previous work. Reactions are illustrated in Fig. 6.3.

$d\,[\text{DISC}]\,/dt = \mu_{\text{DISC}}(f_{\text{DISC}}([\text{FasL}]_0\,,[\text{FasR}]_0\,;K_{\text{DISC}}) - [\text{DISC}])$	$v_1 = k_1\,[\text{DISC}]\,[\text{Casp8}]$
$d\,[\text{Casp8}]\,/dt = -v_1 - v_2 + \alpha_{\text{Casp8}} - \mu_{\text{Casp8}}\,[\text{Casp8}]$	$v_2 = k_2\,[\text{Casp3}^*]\,[\text{Casp8}]$
$d\,[\text{Casp8}^*]\,/dt = v_1 + v_2 - v_6 - \mu_{\text{Casp8}^*}\,[\text{Casp8}^*]$	$v_3 = k_3\,[\text{Casp8}^*]\,[\text{Casp3}]$
$d\,[\text{Casp3}]\,/dt = -v_3 - v_{13} + \alpha_{\text{Casp3}} - \mu_{\text{Casp3}}\,[\text{Casp3}]$	$v_4 = k_4\,[\text{Casp3}^*]\,[\text{XIAP}] - k_{-4}\,[\text{Casp3}^*\text{-XIAP}]$
$d\,[\text{Casp3}^*]\,/dt = v_3 - v_4 + v_{13} - \mu_{\text{Casp3}^*}\,[\text{Casp3}^*]$	$v_5 = k_5\,[\text{Casp3}^*]\,[\text{XIAP}]$
$d\,[\text{XIAP}]\,/dt = -v_4 - v_5 - v_{10} - v_{14} + \alpha_{\text{XIAP}} - \mu_{\text{XIAP}}\,[\text{XIAP}]$	$v_6 = k_6\,[\text{Casp8}^*]\,[\text{BAR}] - k_{-6}\,[\text{Casp8}^*\text{-BAR}]$
$d\,[\text{Casp3}^*\text{-XIAP}]\,/dt = v_4 - \mu_{\text{Casp3}^*\text{-XIAP}}\,[\text{Casp3}^*\text{-XIAP}]$	$v_7 = k_7\,[\text{Casp8}^*]\,[\text{Bid}]$
$d\,[\text{BAR}]\,/dt = -v_6 + \alpha_{\text{BAR}} - \mu_{\text{BAR}}\,[\text{BAR}]$	$v_8 = k_8\,[\text{tBid-Bax}_2]\,[\text{Cyt}c]$
$d\,[\text{Casp8}^*\text{-BAR}]\,/dt = v_6 - \mu_{\text{Casp8}^*\text{-BAR}}\,[\text{Casp8}^*\text{-BAR}]$	$v_9 = k_9\,[\text{tBid-Bax}_2]\,[\text{Smac}]$
$d\,[\text{Bid}]\,/dt = -v_7 + \alpha_{\text{Bid}} - \mu_{\text{Bid}}\,[\text{Bid}]$	$v_{10} = k_{10}\,[\text{Smac}^*]\,[\text{XIAP}] - k_{-10}\,[\text{Smac}^*\text{-XIAP}]$
$d\,[\text{tBid}]\,/dt = v_7 - \mu_{\text{tBid}}\,[\text{tBid}]$	$v_{11} = k_{11}\,[\text{Apop}]\,[\text{Casp9}]$
$d\,[\text{tBid-Bax}_2]\,/dt = \mu_{\text{tBid-Bax}_2}$	$v_{12} = k_{12}\,[\text{Casp3}^*]\,[\text{Casp9}]$
$\quad(f_{\text{tBid-Bax}_2}([\text{tBid}]\,,[\text{Bax}]_0\,;K_{\text{tBid-Bax}_2}) - [\text{tBid-Bax}_2])$	$v_{13} = k_{13}\,[\text{Casp9}^*]\,[\text{Casp3}]$
$d\,[\text{Cyt}c]\,/dt = -v_8 + \alpha_{\text{Cyt}c} - \mu_{\text{Cyt}c}\,[\text{Cyt}c]$	$v_{14} = k_{14}\,[\text{Casp9}^*]\,[\text{XIAP}] - k_{-14}\,[\text{Casp9}^*\text{-XIAP}]$
$d\,[\text{Cyt}c^*]\,/dt = v_8 - \mu_{\text{Cyt}c^*}\,[\text{Cyt}c^*]$	
$d\,[\text{Smac}]\,/dt = -v_9 + \alpha_{\text{Smac}} - \mu_{\text{Smac}}\,[\text{Smac}]$	
$d\,[\text{Smac}^*]\,/dt = v_9 - v_{10} - \mu_{\text{Smac}^*}\,[\text{Smac}^*]$	
$d\,[\text{Smac}^*\text{-XIAP}]\,/dt = v_{10} - \mu_{\text{Smac}^*\text{-XIAP}}\,[\text{Smac}^*\text{-XIAP}]$	
$d\,[\text{Apop}]\,/dt = \mu_{\text{Apop}}(f_{\text{Apop}}([\text{Cyt}c^*]\,/\,[\text{Apaf}]_0\,;\lambda_{\text{Apop}}) - [\text{Apop}])$	
$d\,[\text{Casp9}]\,/dt = -v_{11} - v_{12} + \alpha_{\text{Casp9}} - \mu_{\text{Casp9}}\,[\text{Casp9}]$	
$d\,[\text{Casp9}^*]\,/dt = v_{11} + v_{12} - v_{14} - \mu_{\text{Casp9}^*}\,[\text{Casp9}^*]$	
$d\,[\text{Casp9}^*\text{-XIAP}] = v_{14} - \mu_{\text{Casp9}^*\text{-XIAP}}\,[\text{Casp9}^*\text{-XIAP}]$	

Table 6.3: Ordinary differential equations for the full system are given in the left hand column. Corresponding reaction velocities use mass-action kinetics and are found in the right hand column.

Species	Initial concentration (nM) HeLa	Jurkat T	Parameter	Value
Casp8	216.67 (Eissing *et al*., 2004)	33.33 (Hua *et al*., 2005; Okazaki *et al*., 2008)	$[\mathrm{FasL}]_0$	2 nM (Hua *et al*., 2005; Okazaki *et al*., 2008)
Casp3	35 (Eissing *et al*., 2004)	200 (Hua *et al*., 2005; Okazaki *et al*., 2008)	$[\mathrm{FasR}]_0$	10 nM (Hua *et al*., 2005; Okazaki *et al*., 2008)
XIAP	66.67 (Eissing *et al*., 2004)	30 (Hua *et al*., 2005; Okazaki *et al*., 2008)	K_{DISC}	1.032 nM (Hua *et al*., 2005; Okazaki *et al*., 2008)
BAR	66.67 (Eissing *et al*., 2004)	66.67 (Eissing *et al*., 2004)	$[\mathrm{Bax}]_0$	83.33 nM (Hua *et al*., 2005; Okazaki *et al*., 2008)
Bid	25 (Hua *et al*., 2005; Okazaki *et al*., 2008)	25 (Hua *et al*., 2005; Okazaki *et al*., 2008)	$K_{\mathrm{tBid\text{-}Bax_2}}$	100 nM (Hua *et al*., 2005; Okazaki *et al*., 2008)
Cytc	100 (Hua *et al*., 2005; Okazaki *et al*., 2008)	100 (Hua *et al*., 2005; Okazaki *et al*., 2008)	$[\mathrm{Apaf}]_0$	100 nM (Hua *et al*., 2005; Okazaki *et al*., 2008)
Smac	100 (Hua *et al*., 2005; Okazaki *et al*., 2008)	100 (Hua *et al*., 2005; Okazaki *et al*., 2008)	λ_{Apop}	1 (Nakabayashi and Sasaki, 2006)
Casp9	20 (Hua *et al*., 2005; Okazaki *et al*., 2008)	20 (Hua *et al*., 2005; Okazaki *et al*., 2008)		

Table 6.4: Initial conditions for the model variables and oligomerization parameters. Some species initial conditions differ between HeLa or Jurkat T cell type. Parameters and values are given for steady-state oligomerization modules.

Forward rate		Reverse rate		Synthesis rate		Degradation rate		Parameter	
1	k_1	15	k_{-4}	19	α_{Casp8}	27	μ_{DISC}	48	$[\text{FasL}]_0$
2	k_2	16	k_{-6}	20	α_{Casp3}	28	μ_{Casp8}	49	$[\text{FasR}]_0$
3	k_3	17	k_{-10}	21	α_{XIAP}	29	$\mu_{\text{Casp8*}}$	50	K_{DISC}
4	k_4	18	k_{-14}	22	α_{BAR}	30	μ_{Casp3}	51	$[\text{Bax}]_0$
5	k_5			23	α_{Bid}	31	$\mu_{\text{Casp3*}}$	52	$K_{\text{tBid-Bax}_2}$
6	k_6			24	$\alpha_{\text{Cyt}c}$	32	μ_{XIAP}	53	$[\text{Apaf}]_0$
7	k_7			25	α_{Smac}	33	$\mu_{\text{Casp3*-XIAP}}$	54	λ_{Apop}
8	k_8			26	α_{Casp9}	34	μ_{BAR}		
9	k_9					35	$\mu_{\text{Casp8*-}BAR}$		
10	k_{10}					36	μ_{Bid}		
11	k_{11}					37	μ_{tBid}		
12	k_{12}					38	$\mu_{\text{tBid-Bax}_2}$		
13	k_{13}					39	$\mu_{\text{Cyt}c}$		
14	k_{14}					40	$\mu_{\text{Cyt}c^*}$		
						41	μ_{Smac}		
						42	$\mu_{\text{Smac*}}$		
						43	$\mu_{\text{Smac*-XIAP}}$		
						44	μ_{Apop}		
						45	μ_{Casp9}		
						46	$\mu_{\text{Casp9*}}$		
						47	$\mu_{\text{Casp9*-XIAP}}$		

Table 6.5: Summary of all rates and parameters for the system. The counter on the left hand columns totals the 54 model rates and parameters for the full system. Each subscript for k, α and μ corresponds to its reaction number. The final column are the parameters used in the abstraction of oligomerization kinetics for the three modules.

6.3.4 Regression analyses and model reduction

Integration of the model ODEs at baseline parameter values (Table 6.5) gives the $[\mathrm{Casp3}^*]$ time courses shown in Fig. 6.5. Both the HeLa and Jurkat T cells (the Jurkat T* case which differs from the other two cells will be addressed in the results) demonstrate a characteristic behavior, whereby $[\mathrm{Casp3}^*]$ stays low initially, then quickly switches to a high state at some threshold time. Furthermore, the steady-state values of $[\mathrm{Casp3}^*]$ in HeLa cells is consistent with experimental findings [1] (Albeck *et al.*, 2008a) and the Jurkat T cell steady-state value is in line with the results from previous models of Jurkat T cells (Hua *et al.*, 2006; Legewie *et al.*, 2006).

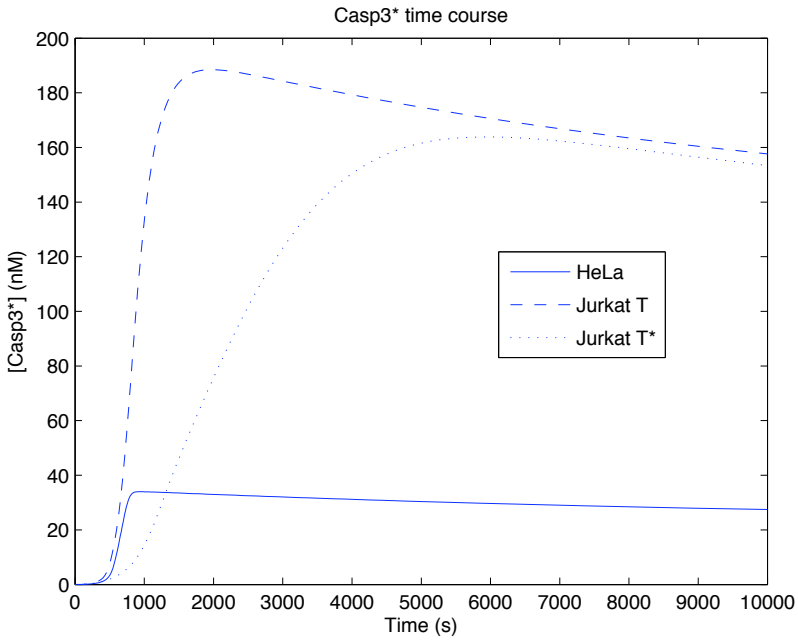

Figure 6.5: Time course of caspase-3 activation ($[\mathrm{Casp3}^*]$) in HeLa and Jurkat T cells represented by solid and dashed lines, respectively. The time course for a modification of the Jurkat T cell with $k_2 = k_5 = k_{12} = 0$ based on the formulation of Hua *et al.*, 2005; Okazaki *et al.*, 2008 is denoted Jurkat T* and represented by the dotted line.

Two quantitative descriptors are used to capture the form of these time courses: the *peak activation*, the maximum value of $[\mathrm{Casp3}^*]$ attained over the time course; and the *activation time*, the time at which this peak is achieved. To determine the most significant aspects of the model within a given parameter regime, sensitivity analysis is performed with respect to these descriptors according to the following procedure: for a given set of

[1] Eissing *et al.*, 2004 assume that the volume of an individual cell of approximately 1 picoliter shows that 600 molecules/cell $\sim$ 1nM and Albeck *et al.*, 2008a find that after stimulation there are $10^4 - 10^5$ molecules of $\mathrm{Casp3}^*$/ HeLa cell $\sim$ 16.6 -166 nM.

baseline parameter values, normally distributed random parameters are generated about the baseline with a standard deviation of 5% of the baseline values. The model is simulated at these parameters, descriptors are computed and the process is repeated 100 times (the model has 54 parameters) to collect a set of synthetic data.

Since only local parameter perturbations have been considered, the linear relationship $\boldsymbol{y} = (\mathbf{1}\boldsymbol{X})\boldsymbol{b}$ is assumed between the standardized descriptors $\boldsymbol{y}$ ($\boldsymbol{y}$ being one of $[\mathrm{Casp3}^*]_{\max}$ and τ in standardized form) and the standardized random parameters $\boldsymbol{X}$, where each row of $\boldsymbol{X}$ is a concatenation of the 54 model parameters in the order given by Table 6.5. The relation $\boldsymbol{b}$ is solved by multiple linear regression and large regression coefficients are taken to indicate essential components of the network. This information is used to guide the formulation of reduced models.

6.4 Results and Discussion

6.4.1 Regression analyses and reduced models for FasL induction

Regression analysis as described previously is performed for baseline HeLa parameter values. Regression coefficients for each of the descriptors show isolated peaks, indicating that only a small subset of the network is responsible for the system behavior. Particularly, the coefficients for the peak activation ($r^2 = 0.9991$) show strong components only at the synthesis and degradation rates α_{Casp3} and μ_{Casp3}, which together control the initial concentration $[\mathrm{Casp3}]_0$; evidently, this turns out to largely be the case for all parameter sets considered; thus, the peak activation will not be further discussed. More interesting is the result for the activation time ($r^2 = 0.9958$; see Fig. 6.6a), which, notably, shows that only the reactions of the extrinsic subnetwork appear to be essential. Accordingly, a reduced model (Fig. 6.7a) consisting only of the extrinsic subnetwork is formulated, and validation of the reduction is given by comparison of the $[\mathrm{Casp3}^*]$ time courses between the full and reduced models.

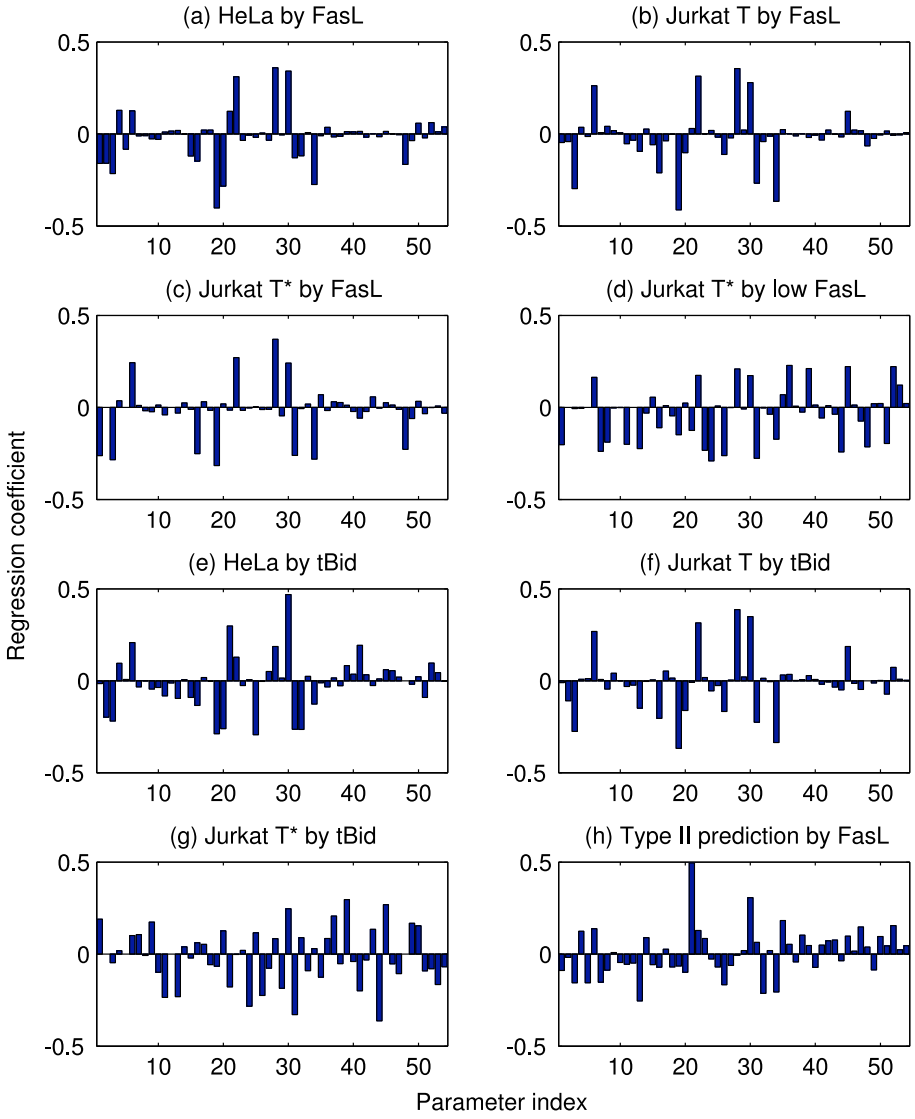

Figure 6.6: Regression analyses of apoptosis under various conditions. Activation time regression coefficients for sample model cases. The activation time is defined as the time at which the peak caspase-3 concentration over the time course occurs. The regression coefficients are ordered by their parameter indices as shown in Table 6.5. Induction by FasL ($[\mathrm{FasL}]_0 = 2$ nM unless noted) corresponds to receptor-mediated apoptosis, while induction by tBid corresponds to mitochondrial apoptosis ($[\mathrm{tBid}]_0 = 25$ nM and $[\mathrm{FasL}]_0 = 0$ unless otherwise noted). (a) HeLa cell induced by FasL ($r^2 = 0.9958$). (b) Jurkat T cell induced by FasL ($r^2 = 0.9903$). (c) Jurkat T* cell induced by FasL ($r^2 = 0.9846$). (d) Jurkat T* cell induced by low FasL ($[\mathrm{FasL}]_0 = 0.01$ nM; $r^2 = 0.9569$). (e) HeLa cell induced by tBid ($r^2 = 0.9705$). (f) Jurkat T cell induced by tBid ($r^2 = 0.9879$). (g) Jurkat T* cell induced by tBid ($r^2 = 0.8873$). (h) Predicted type II apoptosis cell parameters ($k_{-4} = k_{-6} = 10^{-3}$ s^{-1}, $[\mathrm{XIAP}]_0 = 200$ nM, $[\mathrm{FasR}]_0 = 1$ nM) induced by FasL ($r^2 = 0.9264$).

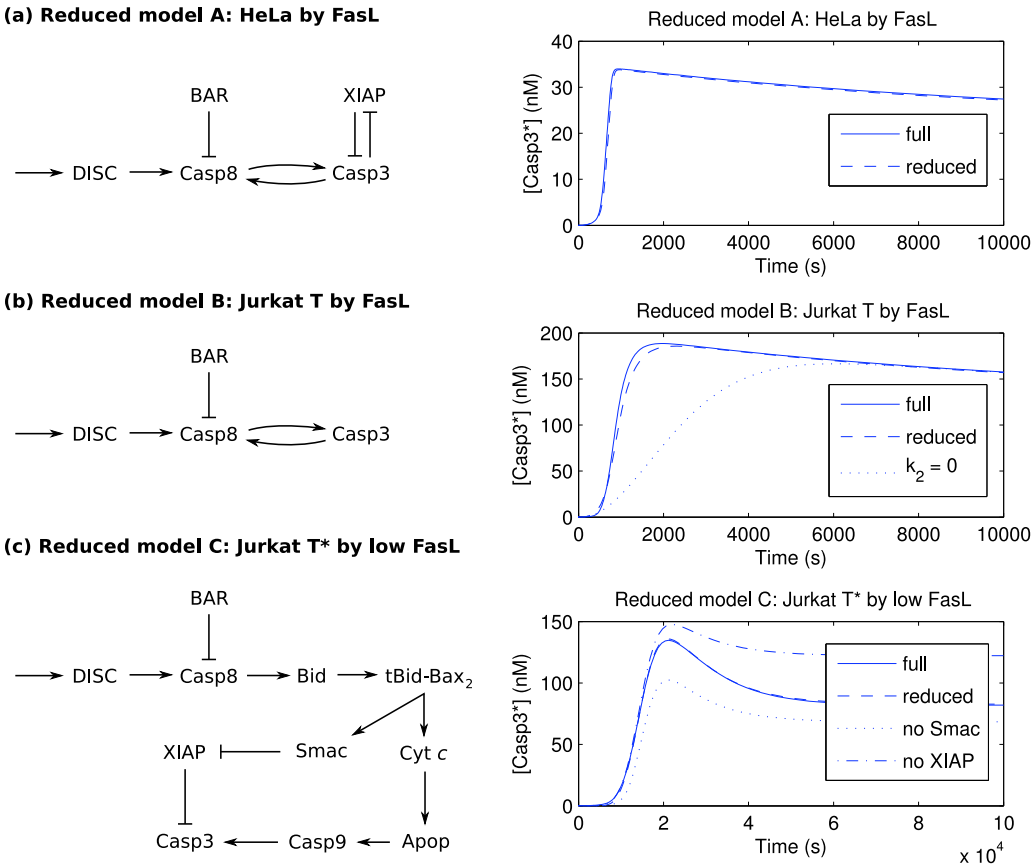

Figure 6.7: Reduced models under induction by FasL (receptor-mediated apoptosis; $[\mathrm{FasL}]_0 = 2$ nM unless noted), with time course validations. In (a) and (c), the time courses of the full and reduced models essentially overlap. (a) HeLa cell induced by FasL. (b) Jurkat T cell induced by FasL. (c) Jurkat T* cell induced by low FasL ($[\mathrm{FasL}]_0 = 0.01$ nM).

Note that this result should be expected since the HeLa cell was used in Eissing *et al*., 2004 to study type I apoptosis. Surprisingly, a similar analysis of the Jurkat T cell, whose initial concentration parameters were used to study type II apoptosis by Hua *et al*., 2005; Okazaki *et al*., 2008, leads to a similar reduction. The regression coefficients (for the activation time; $r^2 = 0.9903$) are shown in Fig. 6.6b, with reduction shown in Fig. 6.7b, which is just that for the HeLa case but with XIAP omitted. It should be noted that the regression analysis does not show a strong component at k_2, perhaps due to the corresponding reaction occurring at saturation; therefore not sensitive to small perturbations. Nevertheless, simulations show the necessity to capture the correct dynamics.

Review of the literature reveals that Hua *et al*., 2005 and Okazaki *et al*., 2008 used the model variant denoted as Jurkat T* in this work; for completeness, analysis of the Jurkat T* was hence considered. While induction of the Jurkat T* cell by baseline FasL returns characteristic type I behavior (Fig. 6.6c, $r^2 = 0.9846$; see also the delayed activation in Fig. 6.5), a transition to type II apoptosis is observed for low FasL ($[\mathrm{FasL}]_0 = 0.01$ nM), in accordance with the transition reported in Okazaki *et al*., 2008. This is to be compared against the low FasL cases for the HeLa and Jurkat T cells, which do not exhibit such a transition. The activation time regression coefficients for the Jurkat T* cell induced by low FasL case are shown in Fig. 6.6d ($r^2 = 0.9569$), which in particular has strong components at k_7 and k_8, which describe Bid truncation and the release of $\mathrm{Cyt}c$. Moreover, the peak activation regression coefficients ($r^2 = 0.9972$, not shown) exhibit a strong contribution by α_{Smac}. The reduced model (Fig. 6.7c) is correspondingly dominated by the intrinsic pathway; indeed, there is no direct interaction between $\mathrm{Casp8}$ and $\mathrm{Casp3}$. Furthermore, as implicated by the synthesis rate of its inactive form, Smac^*, and correspondingly its target XIAP, plays a vital role in achieving the correct activation level, which in particular illustrates the critical role of the shared-inhibitor motif in apoptosis as discussed by Legewie *et al*., 2006.

6.4.2 Regression analysis and reduced models for mitochondrial apoptosis

The behavior of the system pathways under mitochondrial apoptosis have also been studied. Cell stressors that cause the depolarization and permeabilization of the mitochondrial membrane are functionally represented in the model by an input $[\mathrm{tBid}]_0 = 25$ nM (now $[\mathrm{FasL}]_0 = 0$). As for the FasL case, peak activation regression coefficients for the cases considered below are dominated by α_{Casp3} and μ_{Casp3}; therefore, there will not be further discussed.

Performing the regression analysis on the HeLa cell induced by tBid produces the activation time regression coefficients shown in Fig. 6.6e ($r^2 = 0.9705$). Strong components corresponding to the reactions of the intrinsic subnetwork are observed; interestingly, the system behavior is sensitive to several extrinsic reactions as well. The model reduction is shown in Fig. 6.8a, which demonstrates that the extrinsic caspase feedback between Casp8 and Casp3 is essential to capturing the correct dynamics (compare the time course with $k_2 = 0$). Thus, the HeLa cell displays an apoptotic mechanism that involves the intrinsic pathway triggering the extrinsic pathway. Furthermore, the role of Smac* as an indirect activator of Casp3 through the sequestration of XIAP is recovered. Although Casp9* possesses a similar sequestration ability, this analysis reveals that the primary role of Casp9* is through direct activation of Casp3.

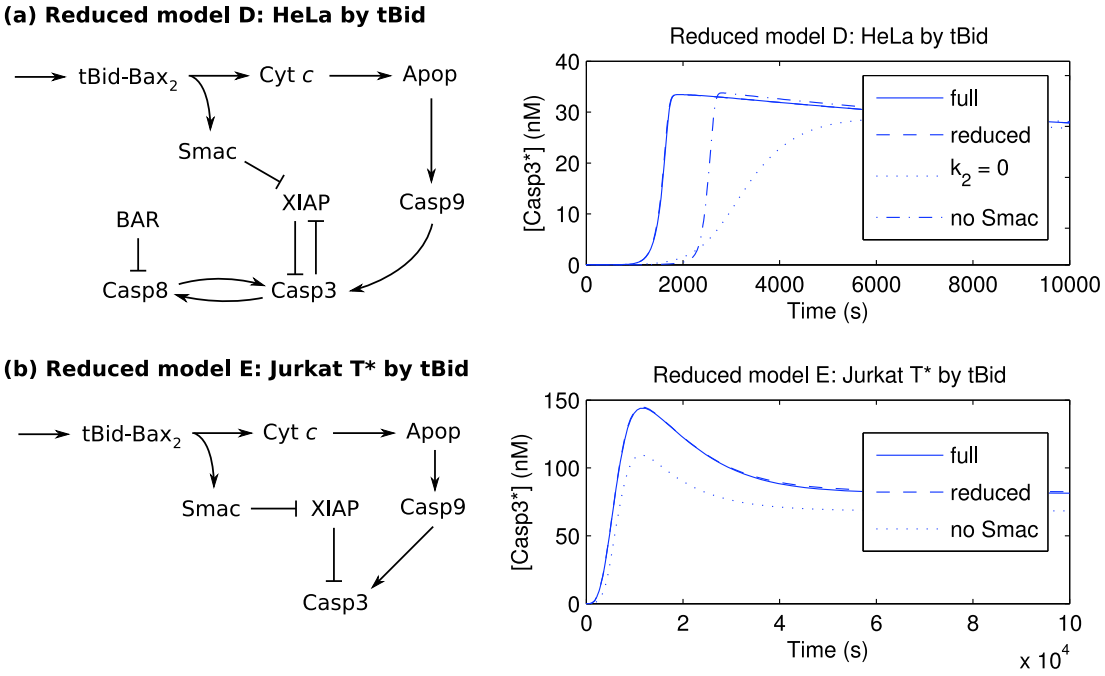

Figure 6.8: Reduced models of apoptosis under induction by tBid (mitochondrial apoptosis; $[\text{tBid}] = 25$ nM and $[\text{FasL}]_0 = 0$), with time course validations. In both cases, the time courses of the full and reduced models essentially overlap. (a) HeLa cell induced by tBid. (b) Jurkat T* cell induced by tBid.

Analysis of the Jurkat T cell induced by tBid gives similar results (Fig. 6.6f, $r^2 = 0.9879$; reduced model not shown), though the magnitude of the regression coefficient of k_{13}, which describes the activation of Casp3 by Casp9*, is larger than in the HeLa case, suggesting a stronger role for the intrinsic caspase.

For completeness, the Jurkat T* cell induced by tBid is also considered. The activation time regression coefficients are shown in Fig. 6.6g. In this case, the fit is relatively poor ($r^2 = 0.8873$) and some parameters are selected in error (e.g., k_1, which has no

effect on the system by construction; also note the larger number of significant components). Nevertheless, the regression serves to guide the model reduction, which in this case required manual correction. The reduced model (Fig. 6.8b) reveals a purely intrinsic mechanism of caspase activation. Similarly to the HeLa and Jurkat T cells, the sequestration of XIAP by Smac^* is essential, while that by $\mathrm{Casp9}^*$ may be neglected.

Although the peak activation for each of the HeLa, Jurkat T, and Jurkat T* cells is essentially identical to that obtained under FasL induction, the activation time shows a significant increase (factor increase of 2.1457, HeLa; 1.3003, Jurkat T; 1.9920, Jurkat T*). This is in general agreement with experimental evidence that caspase activation through the intrinsic pathway is delayed relative to that through the extrinsic pathway (Scaffidi *et al*., 1998).

Type II apoptosis prediction

In the preceding cases considered, type II apoptosis was observed only for the Jurkat T* cell under low FasL induction. This may be unsatisfactory since the Jurkat T* cell omits caspase feedback interactions which suggest potentially questionable biological relevance. Thus, a natural idea is to determine whether parameters leading to type II apoptosis may be predicted for the full reaction network rather than resorting to the Jurkat T* formulation.

An attempt to use the regression analysis for this task was made based on the idea of performing regression with respect to differences in the peak activation and in the activation times between a given parameter set and the corresponding set with $k_7 = 0$ (no Bid truncation, i.e., no extrinsic-intrinsic coupling). The intuition in this analysis is that strong regression coefficients (assuming the modified descriptors are taken with the appropriate sign) now select parameters whose increase may affect a transition from type I to type II behavior. Furthermore, the parameters randomly perturbed are now restricted to only the synthesis and degradation rates, and to $[\mathrm{FasL}]_0$, $[\mathrm{FasR}]_0$, $[\mathrm{Bax}]_0$, and $[\mathrm{Apaf}]_0$, i.e., the parameters that control only the initial concentration, referred to as *cell-specific parameters*, as these are assumed to be the only parameters which may vary between different cell types.

Unfortunately, the regression coefficients for this analysis give poor fits ($0.3884 \leq r^2 \leq 0.7714$ for the activation time difference) for the cases considered, so the method fails. However, progress may nevertheless be made by considering the result from the case of Jurkat T* induced by low FasL. The strategy is to transform the conditions of that case into equivalent cell-specific parameter conditions. For example, the Jurkat T*

cell mutes the reactions involving the action of $\mathrm{Casp3}^*$ on other molecules. This effect may be achieved in principle by increasing $[\mathrm{XIAP}]_0$ and hence the inhibition of $\mathrm{Casp3}^*$. However, this turns out to be insufficient as a result of the strong positive feedback between $\mathrm{Casp8}$ and $\mathrm{Casp3}$. Therefore, it is further necessary to decrease the rate at which $\mathrm{Casp8}$ is activated. This may be controlled at the DISC module, so accordingly decrease $[FasR]_0$ (for the dependence, see Fig. 6.4a).

At the assumed rate parameters, however, the changes in $[\mathrm{XIAP}]_0$ and $[\mathrm{FasR}]_0$ required to achieve type II apoptosis are rather dramatic. Note that the dissociation rates k_{-4} and k_{-6} of $\mathrm{Casp3}^*$-XIAP and $\mathrm{Casp8}^*$-BAR, respectively, as estimated from Eissing *et al.*, 2004 seem large; if the estimate $k_{-4} = k_{-6} = 10^{-3}$ s^{-1} is taken instead, more consistent with, e.g., Hua *et al.*, 2005; Legewie *et al.*, 2006; Okazaki *et al.*, 2008, then the changes required are no more than an order of magnitude. Specifically, starting with Jurkat T parameters, increasing $[\mathrm{XIAP}]_0$ from 20 to 200 nM, and decreasing $[\mathrm{FasR}]_0$ from 10 to 1 nM gives a cell type for which the intrinsic pathway is significant even under high FasL induction. The sensitivity regression analysis for this cell is shown in Fig. 6.6h ($r^2 = 0.9264$), which displays significant components corresponding to the intrinsic subnetwork, notably at k_{13}. The influence of the intrinsic pathway demonstrated by the comparison of time courses in Fig. 6.9 shows a significant delay of caspase activation upon disabling the pathway coupling through tBid. In comparison, control results for the HeLa and Jurkat T cells show no such dependence (not shown).

Perhaps in light of this result, an alternative interpretation of the fact that the modified regressions produced poor fits occurs due to type II transitions requiring large changes that the local character of the linear regression cannot capture. This is consistent with the changes that Hua *et al.*, 2005 and Okazaki *et al.*, 2008 report to effect transitions in their models (without caspase feedback), where, effectively, $[\mathrm{Casp8}]_0$ was modified by a similar amount. As a final note, changes of this magnitude are expected to be reasonable given the inherent variability observed experimentally (see, e.g., Svingen *et al.*, 2004).

6.4.3 Activation thresholds and stability

It should be noted that the model in its present formulation is unstable, even to transient signals, as Fig. 6.9 suggests. However, some notion of stability may nevertheless be achieved by considering activation times. This is shown for HeLa, Jurkat T, and Jurkat T* cells in Fig. 6.10.

Consider first the case of receptor-mediated apoptosis, i.e., by FasL induction. For HeLa and Jurkat T cells, the peak activation is essentially constant (Fig. 6.10a) with

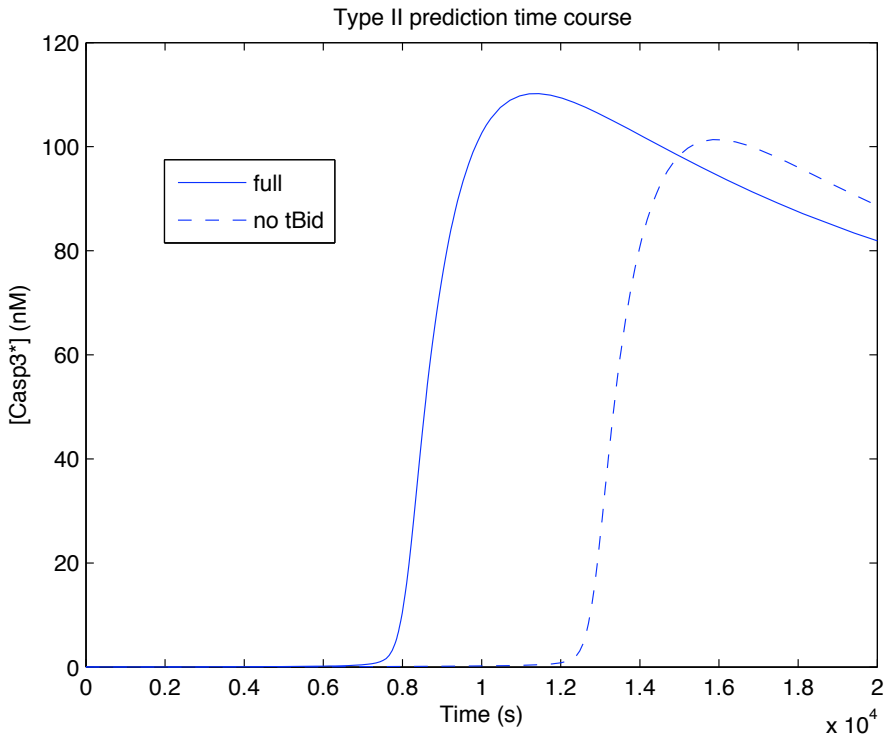

Figure 6.9: Type II prediction. Time course of caspase-3 activation ($[\mathrm{Casp3}^*]$) for the type II apoptosis cell prediction parameters ($k_{-4} = k_{-6} = 10^{-3}$ s^{-1}, $[\mathrm{XIAP}]_0 = 200$ nM, $[\mathrm{FasR}]_0 = 1$ nM) induced by $[\mathrm{FasL}]_0 = 2$ nM. The solid line gives the time course of the full model, while the dashed line gives the time course with $k_7 = 0$ (i.e., no Bid truncation, hence no extrinsic-intrinsic coupling). Note the significant delay in caspase activation.

$[\mathrm{FasL}]_0$, in accordance with the observation from the regression analysis that the peak activation is relatively insensitive. However, the activation time (Fig. 6.10b) varies significantly, showing first a sharp decrease with $[\mathrm{FasL}]_0$ for low $[\mathrm{FasL}]_0$, then a gradual leveling-off as $[\mathrm{FasL}]_0$ increases thereafter. Clearly, this latter portion may be interpreted as the cell undergoing apoptosis in a saturated manner, in which further increase of the death signal no longer affects the response time. Analogously, the initial drop appears to define a transition region, wherein the cell switches from slow to fast apoptotic dynamics over a narrow range of the death signal input; this is indicative of some threshold-like behavior. Although this is not bistability, a sense of the existence of both low and high apoptotic states is nevertheless furnished, which, may be made precise by introducing an artificial cutoff on the activation time to discount activations which take too long to occur. The case of the Jurkat T* cell is similar, though now the peak activation does show nontrivial variation with $[\mathrm{FasL}]_0$. However, the peak activation remains uniformly high which questions the biological significance.

Corresponding data for mitochondrial apoptosis (variable $[\mathrm{tBid}]_0$ with $[\mathrm{FasL}]_0 = 0$)

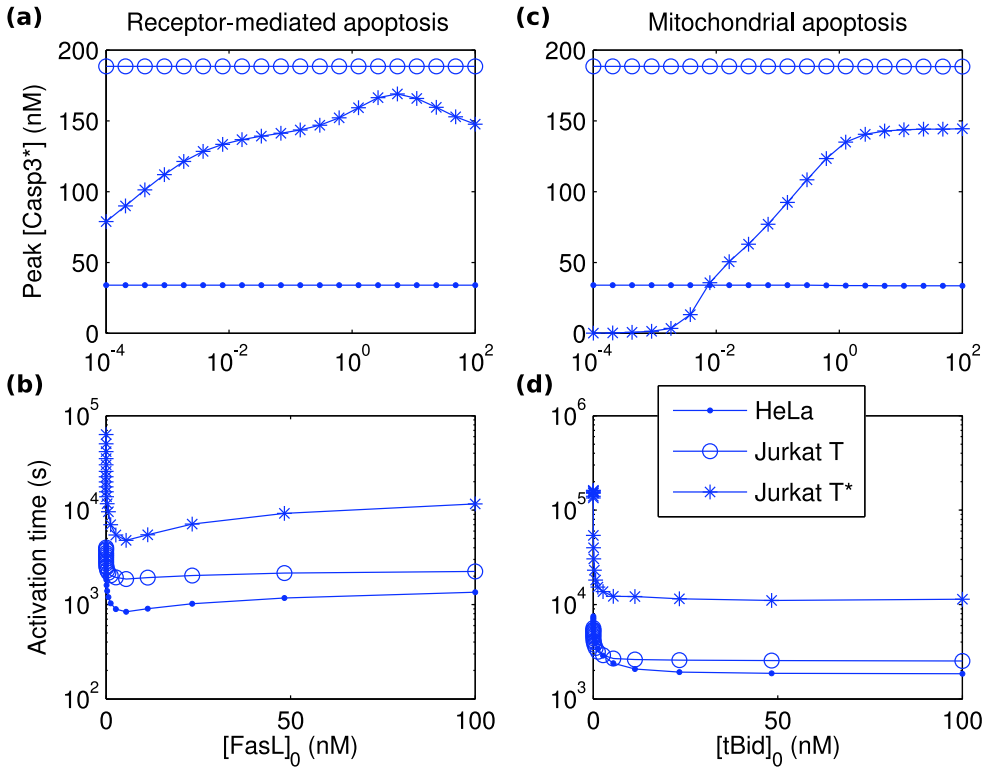

Figure 6.10: Peak caspase-3 activations and activations times for HeLa (dots), Jurkat T (circles), and Jurkat T* (asterisks) cells under receptor-mediated apoptosis (variable $[\mathrm{FasL}]_0$) and mitochondrial apoptosis (variable $[\mathrm{tBid}]_0$ with $[\mathrm{FasL}]_0 = 0$). (a) Peak activations for receptor-mediated apoptosis. (b) Activation times for receptor-mediated apoptosis. (c) Peak activations for mitochondrial apoptosis. (d) Activation times for mitochondrial apoptosis.

are shown in Fig. 6.10c, d. The cases for the HeLa and Jurkat T cells are similar to the receptor-mediated case; however, the Jurkat T* cell appears to exhibit bistability (Fig. 6.10c). For low FasL (approximately $[\mathrm{FasL}]_0 < 10^{-2}$ nM), the peak activation stays low (near zero), whereas for high FasL ($[\mathrm{FasL}]_0 > 1$ nM), the peak activation reaches a high state around 145 nM. Intermediate concentrations define a transition region where the cell may be interpreted to switch from life to death.

The present data was computed with a constant input for the receptor-mediated case and an exponentially decaying (i.e., transient) input for the mitochondrial case (since tBid has a constitutive degradation rate in the model). Interestingly, instituting a transient FasL signal, with estimated degradation rate $\mu_{\mathrm{FasL}} = 10^{-5}$ s^{-1}, produces no discernible change to the receptor-mediated data, while setting $\mu_{\mathrm{tBid}} = 0$ degrades the quality of the bistability result of the Jurkat T* case for mitochondrial apoptosis (not shown). This affords some insight into why the noted bistability is observed: by virtue of the delay of apoptosis incurred by the intrinsic pathway through the necessary activation of the mitochondrial apoptogenic factors and the assembly of the apoptosome (compare Figs. 6.10b

and d), the intrinsic pathway is able to better filter out transient signals.

With regard to stability, perhaps these results imply that future models of apoptosis should be careful to include potentially important regulators such as cFLIP, which inhibits DISC and hence imposes a delay on Casp8 activation (Hua *et al*., 2005; Okazaki *et al*., 2008). Moreover, it may likewise be prudent to expand in full any series of activations occuring sequentially; an example might be the interactions between Bid and Bax to form the MAC, which currently is not mechanistically understood and consequently may be inappropriately abstracted; although in defense of the abstraction, it is experimentally suggested that component levels (such as Apaf-1 or Casp9) may determine how quickly some cells die (Svingen *et al*., 2004). Finally, the steady-state abstractions presented are unsuitable for the purposes of model stability; however, modulation of the given abstracted dynamics by appropriate time-dependent functions (e.g., by an appropriate Heaviside function) may suffice.

6.5 Conclusion

This study has presented a methodological construction of a straightforward and informative mathematical model of apoptosis. This was done by combining both the extrinsic and intrinsic pathways through the implementation of functional modules and subnetworks motivated by previous models and findings (Eissing *et al*., 2004; Fussenegger *et al*., 2000; Hua *et al*., 2005, 2006; Lai and Jackson, 2004; Legewie *et al*., 2006; Nakabayashi and Sasaki, 2006; Okazaki *et al*., 2008). The subnetworks, responsible for the activation of Casp3 and ultimately apoptosis, included descriptions of both the extrinsic and intrinsic pathways as well as the coupling between them. Modularization of the oligomerization kinetics of the DISC, MAC, and apoptosome were achieved through the implementation of steady-state abstraction techniques.

Sensitivity analysis by linear regression was used to identify key components of the apoptotic network under various cell conditions. This allowed for the formulation of reduced models to capture the essential dynamics of the system. Importantly, these reductions allowed the extraction of biological insight and helped clarify the roles of specific molecular components. For example, the model predicts, for the parameter regimes considered, that Casp9* contributes to the activation of Casp3 by direct catalytic activation rather than through sequestration of their common inhibitor XIAP. Furthermore, the reduced models validated many previous findings, including the critical role of XIAP and the shared-inhibitor motif in mediating apoptosis (Chauhan *et al*., 2001; Deveraux *et al*., 1998; Legewie *et al*., 2006; McNeish *et al*., 2003; Oost *et al*., 2004), as well as

the transition from type I to type II apoptosis as the induction of the extrinsic pathway is decreased (Hua *et al*., 2005; Okazaki *et al*., 2008). Finally, the analysis revealed the variety of modes through which caspase activation can be achieved. In the cases considered, caspase activation was observed to occur in four modes: 1) solely through the extrinsic pathway; 2) solely through the intrinsic pathway; 3) through the extrinsic triggering the intrinsic pathway; and 4) through the intrinsic triggering the extrinsic pathway. Whether cells employ all of these modes is an interesting experimental question, with possibly profound biological significance.

The results of the regression analysis were also used to predict cell parameters (i.e., initial concentrations) that would elicit type II apoptosis, even under high FasL induction, without having to use the Jurkat T* model of Hua *et al*., 2005; Okazaki *et al*., 2008, which omits important caspase feedback interactions (Eissing *et al*., 2004; Legewie *et al*., 2006). This adheres to the notion of highly conserving the apoptosis pathway (Hengartner, 2000; Lockshin and Zakeri, 2001; Thornberry and Lazebnik, 1998), and in principle, achieving both type I and type II apoptosis using the same network. Naturally, the type II cell prediction invites experimental investigation.

Furthermore, remarks on caspase activation thresholds and stability were given. The critical element in achieving bistability in the system (at least to transient signals) appears to be related to whether sufficient delays are included. In particular, this implies the importance of modeling regulators, especially inhibitors, of the system, as well as the correct dynamical description of complex formation. Specifically, for this latter point, the present formulation neglects the time dependence of the oligomerization rate and assumes that the formation of a given final complex proceeds without delay. This, however, does not reflect actual dynamics; for example, the model of apoptosome assembly by Nakabayashi and Sasaki, 2006 at the parameter values considered in this study exhibits a characteristic time delay on the order of 100 minutes. A simple improvement is the delayed initiation of the present approximation by an appropriate time. A general theory of oligomerization that gives such a time would be particularly useful. Finally, of special interest is whether the incorporation of such delays can recover the expected type II behavior of the Jurkat T cell while maintaining the type I behavior of the HeLa cell.

Future directions for model refinement include more sophisticated treatment of oligomerization kinetics as described. A more comprehensive procedure for model reduction would also be helpful. The current method of sensitivity analysis is unable to eliminate reactions near saturation; however these cases should intuitively be treatable analytically. Moreover, the implementation of a faithful model exhibiting bistability is of primary biological interest as this would allow the formal definition and investigation of “a point of

no return" in apoptosis. Furthermore, it may be profitable to adapt and apply the model to other cell types, e.g., mature neurons, which have repressed Apaf-1 expression and hence apoptosome formation (Wright *et al*., 2004; Yakovlev *et al*., 2001). Extending the presented work to model apoptosis at a cell population level may predict key mechanisms; and perhaps, prove fruitful for understanding drug sensitivity in various cell lines.

The model thus presented serves as a guide for future theoretical and experimental work in analyzing apoptosis and achieves progress toward a full model of this important biological process.

Chapter 7

Fas trimerization model

7.1 Overview

In this work, a simple model of death ligand-receptor interaction in apoptosis is developed based on recent structural data (Scott *et al*., 2009) that exhibits hysteresis. Thus, formal demonstration that the data are compatible with bistability is provided, which is important for enabling robust threshold switching between coherent life and death states. The model is kept deliberately simple, both for analytical tractability and for lack of mechanistic specificity. The model offers an explanation for the homotrimeric character of the death ligand FasL in terms of bistability. This chapter is heavy on mathematical analysis, which has, as yet, not been confirmed by experimentation. Though purely theoretical at this stage, the conclusion that death receptors are potentially capable of bistability is significant, particularly as it implies an additional life-or-death decision in apoptosis operating upstream of all other identified components. The lack of data notwithstanding, parameter-free measures are also derived that may be used for model assessment or selection when data becomes available. Notably, the analysis was done using computational algebraic geometry, which may prove a welcome partner for mathematical and systems biology. This work, therefore, also serves to motivate the use of novel mathematical tools within the biological community.

The work presented in this chapter was a joint collaboration with Kenneth L. Ho. The fas-trimer model idea commenced after a conversation questioning the receptor-ligand activation dynamics in the modularized model. Following biological developments, an initial exploration of the hypothesis was conducted and led to an invitation to spend a summer working with Kenneth L. Ho at NYU Courant Institute of Mathematical Sciences. The model was jointly developed, and my contribution was exploring model discrimination, determining that the most suitable model selection tool and adapting this

technique, performing sensitivity and robustness analysis, and SBML implementation. Throughout the project, code was shared through an interactive and collaborative online mathematics software environment Sage (http://www.sagemath.org/). The initial manuscript was drafted by Kenneth L. Ho, revisions were made jointly and this work has been accepted by *PLoS Comput Biol* for publication.

7.2 Introduction

Recall from Chapters 2 and 6 that the current model of death ligand-receptor dynamics supposes that FasL recruits Fas independently at each of three binding sites, thereby producing a steady-state DISC concentration that varies smoothly with the input ligand concentration (Harrington *et al*., 2008; Lai and Jackson, 2004). However, recent structural data by Scott *et al*. (2009) suggests a different view. Briefly, Fas was found to exist in both closed and open forms, only the latter of which allows FADD binding and hence transduction of the apoptotic signal. Moreover, open Fas were shown to be capable of self-stabilization through stem helix and globular interactions; this immediately affords a mechanism for bistability. Open Fas are disfavored relative to their native closed forms and are able to sustain their conformations even after removal of the initial stimulus. This process may promote receptor opening and, past a certain critical density of open Fas, may induce hysteretic behavior in the concentration of active, signaling receptors. Therefore, this stabilized open form may activate the signaling cascade that induces apoptosis. The Fas trimer hysteron model is a mathematical formulation of this idea, which provides a possible rationale for the observed 1:3 binding stoichiometry. The essential interpretation is that FasL acts as a clustering platform for Fas (Fig. 7.1A), which then establish contacts through pairwise and higher-order interactions to form units capable of hysteresis, i.e., hysterons. In this work, we propose that bistability may be induced upstream by the death receptors themselves.

7.3 Results

7.3.1 Model formulation and bistability

The bistable character of the hysteron model is contingent on the necessity of receptor clustering by FasL for high-order Fas interactions (i.e., termolecular and above); thus, a simple estimate of Fas density in the membrane is needed. Previous models incorporating ligand-receptor dynamics have all used Fas cell surface receptors, not soluble

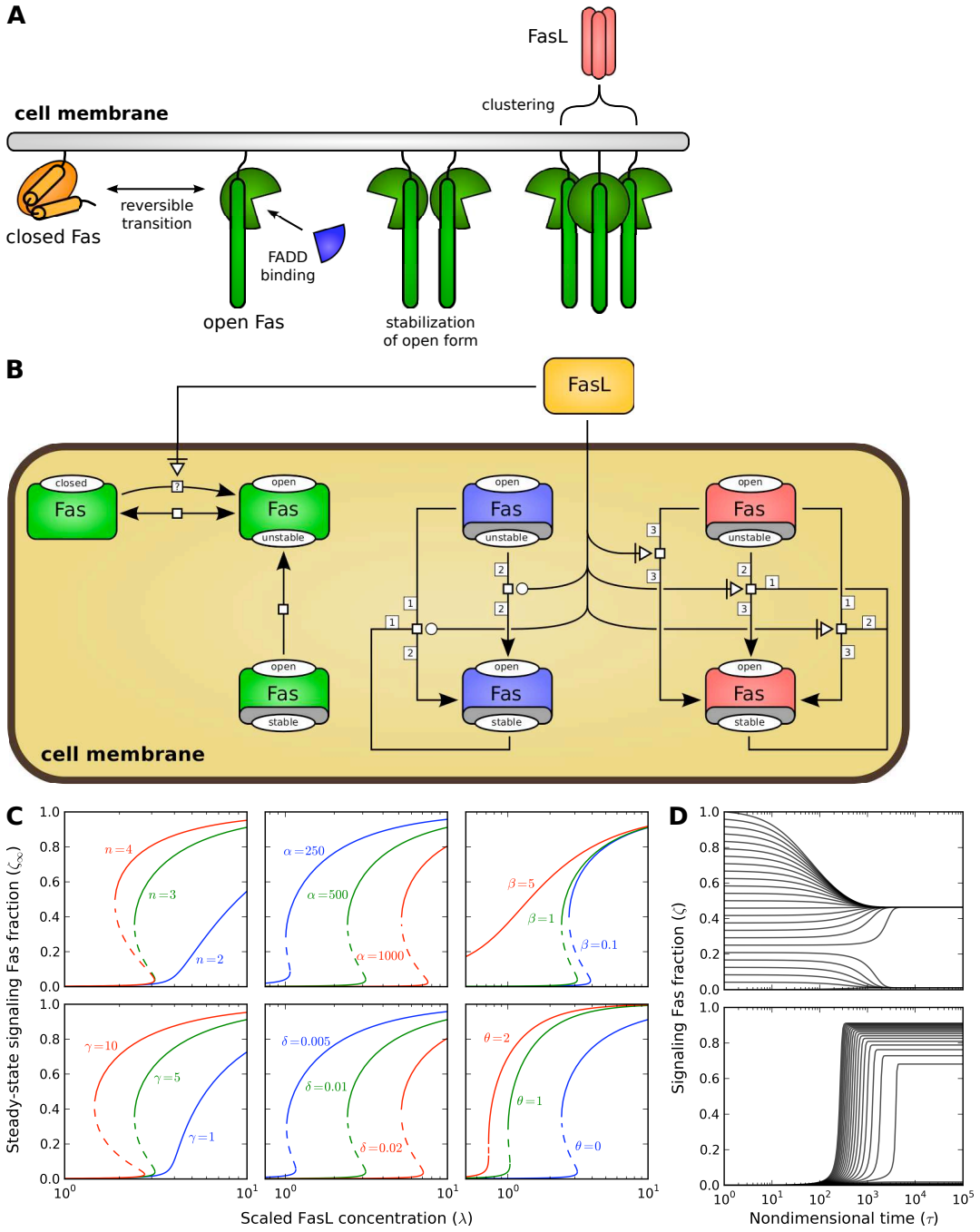

Figure 7.1: The Fas trimer hysteron model. All parameters were set at baseline values (Table 7.1) unless otherwise stated. (**a**) The transmembrane death receptor Fas natively adopts a closed conformation, but can open to allow the binding of FADD, an adaptor molecule that facilitates apoptotic signal transduction. Open Fas can self-stabilize via stem helix and globular interactions, which may be enhanced by receptor clustering through association with the ligand FasL. (**b**) Process diagram (complying with the SBGN Process Description language Level 1 (Le Novère *et al.*, 2009)) of the hysteron model with $n = 3$. Fas exists in three forms: closed; open, unstable; and open, stable. Green entities are capable of ligand-independent processes, where we have marked ligand-induced receptor opening as uncertain; blue, ligand-catalyzed processes of molecularity two; and red, ligand-necessary processes of molecularity three. (**c**) Variational effects of model parameters on the steady-state signaling Fas fraction ζ_∞ as a function of the scaled FasL concentration λ. Full and dashed lines indicate stable and unstable steady-states, respectively. Bistability requires $n \geq 3$ ($n = 3$ for receptor trimerization). (**d**) Time courses at baseline parameters for λ fixed within the bistable regime and variable ζ^0, the initial signaling Fas fraction (top); and fixed ζ^0 and variable λ (bottom).

Fas, where the number of receptors have been estimated in terms of concentrations of the order 10–100 nM (Albeck *et al*., 2008a,b; Bentele *et al*., 2004; Harrington *et al*., 2008; Hua *et al*., 2005; Okazaki *et al*., 2008), so conservatively taking an estimate of 100 nM (approximately 60,000 receptors) gives an areal density of $\sim 10^{-4}$ molecules/nm^2 (see Methods). Receptors are found to be sparsely distributed, with only about one Fas molecule in the area accessible around each receptor, assuming a characteristic size of 100 nm. High-order Fas interactions in the absence of FasL were therefore neglected.

The model includes constitutive receptor opening and closing, pairwise open Fas stabilization, higher-order open Fas stabilization enabled by FasL, and ligand-induced receptor opening (Fig. 7.1). According to its conformational states, Fas is assumed to be one of three species: closed (X); open, unstable (Y); and open, stable (Z), i.e., active and signaling. Furthermore, let the ligand FasL be denoted by L. For a general clustering parameter n, giving the maximum number of receptors that each ligand can coordinate, assign the reactions

$$Y \underset{k_{-1}}{\overset{k_1}{\rightleftharpoons}} X, \tag{7.1}$$

$$\{2Y, Y + Z\} \xrightarrow{k_2} 2Z, \tag{7.2}$$

$$Z \xrightarrow{k_3} Y, \tag{7.3}$$

$$L + X \xrightarrow{k_4} L + Y, \tag{7.4}$$

$$L + jY + (i - j)\, Z \xrightarrow{k_l^{(i)}} L + iZ, \tag{7.5}$$

where $i = 2, \ldots, n$, and $j = 1, \ldots, i$. The first reaction describes spontaneous receptor opening and closing. The second reaction describes pairwise stabilization by open Fas, irrespective of the presence of FasL; higher-order analogues, though in principle available, are neglected as justified by the low estimated receptor density. The third reaction describes the constitutive destabilization of open Fas; and the fourth, ligand-induced receptor opening. Finally, the fifth reaction captures all cluster-stabilization events enabled by FasL, the order being limited by n.

Throughout earlier chapters, concentrations were denoted by $[-]$ to avoid confusion with gene names; however, normal convention is that lowercase letters denote the concentrations of their uppercase counterparts and is used in this chapter. The five reaction forms of the model dynamics, given by mass action for simplicity, are

$$\frac{dx}{dt} = v_1 - v_4, \quad \frac{dy}{dt} = -v_1 - v_2 + v_3 + v_4 - v_l, \quad \frac{dz}{dt} = v_2 - v_3 + v_l,$$

where

$$\begin{aligned} v_1 &= k_1 y - k_{-1} x, \\ v_2 &= 2k_2 y^2 + k_2 yz, \\ v_3 &= k_3 z, \\ v_4 &= k_4 lx, \\ v_l &= l \sum_{i=2}^{n} k_l^{(i)} \sum_{j=1}^{i} j y^j z^{i-j}. \end{aligned}$$

Clearly, ligand is conserved and may be treated as a parameter. The system can be rescaled by introducing the nondimensional variables

$$\xi = \frac{x}{s}, \quad \eta = \frac{y}{s}, \quad \zeta = \frac{z}{s}, \quad \lambda = \frac{k_l^{(2)} ls}{k_{-1}}, \quad \tau = k_{-1} t,$$

where $s \equiv x + y + z$ is the conserved receptor concentration. Further, let

$$\alpha = \frac{k_1}{k_{-1}}, \quad \beta = \frac{k_2 s}{k_{-1}}, \quad \delta = \frac{k_3}{k_{-1}}, \quad \theta = \frac{k_4}{k_l^{(2)} s},$$

and, for simplicity, enforce the uniformity condition

$$\gamma = \frac{k_l^{(i)} s^{i-2}}{k_l^{(2)}}, \quad i = 3, \ldots, n.$$

Then the steady-state, denoted by the subscript ∞,

$$\xi_\infty = \frac{\alpha \eta_\infty}{1 + \theta\lambda}, \quad \eta_\infty = \frac{1 - \zeta_\infty}{1 + \alpha / (1 + \theta\lambda)}, \tag{7.6}$$

so ζ_∞ is given by considering

$$\frac{d\zeta}{d\tau} = 2(\beta + \lambda)\eta^2 + (\beta + \lambda)\eta\zeta + \gamma\lambda \sum_{i=3}^{n} \sum_{j=1}^{i} j \eta^j \zeta^{i-j} - \delta\zeta \tag{7.7}$$

and solving $d\zeta/d\tau = 0$ with $\eta \mapsto \eta_\infty$ and $\zeta \mapsto \zeta_\infty$. The steady-state is obtained by solving a polynomial equation in ζ_∞ of degree n, denoting the number of receptors that each ligand can coordinate, which admits bistability only if $n \geq 3$. In the context of this model, the biologically observed value of $n = 3$ demonstrates the lowest order complexity required for bistability; therefore, the biological case of $n = 3$ is considered

Model	Parameter	Value
hysteron	n	3
	α	500
	β	1
	γ	5
	δ	0.01
	θ	0
crosslinking	κ	0.1
caspase	π_ϕ	10
	π_ψ	10
	π_δ	1
	σ	0.1

Table 7.1: Baseline nondimensional parameter values for models. Baseline nondimensional parameter values for the hysteron, crosslinking, and caspase models.

in further detail. The model was shown to exhibit bistability (Figs. 7.1C and D) for reasonable parameter choices (see Table 7.1). Notably, the bistability is reversible, as the governing polynomial reduces to a quadratic in the absence of ligand; alternatively, from a dynamical systems perspective, the steady-state structure undergoes a saddle-node bifurcation as FasL is decreased. Moreover, intuition suggests that ligand-induced receptor opening is not crucial for bistability, hence for simplicity, we further set $\theta = 0$, with the understanding that the error incurred is only cursory at this level and thus unlikely to change the essential character of the following results.

7.3.2 Bistability thresholds, parameter identification and robustness

Having established the capacity of the model for bistability, a study of its defining features in more detail was sought by using a combination of analytical and numerical tools. In particular, focus was given to the activation and deactivation thresholds $\lambda_\pm$, respectively, that define the bistable regime; these are the points at which the steady-state switches discontinuously from one branch to the other, and are given by the values of λ at which the hysteresis curve turns, i.e., at $\partial\lambda/\partial\zeta_\infty = 0$ (Fig. 7.2A). These critical values of λ imply a polynomial equation in ζ_∞ of order four, which, through an asymptotic analysis with $\alpha = \mathcal{O}(1/\varepsilon)$, $\beta, \gamma = \mathcal{O}(1)$, and $\delta = \mathcal{O}(\varepsilon)$ for $\varepsilon \ll 1$, we showed to have at most

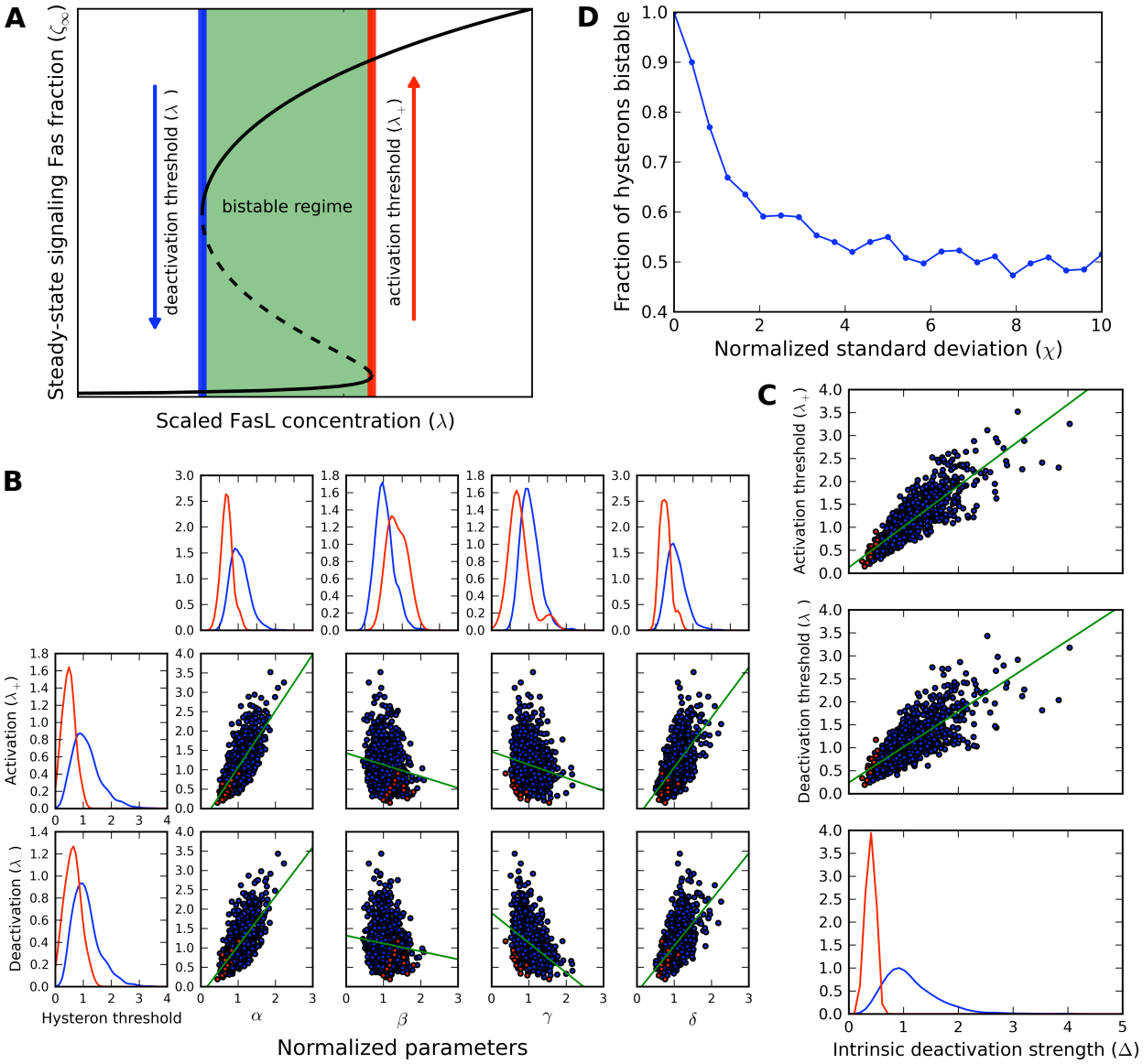

Figure 7.2: Bistability thresholds and robustness. (**A**) Definition of the activation and deactivation thresholds $\lambda_\pm$, which bound the bistable regime of the model. (**B**) Parameter and threshold variation for $N = 10^3$ samples (Appendix D, Dataset 1), where the parameters α, β, γ, and δ were drawn independently from log-normal distributions with scaled standard deviation $\chi = 0.25$ about baseline median values (Table 7.1). Parameters are expressed relative to their baseline values, and thresholds relative to their values at baseline parameters. Scatter plots reveal relationships between the parameters and their induced thresholds (green, linear regressions), and marginal probability distributions (top, parameters; side, thresholds) characterize the total variation of each quantity. For both visualizations, blue corresponds to samples with bistability, and red to those without. (**C**) Threshold variation with the intrinsic deactivation strength Δ (data and visualization as in B). (**D**) Robustness of bistability. Data were generated over $0 \leq \chi \leq 10$ (N samples each; protocol as in B), and the fraction of bistable samples recorded (Appendix D, Dataset 2). The bistable proportion remains substantial at ≈ 0.5 even under extreme variation.

two nonnegative roots, namely

$$\zeta_+ \sim \sqrt{\frac{2\Delta}{\alpha\left[\gamma\left(\Delta-1\right)-\Delta\right]}}, \tag{7.8}$$

$$\zeta_- \sim \sqrt{\frac{\Delta\Theta}{\gamma}} - \left(\Delta-1\right), \tag{7.9}$$

where

$$\Delta = \frac{\alpha\delta}{\beta}, \tag{7.10}$$

$$\Theta = \gamma\left(\Delta-1\right)-1, \tag{7.11}$$

with the consistency requirement that $\zeta_+ = \mathcal{O}(\sqrt{\varepsilon})$ and $\zeta_- = \mathcal{O}(1)$ (Appendix A). These correspond to

$$\lambda_+ \sim \beta\left(\Delta-1\right), \tag{7.12}$$

$$\lambda_- \sim \frac{\beta}{\gamma\Delta+\Theta-2\sqrt{\gamma\Delta\Theta}}, \tag{7.13}$$

respectively, which are both of $\mathcal{O}(1)$. This fully characterizes the bistability in the asymptotic limit (Appendix A.1).

The values of the thresholds $\zeta_\pm$ and $\lambda_\pm$ may be used to estimate the model parameters in the asymptotic limit (A.1). To facilitate the estimation, we further require the unique value ζ_0 of ζ_∞ at $\lambda = 0$, which is given by solving $p_\lambda = 0$. Performing an order balance for p_λ as in Appendix Sec. A, it was found that $\nu = 0$ and 1 (Table 7.2), so

$$\zeta_0 \sim \begin{cases} 2/\left[\alpha\left(\Delta-1\right)\right], & \Delta > 1, \\ 1-\Delta, & \Delta \leq 1. \end{cases} \tag{7.14}$$

As the $\zeta_\pm$ and $\lambda_\pm$ are assumed to exist; therefore, it was defined ζ_0 by the first formula.

The parameters, for example, ζ_0, λ_+, and ζ_+ for α, β, and γ, respectively may be solved for as functions of Δ, i.e.,

$$\alpha = \frac{2}{\left(\Delta-1\right)\zeta_0}, \quad \beta = \frac{\Delta-1}{\lambda_+}, \quad \gamma = \frac{\Delta}{\Delta-1}\left(1+\frac{2}{\alpha\zeta_+^2}\right), \tag{7.15}$$

and finally, obtain Δ by simultaneous optimization of both ζ_- and λ_-, subject to the bistability constraint $\Delta > \Delta^*$. The value of δ is recovered through Δ.

	$c_2 = \mathcal{O}(\varepsilon^{2\nu-2})$	$c_1 = \mathcal{O}(\varepsilon^{\nu-2})$	$c_0 = \mathcal{O}(\varepsilon^{-1})$
c_2	—	0	1/2
c_1		—	1
c_0			—
(1)	0	(−1)	(−1)
1/2	−1	−3/2	−1
(0)	(−2)	(−2)	−1

Table 7.2: Order balance of $p_\lambda = \sum_{i=0}^{2} c_i \zeta_\infty^i$. Top, critical values of ν, where $\zeta_\infty = \mathcal{O}(\varepsilon^\nu)$ for $\varepsilon \ll 1$, balancing each pair of terms in p_λ; bottom, corresponding ε-exponent of the order of each term. Admissible balances are enclosed in parentheses.

To set the nondimensional timescale k_{-1}, the characteristic time was considered for convergence to the steady-state. The Jacobian matrix

$$J = \begin{pmatrix} \xi_{\tau\xi} & \xi_{\tau\zeta} \\ \zeta_{\tau\xi} & \zeta_{\tau\zeta} \end{pmatrix}\Bigg|_\infty$$

evaluated at steady-state, i.e., at $\eta = (1-\zeta_\infty)/(1+\alpha)$, has the eigenvalues

$$\mu_1 = -1, \quad \mu_2 = -\frac{\delta}{\varepsilon} + \mathcal{O}(\varepsilon), \tag{7.16}$$

where it was assumed $\zeta_\infty, \lambda = \mathcal{O}(1)$ for cell death. Therefore, the nondimensional relaxation time is $\tau_{\text{relax}} = \max\{-1/\mu_{1,2}\} = \mathcal{O}(1)$, so by rescaling, $k_{-1} = \tau_{\text{relax}}/t_{\text{relax}} = \mathcal{O}(1/t_{\text{relax}})$, where t_{relax} is the experimentally measured relaxation time. This leaves only one of $k_l^{(2)}$ and $k_l^{(3)}$ undetermined.

Note that α and δ only enter these expressions through Δ; which also explains their similar variational effects (see Fig. 7.2C). The asymptotic forms of the thresholds reveal their critical dependence on Δ, the relative intrinsic deactivation strength. In particular, provided that $\gamma > 1$, all thresholds are real and nonnegative if

$$\Delta > \Delta^* \equiv \max\left\{\frac{\gamma}{\gamma-1}, \frac{\gamma+1}{\gamma}\right\} > 1. \tag{7.17}$$

Hence it is assumed that $\gamma > 1$, which quantifies the intuition that ligand-enabled higher-order receptor cluster-stabilization is favored over the corresponding pairwise stabilization, as due to, e.g., aggregate globular interactions. Thus, given the well-ordering of the $\zeta_\pm$, the asymptotic bistability condition is $\Delta > \Delta^*$. Robustness of bistability is therefore

immediate if $\Delta \gg \Delta^*$ at baseline values; in this regime, the model is expected to retain sharp switching behavior, and hence a robust distinction between coherent life and death states over a wide operating range.

To study the bistability thresholds in general, numerical computation was undertaken. Parameters were drawn independently from log-normal distributions with scaled standard deviations of $\chi = 0.25$ relative to baseline median values (Table 7.1 and Appendix Table A.3; Appendix D, Dataset 1). The resulting thresholds are not particularly robust, exhibiting variations of $\chi(\lambda_\pm) \approx 0.5$. However, robustness to specific parameters was observed, notably both $\lambda_\pm$ to β, and λ_+ additionally to γ (Fig. 7.2B and Appendix Table A.4).

Almost 99% of parameter sets were bistable, despite significant variation in the parameters and corresponding thresholds. Thus, the model exhibits robustness of bistability. While none of the natural system parameters provided effective discrimination for bistability, consistent with the analysis, we found that the simplified condition $\Delta > 1$ accurately characterizes the data, correctly classifying over 98% of parameter sets (Fig. 7.2C). Our baseline parameters give $\Delta = 5$, so the expected robustness is substantial, as observed. A simple argument further suggests that, given $\gamma > 1$, this robustness asymptotes toward 50% bistability as $\chi \to \infty$ (Table 7.2). Parameters sampled widely over $0 \leq \chi \leq 10$ support this (Fig. 7.2D and Appendix D, Dataset 2).

7.3.3 Cell-level analysis using relay hysterons

The model thus far has been formulated based on constant parameters. At the level of the cell, however, this is unlikely to be true due to local inhomogeneities, e.g., variations in receptor concentration, lipid composition, and other membrane factors. These issues may be treated simultaneously by applying the model locally within a membrane patch—i.e., by dividing the cell into individual hysteretic units—and positing the cell as an array of such hysterons, each with parameters drawn randomly from an appropriate distribution. For ease of analysis, a digital abstraction was applied, whereby each hysteron is either *active* or *inactive*, depending on the local ligand concentration and its activation and deactivation thresholds. More precisely, the abstracted activity of a given hysteron is

$$\hat{\zeta} = \begin{cases} 0, & \lambda \leq \lambda_-, \\ 1, & \lambda \geq \lambda_+, \\ \hat{\zeta}_0, & \lambda_- < \lambda < \lambda_+, \end{cases} \tag{7.18}$$

where $\hat{\zeta}_0$ is its previous activity level and hence accounts for its memory (Fig. 7.3A). Thus, the cell is viewed as a set of relay hysterons connected in parallel, whose sum activity gives the total (normalized) cell response

$$\zeta_{\text{cell}} = \frac{1}{N}\sum_{i=1}^{N}\hat{\zeta}_i, \tag{7.19}$$

where $\hat{\zeta}_i$ is the activity of hysteron i (Fig. 7.3B). Observe that this is simply the classical Preisach model (Preisach, 1935), which has enjoyed remarkable success in describing magnetic hysteresis (Barker *et al*., 1983).

Previously generated data was used at $\chi = 0.25$ (Appendix D, Dataset 1) to trace out a cell-level hysteresis curve under the assumption of a uniform ligand distribution (Fig. 7.3C). Clearly, this is a smoothing operator, averaging over the sudden shifts associated with each hysteron. Indeed, this idea has been applied previously to explain experimentally measured population-level data: by summing over individual hysteretic cells, sharp thresholds are smeared out, producing a smooth, graded population response (Eissing *et al*., 2004). Note, though, that the current analysis predicts a graded response at the cell level; whether this is true remains as yet beyond the reach of experiment. Moreover, the lack of a sharp switch from low to high Fas signaling does not necessarily imply the same at the level of the caspases which ultimately govern cell death, as downstream components may possess switching dynamics (see, e.g., Bagci *et al*., 2006; Bentele *et al*., 2004; Cui *et al*., 2008; Eissing *et al*., 2004; Legewie *et al*., 2006). In principle, the bistability thresholds may be distributed randomly on the Preisach plane, but in fact a strong linear dependence was observed between the $\lambda_{\pm}$ ($r > 0.95$; Fig. 7.3D). This suggests an intrinsic ordering of the thresholds that promotes bistability and hence robustness.

7.3.4 Comparison with the crosslinking model

The prevailing model of ligand-receptor interaction in apoptosis is based on a crosslinking formulation, whereby FasL recruits Fas independently at each of three binding sites. As a representative of such models, we analyzed a variant of that by Lai and Jackson, 2004, as introduced in Chapter 6 as well as Harrington *et al*., 2008; other formulations include Hua *et al*., 2005 and, for more simplified versions, see Albeck *et al*., 2008a,b; Bentele *et al*., 2004; Fussenegger *et al*., 2000.

Recall the crosslinking model (Fig. 7.4A) assumes five species: FasL (L), Fas (R), and the complexes FasL:Fas (C_1), FasL:Fas$_2$ (C_2), and FasL:Fas$_3$ (C_3). These obey the

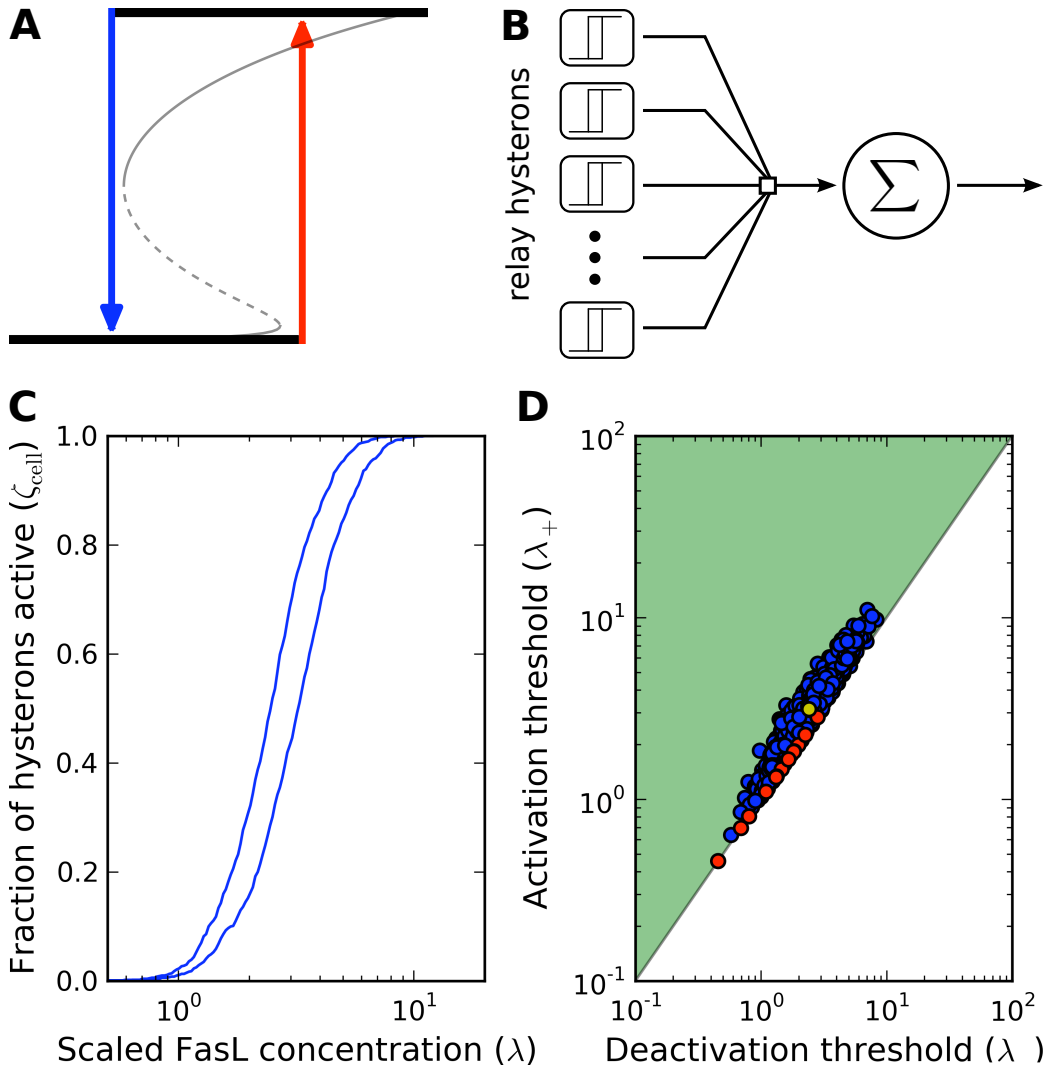

Figure 7.3: Cell-level analysis using relay hysterons. (**A**) Digital abstraction as a relay hysteron, defined as either *active* or *inactive*, corresponding to high or low Fas signaling, respectively (thick black lines). State switching occurs according to the activation and deactivation thresholds (red and blue arrows, respectively) and the local FasL concentration. (**B**) Schematic diagram of the Preisach model. The activities of an ensemble of independent relay hysterons are summed to give the total output activity; in our case, due to normalization, the total activity is an average. (**C**) and (**D**) Cell analysis using Preisach averaging on relay hysterons defined on the threshold variation data (Appendix D, Dataset 1). (**C**) Hysteresis curve of cell activity ζ_{cell}. (**D**) Distribution of thresholds on the Preisach plane (green); coloring as in Fig. 7.2B and C, where additionally, the thresholds at baseline parameters (Table 7.1 are shown in yellow.

reversible reactions

$$L + R \underset{k_-}{\overset{3k_+}{\rightleftharpoons}} C_1, \quad C_1 + R \underset{2k_-}{\overset{2k_+}{\rightleftharpoons}} C_2, \quad C_2 + R \underset{3k_-}{\overset{k_+}{\rightleftharpoons}} C_3,$$

which describe the independent recruitment of Fas at each of three binding sites by FasL; note that the reaction rates have been adjusted for combinatorial factors. The dynamics are

$$\frac{dl}{dt} = -v_1, \quad \frac{dr}{dt} = -v_1 - v_2 - v_3, \quad \frac{dc_1}{dt} = v_1 - v_2, \quad \frac{dc_2}{dt} = v_2 - v_3, \quad \frac{dc_3}{dt} = v_3,$$

where

$$v_1 = 3k_+ lr - k_- c_1, \quad v_2 = 2k_+ c_1 r - 2k_- c_2, \quad v_3 = k_+ c_2 r - 3k_- c_3.$$

Nondimensionalize by setting

$$\lambda = \frac{l}{r_0}, \quad \rho = \frac{r}{r_0}, \quad \gamma_i = \frac{c_i}{r_0}, \quad \tau = k_- t, \quad \kappa = \frac{k_-}{k_+ r_0},$$

where r_0 is the total receptor concentration. In these variables, the system admits the conservation relations

$$\lambda_0 = \lambda + \gamma_1 + \gamma_2 + \gamma_3, \quad 1 = \rho + \gamma_1 + 2\gamma_2 + 3\gamma_3,$$

interpreted as ligand and receptor conservation, respectively. At steady-state,

$$\gamma_{1,\infty} = 3\lambda_\infty \left(\frac{\rho_\infty}{\kappa}\right), \quad \gamma_{2,\infty} = 3\lambda_\infty \left(\frac{\rho_\infty}{\kappa}\right)^2, \quad \gamma_{3,\infty} = \lambda_\infty \left(\frac{\rho_\infty}{\kappa}\right)^3,$$

where

$$\lambda_\infty = \frac{\lambda_0}{1 + 3\left(\rho_\infty/\kappa\right) + 3\left(\rho_\infty/\kappa\right)^2 + \left(\rho_\infty/\kappa\right)^3}$$

and

$$\rho_\infty = \frac{1}{2}\left[\sqrt{\left(3\lambda_0 + \kappa - 1\right)^2 + 4\kappa} - \left(3\lambda_0 + \kappa - 1\right)\right].$$

In analogy with the hysteron model,

$$\zeta \equiv \gamma_1 + 2\gamma_2 + 3\gamma_3 = 1 - \rho \tag{7.20}$$

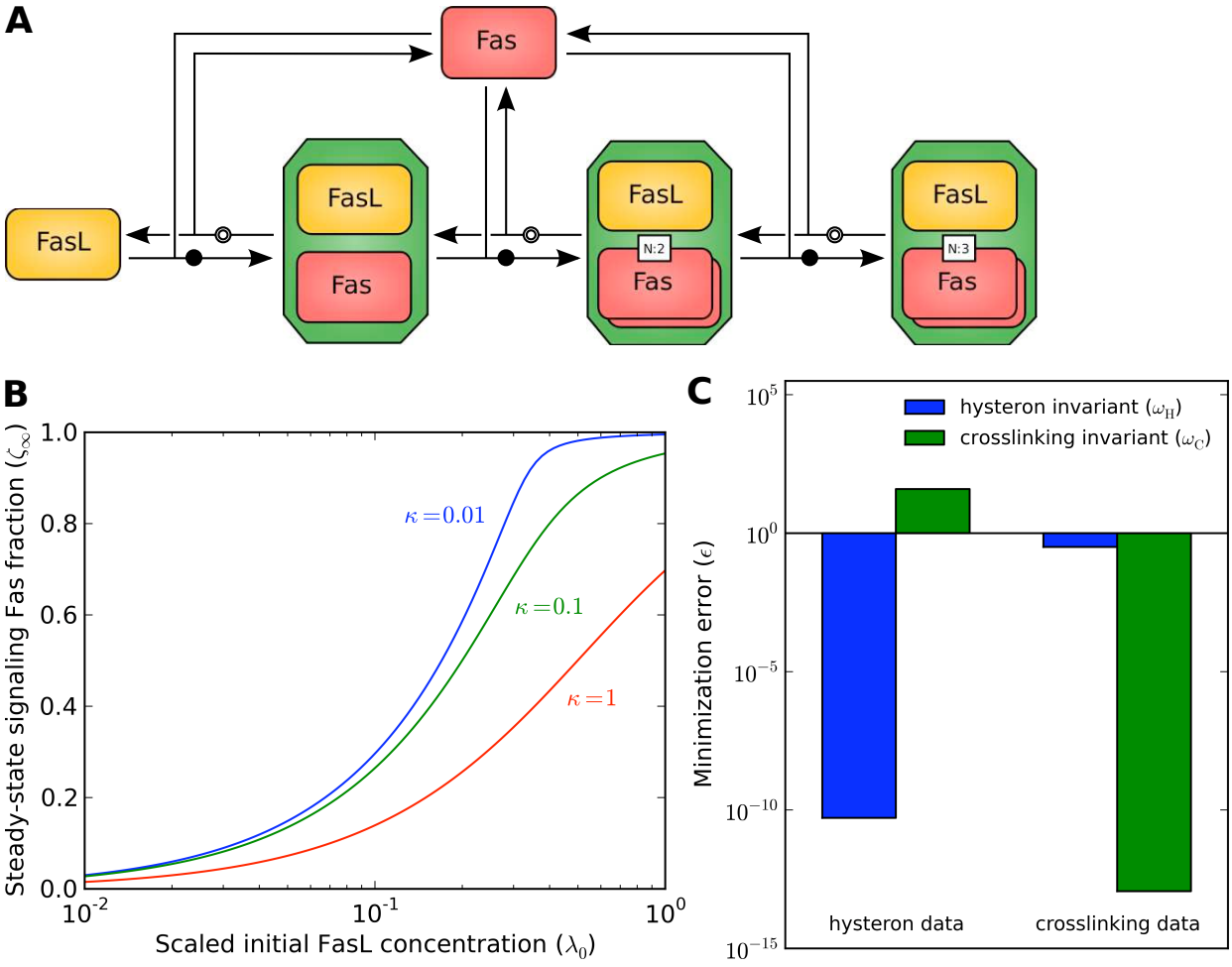

Figure 7.4: Comparison with the crosslinking model. (**A**) Process diagram (comply with the SBGN Process Description language Level 1 (Le Novère *et al.*, 2009)) of the crosslinking model. (**B**) Variation of the steady-state signaling Fas fraction ζ_∞ with respect to the model parameter κ. (**C**) Minimization errors ϵ of the steady-state invariants ω_H and ω_C for the hysteron and crosslinking models, respectively (Appendix B.2), over data generated from each model (Datasets 3 and 4) using nonnegative least squares (see Materials and methods for details).

is used as a measure of the signaling Fas fraction (Fig. 7.4B). The crosslinking model admits only one steady-state and cannot be bistable, in contrast to the hysteron model. In principle, therefore, this provides a ready criterion for model discrimination, assuming that the ligand-receptor dynamics can be isolated. Alternatively, if this level of experimental control cannot be exercised, a discrimination test based on steady-state invariants derived using tools from algebraic geometry can be provided, following Manrai and Gunawardena, 2008. The basic idea is that dynamics resulting from mass action chemical kinetics are polynomial equations in the species concentrations; consequently, their steady-states describe algebraic curves, whose intersection—describing the steady-states of the system—is an algebraic variety that can be studied using algebraic geometry.

The primary model selection tool is the Gröbner basis, which was used to compute steady-state invariants of each model, i.e., polynomials in the species concentrations that vanish at steady-state (Appendix B.2), with respect to the observables λ_0, the total FasL concentration, presumably a controlled experimental input; and ζ, the active Fas concentration, which may be measured, for example, by using FADD binding as an indicator. The identification of experimental observables is important as concentrations that cannot be measured must, in principle, remain unknown and hence be eliminated from any experimentally relevant invariant. Gröbner bases readily allow such elimination to be performed. With each system expressed in terms of λ_0 and ζ, and all other variables eliminated, the resulting steady-state invariants ω_{H} and ω_{C} for the hysteron and crosslinking models, respectively, are polynomials of the form $\sum_{i,j} c_{ij}\lambda_0^i\zeta^j$ (Appendix B).

These invariants may be used for model discrimination by comparing the errors $\epsilon_{\mathrm{H}} = |\omega_{\mathrm{H}}|$ and $\epsilon_{\mathrm{C}} = |\omega_{\mathrm{C}}|$ for the hysteron and crosslinking models, respectively, given experimental data $(\lambda_0, \zeta_\infty)$. If the model parameters are unknown, then ϵ_{H} and ϵ_{C} may be minimized over the space of respective parameters and compared to their optimal values. As a demonstration that such discrimination is feasible, sample steady-state concentrations from each model were generated (Datasets 3 and 4) and the data minimized with respect to each invariant. The problem is highly nonlinear, so to improve the optimization, each term $\lambda_0^i\zeta^j$ was considered as an independent variable, thus effectively linearizing the problem with respect to the associated coefficients c_{ij}. The c_{ij} were further constrained, and hence, by relabeling, the minimization was cast as a nonnegative least squares (NNLS) problem, which can be solved exactly in that the error achieved is a global minimum (Lawson and Hanson, 1995). The results show that the errors are small if the models underlying the data generation and the invariant minimization are the same, and large otherwise (Fig. 7.4C). This is precisely the condition necessary for effective model discrimination.

7.3.5 Feedforward caspase bistability

Bistability is often taken as a required property of apoptosis, under the intuitive reasoning that a cell must possess both stable life and death states. One common way of achieving bistability is by using positive feedback; in fact, positive feedback between caspases-8 and -3, e.g., through caspase-6 (Cowling and Downward, 2002; Slee *et al*., 1999), has been shown to mediate bistability in the extrinsic pathway (Eissing *et al*., 2004). However, whether this feedback is relevant appears controversial, due, first, to its omission in several recent models (Bentele *et al*., 2004; Hua *et al*., 2005; Okazaki *et al*., 2008); and second, to the prediction that it does not contribute significantly to the qualitative dynamics of the system (Albeck *et al*., 2008b). While numerous apoptotic processes generating bistability have been identified in the intrinsic pathway (Bagci *et al*., 2006; Cui *et al*., 2008; Legewie *et al*., 2006), such mechanisms operating independently of caspase feedback in the extrinsic pathway are scarce, including, so far, only direct inhibition of DISC by cFLIP (Bentele *et al*., 2004). It is immediate, however, that the proposed hysteron model offers another solution by moving the burden of bistability from the caspases to the upstream death receptors; the model therefore provides a welcome resolution to the problem of bistability in feedforward extrinsic caspase networks.

To demonstrate this, a rudimentary feedforward model of caspase activation was constructed capturing only the most basic interactions, particularly the activation of caspase-3 by caspase-8, which itself is activated by DISC (Fig. 7.5A). Posit the inactive caspase zymogens procaspase-8 ($\mathrm{Casp8}$) and procaspase-3 ($\mathrm{Casp3}$), and their corresponding active forms caspase-8 ($\mathrm{Casp8}^*$) and caspase-3 ($\mathrm{Casp3}^*$). Caspase-3 represents all effector caspases in the system, so its concentration will be considered a measure of the degree of apoptotic activation. The model reactions are

$$Z + \mathrm{Casp8} \xrightarrow{k_1} Z + \mathrm{Casp8}^*, \quad \mathrm{Casp8}^* + \mathrm{Casp3} \xrightarrow{k_2} \mathrm{Casp8}^* + \mathrm{Casp3}^*,$$

where the first reaction describes the activation of caspase-8; and the second, the activation of caspase-3. In general, Z denotes a death signal such as the DISC, but here it will refer to active Fas, so as to provide a link to the hysteron and crosslinking models. For reasons of stability, we further supplement with the constitutive synthesis and degradation reactions

$$\underset{k_{-3}}{\overset{k_3}{\rightleftharpoons}} \left\{\begin{matrix}\mathrm{Casp8}\\ \mathrm{Casp3}\end{matrix}\right\}, \quad \left\{\begin{matrix}\mathrm{Casp8}^*\\ \mathrm{Casp3}^*\end{matrix}\right\} \xrightarrow{k_4},$$

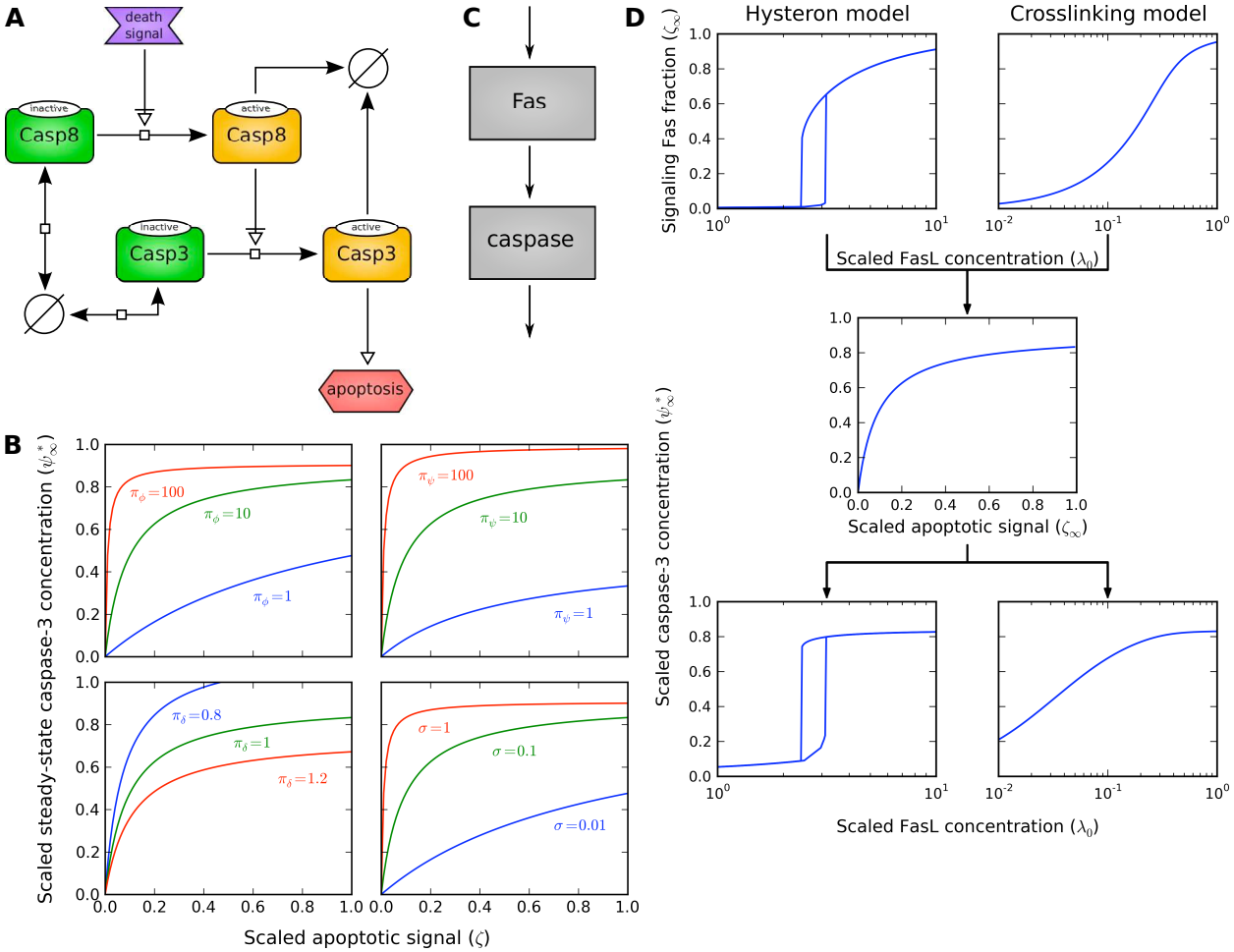

Figure 7.5: Feedforward caspase bistability. All parameters were set at baseline values (Table 7.1) unless otherwise stated. (**A**) Process diagram (comply with the SBGN Process Description language Level 1 (Le Novère *et al.*, 2009)) of the feedforward caspase model. Caspases-8 and -3 represent all initiator and effector caspases, respectively, and can each be active (orange) or inactive (green; procaspases-8 and -3, respectively). The system input is a death signal (purple; e.g., DISC or active Fas) and its output, the degree of apoptotic activation (red, taken as the caspase-3 concentration). (**B**) Variation of the steady-state caspase-3 concentration ψ^*_∞ with respect to the model parameters as a function of the scaled apoptotic signal ζ. (**C**) Systems diagram of Fas-caspase coupling. The apoptotic signal generated by the Fas module (e.g., hysteron or crosslinking) is used as input to the downstream caspase module. (**D**) Hysteresis curves of caspase-coupled models using either the hysteron (left) or crosslinking (right) models for the Fas subsystem. Flow of information as in C. In the absence of caspase feedback, only the hysteron model provides a mechanism for bistability.

which are taken to be symmetric for simplicity. Letting

$$x = [\text{Casp8}]\,, \quad x^* = [\text{Casp8}^*]\,, \quad y = [\text{Casp3}]\,, \quad y^* = [\text{Casp3}^*]\,,$$

the dynamics are

$$\frac{dx}{dt} = -v_1 + v_x, \quad \frac{dx^*}{dt} = v_1 - v_{x^*}, \quad \frac{dy}{dt} = -v_2 + v_y, \quad \frac{dy^*}{dt} = v_2 - v_{y^*},$$

where

$$v_1 = k_1 xz, \quad v_2 = k_2 x^* y, \quad \begin{Bmatrix} v_x \\ v_y \end{Bmatrix} = k_3 - k_{-3} \begin{Bmatrix} x \\ y \end{Bmatrix}, \quad \begin{Bmatrix} v_{x^*} \\ v_{y^*} \end{Bmatrix} = k_4 \begin{Bmatrix} x^* \\ y^* \end{Bmatrix}.$$

Define $\Omega = k_3/k_{-3}$ and $\sigma = s/\Omega$, i.e., the equilibrium procaspase and relative receptor concentrations, respectively, and let

$$\phi = \frac{x}{\Omega}, \quad \phi^* = \frac{x^*}{\Omega}, \quad \psi = \frac{y}{\Omega}, \quad \psi^* = \frac{y^*}{\Omega}.$$

Then expressing the dynamics in terms of

$$\pi_\phi = \frac{k_1\Omega}{k_{-3}}, \quad \pi_\psi = \frac{k_2\Omega}{k_{-3}}, \quad \pi_\delta = \frac{k_4}{k_{-3}}, \quad \tau = k_{-3}t,$$

obtained, at steady-state,

$$\phi_\infty = \frac{1}{1+\pi_\phi\sigma\zeta}, \quad \phi^*_\infty = \frac{1-\phi_\infty}{\pi_\delta}, \quad \psi_\infty = \frac{1}{1+\pi_\psi\phi^*_\infty}, \quad \psi^*_\infty = \frac{1-\psi_\infty}{\pi_\delta}.$$

Significantly, the model has only one steady-state; therefore, in the absence of bistability at the DISC, hysteresis is clearly not possible (Fig. 7.5B). To probe this directly, the model was coupled to the upstream hysteron and crosslinking models by using active Fas as a functional surrogate for DISC (Fig. 7.5C). The results confirm that only the hysteron-caspase model achieves hysteresis (Fig. 7.5D). The hysteron model thus provides a possible mechanism for extrinsic apoptosis to function as a bistable switch even in cells with nonexistent or weak caspase feedback.

7.4 Materials and methods

7.4.1 Model set-up

Receptor density estimate

Approximating the cell as a cube of linear dimension $l \sim 10$ μm, the associated volume $v = l^3 \sim 1$ pL implies the correspondence 1 nM ~ 600 molecules $\sim 10^{-6}$ molecules/nm^2 on restricting to the membrane, i.e., by averaging over the surface area $s = 6l^2 \sim 600$ μm^2. Thus, for the typical cell, there are 40,000 Fas receptors (Bentele *et al.*, 2004), which with slight abuse of notation, is approximated as a concentration of ~ 66.6 nM. As the range varies between 10–100 nM, then for a receptor concentration of 100 nM, the number of Fas molecules in the region about each receptor is only ~ 1, assuming a square patch of size 100 nm.

Parameter selection

The baseline value of $n = 3$ was chosen for its biological relevance; the remaining parameters were set according to the following dimensional considerations. The characteristic Fas concentration is $s \sim 10$ nM, so the characteristic FasL concentration, estimated as its threshold concentration, is $l \sim 0.1$ nM (Bentele *et al.*, 2004). Estimating $k_{-1} \sim 10^{-2}$ min^{-1} gives a reaction rate of $v \sim 0.1$ nM/min for spontaneous receptor opening. Referencing the respective reactions against v hence gives $k_2 \sim 10^{-3}$ nM^{-1} min^{-1} and $k_l^{(2)} \sim 10^{-2}$ nM^{-2} min^{-1}, so $\beta \sim 1$ and $\lambda \sim 10l$ nM^{-1}. Therefore, the nondimensional threshold ligand concentration is $\lambda_+ \sim 1$; α, γ, and δ were set, where intuitively $\alpha \gg 1$ and $\delta \ll 1$, to match this. Similarly, $k_4 \sim 0.1$ nM^{-1} min^{-1}, i.e., $\theta = 1$, but $\theta = 0$ for simplicity.

7.4.2 Model analysis

Steady-state solution

The steady-states of the hysteron model are given by solving $d\zeta/d\tau = 0$, with each steady-state classified as either stable if $d\zeta/d\tau|_{\zeta=\zeta_\infty} < 0$ and unstable otherwise (Eqs. 7.6-7.7); this was done analytically if $\theta = 0$ and numerically otherwise.

Dynamic characterization

Trajectory families were generated under two conditions: first, by fixing FasL at $\lambda = 2.5$ (within the bistable regime) and imposing the initial conditions $(\xi^0, \eta^0, \zeta^0) = (1 - \zeta^0, 0, \zeta^0)$ for $0 \leq \zeta^0 \leq 1$; and second, by fixing $(\xi^0, \eta^0, \zeta^0) = (1, 0, 0)$ and letting $0 \leq \lambda \leq 10$. Integrations were performed at baseline parameter values (Table 7.1) over $0 \leq \tau \leq 10^4$ using ODEPACK (Hindmarsh, 1983).

Asymptotic analysis

Solving $d\zeta/d\tau = 0$ for λ at $n = 3$ and $\theta = 0$ gives

$$\lambda = f_\lambda(\zeta_\infty) \equiv \frac{p_\lambda(\zeta_\infty)}{q_\lambda(\zeta_\infty)},$$

where p_λ and q_λ are polynomials of degrees two and three, respectively, so

$$\frac{\partial \lambda}{\partial \zeta_\infty} = f_{\partial\lambda/\partial\zeta}(\zeta_\infty) \equiv \frac{p_{\partial\lambda/\partial\zeta}(\zeta_\infty)}{q_{\partial\lambda/\partial\zeta}(\zeta_\infty)},$$

where $p_{\partial\lambda/\partial\zeta}$ and $q_{\partial\lambda/\partial\zeta}$ are of degrees four and six, respectively. The Fas activation and deactivation thresholds $\zeta_\pm$ are given by solving $\partial\lambda/\partial\zeta_\infty = 0$, i.e., $p_{\partial\lambda/\partial\zeta} = 0$. Assuming that $\zeta_\infty = \mathcal{O}(\varepsilon^\nu)$ with $\alpha = \mathcal{O}(1/\varepsilon)$, $\beta, \gamma = \mathcal{O}(1)$, and $\delta = \mathcal{O}(\varepsilon)$ for $\varepsilon \ll 1$, and balancing the orders of each pair of terms in $p_{\partial\lambda/\partial\zeta}$, the admissible values $\nu = 0$ and $1/2$ were found (Appendix A Table A.1). Solving the asymptotic forms of $p_{\partial\lambda/\partial\zeta}$ then gives $\zeta_+ = \mathcal{O}(\sqrt{\varepsilon})$ and $\zeta_- = \mathcal{O}(1)$ as the only nonnegative roots; the corresponding FasL thresholds are $\lambda_\pm = f_\lambda(\zeta_\pm)$.

Numerical computation of thresholds

Given α, β, γ, and δ, the bistability thresholds are computed by solving $p_{\partial\lambda/\partial\zeta}$ numerically for $\zeta_\pm$ and then computing $\lambda_\pm = f_\lambda(\zeta_\pm)$. If the $\zeta_\pm$ do not exist (i.e., all solutions are negative or complex), then set $\zeta_\pm = 1/2$ and $\lambda_\pm$ accordingly.

Log-normal distribution with scaled standard deviation

If $X \sim \text{Log-N}(\mu, \sigma^2)$, then the median and standard deviation of X are

$$\begin{aligned} \text{med}\,(X) &= e^{\mu}, \\ \text{std}\,(X) &= \sqrt{(e^{\sigma^2} - 1)\, e^{2\mu+\sigma^2}}, \end{aligned}$$

respectively. Hence rescaling the standard deviation by defining $\chi = \text{std}(X)/\,\text{med}(X)$, i.e., the median analogue of the coefficient of variation,

$$\sigma = \sqrt{\log\left(\frac{1+\sqrt{1+4\chi^2}}{2}\right)}.$$

Parameter generation for threshold analysis

For the threshold variation analysis, $N = 10^3$ parameter sets $(\alpha, \beta, \gamma, \delta)$ were drawn from a log-normal distribution with baseline median values (Table 7.1) at $\chi = 0.25$ (Appendix D, Dataset 1). For the robustness of bistability analysis, χ was taken at equally spaced points over $0 \leq \chi \leq 10$, at each similarly drawing N parameter sets about baseline values (Appendix D, Dataset 2).

Estimation of probability distributions

Probability distributions of parameters and thresholds were estimated using Gaussian kernel density estimation, with automatic bandwidth selection using the Scott factor (Scott, 1992).

Cell-level analysis

The cell-level analysis was performed using the data computed at $\chi = 0.25$ (Appendix D, Dataset 1), i.e., the cell was partitioned into $N = 10^3$ relay hysterons. The hysteresis curve was traced out by ranging FasL over $0 \leq \lambda \leq \lambda_+^{\max}$, where $\lambda_+^{\max}$ is the maximum activation threshold over all parameters drawn, and then back, updating ζ_{cell} whenever a threshold is crossed.

7.4.3 Model discrimination

Steady-state invariants

Gröbner bases were computed over $K = \mathbb{Z}(\boldsymbol{a})$ using the lexicographic monomial ordering (Appendix B.2). For the hysteron invariant, $\lambda = \lambda_0$ and $\xi = 1-\eta-\zeta$, hence expressing the dynamics $\boldsymbol{f} = \partial_\tau(\xi, \eta, \zeta)$ in terms of the variables $\boldsymbol{x} = (\eta, \lambda_0, \zeta)$; the variables are $\boldsymbol{a} = (\alpha, \beta, \gamma, \delta)$. A Gröbner basis of $\langle \boldsymbol{f} \rangle$ was computed, from which elimination of η gives ω_{H}. Similarly, for the crosslinking invariant was $\lambda = \lambda_0 - \gamma_1 - \gamma_2 - \gamma_3$, $\rho = 1 - \zeta$, and $\gamma_1 = \zeta - 2\gamma_2 - 3\gamma_3$, and a Gröbner basis was computed with $\boldsymbol{f} = \partial_\tau(\lambda, \rho, \gamma_1, \gamma_2, \gamma_3)$, $\boldsymbol{x} = (\gamma_2, \gamma_3, \lambda_0, \zeta)$, and $\boldsymbol{a} = \kappa$; eliminating γ_2 and γ_3, to obtain ω_{C}.

Nonnegative least squares for model discrimination

Considering each term $\pm\lambda_0^i\zeta^j$ (with sign chosen as appropriate) in ω_{H} and ω_{C} as an independent variable, the associated constant c_{ij} was split into variable and constant parts $c_{ij}^{\text{var}}(\boldsymbol{a})$ and c_{ij}^{const}, respectively, so that $c_{ij}^{\text{var}} \geq 0$, assuming the asymptotic ordering $\alpha = \mathcal{O}(1/\varepsilon)$, $\beta, \gamma = \mathcal{O}(1)$, and $\delta = \mathcal{O}(\varepsilon)$ for $\epsilon \ll 1$, with $\Delta > 1$. The required optimization is then a nonnegative least squares problem (Lawson and Hanson, 1995) minimizing $\epsilon = \|Uc^{\text{var}} + Uc^{\text{const}}\|_2$, suppressing model reference for generality, where $U = (u_1, \ldots, u_N)$ is a matrix of experimental data, for each u_i a row vector corresponding to an experimental trial; $c^{\text{var}} = (c_{ij}^{\text{var}})$ is a column vector of nonnegative coefficients to be determined; and $c^{\text{const}} = (c_{ij}^{\text{const}})$ is a column vector of constants.

Parameter generation for model discrimination

Parameters were randomly drawn for each model using the following procedure. The initial FasL concentration λ^0 was sampled from a log-normal distribution with median $\mathrm{med}(\lambda_{\mathrm{H}}^0) = 2.5$ and $\mathrm{med}(\lambda_{\mathrm{C}}^0) = 0.25$ for the hysteron and crosslinking models, respectively (FasL is nondimensionalized differently in the two models), and scaled standard deviation $\chi(\lambda^0) = 1$. The concentrations of the remaining species, which are all constrained by nondimensionalization, were drawn uniformly in sequence over the appropriate range, i.e., for the hysteron model, $\xi^0 \in [0, 1]$ was sampled, then $\eta^0 \in [0, 1-\xi^0]$, then $\zeta^0 \in [0, 1-\xi^0-\eta^0]$, while for the crosslinking model, $\rho^0 \in [0, 1]$ was taken, next $\gamma_1^0 \in [0, 1-\rho^0]$, then $\gamma_2^0 \in [0, (1-\rho^0-\gamma_1^0)/2]$, and finally $\gamma_3^0 \in [0, (1-\rho^0-\gamma_1^0-2\gamma_2^0)/3]$. Steady-state experimental data were obtained for each parameter set by solving the steady-state equations governing each model and making the identifications $\lambda_0 = \lambda_\infty$ for the hys-

teron model, and $\lambda_0 = \lambda_\infty + \gamma_{1,\infty} + \gamma_{2,\infty} + \gamma_{3,\infty}$ and $\zeta_\infty = \gamma_{1,\infty} + 2\gamma_{2,\infty} + 3\gamma_{3,\infty}$ for the crosslinking model. For each model, $N = 100$ parameter sets were drawn (Datasets 3 and 4).

7.4.4 SBML implementation

For standards compliance, the hysteron and hysteron-caspase models were implemented in dimensional form using the Systems Biology Markup Language (SBML) Level 2 Version 1 (Finney and Hucka, 2003; Hucka *et al*., 2003). The models and sample analyses performed on them are given in the Appendix C.

7.5 Discussion

7.5.1 Summary and biological significance

In this work, a mathematical model of death ligand-receptor clustering was presented, demonstrating bistability and hysteresis in apoptosis through biologically observed Fas pair-stabilization (Scott *et al*., 2009). This work contributes to the signal processing activities in which receptor clustering has been suggested to participate (Bray *et al*., 1998; Endres *et al*., 2008; Sourjik, 2004). The Fas trimer hysteron model is a mathematical formulation of the observation that Fas can aggregate and self-stabilize in their active signaling forms; in this interpretation, FasL provides a clustering platform for Fas, promoting receptor activation and hence apoptosis by enabling proximity-induced receptor interactions. Although the precise mechanisms by which this may occur is unclear, this bistability plays an important functional role by enabling robust threshold switching between life and death states. Significantly, the model predicts that bistability is a consequence of receptor trimerization, furthermore, it provides an explanation for the homotrimeric character of FasL.

The hysteron model implies an additional all-or-none switch in apoptosis, supplementing those that have been studied previously (Bagci *et al*., 2006; Bentele *et al*., 2004; Cui *et al*., 2008; Eissing *et al*., 2004; Legewie *et al*., 2006). Critically, the proposed mechanism is triggered upstream at the death receptors that initially detect the death signal encoded by FasL; therefore, this switch is apical in that it precedes and hence provides context for all other switches in the system. Consequently, it thus operates independently of all intracellular components and offers a general mechanism for bistability, even in cell lines deficient in, for example, caspase feedback (see Albeck *et al*., 2008b). As the

signal received by all downstream components is convolved with the signature of Fas activation, the importance of understanding the mechanism and kinetics of death ligand-receptor interaction was highlighted. More generally, this provides encouragment for further research into the formation of the DISC, which, in this view, may be considered the macromolecular aggregates of active Fas. It should be noted that the hysteron model may also be applied to related death receptors such as those in the tumor necrosis factor receptor (TNFR) family, provided that they similarly possess an active form which is capable of aggregate self-stabilization.

7.5.2 Model assumptions and analysis

In formulating the hysteron model, the emphasis was on simplicity and tractability, though often at the expense of biological realism. For instance, it is more appropriate to use Michaelis-Menten kinetics with generalized loads for all ligand-dependent reactions; however, it is clear that this should not change the essential character of the model as no new physical steady-state can be introduced. Although the emergence of a new phenotype in which apoptosis cannot occur due to saturation of reaction rates is possible, this is not of practical novelty as, within the biological regime $\lambda \sim 1$ is of interest, it is essentially equivalent to a mass-action hysteron with activation threshold $\lambda_+ \gg 1$.

The model invokes the assumption that higher-order Fas interactions are not permitted in the absence of FasL. This is a strong statement and should be replaced by the requirement only that any such interaction, characterized by the analogous parameter $\tilde{\gamma}$, is weak, i.e., $\tilde{\gamma} \ll 1$. But clearly this relaxation poses no difficulty, since by rescaling it can be seen that this modification has an effect only if $\tilde{\gamma} \sim \gamma\lambda_+ = \mathcal{O}(1)$. In particular, this also shows that irreversible bistability cannot be achieved in this way.

Although monomeric Fas has been assumed, the model is not strictly incompatible with pre-ligand receptor assembly, in which Fas dimerizes or trimerizes prior to ligand exposure (Chan, 2007; Chan *et al*., 2000; Siegel *et al*., 2000). Indeed, it is necessary only that pre-associated Fas be inactive with respect to signaling via FADD binding, and furthermore be incapable of ligand-independent cluster-activation. We may then essentially apply our model locally to the region about each pre-assembled receptor complex, with the result that bistability is yet to be achieved. The interpretation now is that FasL acts on pre-associated Fas to induce a structural shift from a metastable pre-assembled conformation to a preferred state of aggregate activation. Notably, conformational change of the pre-assembled complex upon ligand binding has been confirmed experimentally (Chan *et al*., 2001); this is furthermore consistent with the finding that receptor pre-assembly

promotes sensitivity to apoptosis, presumably by increasing the local receptor concentration (Muppidi and Siegel, 2004).

Presently only the asymptotic limit $\alpha \gg 1$ and $\delta \ll 1$ has been considered. In the event that this does not reflect reality, however, this analysis should be viewed only as a representative application of asymptotics in general, which, in this particular case, revealed the criticality of the derived parameter Δ, whose importance would likely have eluded standard numerical sensitivity tests operating on the explicit system parameters. The value of such mathematical treatment is thus apparent. Moreover, it should be noted that asymptotic analysis is an effective tool for biology in general, particularly for model reduction, as biological systems often contain multiple timescales that separate naturally.

7.5.3 Tools for model selection

A primary goal of systems biology is to construct quantitative models of biochemical processes that are mechanistically correct. However, for any given process, a number of descriptions may exist—as due to, e.g., a lack of specificity from unresolved experimental data—of which only one can in principle be correct. Model selection is therefore essential; and a scalable unbiased algorithm for doing so is particularly desirable (see, e.g., Apgar *et al.*, 2008).

In discriminating the hysteron and crosslinking models, Gröbner basis methods were used to compute steady-state invariants, whose satisfiability can assess model correctness. This approach possesses three significant advantages: first, model parameters can be absorbed into the coefficient field over which the dynamics are described, resulting in invariants that are valid for all parameter choices and thus parameter-free selection criteria; second, experimentally relevant invariants can be generated through the elimination of variables that cannot be measured; and third, application of the method requires no sophisticated experimental control, e.g., gene knockdowns or knockouts, revealing only natural relations between the system variables. This last point deserves particular emphasis: steady-state invariants can be applied passively, tailored to the data at hand—which, for example, may be existing data—and hence present a flexible, cost-effective basis for model selection. Furthermore, note, that although this model was a mass-action systems, the described approach can be generalized for other types of kinetics by using different fields; in fact, the current choice of $\mathbb{Z}(\boldsymbol{a})$ is appropriate for Michaelis-Menten and Hill reaction forms, as well as their integral polynomial generalizations.

Invariant assessment may be performed in a number of different ways. For example, Manrai and Gunawardena, 2008 exploited the low effective dimensionality of invariants

in multisite phosphorylation to derive a discrimination criterion based on the visual assessment of planarity. In the current work, this was not feasible; therefore, numerical optimization was used, specifically, nonnegative least squares (NNLS), for performance. It is profitable to remember that an invariant is simply a polynomial that vanishes, so a wide variety of methods may be well used for its analysis. For large systems, however, the method of choice will likely be optimization, and, in such cases, it is believed that NNLS is a particularly strong tool: assuming effective linearization by introducing additional degrees of freedom, NNLS provides an efficient scheme for minimizing the resulting linear form exactly subject to physical constraints (Lawson and Hanson, 1995). Thus, steady-state invariants and NNLS seem to form the basis for an effective procedure for model selection and, more generally, model assessment. Scaling this up, however, is difficult, owing primarily to the bottleneck of computing Gröbner bases for large systems, though this may be overcome by embracing parallelism (Neun and Melenk, 1992) or by implementing more sophisticated algorithms such as Faugère's F_4 and F_5 (Faugère, 1999, 2002). With such enhancements in place, a large-scale automated model assessment tool may well be achievable.

Broadly, algebraic geometry is concerned with the solutions of systems of polynomial equations; for an application of Gröbner basis methods in membrane biophysics, see Faugère *et al*., 2003. Given its generality, we hence expect algebraic geometry to find wide application across all of biology, not limited only to steady-state model characterization.

7.6 Concluding remarks

A mathematical model of death ligand-receptor interaction has been presented that strongly implicates Fas aggregation, e.g., through trimerization, in generating bistability at the level of the DISC. Naturally, this has profound consequences for apoptosis and therefore deserves further investigation. The model assumptions of receptor clustering by FasL and of cluster-stabilization of open Fas should hence be verified, either, ideally, experimentally or by using atomistic simulations, e.g., molecular dynamics. Moreover, such properties should also be tested for functional homologues like other death receptors, as well as the PIDDosome, the apoptosome, and the inflammosome, as they may all share a conserved mode of operation. Furthermore, the current work has highlighted the critical role of receptor clustering, particularly in the context of pre-association, which enhances sensitivity to extrinsic apoptosis and additionally is upregulated by localization to lipid rafts (Muppidi *et al*., 2004). Therefore, future models of Fas signaling are likely to ben-

efit from a spatial component modeling receptor distribution, which, in the continuum limit, generates a system of partial differential equations rather than the simpler ordinary differential equations presently considered. Finally, it is hoped that this study demonstrates the tremendous insight that can provided by structural biology (see, e.g., Fesik, 2000), especially in collaboration with mathematical and computational modeling.

Chapter 8

General conclusions

This thesis presented mathematical models of cellular decisions; specifically, those that govern immune response and apoptosis. The development of models required an interdisciplinary approach whereby biology motivated the models and mathematics provided a theoretical and quantitative framework. Often, constructing a model was an iterative process requiring refinement as biological data was obtained. After developing a model, mathematical analysis and numerical techniques were used to gain insights into the mechanisms governing the cellular response.

The two systems of interest, immune response in vascular plaque macrophages and apoptosis, have different functions, yet share similarities. Both responses may be thought of as an all-or-none switch, in the case of macrophage response, it is often characterized by pro- or anti-inflammatory function; similarly, in the context of apoptosis, a cell is either alive or dead. Systems exhibiting this type of qualitative behavior, i.e., changing from one state to another over a given time, are perfect candidates to model and analyze. As a consequence of the inherent complexity of these systems, due to the many protein interactions during signal transduction such as feedback loops, mathematics of nonlinear ODEs offered suitable methods of analysis to study these systems, and as seen in Chapters 4 and 7, the biological system may exhibit bistable behavior. Furthermore, the vascular and apoptosis systems investigated in this thesis presented a number theoretical and biological contributions.

Mathematical models of vascular immune response were developed describing the response of macrophage scavenger receptor CD163 and anti-inflammatory mediators to different stimuli. Simple models were understood analytically and their behavior was characterized, revealing a rich variety of bifurcations. Mechanisms were uncovered within the macrophage scavenger receptor CD163 and its anti-inflammatory response

to Hb:Hp complexes. We specifically predicted the existence of a positive feedback loop between CD163 and IL-10. We also identified that the Hb:Hp responsible for the phenotypic switch occurs at a threshold H^*, which was supported experimentally. It would be useful to extend the work presented here to include the behavior of groups of cells and develop multi-scale models to capture the dynamics at the cell and population level for the monocyte/macrophage lineage. Overall, constructing a number of models allowed the investigation of specific system components and enabled a better understanding of the benefits and limitations of each model and its assumptions. The model development process may serve as an example and provide a theoretical framework for future modeling of cellular mechanisms.

The simple models motivated the development of mechanistic models which included CD163, IL-10 and HO-1 species. Data fitting and model selection was performed using approximate Bayesian computation based on sequential Monte Carlo sampling which determined parameter values and initial conditions; furthermore, ABC-SMC also served as a model discrimination tool. The model selection identified a key mechanism necessary for an anti-inflammatory response; specifically, the existence of a HO-1/IL-10 positive feedback. While this model is rather simple, it provides a first step in understanding the anti-inflammatory effects of hemoglobin and its intermediates and it may be beneficial to include regulators of this response in future models. The parameter inference provided a posterior distribution of estimated parameters which allowed us to identify parameters that fit to the data and those that require additional refinement. Future work requires additional experimentation; ideally, conducted under the same conditions to minimize the prior parameter space. Additionally, the region of bistability of the CD163 system could be enhanced by improving estimation of parameters. Our results also motivate further study of the intracellular mechanisms in this system and others, consider the monocyte differentiation into a M1/M2 lineage macrophage; and this work also serves as another step to understanding the interactions of macrophage anti-inflammatory response.

The full system model of apoptosis, a conglomeration of many existing models, provided novel predictions. The modularized model was created by combining both the extrinsic and intrinsic pathways through the implementation of functional modules and subnetworks motivated by previous models and findings (Eissing *et al*., 2004; Fussenegger *et al*., 2000; Hua *et al*., 2005, 2006; Lai and Jackson, 2004; Legewie *et al*., 2006; Nakabayashi and Sasaki, 2006; Okazaki *et al*., 2008). The subnetworks, responsible for the activation of $\mathrm{Casp3}$ and ultimately apoptosis, included descriptions of both the extrinsic and intrinsic pathways as well as the coupling between them. The model identified key components of the apoptotic network under various cell conditions, despite

the abstraction of activation complexes. This allowed the formulation of reduced models to capture only the essential dynamics of the system. Importantly, these reductions allowed the extraction of biological insight and helped clarify the roles of specific molecular components. The model identified the critical role of the inhibitor XIAP and the shared-inhibitor motif, and characterized the transition from type I to type II apoptosis as the induction of the extrinsic pathway is decreased. Finally, the analysis revealed the variety of modes through which caspase activation can be achieved. In the cases considered, caspase activation was observed to occur

1. solely through the extrinsic pathway;
2. solely through the intrinsic pathway;
3. through the extrinsic triggering the intrinsic pathway; and
4. through the intrinsic triggering the extrinsic pathway.

Whether cells employ all of these modes is an interesting experimental question, with possibly profound biological significance.

The modularized model also presented a methodological construction of a straightforward and informative mathematical model of apoptosis. Modularization of the oligomerization kinetics of the DISC, MAC, and apoptosome were achieved through the implementation of steady-state abstraction techniques. These techniques allowed the system complexity to be reduced; however, the system was no longer bistable as a result of removing the temporal dynamics of oligomerization. Future directions may include exploring model reduction in such a manner that the overall stability of the system is not affected. Despite the instability, modularization enabled the full system to be analyzed for a minimum number of variables and parameters. Sensitivity analysis was conducted using linear regression, which motivated the formulation of reduced models and the study of type I and type II cell mechanisms. As there are now many models describing the full apoptosis signaling pathway, future work must focus on developing the steady-state abstraction in such a way that stability is maintained, that is, allowing a model of apoptosis that is representative of the full system dynamics for different cell types, while maintaining stability. It is hoped, in the future, that modularization through the use of steady-state abstraction, becomes a common method for understanding larger systems and a tool for model reduction.

The work by Scott *et al.*, 2009 (crystallography data that Fas death receptors exist in two states: open and closed, and that Fas can stabilize each other) motivated the

development of a new model to describe the receptor-ligand trimerization, responsible for activating the extrinsic pathway of apoptosis. The pre-existing cross-linking model (Lai and Jackson, 2004) exhibited monostable behavior (the model results of Lai and Jackson, 2004 predicted an optimal ratio of receptor/ligand for activation); however, this hysteron model strongly implicated Fas aggregation, e.g., through trimerization, in generating bistability at the level of the DISC and hypothesized a threshold amount of ligand. The consequence of this result suggested that the switching mechanism in apoptosis may occur as early as at the receptor, rather than during caspase positive feedback loops. This model assumptions of receptor clustering by FasL and of cluster-stabilization of open Fas should hence be verified, ideally by experimentation or by using atomistic simulations, e.g., molecular dynamics. This theoretical and relatively simple model was thoroughly analyzed, and the model bistability was found to be robust. The model was also extended to the cell-level using relay hysterons; furthermore, comparison of this model with the crosslinking model using steady-state invariants derived from Gröbner bases, provided a heuristic for model selection, irrespective of confidence in parameter values. In addition to the strong mathematical analysis, this model highlighted the critical role of receptor clustering, particularly in the context of pre-association, which enhances sensitivity to extrinsic apoptosis and additionally is upregulated by localization to lipid rafts (Muppidi *et al*., 2004). The receptor clustering mechanism may also be tested for other death receptors with functional homologues, or intrinsic pathway activators. Future models of Fas signaling are likely to benefit from a spatial component modeling receptor distribution, which, in the continuum limit, generates a system of partial differential equations rather than the simpler ordinary differential equations presently considered.

This thesis attempted to gain a better insight into the mechanisms underlying the biological behavior of macrophage response in the vascular system and the apoptotic machinery responsible for cellular fate. The ability to quantitatively and theoretically realize the behavior of vascular inflammation and apoptosis, as presented in this thesis, may prove useful insight for the development of medical therapies for diseases associated with their dysregulation.

Appendix A

Bistability thresholds and robustness

A.1 Asymptotic analysis

The activation and deactivation thresholds $\lambda_{\pm}$ that define the bistable regime are given by the values of λ at which $\partial\lambda/\partial\zeta_{\infty} = 0$. As mentioned in Sec. 7.3.1, we restricted to the biological context of $n = 3$ and further fixed $\theta = 0$. Thus, solving $d\zeta/d\tau = 0$ gives

$$\lambda = f_{\lambda}\left(\zeta_{\infty}\right) \equiv \frac{p_{\lambda}\left(\zeta_{\infty}\right)}{q_{\lambda}\left(\zeta_{\infty}\right)},$$

where p_{λ} and q_{λ} are polynomials of degrees two and three, respectively, hence

$$\frac{\partial\lambda}{\partial\zeta_{\infty}} = f_{\partial\lambda/\partial\zeta}\left(\zeta_{\infty}\right) \equiv \frac{p_{\partial\lambda/\partial\zeta}\left(\zeta_{\infty}\right)}{q_{\partial\lambda/\partial\zeta}\left(\zeta_{\infty}\right)},$$

where $p_{\partial\lambda/\partial\zeta}$ and $q_{\partial\lambda/\partial\zeta}$ are polynomials of degrees four and six, respectively. Since we are concerned with $\partial\lambda/\partial\zeta_{\infty} = 0$, only $p_{\partial\lambda/\partial\zeta}$ was considered in solving for $\lambda_{\pm}$. The strategy then is to solve $p_{\partial\lambda/\partial\zeta}$ for the Fas thresholds $\zeta_{\pm}$, then to compute $\lambda_{\pm} = f_{\lambda}(\zeta_{\pm})$.

In the asymptotic limit

$$\alpha = \mathcal{O}\left(\frac{1}{\varepsilon}\right), \quad \beta, \gamma = \mathcal{O}\left(1\right), \quad \delta = \mathcal{O}\left(\varepsilon\right) \tag{A.1}$$

for $\varepsilon \ll 1$,

$$p_{\lambda}\left(\zeta\right) \sim -\alpha^2\beta\zeta^2 - \alpha^2\left(\alpha\delta - \beta\right)\zeta + 2\alpha\beta, \quad q_{\lambda}\left(\zeta\right) \sim \alpha^2\gamma\zeta^3 - \alpha^2\left(\gamma - 1\right)\zeta^2 - \alpha^2\zeta - 2\alpha,$$

	$c_4 = \mathcal{O}(\varepsilon^{4\nu-4})$	$c_3 = \mathcal{O}(\varepsilon^{3\nu-4})$	$c_2 = \mathcal{O}(\varepsilon^{2\nu-4})$	$c_1 = \mathcal{O}(\varepsilon^{\nu-3})$	$c_0 = \mathcal{O}(\varepsilon^{-3})$
c_4	—	0	0	$1/3$	$1/4$
c_3		—	0	$1/2$	$1/3$
c_2			—	1	$1/2$
c_1				—	0
c_0					—
1	0	-1	-2	-2	-3
$(1/2)$	-2	$-5/2$	(-3)	$-5/2$	(-3)
$1/3$	$-8/3$	-3	$-10/3$	$-8/3$	-3
$1/4$	-3	$-13/4$	$-7/2$	$-11/4$	-3
(0)	(-4)	(-4)	(-4)	-3	-3

Table A.1: Order balance of $p_{\partial\lambda/\partial\zeta} = \sum_{i=0}^{4} c_i \zeta_\infty^i$. Top, critical values of ν, where $\zeta_\infty = \mathcal{O}(\varepsilon^\nu)$ for $\varepsilon \ll 1$, balancing each pair of terms in $p_{\partial\lambda/\partial\zeta}$; bottom, corresponding ε-exponent of the order of each term. Admissible balances are enclosed in parenthesis.

and

$$p_{\partial\lambda/\partial\zeta}(\zeta) \sim \alpha^4\beta\gamma\zeta^4 + 2\alpha^4(\alpha\delta - \beta)\gamma\zeta^3 - \alpha^2[(\alpha\delta - \beta)\gamma - \alpha\delta]\zeta^2 + 4\alpha^3\beta\gamma\zeta + 2\alpha^4\delta$$

on asympotically expanding each coefficient. Thus, suppose that $\zeta_\infty = \mathcal{O}(\varepsilon^\nu)$ and find the critical values of ν that balance the orders of each pair of terms in $p_{\partial\lambda/\partial\zeta}$. Clearly, the values of ν such that only one dominant term exists must be discounted, hence the admissible values $\nu = 0$ and $1/2$ (Table A.1) have been obtained.

For $\nu = 1/2$,

$$p_{\partial\lambda/\partial\zeta}(\zeta) \sim -\alpha^4\gamma(\alpha\delta - \beta)\delta\zeta^2 + 2\alpha^4\delta,$$

so

$$\zeta_+ \sim \sqrt{\frac{2\Delta}{\alpha[\gamma(\Delta - 1) - \Delta]}} \tag{A.2}$$

is the unique nonnegative root, provided that $\gamma > 1$ and $\Delta > \gamma/(\gamma - 1)$, where, recall,

$$\Delta = \frac{\alpha\delta}{\beta} = \mathcal{O}(1) \tag{A.3}$$

is the relative intrinsic deactivation strength. Similarly, for $\nu = 0$,

$$p_{\partial\lambda/\partial\zeta}(\zeta) \sim \alpha^4\beta\gamma\zeta^4 + 2\alpha^4(\alpha\delta - \beta)\gamma\zeta^3 - \alpha^4[(\alpha\delta - \beta)\gamma - \alpha\delta]\zeta^2,$$

so

$$\zeta_- \sim \sqrt{\frac{\Delta\Theta}{\gamma}} - (\Delta - 1), \tag{A.4}$$

where

$$\Theta = \gamma(\Delta - 1) - 1 = \mathcal{O}(1), \tag{A.5}$$

which exists if $\Theta \geq 0$, i.e., $\Delta \geq 1 + 1/\gamma$; note that the trivial root $\zeta_\infty \sim 0$ of multiplicity two recovers the solutions of order $\mathcal{O}(\sqrt{\varepsilon})$. As physical intuition demands, $p_{\partial\lambda/\partial\zeta}$ has at most two nonnegative roots, which both exist if

$$\Delta > \Delta^* \equiv \max\left\{\frac{\gamma}{\gamma - 1}, \frac{\gamma + 1}{\gamma}\right\} > 1, \tag{A.6}$$

given $\gamma > 1$.

Clearly, the $\zeta_\pm$ give, under the map f_λ, the activation and deactivation thresholds $\lambda_\pm$, respectively. Proceeding first with $\zeta_+ = \mathcal{O}(\sqrt{\varepsilon})$,

$$p_\lambda(\zeta_+) \sim -\alpha^2(\alpha\delta - \beta)\zeta_+, \quad q_\lambda(\zeta_+) \sim -\alpha^2\zeta_+,$$

so

$$\lambda_+ = f_\lambda(\zeta_+) \sim \beta(\Delta - 1). \tag{A.7}$$

Similarly, for $\zeta_- = \mathcal{O}(1)$,

$$p_\lambda(\zeta_-) \sim -\alpha^2\beta\zeta_-^2 - \alpha^2(\alpha\delta - \beta)\zeta_-, \quad q_\lambda(\zeta_-) \sim \alpha^2\gamma\zeta_-^3 - \alpha^2(\gamma - 1)\zeta_-^2 - \alpha^2\zeta_-,$$

so

$$\lambda_- = f_\lambda(\zeta_-) \sim \frac{\beta}{\gamma\Delta + \Theta - 2\sqrt{\gamma\Delta\Theta}}, \tag{A.8}$$

which, in particular, is positive if $\Theta \geq 0$ as, in this case, the nontrivial positivity condition

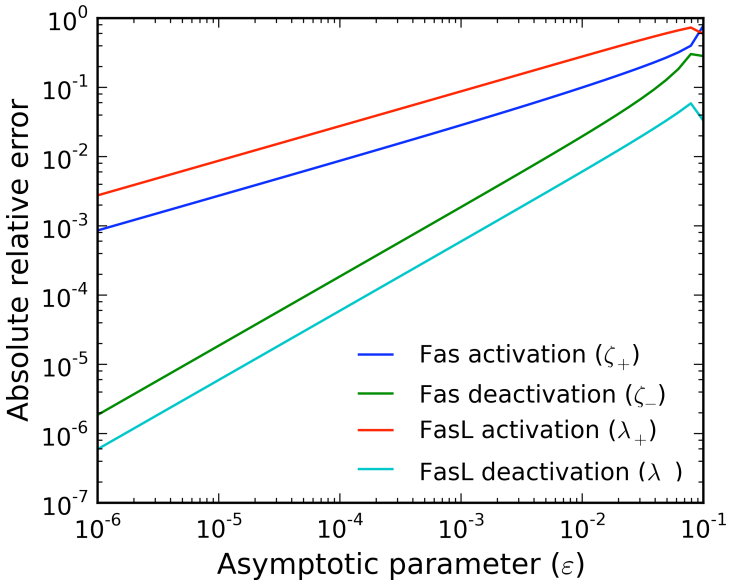

Figure A.1: Relative errors of approximation of the asymptotic forms. Relative errors of approximation of the asymptotic forms of the Fas and FasL thresholds $\zeta_\pm$ and $\lambda_\pm$, respectively, with respect to the numerically computed thresholds.

is

$$\sqrt{\frac{\gamma\Delta}{\Theta}} + \sqrt{\frac{\Theta}{\gamma\Delta}} > 2,$$

which is satisfied since $\Theta = \gamma\Delta - (\gamma+1) < \gamma\Delta$, so $\gamma\Delta/\Theta \neq 1$. Therefore, all thresholds $\zeta_\pm$ and $\lambda_\pm$ are real and nonnegative if (A.6) holds.

The accuracy of the asymptotic forms of $\zeta_\pm$ and $\lambda_\pm$ were verified by letting

$$\alpha = \frac{5}{\varepsilon}, \quad \beta = 1, \quad \gamma = 5, \quad \delta = \varepsilon$$

(so that the baseline is achieved with $\varepsilon = 10^{-2}$) and comparing with the numerically computed thresholds over $10^{-6} \leq \varepsilon \leq 10^{-1}$. The results confirm the analysis and furthermore reveal that ζ_+ and λ_+ have relative approximation errors of $\mathcal{O}(\sqrt{\varepsilon})$; and ζ_- and λ_-, $\mathcal{O}(\varepsilon)$ (Fig. A.1).

A.2 Threshold variation data statistics

The statistics of the threshold variation data (Dataset 1; $N = 10^3$, $\chi = 0.25$) are observed to match well with expectations and furthermore reveal the effect of total parameter vari-

	Quantity	Maximum	Minimum	Median	Norm. std. dev.
parameters	α	1116.760	225.184	505.387	0.252
	β	2.086	0.453	1.007	0.252
	γ	10.859	1.887	4.989	0.254
	δ	0.023	0.005	0.010	0.250
thresholds	λ_+	11.020	0.636	3.258	0.504
	λ_-	8.297	0.579	2.482	0.480

Table A.2: Parameter and threshold statistics for threshold variation data (Dataset 1). The data comprise $N = 10^3$ trials drawn by independently sampling each parameter from a log-normal distribution with a scaled standard deviation of $\chi = 0.25$ about its baseline median value. Bistability thresholds were computed numerically for each parameter set, with statistics computed only over bistable sets.

Threshold	Parameter	Correlation
λ_+	α	$+0.724982$
	β	-0.148639
	γ	-0.168286
	δ	$+0.638670$
	Δ	$+0.855905$
λ_-	α	$+0.663543$
	β	-0.105978
	γ	-0.404652
	δ	$+0.620883$
	Δ	$+0.783721$

Table A.3: Parameter-threshold correlations for threshold variation data (Dataset 1). Correlations were computed only over bistable parameter sets.

ation on the bistability thresholds $\lambda_\pm$ (Table A.2). Moreover, parameter-threshold correlations suggest that both $\lambda_\pm$ are relatively insensitive to β, with λ_+ being additionally robust to γ (Table A.3).

A.3 Discrete variation analysis for robustness of bistability

In Sec. 7.3.2 Dataset 2 was described that suggested convergence of the bistable fraction to 0.5 as the magnitude of parameter variation $\chi \to \infty$. This asymptotic value may be explained using a very simple discrete analysis. Characterize the variation of each parameter as either greater or less than the baseline, and assume that all variation is identical in proportion. Propagate changes in α, β, and δ to Δ using (A.3), and further assume that

Parameter	Variation							
α	$+$	$+$	$+$	$+$	$-$	$-$	$-$	$-$
β	$+$	$+$	$-$	$-$	$+$	$+$	$-$	$-$
δ	$+$	$-$	$+$	$-$	$+$	$-$	$+$	$-$
Δ	$+$	$-$	$+$	$+$	$-$	$-$	$+$	$-$

Table A.4: Discrete variation analysis for robustness of bistability. All variation is independent and assumed binary ($+/-$, above/below baseline), identical in proportion, and large ($\Delta > \Delta^*$ if $+$; $\Delta < \Delta^*$ if $-$). Variations are propagated through $\Delta = \alpha\delta/\beta$, which predicts a 50% bistable fraction, assuming that $\gamma > 1$.

variation is large so that $\Delta > \Delta^*$ if the net result is an overall increase, and $\Delta < \Delta^*$ if a decrease (Table A.4); recall that, given $\gamma > 1$, $\Delta > \Delta^*$ is the asymptotic bistability condition, which has been validated against the threshold variation data (Dataset 1). Since the baseline values are also the median values of the parameter distributions, each variation occurs independently with probability $1/2$, so each outcome is equally likely. Therefore, assuming that $\gamma > 1$, the bistable fraction (Δ with $+$ variation) is also $1/2$.

Appendix B

Comparison with the crosslinking model

B.1 Solution of crosslinking model

From Sec. 7.3.4, the steady-state FasL-Fas complex concentrations are

$$\gamma_{1,\infty} = 3\lambda_\infty \left(\frac{\rho_\infty}{\kappa}\right), \quad \gamma_{2,\infty} = 3\lambda_\infty \left(\frac{\rho_\infty}{\kappa}\right)^2, \quad \gamma_{3,\infty} = \lambda_\infty \left(\frac{\rho_\infty}{\kappa}\right)^3, \tag{B.1}$$

so apply ligand conservation, i.e., $\lambda_0 = \lambda + \gamma_1 + \gamma_2 + \gamma_3$, at steady-state to obtain

$$\lambda_\infty = \frac{\lambda_0}{1 + 3\left(\rho_\infty/\kappa\right) + 3\left(\rho_\infty/\kappa\right)^2 + \left(\rho_\infty/\kappa\right)^3}, \tag{B.2}$$

where ρ_∞ is given by applying receptor conservation, i.e., $1 = \rho + \gamma_1 + 2\gamma_2 + 3\gamma_3$, and solving

$$\rho_\infty^4 + \left(3\lambda_0 + 3\kappa - 1\right)\rho_\infty^3 + 3\kappa\left(2\lambda_0 + \kappa - 1\right)\rho_\infty^2 + \kappa^2\left(3\lambda_0 + \kappa - 3\right)\rho - \kappa^3 = 0,$$

which has the unique nonnegative root

$$\rho_\infty = \frac{1}{2}\left[\sqrt{\left(3\lambda_0 + \kappa - 1\right)^2 + 4\kappa} - \left(3\lambda_0 + \kappa - 1\right)\right]. \tag{B.3}$$

B.2 Steady-state invariants

A brief overview of the relevant mathematics is given; for details, see, e.g., Cox *et al.*, 1997.

Let $\boldsymbol{f} = (f_1, \ldots, f_m) \in K[\boldsymbol{x}]$ be a system of polynomials in $\boldsymbol{x} = (x_1, \ldots, x_n)$ with coefficients from a field K. For this context, $\boldsymbol{f}$ is a set of mass-action dynamics, where $\boldsymbol{x}$ is a set of species concentrations, and K is, e.g., the real numbers $\mathbb{R}$; or the field $\mathbb{R}(\boldsymbol{a})$ of rational functions in the kinetic parameters $\boldsymbol{a} = (a_1, \ldots, a_k)$ with coefficients in $\mathbb{R}$; or the field $\mathbb{Z}(\boldsymbol{a})$ of rational functions in $\boldsymbol{a}$ with coefficients in the integers $\mathbb{Z}$. Consider the variety $V = \{\boldsymbol{x} \in K^n : \boldsymbol{f}(\boldsymbol{x}) = \boldsymbol{0}\}$ on which $\boldsymbol{f}$ vanishes—this is simply the set of steady-states of $\boldsymbol{f}$—and let $I = \langle \boldsymbol{f} \rangle$ be the ideal generated by $\boldsymbol{f}$, containing all polynomials of the form $\sum_{i=1}^{m} f_i h_i$, where the $h_i \in K[\boldsymbol{x}]$ are arbitrary polynomials. Clearly, I consists of all polynomials in $K[\boldsymbol{x}]$ that vanish on V. Thus, I is invariant on and hence characterizes V, in particular, through the requirement that for any $\boldsymbol{x} \in V$, $h(\boldsymbol{x}) = 0$ for all $h \in I$.

The elements $f_1, \ldots, f_m$ of $\boldsymbol{f}$ form a basis for I. This basis is not unique; notably, may be expressed $I = \langle \boldsymbol{g} \rangle$ in terms of a Gröbner basis $\boldsymbol{g} = (g_1, \ldots, g_l)$, which has particularly useful properties, chief among them, for this application, the *elimination property*, which states that, relative to the lexicographic ordering $x_1 > \cdots > x_n$, the elimination ideal $\tilde{I} = I \cap K[\tilde{\boldsymbol{x}}]$ of I containing only the variables $\tilde{\boldsymbol{x}} = (x_{i+1}, \ldots, x_n)$ is simply $\tilde{I} = \langle \boldsymbol{g} \cap K[\tilde{\boldsymbol{x}}] \rangle$. Gröbner bases thus give a straightforward method of computing elimination ideals, which may be useful, for example, if the concentrations of certain molecular species $x_1, \ldots, x_i$ cannot be measured experimentally and hence, in principle, must remain unknown. The generators $\tilde{\boldsymbol{g}} = \boldsymbol{g} \cap K[\tilde{\boldsymbol{x}}]$ of $\tilde{I}$ then constitute experimentally measurable steady-state invariants of the system, i.e., $\tilde{\boldsymbol{g}}(\tilde{\boldsymbol{x}}) = \boldsymbol{0}$ for all $\tilde{\boldsymbol{x}} \in \tilde{V}$, where $\tilde{V}$ is the projection of V onto the coordinates $\tilde{\boldsymbol{x}}$.

In the current context, since $\boldsymbol{f}$ comes from mass action, then $K = \mathbb{Z}(\boldsymbol{a})$, thus treating parameters symbolically and hence allowing the derivation of invariants valid for all choices of $\boldsymbol{a}$.

Gröbner bases are a standard tool in computational algebraic geometry and can be computed by many software packages, including Maple (Waterloo Maple Inc., Waterloo, Ontario, Canada), Mathematica (Wolfram Research, Inc., Champaign, IL, USA), and Sage (http://www.sagemath.org/).

Steady-state invariants for the hysteron and crosslinking models were computed as outlined in the Materials and methods using Sage (http://www.sagemath.org/), giving

$$\omega_{\mathrm{H}}(\lambda_0, \zeta) = c_{13}\lambda_0\zeta^3 + c_{12}\lambda_0\zeta^2 + c_{11}\lambda_0\zeta + c_{02}\zeta^2 + c_{10}\lambda_0 + c_{01}\zeta + c_{00}, \tag{B.4}$$

where

$$
\begin{aligned}
c_{13} &= -\alpha^2\gamma - 2\gamma, \\
c_{12} &= \alpha^2(\gamma - 1) - 2\alpha\gamma + 6\gamma + 1, \\
c_{11} &= \alpha^2 + 2\alpha(\gamma - 1) - (7\gamma + 3) \\
c_{02} &= -\alpha^2\beta + \beta, \\
c_{10} &= 2\alpha + 3\gamma + 2, \\
c_{01} &= -\alpha^2(\alpha\delta - \beta) - \alpha(3\alpha\delta + 2\beta) - 3(\alpha\delta + \beta) - \delta, \\
c_{00} &= 2\alpha\beta + 2\beta,
\end{aligned}
$$

and

$$
\omega_{\mathrm{C}}(\lambda_0, \zeta) = 3\lambda_0\zeta - \zeta^2 - 3\lambda_0 + (\kappa + 1)\zeta, \tag{B.5}
$$

respectively. Correctness of ω_{H} may be shown by observing that $\omega_{\mathrm{H}}/\zeta_\tau = (\alpha + 1)^3$ is constant under the identification $\lambda = \lambda_0$; similarly, the correctness of ω_{C} is demonstrated by verifying that $\omega_{\mathrm{C}} = 0$ for $\zeta = \gamma_{1,\infty} + 2\gamma_{2,\infty} + 3\gamma_{3,\infty}$.

B.3 Nonnegative least squares for model discrimination

To cast the optimization of ω_{H} and ω_{C} into nonnegative least squares (NNLS) form, the problem was linearized by considering ω_{H} and ω_{C} as functions of

$$
\boldsymbol{x}_{\mathrm{H}} = \left(-\lambda_0\zeta^3,\ \lambda_0\zeta^2,\ \lambda_0\zeta,\ -\zeta^2,\ \lambda_0,\ -\zeta,\ 1\right), \quad \boldsymbol{x}_{\mathrm{C}} = \zeta,
$$

respectively. Then, given experimental data $U = (\lambda_0, \zeta_\infty)$, we may write

$$
\omega(U; c) = Uc(\boldsymbol{a}) - b(U), \tag{B.6}
$$

suppressing model reference for generality, where U is a row vector corresponding to the data represented in terms of the variables $\boldsymbol{x}$; $c(\boldsymbol{a})$ is a column vector of nonnegative coefficients in the model parameters $\boldsymbol{a}$ to be determined, constrained by the limit (A.1) with $\Delta > 1$; and b is a column vector of constants given the data. For the hysteron model,

$$
c_{\mathrm{H}} \in \mathbb{R}^7_+, \quad b_{\mathrm{H}} = -\lambda_0\zeta^2 + 3\lambda_0\zeta - 2\lambda_0,
$$

where subscript notation has been used in the obvious manner and $\mathbb{R}_+$ denotes the nonnegative real numbers, while for the crosslinking model,

$$c_{\mathrm{C}} \in \mathbb{R}_+, \quad b_{\mathrm{C}} = -3\lambda_0\zeta + \zeta^2 + 3\lambda_0 - \zeta.$$

For many experimental trials, U is considered instead as a matrix, with each row denoting an individual sample, so that $\omega(U; c) = 0$ now gives an overdetermined system. This leads to a natural least squares problem for $\epsilon = \|\omega\| = \|Uc - b\|$ as a function of c, which in particular is in NNLS form given the nonnegativity of c. A significant advantage of NNLS over direct nonlinear optimization is that ϵ is minimized exactly, producing an error that is indeed a global minimum (Lawson and Hanson, 1995).

B.4 Performance of model discrimination

As described in Sec. 7.3.4, the NNLS formulation for model discrimination was tested, using $N = 100$ samples generated from each model (Datasets 3 and 4), chosen based on the dimensions of c_{H} and c_{C}. The results show that errors are low if the models underlying the data generation and the invariant minimization are the same, and large otherwise. Note that NNLS provides a lower bound to the cross-model errors due to the introduction of additional degrees of freedom for linearization. Furthermore, it is remarked that the crosslinking-crosslinking optimization was able to recover the coefficient $\kappa + 1$ of ζ in ω_{C}.

To verify that these results should hold generally, the distributions of the data λ_0 and ζ_∞ were analyzed (Fig. B.1). The data are clearly nondegenerate, thus it is believed that the results are representative.

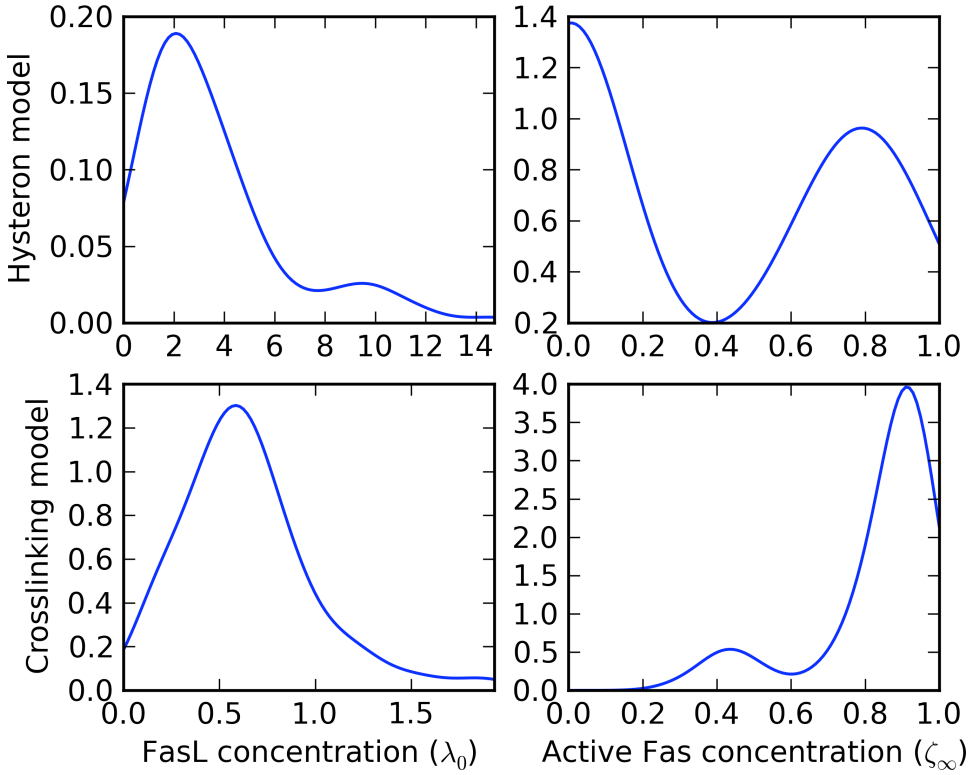

Figure B.1: Distributions of the invariant measurables λ_0, the total FasL concentration, and ζ_∞, the steady-state active Fas concentration, for data generated from the hysteron and crosslinking models (Datasets 3 and 4).

Appendix C

SBML implementation

C.1 Model definition

The hysteron and hysteron-caspase models with $n = 3$ were implemented in dimensional form using the Systems Biology Markup Language (SBML) Level 2 Version 1 (Finney and Hucka, 2003; Hucka *et al*., 2003) and are named `hysteron.xml` and `hysteron-caspase.xml`, respectively.

Corresponding dimensional baseline parameters were used, though $k_4 = 0$ ($\theta = 0$) was not restricted as in the nondimensional case (Table **??**). Initial concentrations (Table C.1) were estimated from the literature (Albeck *et al*., 2008a,b; Bagci *et al*., 2006; Bentele *et al*., 2004; Eissing *et al*., 2004; Harrington *et al*., 2008; Hua *et al*., 2005; Legewie *et al*., 2006; Okazaki *et al*., 2008; Rangamani and Sirovich, 2007), though it should be noted that substantial variation exists (see Svingen *et al*., 2004). Time course simulation of the models validates their definition (Fig. C.1).

The SBML models are demonstrated below by using standard SBML-compliant software (see Bergmann and Sauro, 2006).

C.2 Sensitivity analysis

Sensitivity analysis of the hysteron model was performed with respect to the steady-state by using openly available toolboxes such as SBML-SAT (Zi *et al*., 2008) and SBTOOLBOX2 (Schmidt and Jirstrand, 2006). Local sensitivity analysis was conducted using SBML-SAT with a perturbation coefficient of 0.01 about baseline parameters (Tables **??** and C.1). The results highlight the importance of the parameters l, the FasL concentration; $k_{\pm 1}$, the rates of constitutive receptor closing and opening, respectively; k_4, the rate of ligand-induced receptor opening; and x_0, the initial Fas concentration (Fig. C.2A).

Model	Species	Initial condition (nM)
hysteron	X	10
	Y	0
	Z	0
	L	0.2 (0.1)
caspase	Casp8	100
	Casp8*	0
	Casp3	100
	Casp3*	0

Table C.1: Initial concentrations for the SBML implementations of the hysteron and hysteron-caspase models. For sensitivity analyses, the FasL (L) concentration was set to $l = 0.1$ nM (within the bistable regime). FasL is considered a species only nominally and is otherwise treated as a parameter.

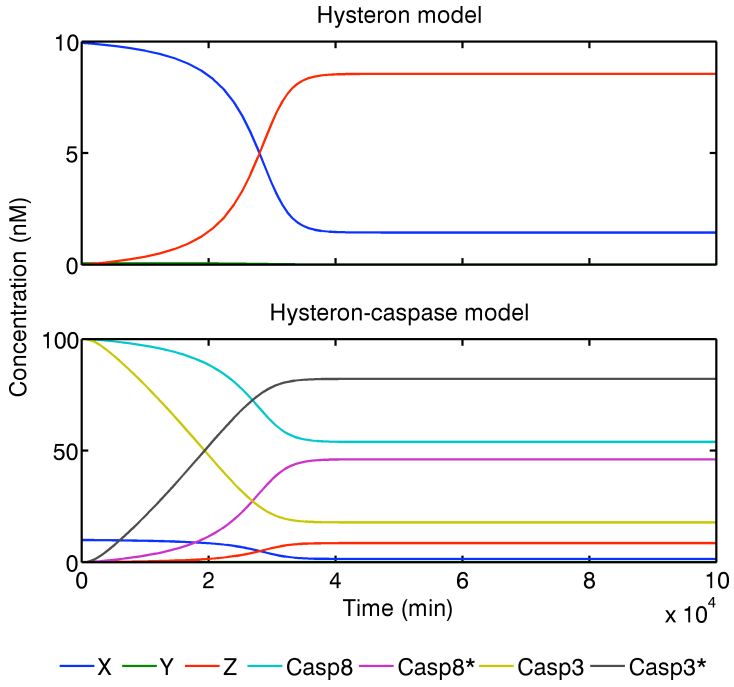

Figure C.1: Time courses of SBML hysteron and hysteron-caspase models at baseline parameters and initial conditions (Tables **??** and C.1).

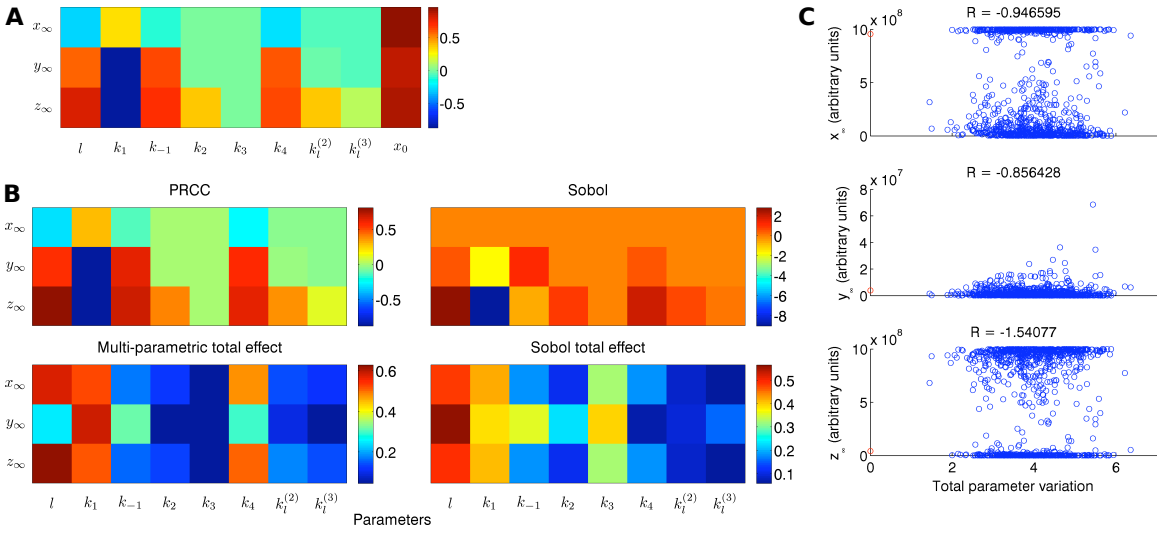

Figure C.2: Sensitivity and robustness analysis of the hysteron model with respect to the steady-state using SBML-SAT. Baseline values as reference (Tables **??** and C.1). (**A**) Local sensitivity analysis using a perturbation coefficient of 0.01. (**B**) Global sensitivity analysis using partial correlation coefficient analysis (PRCC), Sobol's method, and multi-parametric sensitivity analysis. Parameters were perturbed over five orders of magnitude ($N = 2 \times 10^3$ simulations). (**C**) Robustness analysis using $N = 10^3$ perturbations.

These corroborate, but do not completely reproduce, the nondimensional analysis.

Global sensitivity analyses were also performed. Methods employed include partial rank correlation coefficient analysis (PRCC), Sobol's method, multi-parametric sensitivity analysis (MPSA), weighted average of local sensitivities (WALS), and the Fourier amplitude sensitivity test (FAST). Briefly, PRCC is based on multiple linear regression, Sobol and FAST are variance-decomposition methods, MPSA uses a classifier-based discrimination scheme, and WALS extends local sensitivity analysis; for details, see Bentele *et al*. (2004); Chan *et al*. (1997); Marino *et al*. (2008); Saltelli *et al*. (2005); Sobol' (2001); Turányi (1990); Zheng and Rundell (2006); Zi *et al*. (2005). Total effect sensitivities account for combinatorial parameter effects. Analyses performed using both SBML-SAT and SBTOOLBOX2 exhibit general consistency in emphasizing the parameters l, $k_{\pm 1}$, and k_4 (Figs. C.2B and C.3).

C.3 Robustness analysis

Robustness analysis was also conducted using SBML-SAT. The robustness is defined as

$$R = -\frac{1}{N}\sum_{i=1}^{N}\left|\log_{10}\left(\frac{\tilde{f}_i}{f}\right)\right|, \tag{C.1}$$

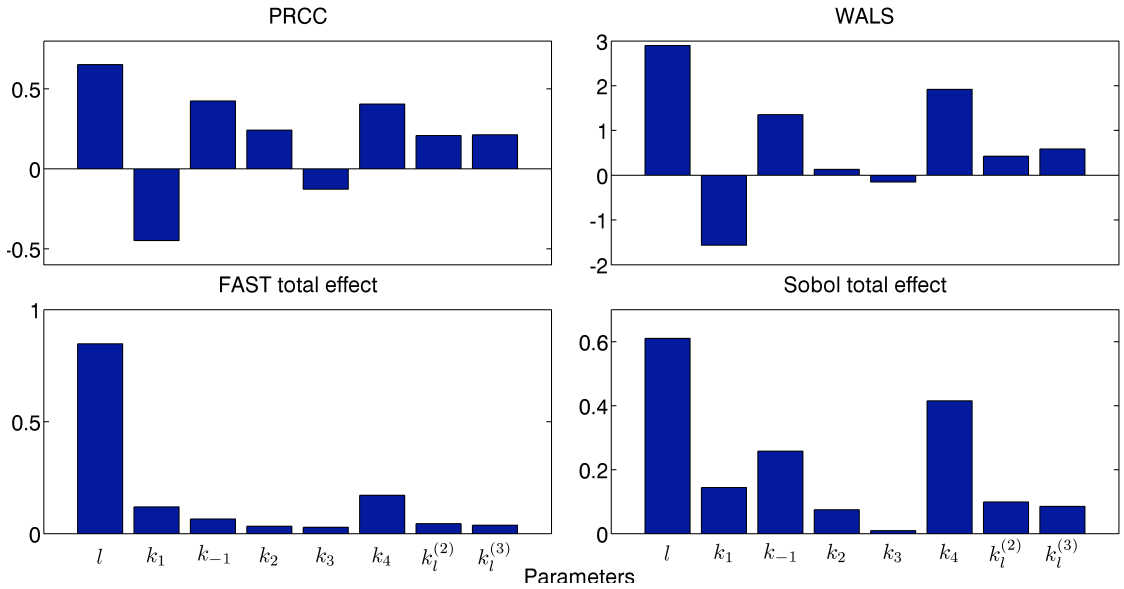

Figure C.3: Global sensitivity analysis of the hysteron model with respect to the steady-state using SBTOOLBOX2. Baseline values as reference (Tables **??** and C.1). Parameters were perturbed over five orders of magnitude ($N = 2 \times 10^3$ simulations for PRCC, FAST, and Sobol; $N = 10^3$ for WALS).

where f is the reference model output, $\tilde{f}_i$ is the perturbed model output of parameter set i, and N is the number of randomly generated parameter sets (see Kitano, 2007). Note that $R \leq 0$; the closer that R is to zero, the more robust the system. Parameter generation was done using Latin hypercube sampling, with each parameter set characterized by the total parameter variation

$$\text{TPV} = \sum_{i=1}^{M} \left| \log_{10} \left(\frac{\tilde{k}_i}{k_i} \right) \right|, \tag{C.2}$$

where k_i and $\tilde{k}_i$ are the reference and perturbed values of parameter i, and M is the number of model parameters. For details, see Barkai and Leibler, 1997; Blüthgen and Herzel, 2003; Zi and Sun, 2005. Results exhibit a double-banded structure for the steady-state concentrations x_∞ and z_∞, demonstrating robustness in the context of bistability (Fig. C.2C).

Appendix D

Datasets

Threshold variation (Dataset 1), bistability robustness (Dataset 2), and hysteron and crosslinking model discrimination (Datasets 3 and 4) data are consolidated in space-delimited format (Table D.1), and are named `threshold-variation.txt`, `bistability-robustness.txt`, `hysteron-discrimination.txt`, and `crosslinking-discrimination.txt`, respectively.

Dataset	Column						
	1	2	3	4	5	6	7
1	α	β	γ	δ	λ_+	λ_-	[1]b
2	χ	[2]b.f.					
3	λ^0	ξ^0	η^0	ζ^0	λ_0	ζ_∞	
4	λ^0	ρ^0	γ_1^0	γ_2^0	γ_3^0	λ_0	ζ_∞

Table D.1: Space-delimited format for stored data. Dataset 1, threshold variation; dataset 2, bistability robustness; dataset 3, hysteron model discrimination; dataset 4, crosslinking model discrimination. Notation as in main text; [1]bistable (true/false), and [2]bistable fraction.

References

Abraham, N. G. and Drummond, G. Cd163-mediated hemoglobin-heme uptake activates macrophage ho-1, providing an antiinflammatory function. *Circ Res*, 99(9):911–914, 2006.

Acehan, D., Jiang, X., Morgan, D. G., Heuser, J. E., Wang, X., and Akey, C. W. Three-dimensional structure of the apoptosome: Implications for assembly, procaspase-0 binding, and activation. *Mol Cell*, 9:423–432, 2002.

Adams, J. M. and Cory, S. The bcl-2 protein family: arbiters of cell survival. *Science*, 281(5381):1322–6, 1998.

Aksan, I. and Kurnaz, M. L. A computer-based model for the regulation of mitogen activated protein kinase (mapk) activation. *J Recept Signal Transduct Res*, 23(2-3): 197–209, 2003.

Albeck, J. G., MacBeath, G., White, F. M., Sorger, P. K., Lauffenburger, D. A., and Gaudet, S. Collecting and organizing systematic sets of protein data. *Nat Rev Mol Cell Biol*, 7(11):803–812, 2006.

Albeck, J. G., Burke, J. M., Aldridge, B. B., Zhang, M., Lauffenburger, D. A., and Sorger, P. K. Quantitative analysis of pathways controlling extrinsic apoptosis in single cells. *Mol Cell*, 30(1):11–25, 2008a.

Albeck, J. G., Burke, J. M., Spencer, S. L., Lauffenburger, D. A., and Sorger, P. K. Modeling a snap-action, variable-delay switch controlling extrinsic cell death. *PLoS Biol*, 6(12):2831–52, 2008b.

Alberts, B., Johnson, A., Lewin, J., Raff, M., Roberts, K., and Walter, P. *Molecular biology of the cell*. Garland Science, 2002.

Alcaraz, M. J., Habib, A., Créminon, C., Vicente, A. M., Lebret, M., Lévy-Toledano, S., and Maclouf, J. Heme oxygenase-1 induction by nitric oxide in raw 264.7

macrophages is upregulated by a cyclo-oxygenase-2 inhibitor. *Biochim Biophys Acta*, 1526(1):13–6, 2001.

Aldridge, B. B., Burke, J. M., Lauffenburger, D. A., and Sorger, P. K. Physicochemical modelling of cell signalling pathways. *Nat Cell Biol*, 8(11):1195–1203, 2006.

Alon, U. *An Introduction to Systems Biology: Design Principles of Biological Circuits*. Chapman & Hall/Crc, 2007.

Angeli, D., Ferrell, Jr, J. E., and Sontag, E. D. Detection of multistability, bifurcations, and hysteresis in a large class of biological positive-feedback systems. *Proc Natl Acad Sci U S A*, 101(7):1822–1827, 2004.

Antonsson, B., Montessuit, S., Lauper, S., Eskes, R., and Martinou, J. Bax oligomerization is required for channel-forming activity in liposomes and to trigger cytochrome c release from mitochondria. *Biochem J*, 345:271–278, 2000.

Apgar, J. F., Toettcher, J. E., Endy, D., White, F. M., and Tidor, B. Stimulus design for model selection and validation in cell signaling. *PLoS Comput Biol*, 4(2):e30, 2008.

Arends, M. and Wyllie, A. Apoptosis: mechanisms and roles in pathology. *Int Rev Exp Pathol*, 32:223–254, 1991.

Arnol'd, V. I. *Catastrophe Theory*. Springer-Verlag, Berlin, Germany, 3rd edition, 1992.

Ascenzi, P., Bocedi, A., Visca, P., Altruda, F., Tolosano, E., Beringhelli, T., and Fasano, M. Hemoglobin and heme scavenging. *IUBMB Life*, 57(11):749–759, 2005.

Ashkenazi, A. and Dixit, V. Death receptors: signaling and modulation. *Science*, 281 (5381):1305–1308, 1998.

Atkinson, K. E. *An Introduction to Numerical Analysis*. John Wiley & Sons, 2nd edition, 1988.

Bagci, E. Z., Vodovotz, Y., Billiar, T., Ermentrout, G., and Bahar, I. Bistability in apoptosis: roles of bax, bcl-2, and mitochondrial permeability transition pores. *Biophys J*, 90(5):1546–59, 2006.

Bagowski, C. P. and Ferrell, Jr, J. E. Bistability in the jnk cascade. *Curr Biol*, 11: 1176–1182, 2001.

Balaban, N. Q., Merrin, J., Chait, R., Kowalik, L., and Leibler, S. Bacterial persistence as a phenotypic switch. *Science*, 305(5690):1622–1625, 2004.

Barkai, N. and Leibler, S. Robustness in simple biochemical networks. *Nature*, 387 (6636):913–917, 1997.

Barker, J. A., Schreiber, D. E., Huth, B. G., and Everett, D. H. Magnetic hysteresis and minor loops: Models and experiments. *Proc R Soc Lond A*, 386(1791):251–261, 1983.

Barnhart, B., Alappat, E., and ME, P. The cd95 type i/type ii model. *Semin Immunol*, 15: 185–193, 2003.

Bender, C. M. and Orszag, S. A. *Advanced Mathematical Methods for Scientists and Engineers Asymptotic Methods and Perturbation Theory*. Springer, 1999.

Bentele, M., Lavrik, I., Ulrich, M., Stosser, S., Heermann, D. W., Kalthoff, H., Krammer, P. H., and Eils, R. Mathematical modeling reveals threshold mechanism in cd95-induced apoptosis. *J Cell Biol*, 166(6):839–851, 2004.

Bergmann, F. T. and Sauro, H. M. SBW - a modular framework for systems biology. In Perrone, L. F., Wieland, F. P., Liu, J., Lawson, B. G., Nicol, D. M., and Fujimoto, R. M., editors, *Proceedings of the 2006 Winter Simulation Conference*, pages 1637–1645. Winter Simulation Conference, 2006.

Bhalla, U. S. and Iyengar, R. Emergent properties of networks of biological signaling pathways. *Science*, 283(5400):381–7, 1999.

BioCarta. http://cgap.nci.nih.gov/pathways/biocarta/h_il10pathway. 2010.

Blüthgen, N. and Herzel, H. How robust are switches in intracellular signaling cascades? *J Theor Biol*, 225(3):293–300, 2003.

Boldin, M., Mett, I., Varfolomeev, E., Chumakov, I., Shemer-Avni, Y., and Camonis, J. Self-association of the "death domains" of the p55 tumor necrosis factor (tnf) receptor and fas/apo1 prompts signaling for tnf and fas/apo1 effects. *J Biol Chem*, 270(1): 387–391, 1995.

Boyle, J. J., Harrington, H. A., Piper, E., Elderfield, K., Stark, J., Landis, R. C., and Haskard, D. O. Coronary intraplaque hemorrhage evokes a novel atheroprotective macrophage phenotype. *Am J Pathol*, 174(3):1097–1108, 2009.

Brandman, O., Ferrell, Jr, J. E., Li, R., and Meyer, T. Interlinked fast and slow positive feedback loops drive reliable cell decisions. *Science*, 310(5747):496–498, 2005.

Bray, D., Levin, M. D., and Morton-Firth, C. J. Receptor clustering as a cellular mechanism to control sensitivity. *Nature*, 393(6680):85–8, 1998.

Brewer, D., Barenco, M., Callard, R., Hubank, M., and Stark, J. Fitting ordinary differential equations to short time course data. *Philos Transact A Math Phys Eng Sci*, 366 (1865):519–544, 2008.

Brightman, F. A. and Fell, D. A. Differential feedback regulation of the mapk cascade underlies the quantitative differences in egf and ngf signalling in pc12 cells. *FEBS Lett*, 482(3):169–174, 2000.

Britton, N. F. *Essential Mathematical Biology*. Springer, 2003.

Budihardjo, I., Oliver, H., Lutter, M., Luo, X., and Wang, X. Biochemical pathways of caspase activation during apoptosis. *Ann Rev Cell Dev Biol*, 15:269–290, 1999.

Buechler, C., Ritter, M., Orsó, E., Langmann, T., Klucken, J., and Schmitz, G. Regulation of scavenger receptor cd163 expression in human monocytes and macrophages by pro- and antiinflammatory stimuli. *J Leukoc Biol*, 67(1):97–103, 2000.

Cain, K., Brown, D., Langlais, C., and Cohen, G. Caspase activation involes the formation of the apoptsome, a large ($\sim$700 kda) caspase-activating complex. *J Biol Chem*, 274(32):22686–22692, 1999.

Cain, K., Bratton, S., Langlais, C., Walker, G., Brown, D., Sun, X., and Cohen, G. Apaf-1 oligomerizes into biologically active $\sim$700-kda and inactive $\sim$1.4-mda apoptosome complexes. *J Biol Chem*, 275(9):6067–6070, 2000.

Cain, K., Bratton, S., and Cohen, G. The apaf-1 apoptosome: a large caspase-activating complex. *Biochimie*, 84(2–3):203–214, 2002.

Callard, R., George, A. J. T., and Stark, J. Cytokines, chaos, and complexity. *Immunity*, 11(5):507–513, 1999.

Campbell, N. A. and Reece, J. B. *Biology*. Benjamin Cummings, 6th edition, 2002.

Chan, F. K.-M. Three is better than one: Pre-ligand receptor assembly in the regulation of TNF receptor signaling. *Cytokine*, 37(2):101–107, 2007.

Chan, F. K.-M., Chun, H. J., Zheng, L., Siegel, R. M., Bui, K. L., and Lenardo, M. J. A domain in TNF receptors that mediates ligand-independent receptor assembly and signaling. *Science*, 288(5475):2351–2354, 2000.

Chan, F. K.-M., Siegel, R. M., Zacharias, D. A., Swofford, R., Holmes, K. L., Tsien, R. Y., and Lenardo, M. J. Fluorescence resonance energy transfer analysis of cell surface receptor interactions and signaling using spectral variants of the green fluorescent protein. *Cytometry*, 44(4):361–368, 2001.

Chan, K., Saltelli, A., and Tarantola, S. Sensitivity analysis of model output: variance-based methods make the difference. In Andradóttir, S., Healy, K. J., Withers, D. H., and Nelson, B. L., editors, *Proceedings of the 1997 Winter Simulation Conference*, pages 261–268, Washington, DC, USA, 1997. IEEE Computer Society.

Chang, D. W., Ditsworth, D., Liu, H., Srinivasula, S. M., Alnemri, E. S., and Yang, X. Oligomerization is a general mechanism for the activation of apoptosis initiator and inflammatory procaspases. *J Biol Chem*, 278(19):16466–9, 2003.

Chang, H. and Yang, X. Proteases for cell suicide: Functions and regulation of caspases. *Microbiol Mol Biol Rev*, 64:821–846, 2000.

Chauhan, D., Hideshima, T., Rosen, S., Reed, J., Kharbanda, S., and Anderson, K. Apaf-1/cytochrome c-independent and smac-dependent induction of apoptosis in multiple myeloma (mm) cells. *J Biol Chem*, 276(27):24453–24456, 2001.

Chávez-Ross, A., Franks, S., Mason, H. D., Hardy, K., and Stark, J. Modelling the control of ovulation and polycystic ovary syndrome. *J Math Biol*, 36:95–118, 1997.

Cheng, C., Noordeloos, A. M., Jeney, V., Soares, M. P., Moll, F., Pasterkamp, G., Serruys, P. W., and Duckers, H. J. Heme oxygenase 1 determines atherosclerotic lesion progression into a vulnerable plaque. *Circulation*, 119(23):3017–3027, 2009.

Chinnaiyan, A., O'Rourke, K., Tewari, M., and Dixit, V. Fadd, a novel death domain-containing protein, interacts with the death domain of fas and initiates apoptosis. *Cell*, 81:505–512, 1995.

Conrad, E. http://oscill8.sourceforge.net/doc/. *2008*.

Cowling, V. and Downward, J. Caspase-6 is the direct activator of caspase-8 in the cytochrome c-induced apoptosis pathway: absolute requirement for removal of caspase-6 prodomain. *Cell Death Differ*, 9(10):1046–1056, 2002.

Cox, D., J, L., and D, O. *Ideals, Varieties, and Algorithms: An Introduction to Computational Algebraic Geometry and Commutative Algebra*. Springer-Verlag, New York, NY USA, 3rd edition, 1997.

Crampin, E. J., McSharry, P. E., and Schnell, S. Extracting biochemical reaction kinetics from time series data. *Knowledge-Based Intelligent Information and Engineering Systems, Pt 2, Proceedings*, 3214:329–336, 2004.

Cui, J., Chen, C., Lu, H., Sun, T., and Shen, P. Two independent positive feedbacks and bistability in the bcl-2 apoptotic switch. *PLoS One*, 3(1):e1469, 2008.

Danial, N. and Korsmeyer, S. Cell death critical control points. *Cell*, 116(1):205–219, 2004.

Davies, M. J. and Thomas, A. C. Plaque fissuring–the cause of acute myocardial infarction, sudden ischaemic death, and crescendo angina. *Br Heart J*, 53(4):363–373, 1985.

de Vries, G., Hillen, T., Lewis, M., J.Muller, and Schoenfisch, B. *A Course in Mathematical Biology: Quantitative Modelling with Mathematical and Computational Methods*. Society for Industrial and Applied Mathematics, 2006.

Delisi, C. The biophysics of ligand-receptor interactions. *Q Rev Biophys*, 13(2):201–230, 1980.

Deveraux, Q., Roy, N., Stennicke, H., Van Arsdale, T., Zhou, Q., Srinivasula, S. M., Alnemri, E. S., Salvesen, G. S., and Reed, J. C. Iaps block apoptotic events induced by caspase-8 and cytochrome c by direct inhibition of distinct caspases. *EMBO J*, 17 (8):2215–2223, 1998.

Dhooge, A., Govaerts, W., and Kuznetsov, Y. A. Matcont: A matlab package for numerical bifurcation analysis of odes. *ACM TOMS*, 29:141–164, 2003.

Diekmann, O., Gyllenberg, M., Metz, J., and van der Meer, J. W. Steady-state analysis of structured population models. *Theor Popul Biol*, 63(4):309–38, 2003.

Du, C., Fang, M., Li, Y., Li, L., and Wang, X. Smac, a mitochondrial protein that promotes cytochrome c-dependent caspase activation by eliminating iap inhibition. *Cell*, 102(6):33–42, 2000.

Dzeroski, S. and Todorovski, L. Equation discovery for systems biology: finding the structure and dynamics of biological networks from time course data. *Curr Opin Biotechnol*, 19(4):360–368, 2008.

Edelstein-Keshet, L. *Mathematical Models In Biology*. Society for Industrial and Applied Mathematics, 2004.

Eissing, T., Conzelmann, H., Gilles, E. D., Allgöwer, F., Bullinger, E., and Scheurich, P. Bistability analyses of a caspase activation model for receptor-induced apoptosis. *J Biol Chem*, 279(35):36892–7, 2004.

Eissing, T., Allgower, F., and Bullinger, E. Robustness properties of apoptosis models with respect to parameter variations and intrinsic noise. *IEE Proc Syst Biol*, 152(4): 221–8, 2005.

Ellner, S. P. and Guckenheimer, J. *Dynamic Models in Biology*. Princeton University Press, 2006.

Endres, R. G., Oleksiuk, O., Hansen, C. H., Meir, Y., Sourjik, V., and Wingreen, N. S. Variable sizes of escherichia coli chemoreceptor signaling teams. *Mol Syst Biol*, 4: 211, 2008.

Ermentrout, G. B. http://www.math.pitt.edu/ bard/xpp/download.html. 2009.

Eskes, R., Desagher, S., Antonsson, B., and Martinou, J. Bid induces the oligomerization and insertion of bax into the outer mitochondrial membrane. *Mol Cell Biol*, 20(3):929–935, 2000.

Fadeel, B., Orrenius, S., and Zhivotovsky, B. Apoptosis in human disease: a new skin for the old ceremony? *Biochem Biophys Res Commun*, 266:699–717, 1999.

Faugère, J.-C. A new efficient algorithm for computing Gröbner bases (F4). *J Pure Appl Algebra*, 139(1-3):61–88, 1999.

Faugère, J.-C. A new efficient algorithm for computing Gröbner bases without reduction to zero (F5). In *Proceedings of the 2002 International Symposium on Symbolic and Algebraic Computation*, International Conference on Symbolic and Algebraic Computation, pages 75–83, New York, NY, USA, 2002. Association for Computing Machinery.

Faugère, J.-C., Hering, M., and Phan, J. The membrane inclusions curvature equations. *Adv Appl Math*, 31(4):643–658, 2003.

Ferrell, Jr, J. E. Self-perpetuating states in signal transduction: positive feedback, double-negative feedback and bistability. *Curr Opin Cell Biol*, 14(2):140–148, 2002.

Ferrell, Jr, J. E. Tripping the switch fantastic: how a protein kinase cascade can convert graded inputs into switch-like outputs. *Trends Biochem Sci*, 21(12):460–466, 1996.

Ferrell, Jr, J. E. How responses get more switch-like as you move down a protein kinase cascade. *Trends Biochem Sci*, 22(8):288–9, 1997.

Ferrell, Jr, J. E. and Machleder, E. M. The biochemical basis of an all-or-none cell fate switch in xenopus oocytes. *Science*, 280(5365):895–898, 1998.

Ferrell, J. E. E. and Xiong, W. Bistability in cell signaling: How to make continuous processes discontinuous, and reversible processes irreversible. *Chaos*, 11(1):227–236, 2001.

Fesik, S. W. Insights into programmed cell death through structural biology. *Cell*, 103 (2):273–282, 2000.

Figueiredo, A. S., Hofer, T., Klotz, C., Sers, C., Hartmann, S., Lucius, R., and Hammerstein, P. Modelling and simulating interleukin-10 production and regulation by macrophages after stimulation with an immunomodulator of parasitic nematodes. *FEBS J*, 276(13):3454–3469, 2009.

Finney, A. and Hucka, M. Systems biology markup language: Level 2 and beyond. *Biochem Soc Trans*, 31(Pt 6):1472–1473, 2003.

Fowler, A. C. *Mathematical Models in the Applied Sciences*. Cambridge University Press, 1997.

Fulda, S., Meyer, E., Friesen, C., Susin, S., Kroemer, G., and Debatin, K. Cell type specific involvement of death receptor and mitochondrial pathways in drug-induced apoptosis. *Oncogene*, 20:1063–1075, 2001.

Fumarola, C. and Guidotti, G. Stress-induced apoptosis: Toward a symmetry with receptor-mediated cell death. *Apoptosis*, 9:77–82, 2004.

Fussenegger, M., Bailey, J., and Varner, J. A mathematical model of caspase function in apoptosis. *Nat Biotechnol*, 18:768–774, 2000.

Garby, L. and Noyes, W. D. Studies on hemoglobin metabolism. i. the kinetic properties of the plasma hemoglobin pool in normal man. *J Clin Invest*, 38:1479–83, 1959.

Gershenfeld, N. A. *For a linearized system, it is commonly known eigenvalues of the Jacobian matrix (either in the operating parameters or the state of the system) can determine connectivity and stability at steady state. The nature of mathematical modeling*. Cambridge University Press, 1999.

Glass, C. and Witztum, J. Atherosclerosis. the road ahead. *Cell*, 104:503–516, 2001.

Glendinning, P. *Stability, instability, and chaos : an introduction to the theory of nonlinear differential equations*. Cambridge : Cambridge University Press, 1995, 1995.

Gordon, S. Alternative activation of macrophages. *Nat Rev Immunol*, 3(1):23–35, 2003.

Gordon, S. and Taylor, P. R. Monocyte and macrophage heterogeneity. *Nat Rev Immunol*, 5(12):953–64, 2005.

Green, D. Apoptotic pathways: paper wraps stone blunts scissors. *Cell*, 102(1):1–4, 2000.

Grimbs, S., Selbig, J., Bulik, S., Holzhutter, H.-G., and Steuer, R. The stability and robustness of metabolic states: identifying stabilizing sites in metabolic networks. *Mol Syst Biol*, 3:146, 2007.

Gruss, H. and Dower, S. Tumor necrosis factor ligand superfamily: involvement in the pathology of malignant lymphomas. *Blood*, 85(12):3378–3404, 1995.

Guetta, J., Strauss, M., Levy, N. S., Fahoum, L., and Levy, A. P. Haptoglobin genotype modulates the balance of th1/th2 cytokines produced by macrophages exposed to free hemoglobin. *Atherosclerosis*, 191(1):48–53, 2007.

Gunsalus, I. C., Sligar, S. G., Nordlund, T., and Frauenfelder, H. Oxygen sensing heme proteins: monoxygenases, myoglobin and hemoglobin. *Adv Exp Med Biol*, 78:37–50, 1977.

Gutenkunst, R. N., Waterfall, J. J., Casey, F. P., Brown, K. S., Myers, C. R., and Sethna, J. P. Universally sloppy parameter sensitivities in systems biology models. *PLoS Comput Biol*, 3(10):1871–1878, 2007.

Haass, C. Apoptosis: Dead end for neurodegeneration? *Nature*, 399(6733):263–267, 1999.

Hansson, G., Libby, P., Schonbeck, U., and Yan, Z. Innate and adaptive immunity in the pathogenesis of atherosclerosis. *Circ Res*, 91:281–291, 2002.

Hansson, G. K. and Libby, P. The immune response in atherosclerosis: a double-edged sword. *Nat Rev Immunol*, 6(7):508–19, 2006.

Harrington, H. A., Ho, K. L., Ghosh, S., and Tung, K. C. Construction and analysis of a modular model of caspase activation in apoptosis. *Theor Biol Med Model*, 5(1):26, 2008.

Hartwell, L. H., Hopfield, J. J., Leibler, S., and Murray, A. W. From molecular to modular cell biology. *Nature*, 402(6761 Suppl):C47–52, 1999.

Hashimoto, S., Suzuki, T., Dong, H. Y., Yamazaki, N., and Matsushima, K. Serial analysis of gene expression in human monocytes and macrophages. *Blood*, 94(3):837–44, 1999.

Hatakeyama, M., Kimura, S., Naka, T., Kawasaki, T., Yumoto, N., Ichikawa, M., Kim, J.-H., Saito, K., Saeki, M., Shirouzu, M., Yokoyama, S., and Konagaya, A. A computational model on the modulation of mitogen-activated protein kinase (mapk) and akt pathways in heregulin-induced erbb signalling. *Biochem J*, 373(Pt 2):451–463, 2003.

Hayot, F. and Jayaprakash, C. Nf-kappab oscillations and cell-to-cell variability. *J Theor Biol*, 240(4):583–91, 2006.

Heinecke, J. W. Lipoprotein oxidation in cardiovascular disease: chief culprit or innocent bystander? *J Exp Med*, 203(4):813–816, 2006.

Heinrich, R. and Schuster, S. *The Regulation of Cellular Systems*. Chapman & Hall, 1996.

Hengartner, M. The biochemistry of apoptosis. *Nature*, 407:770–776, 2000.

Higham, D. J. Modeling and simulating chemical reactions. *SIAM Review*, 2008.

Hill, A. V. The possible effects of the aggregation of hte molecules of haemoglobin on its dissociation curves. *J Physiol*, 40(Suppl):iv–vii, 1910.

Hindmarsh, A. C. ODEPACK: a systematized collection of ODE solvers. In Stepleman, R. S., Carver, M., Peskin, R., Ames, W. F., and Vichnevetsky, R., editors, *Scientific Computing*, volume 1 of *IMACS Transactions on Scientific Computation*, pages 55–64. North-Holland Publishing Co, Amsterdam, The Netherlands, 1983.

Hirata, H., Yoshiura, S., Ohtsuka, T., Bessho, Y., Harada, T., Yoshikawa, K., and Kageyama, R. Oscillatory expression of the bhlh factor hes1 regulated by a negative feedback loop. *Science*, 298(5594):840–843, 2002.

Hodgkin, A. and Huxley, A. A quantitative description of membrane current and its application to conduction and excitation in nerve. *J. Physiol*, 117:500–544, 1952.

Hoekstra, K. A., Godin, D. V., and Cheng, K. M. Protective role of heme oxygenase in the blood vessel wall during atherogenesis. *Biochem Cell Biol*, 82(3):351–9, 2004.

Hofbauer, J. *The theory of evolution and dynamical systems : mathematical aspects of selection / Josef Hofbauer, Karl Sigmund*. Cambridge : Cambridge University Press, 1988.

Höfer, T., Nathanson, H., Löhning, M., Radbruch, A., , and Heinrich, R. Gata-3 transcriptional imprinting in th2 lymphocytes: a mathematical model. *Proc Natl Acad Sci U S A*, 99:9364–9368, 2002.

Hoffmann, A., Levchenko, A., Scott, M. L., and Baltimore, D. The i kappa b-nf-kappa b signaling module: Temporal control and selective gene activation. *Science*, 298(5596): 1241–1245, 2002.

Hooper, L. V., Wong, M. H., Thelin, A., Hansson, L., Falk, P. G., and Gordon, J. I. Molecular analysis of commensal host-microbial relationships in the intestine. *Science*, 291(5505):881–4, 2001.

Hornberg, J. J., Binder, B., Bruggeman, F. J., Schoeberl, B., Heinrich, R., and Westerhoff, H. V. Control of mapk signalling: from complexity to what really matters. *Oncogene*, 24(36):5533–42, 2005.

Howison, S. *Practical applied mathematics: modelling analysis, approximation*. Cambridge Texts in Applied Mathematics, 2005.

Hua, F., Cornejo, M. G., Cardone, M. H., Stokes, C. L., and Lauffenburger, D. A. Effects of bcl-2 levels on fas signaling-induced caspase-3 activation: molecular genetic tests of computational model predictions. *J Immunol*, 175(2):985–995, 2005.

Hua, F., Hautaniemi, S., Yokoo, R., and Lauffenburger, D. A. Integrated mechanistic and data-driven modelling for multivariate analysis of signalling pathways. *J R Soc Interface*, 3(9):515–526, 2006.

Huang, C. Y. and Ferrell, Jr, J. E. Ultrasensitivity in the mitogen-activated protein kinase cascade. *Proc Natl Acad Sci USA*, 93(19):10078–10083, 1996.

Hucka, M., Finney, A., Sauro, H. M., Bolouri, H., Doyle, J. C., Kitano, H., Arkin, A. P., Bornstein, B. J., Bray, D., Cornish-Bowden, A., Cueller, A. A., Dronov, S., Gilles, E. D., Ginkel, M., Gor, V., Goryanin, I. I., Hedley, W. J., Hodgman, T. C., Hofmeyr, J.-H., Hunter, P. J., Juty, N. S., Kasberger, J. L., Kremling, P. J., Kummer, U., Le Novère, N., Loew, L. M., Lucio, D., Mendes, P., Minch, E., Mjolsness, E. D., Nakayama, Y., Nelson, M. R., Nielsen, P. F., Sakurada, T., Schaff, J. C., Shapiro, B. E., Shimizu, T. S., Spence, J. C., Stelling, J., Takahashi, K., Tomita, M., Wagner, J., and Wang, J. The systems biology markup language (SBML): a medium for representation and exchange of biochemical network models. *Bioinformatics*, 19(4):524–531, 2003.

Huhn, R. D., Radwanski, E., Gallo, J., Affrime, M. B., Sabo, R., Gonyo, G., Monge, A., and Cutler, D. L. Pharmacodynamics of subcutaneous recombinant human interleukin-10 in healthy volunteers. *Clin Pharmacol Ther*, 62(2):171–80, 1997.

Hunter, J. D. Matplotlib: A 2D graphics environment. *Comput Sci Eng*, 9(3):90–95, 2007.

Hutchins, J. B. and Barger, S. W. Why neurons die: cell death in the nervous system. *Anat Rec*, 253(3):79–90, 1998.

Idriss, N. K., Blann, A. D., and Lip, G. Y. H. Hemoxygenase-1 in cardiovascular disease. *J Am Coll Cardiol*, 52(12):971–978, 2008.

Immenschuh, S. and Ramadori, G. Gene regulation of heme oxygenase-1 as a therapeutic target. *Biochem Pharmacol*, 60(8):1121–1128, 2000.

Ingolia, N. T. and Murray, A. W. The ups and downs of modeling the cell cycle. *Curr Biol*, 14(18):R771–7, 2004.

Ingram, P. J., Stumpf, M. P. H., and Stark, J. Nonidentifiability of the source of intrinsic noise in gene expression from single-burst data. *PLoS Comput Biol*, 4(10):e1000192, 2008.

Jacobson, M., Weil, M., and Raff, M. Programmed cell death in animal development. *Cell*, 88(3), 1997.

Janes, K. A. and Yaffe, M. B. Data-driven modelling of signal-transduction networks. *Nat Rev Mol Cell Biol*, 7(11):820–828, 2006.

Janes, K. A., Albeck, J. G., Gaudet, S., Sorger, P. K., Lauffenburger, D. A., and Yaffe, M. B. A systems model of signaling identifies a molecular basis set for cytokine-induced apoptosis. *Science*, 310(5754):1646–53, 2005.

Jaqaman, K. and Danuser, G. Linking data to models: data regression. *Nat Rev Mol Cell Biol*, 7(11):813–819, 2006.

Jiang, X. and Wang, X. Cytochrome c-mediated apoptosis. *Ann Rev Biochem*, 73:87–106, 2004.

Jiang, X. and Wang, X. Cytochrome c promotes caspase-9 activation by inducing nucleotide binding to apaf-1. *J Biol Chem*, 275(40):31199–31203, 2000.

Johnstone, R. W., Ruefli, A. A., and Lowe, S. W. Apoptosis: a link between cancer genetics and chemotherapy. *Cell*, 108(2):153–64, 2002.

Keener, J. and Sneyd, J. *Mathematical Physiology*. Springer, 1998.

Kholodenko, B. N. Cell-signalling dynamics in time and space. *Nat Rev Mol Cell Biol*, 7(3):165–176, 2006.

Kholodenko, B. N., Demin, O. V., Moehren, G., and Hoek, J. B. Quantification of short term signaling by the epidermal growth factor receptor. *J Biol Chem*, 274(42):30169–30181, 1999.

Kim, H., Du, F., Fang, M., and Wang, X. Formation of apoptosome is initiated by cytochrome c-induced datp hydrolysis and subsequent nucleotide exchange on apaf-1. *Proc Natl Acad Sci U S A*, 102(49):17545–17550, 2005.

Kitamuro, T., Takahashi, K., Ogawa, K., Udono-Fujimori, R., Takeda, K., Furuyama, K., Nakayama, M., Sun, J., Fujita, H., Hida, W., Hattori, T., Shirato, K., Igarashi, K., and Shibahara, S. Bach1 functions as a hypoxia-inducible repressor for the heme oxygenase-1 gene in human cells. *J Biol Chem*, 278(11):9125–9133, 2003.

Kitano, H. Towards a theory of biological robustness. *Mol Syst Biol*, 3:137, 2007.

Kitano, H. Biological robustness. *Nat Rev Genet*, 5(11):826–37, 2004.

Kitano, H. and Oda, K. Robustness trade-offs and host-microbial symbiosis in the immune system. *Mol Syst Biol*, 2:2006 0022, 2006.

Klipp, E., Nordlander, B., Kruger, R., Gennemark, P., and Hohmann, S. Integrative model of the response of yeast to osmotic shock. *Nat Biotechnol*, 23(8):975–982, 2005.

Kolodgie, F., Gold, H., Burke, A., Fowler, D., Kruth, H., Weber, D., Farb, A., Guerrero, L., Hayase, M., Kutys, R., Narula, J., Finn, A., and Virmani, R. Intraplaque hemorrhage and progression of coronary atheroma. *N Engl J Med*, 349:2316–2325, 2003.

Krishna, S., Jensen, M. H., and Sneppen, K. Minimal model of spiky oscillations in nf-kappa b signaling. *Proc Natl Acad Sci U S A*, 103(29):10840–10845, 2006.

Kristiansen, M., Graversen, J. H., Jacobsen, C., Sonne, O., Hoffman, H. J., Law, S. K., and Moestrup, S. K. Identification of the haemoglobin scavenger receptor. *Nature*, 409 (6817):198–201, 2001.

Kussell, E. and Leibler, S. Phenotypic diversity, population growth, and information in fluctuating environments. *Science*, 309(5743):2075–2078, 2005.

Lacker, H. M. How do ovaries count? *Math Biosci*, 90:305–332, 1988.

Lagarias, J. C., Reeds, J. A., Wright, M. H., and Wright, P. E. Convergence properties of the nelder–mead simplex method in low dimensions. *SIAM Journal on Optimization*, 9(1):112–147, 1998.

Lai, R. and Jackson, T. A mathematical model of receptor - mediated apoptosis: Dying to know why fasl is a trimer. *Math Biosci Eng*, 1(2):325 – 338, 2004.

Laslo, P., Spooner, C., Warmflash, A., Lancki, D., Lee, H., Sciammas, R., Gantner, B., Dinner, A., and H., S. Multilineage transcriptional priming and determination of alternate hematopoietic cell fates. *Cell*, 126:755–466, 2006.

Latunde-Dada, G. O., Simpson, R. J., and McKie, A. T. Recent advances in mammalian haem transport. *Trends Biochem Sci*, 31(3):182–188, 2006.

Laurent, M. and Kellershohn, N. Multistability: a major means of differentiation and evolution in biological systems. *Trends Biochem Sci*, 24(11):418–22, 1999.

Lawson, C. L. and Hanson, R. J. *Solving Least Squares Problems*. Society for Industrial and Applied Mathematics, Philadelphia, PA, USA, 1995.

Le Novère, N., Hucka, M., Mi, H., Moodie, S., Schreiber, F., Sorokin, A., Demir, E., Wegner, K., Aladjem, M. I., Wimalaratne, S. M., Bergman, F. T., Gauges, R., Ghazal,

P., Kawaji, H., Li, L., Matsuoka, Y., Villéger, A., Boyd, S. E., Calzone, L., Courtot, M., Dogrusoz, U., Freeman, T. C., Funahashi, A., Ghosh, S., Jouraku, A., Kim, S., Kolpakov, F., Luna, A., Sahle, S., Schmidt, E., Watterson, S., Wu, G., Goryanin, I., Kell, D. B., Sander, C., Sauro, H., Snoep, J. L., Kohn, K., and Kitano, H. The systems biology graphical notation. *Nat Biotechnol*, 27(8):735–741, 2009.

Lee, K., Wood, N., and Xu, X. Ultrasound image-based computer model of a common carotid artery with a plaque. *Med Eng Phys*, 26(10):823–40, 2004.

Lee, T.-S. and Chau, L.-Y. Heme oxygenase-1 mediates the anti-inflammatory effect of interleukin-10 in mice. *Nat Med*, 8(3):240–246, 2002.

Legewie, S., Blüthgen, N., and Herzel, H. Mathematical modeling identifies inhibitors of apoptosis as mediators of positive feedback and bistability. *PLoS Comput Biol*, 2(9): e120, 2006.

Leist, M. and Jäättelä, M. Four deaths and a funeral: from caspases to alternative mechanisms. *Nat Rev Mol Cell Biol*, 2:589–598, 2001.

Levy, A. and Moreno, P. Intraplaque hemorrhage. *Curr Mol Med*, 6(5):479–88, 2006.

Li, H., Zhu, H., Xu, C. J., and Yuan, J. Cleavage of bid by caspase 8 mediates the mitochondrial damage in the fas pathway of apoptosis. *Cell*, 94(4):491–501, 1998.

Li, L., Thomas, R., Suzuki, H., De Brabander, J., Wang, X., and Harran, P. A small molecule smac mimic potentiates trail- and tnfalpha-mediated cell death. *Science*, 305 (5689):1471–1474, 2004.

Li, P., Nijhawan, D., Budihardjo, I., Srinivasula, S., Ahmad, M., Alnemri, E., and Wang, X. Cytochrome c and datp-dependent formation of apaf-1/caspase-9 complex initiates an apoptotic protease cascade. *Cell*, 91:479–489, 1997.

Liepe, J., Barnes, C., Cule, E., Erguler, K., Kirk, P., Toni, T., and Stumpf, M. P. H. Abc-sysbio - approximate bayesian computation in python with gpu support. *Bioinformatics*, In press.

Lockshin, R. A. and Zakeri, Z. Programmed cell death and apoptosis: origins of the theory. *Nat Rev Mol Cell Biol*, 2(7):545–50, 2001.

Lodhi, H. and Muggleton, S., editors. *Elements of Computational Systems Biology*. Wiley Book Series on Bioinformatics, 2009.

Ma, W., Trusina, A., El-Samad, H., Lim, W. A., and Tang, C. Defining network topologies that can achieve biochemical adaptation. *Cell*, 138(4):760–73, 2009.

Madesh, M., Antonsson, B., Srinivasula, S. M., Alnemri, E. S., and Hajnoczky, G. Rapid kinetics of tbid-induced cytochrome c and smac/diablo release and mitochondrial depolarization. *J Biol Chem*, 277(7):5651–5659, 2002.

Mallat, Z., Besnard, S., Duriez, M., Deleuze, V., Emmanuel, F., Bureau, M. F., Soubrier, F., Esposito, B., Duez, H., Fievet, C., Staels, B., Duverger, N., Scherman, D., and Tedgui, A. Protective role of interleukin-10 in atherosclerosis. *Circ Res*, 85(8):e17–24, 1999.

Manrai, A. K. and Gunawardena, J. The geometry of multisite phosphorylation. *Biophys J*, 95(12):5533–5543, 2008.

Marino, S. and Kirschner, D. E. The human immune response to mycobacterium tuberculosis in lung and lymph node. *J Theor Biol*, 227(4):463–486, 2004.

Marino, S., Hogue, I. B., Ray, C. J., and Kirschner, D. E. A methodology for performing global uncertainty and sensitivity analysis in systems biology. *J Theor Biol*, 254(1): 178–196, 2008.

Markevich, N. I., Hoek, J. B., and Kholodenko, B. N. Signaling switches and bistability arising from multisite phosphorylation in protein kinase cascades. *J Cell Biol*, 164(3): 353–359, 2004.

Marsden, V. and Strasser, A. Control of apoptosis in the immune system: Bcl-2, bh3-only proteins and more. *Annu Rev Immunol*, 21:71–105, 2003.

McNeish, I., Bell, S., McKay, T., Tenev, T., Marani, M., and Lemoine, N. Expression of smac/diablo in ovarian carcinoma cells induces apoptosis via a caspase-9-mediated pathway. *Exp Cell Res*, 286(2):186–198, 2003.

Meier, P., Finch, A., and Evan, G. Apoptosis in development. *Nature*, 407(6805):796–801, 2000.

Mense, S. M. and Zhang, L. Heme: a versatile signaling molecule controlling the activities of diverse regulators ranging from transcription factors to map kinases. *Cell Res*, 16(8):681–92, 2006.

Moestrup, S. K. and Moller, H. J. Cd163: a regulated hemoglobin scavenger receptor with a role in the anti-inflammatory response. *Ann Med*, 36(5):347–354, 2004.

Momiji, H. and Monk, N. A. M. Dissecting the dynamics of the hes1 genetic oscillator. *J Theor Biol*, 254(4):784–798, 2008.

Monk, N. A. M. Oscillatory expression of hes1, p53, and nf-kappab driven by transcriptional time delays. *Curr Biol*, 13(16):1409–1413, 2003.

Morita, T. Heme oxygenase and atherosclerosis. *Arterioscler Thromb Vasc Biol*, 25(9): 1786–1795, 2005.

Mosser, D. M. The many faces of macrophage activation. *J Leukoc Biol*, 73(2):209–12, 2003.

Mosser, D. M. and Edwards, J. P. Exploring the full spectrum of macrophage activation. *Nat Rev Immunol*, 8(12):958–69, 2008.

Muppidi, J. R. and Siegel, R. M. Ligand-independent redistribution of Fas (CD95) into lipid rafts mediates clonotypic T cell death. *Nat Immunol*, 5(2):182–189, 2004.

Muppidi, J. R., Tschopp, J., and Siegel, R. M. Life and death decisions: Secondary complexes and lipid rafts in TNF receptor family signal transduction. *Immunity*, 21 (4):461–465, 2004.

Murray, J. D. *Mathematical Biology: I. An Introduction*. Springer, 3rd edition, 2002.

Nagababu, E. and Rifkind, J. M. Heme degradation by reactive oxygen species. *Antioxid Redox Signal*, 6(6):967–78, 2004.

Nagata, S. Apoptosis by death factor. *Cell*, 88(3):355–365, 1997.

Nakabayashi, J. and Sasaki, A. A mathematical model for apoptosome assembly: the optimal cytochrome c/apaf-1 ratio. *J Theor Biol*, 242(2):280–287, 2006.

Nelder, J. A. and Mead, R. A simplex method for function minimization. *Computer Journal*, 7(4):308–313, 1965.

Nelson, D. E., Ihekwaba, A. E. C., Elliott, M., Johnson, J. R., Gibney, C. A., Foreman, B. E., Nelson, G., See, V., Horton, C. A., Spiller, D. G., Edwards, S. W., McDowell, H. P., Unitt, J. F., Sullivan, E., Grimley, R., Benson, N., Broomhead, D., Kell, D. B., and White, M. R. H. Oscillations in nf-kappa b signaling control the dynamics of gene expression. *Science*, 306(5296):704–708, 2004.

Neun, W. and Melenk, H. Very large Gröbner basis calculations. In *Proceedings of the Second International Workshop on Computer Algebra and Parallelism*, volume 584 of *Lecture Notes in Computer Science*, pages 89–99, London, UK, 1992. Springer-Verlag.

Nicholson, D. W. Caspase structure, proteolytic substrates, and function during apoptotic cell death. *Cell Death Differ*, 6(11):1028–42, 1999.

Nicholson, D. W. and Thornberry, N. A. Caspases: killer proteases. *Trends Biochem Sci*, 22(8):299–306, 1997.

Nielsen, M. J. and Moestrup, S. K. Receptor targeting of hemoglobin mediated by the haptoglobins: roles beyond heme scavenging. *Blood*, 114(4):764–771, 2009.

Nocedal, J. and Wright, S. J. *Numerical Optimization*. Springer, 2nd edition, 2006.

Nunez, G., Benedict, M., Hu, Y., and Inohara, N. Caspases: the proteases of the apoptotic pathway. *Oncogene*, 17(25):3237–3245, 1998.

Odegaard, B. and Atassi, M. Z. Haptoglobin-hemoglobin binding involves the heavy chain of haptoglobin and the α and β chains of hemoglobin. *J Protein Chem*, 3(3): 287–292, 1984.

Ogawa, K., Igarashi, K., Nishitani, C., Shibahara, S., and Fujita, H. Heme-regulated transcription factor bach1. *J Health Sci*, 48(1):1–6, 2002.

Okazaki, N., Asano, R., Kinoshita, T., and Chuman, H. Simple computational models of type i/type ii cells in fas signaling-induced apoptosis. *J Theor Biol*, 250(4):621–633, 2008.

Oliphant, T. E. Python for scientific computing. *Comput Sci Eng*, 9(3):10–20, 2007.

Oost, T., Sun, C., Armstrong, R., Al-Assaad, A., Betz, S., Deckwerth, T., Ding, H., Elmore, S., Meadows, R., Olejniczak, E., Oleksijew, A., Oltersdorf, T., Rosenberg, S., Shoemaker, A., Tomaselli, K., Zou, H., and Fesik, S. Discovery of potent antagonists of the antiapoptotic protein xiap for the treatment of cancer. *J Med Chem*, 47(18): 4417–4426, 2004.

Oppenheim, R. Cell death during development of the nervous system. *Ann Rev Neurosci*, 14:453–501, 1991.

Ortega, F., Sameith, K., Turan, N., Compton, R., Trevino, V., Vannucci, M., and Falciani, F. Models and computational strategies linking physiological response to molecular networks from large-scale data. *Philos Transact A Math Phys Eng Sci*, 366(1878): 3067–89, 2008.

Otterbein, L. and Zuckerbraun, B. *Heme oxygenase: the elegant orchestration of its products in medicine*. Hauppauge, New York: Nova Science, 2005.

Otterbein, L. E., Soares, M. P., Yamashita, K., and Bach, F. H. Heme oxygenase-1: unleashing the protective properties of heme. *Trends Immunol*, 24(8):449–455, 2003.

Pae, H.-O., Kim, E.-C., and Chung, H.-T. Integrative survival response evoked by heme oxygenase-1 and heme metabolites. *J Clin Biochem Nutr*, 42(3):197–203, 2008.

Perelson, A. *Cell Surface Dynamics: Concepts and Models*, chapter Some mathematical models of receptor clustering by multivalent ligands, pages 223–225. Marcel Dekker, 1984.

Perelson, A. Receptor clustering on a cell surface. iii. theory of receptor cross-linking by multivalent ligands: description by ligand states. *Math Biosci*, 53:1–39, 1981.

Perkins, T. J. and Swain, P. S. Strategies for cellular decision-making. *Mol Syst Biol*, 5: 326, 2009.

Philippidis, P., Mason, J. C., Evans, B. J., Nadra, I., Taylor, K. M., Haskard, D. O., and Landis, R. C. Hemoglobin scavenger receptor cd163 mediates interleukin-10 release and heme oxygenase-1 synthesis: antiinflammatory monocyte-macrophage responses in vitro, in resolving skin blisters in vivo, and after cardiopulmonary bypass surgery. *Circ Res*, 94(1):119–126, 2004.

Polynikis, A., Hogan, S., and di Bernardo, M. Comparing different ode modelling approaches for gene regulatory networks. *J Theor Biol*, 261(4):511 – 530, 2009.

Pomerening, J. R., Sontag, E. D., and Ferrell, Jr, J. E. Building a cell cycle oscillator: hysteresis and bistability in the activation of cdc2. *Nat Cell Biol*, 5(4):346–351, 2003.

Potteaux, S., Esposito, B., van Oostrom, O., Brun, V., Ardouin, P., Groux, H., Tedgui, A., and Mallat, Z. Leukocyte-derived interleukin 10 is required for protection against atherosclerosis in low-density lipoprotein receptor knockout mice. *Arterioscler Thromb Vasc Biol*, 24(8):1474–1478, 2004.

Preisach, F. Über die magnetische nachwirkung. *Z Phys*, 94:277–302, 1935.

Pritchard, J. and Hickman, J. Why does stage 4s neuroblastoma regress spontaneously? *Lancet*, 344(8926):869–870, 1994.

PubChem, C. S. C. . http://pubchem.ncbi.nlm.nih.gov/summary/summary.cgi?cid=444098. 2009.

Raff, M. Cell suicide for beginners. *Nature*, 396(6707):119–122, 1998.

Rangamani, P. and Sirovich, L. Survival and apoptotic pathways initiated by tnf-alpha: modeling and predictions. *Biotechnol Bioeng*, 97(5):1216–29, 2007.

Ray, J. C. J., Wang, J., Chan, J., and Kirschner, D. E. The timing of tnf and ifn-gamma signaling affects macrophage activation strategies during mycobacterium tuberculosis infection. *J Theor Biol*, 252(1):24–38, 2008.

Ricchetti, G. A., Williams, L. M., and Foxwell, B. M. J. Heme oxygenase 1 expression induced by il-10 requires stat-3 and phosphoinositol-3 kinase and is inhibited by lipopolysaccharide. *J Leukoc Biol*, 76(3):719–726, 2004.

Rodriguez, J. and Lazebnik, Y. Caspase-9 and apaf-1 form an active holoenzyme. *Genes Dev*, 13:3179–3184, 1999.

Rubinow, S. I. *Introduction to Mathematical Biology*. John Wiley, 1975.

Ryter, S. W., Otterbein, L. E., Morse, D., and Choi, A. M. K. Heme oxygenase/carbon monoxide signaling pathways: regulation and functional significance. *Mol Cell Biochem*, 234-235(1-2):249–63, 2002.

Ryu, S., Lin, S., Ugel, N., Antoniotti, M., and Mishra, B. Mathematical modeling of the formation of apoptosome in intrinsic pathway of apoptosis. *Syst Synth Biol*, 2(1-2): 49–66, 2008.

Sabosciences. http://www.sabiosciences.com/pathway.php?sn=il-10. 2010.

Saez-Rodríguez, J., Kremling, A., Conzelmann, H., Bettenbrock, K., and Gilles, E. Modular analysis of signal transduction networks. *Control Systems Magazine, IEEE*, 24(4): 35–52, 2004.

Saltelli, A., Chan, K., and Scott, E. M. *Sensitivity Analysis: Gauging the Worth of Scientific Models*. Wiley, 2000.

Saltelli, A., Ratto, M., Tarantola, S., and Campolongo, F. Sensitivity analysis for chemical models. *Chem Rev*, 105(7):2811–2828, 2005.

Sanjabi, S., Zenewicz, L. A., Kamanaka, M., and Flavell, R. A. Anti-inflammatory and pro-inflammatory roles of tgf-beta, il-10, and il-22 in immunity and autoimmunity. *Curr Opin Pharmacol*, 9(4):447–53, 2009.

Sauro, H. M. and Kholodenko, B. N. Quantitative analysis of signaling networks. *Prog Biophys Mol Biol*, 86(1):5–43, 2004.

Sawle, P., Foresti, R., Mann, B. E., Johnson, T. R., Green, C. J., and Motterlini, R. Carbon monoxide-releasing molecules (co-rms) attenuate the inflammatory response elicited by lipopolysaccharide in raw264.7 murine macrophages. *Br J Pharmacol*, 145 (6):800–10, 2005.

Scaffidi, C., Fulda, S., Srinivasan, A., Friesen, C., Li, F., Tomaselli, K., Debatin, K., Krammer, P., and Peter, M. Two cd95 (apo-1/fas) signaling pathways. *EMBO J*, 17 (6):1675–1687, 1998.

Schaer, C. A., Schoedon, G., Imhof, A., Kurrer, M. O., and Schaer, D. J. Constitutive endocytosis of cd163 mediates hemoglobin-heme uptake and determines the noninflammatory and protective transcriptional response of macrophages to hemoglobin. *Circ Res*, 99(9):943–950, 2006.

Schaer, C. A., Vallelian, F., Imhof, A., Schoedon, G., and Schaer, D. J. Heme carrier protein (hcp-1) spatially interacts with the cd163 hemoglobin uptake pathway and is a target of inflammatory macrophage activation. *J Leukoc Biol*, 83(2):325–333, 2008.

Schlesinger, P. and Saito, M. The bax pore in liposomes, biophysics. *Cell Death Differ*, 13:1403–1408, 2006.

Schlitt, T. and Brazma, A. Modelling gene networks at different organisational levels. *FEBS Lett*, 579(8):1859–1866, 2005.

Schmidt, H. and Jirstrand, M. Systems Biology Toolbox for MATLAB: a computational platform for research in systems biology. *Bioinformatics*, 22(4), 2006.

Schmitz, I., Walczak, H., Krammer, P. H., and Peter, M. E. The two cd95 apoptosis signaling pathways may be a way of cells to respond to different amounts and/or forms of cd95 ligand produced in different tissues. *Cell Death Differ*, 7(8):756–758, 2000.

Schoeberl, B., Eichler-Jonsson, C., Gilles, E. D., and Muller, G. Computational modeling of the dynamics of the map kinase cascade activated by surface and internalized egf receptors. *Nat Biotechnol*, 20(4):370–375, 2002.

Scott, D. W. *Multivariate Density Estimation: Theory, Practice, and Visualization*. John Wiley & Sons, Inc., New York, NY, USA, 1992.

Scott, F. L., Stec, B., Pop, C., Dobaczewska, M. K., Lee, J. J., Monosov, E., Robinson, H., Salvesen, G. S., Schwarzenbacher, R., and Riedl, S. J. The fas-fadd death domain complex structure unravels signalling by receptor clustering. *Nature*, 457(7232):1019–1022, 2009.

Secrier, M., Toni, T., and Stumpf, M. P. H. The abc of reverse engineering biological signalling systems. *Mol Biosyst*, 5(12):1925–35, 2009.

Segel, I. H. *Enzyme Kinetics: Behavior and Analysis of Rapid Equilibrium and Steady-State Enzyme Systems*. Wiley-interscience, 1993.

Segel, L. *Mathematical Models Molecular Cellular Biology*. Cambridge : Cambridge University Press, 1980.

Segel, L. A. and Slemrod, M. The quasi-steady-state assumption: A case study in perturbation. *SIAM Review*, 31(3):446–477, 1989.

Siegel, R. M., Frederiksen, J. K., Zacharias, D. A., Chan, F. K.-M., Johnson, M., Lynch, D., Tsien, R. Y., and Lenardo, M. J. Fas preassociation required for apoptosis signaling and dominant inhibition by pathogenic mutations. *Science*, 288(5475):2354–2357, 2000.

Siow, R. C., Sato, H., and Mann, G. E. Heme oxygenase-carbon monoxide signalling pathway in atherosclerosis: anti-atherogenic actions of bilirubin and carbon monoxide? *Cardiovasc Res*, 41(2):385–394, 1999.

Slee, E. A., Harte, M. T., Kluck, R. M., Wolf, B. B., Casiano, C. A., Newmeyer, D. D., Wang, H.-G., Reed, J. C., Nicholson, D. W., Alnemri, E. S., Green, D. R., and Martin, S. J. Ordering the cytochrome c-initiated caspase cascade: Hierarchical activation of caspases-2, -3, -6, -7, -8, and -10 in a caspase-9-dependent manner. *J Cell Biol*, 144 (2):281–292, 1999.

Smith, C., Farrah, T., and Goodwin, R. The tnf receptor superfamily of cellular and viral proteins: Activation, costimulation, and death. *Cell*, 76:959–962, 1994.

Sobol', I. M. Global sensitivity indices for nonlinear mathematical models and their Monte Carlo estimates. *Math Comput Simul*, 55(1-3):271–280, 2001.

Sourjik, V. Receptor clustering and signal processing in e. coli chemotaxis. *Trends Microbiol*, 12(12):569–76, 2004.

Sprick, M. and Walczak, H. The interplay between the bcl-2 family and death receptor-mediated apoptosis. *Biochim Biophys Acta*, 1644(2–3):125–132, 2004.

Srinivasula, S. M., Datta, P., Fan, X. J., Fernandes-Alnemri, T., Huang, Z., and Alnemri, E. S. Molecular determinants of the caspase-promoting activity of smac/diablo and its role in the death receptor pathway. *J Biol Chem*, 275(46):36152–36157, 2000.

Stark, J. and Hardy, K. Mathematics. chaos: useful at last? *Science*, 301(5637):1192–3, 2003.

Stark, J., Brewer, D., Barenco, M., Tomescu, D., Callard, R., and Hubank, M. Reconstructing gene networks: what are the limits? *Biochem Soc Trans*, 31:1519–1525, 2003a.

Stark, J., Callard, R., and Hubank, M. From the top down: towards a predictive biology of signalling networks. *Trends Biotechnol*, 21(7):290–293, 2003b.

Stark, J., Chan, C., and George, A. J. T. Oscillations in the immune system. *Immunol Rev*, 216:213–231, 2007.

Stelling, J., Sauer, U., Szallasi, Z., Doyle, F. J. r., and Doyle, J. Robustness of cellular functions. *Cell*, 118(6):675–685, 2004.

Strasser, A., Harris, A., Huang, D., Krammer, P., and Cory, S. Bcl-2 and fas/apo-1 regulate distinct pathways to lymphocyte apoptosis. *EMBO J*, 14(24):6136–3147, 1995.

Strogatz, S. H. *Nonlinear Dynamics and Chaos:With Applications to Physics, Chemistry, and Engineering*. Perseus Books Publishing LLC, 1994.

Stucki, J. and Simon, H.-U. Mathematical modeling of the regulation of caspase-3 activation and degradation. *J Theor Biol*, 234(1):123–131, 2005.

Sulahian, T. H., Hogger, P., Wahner, A. E., Wardwell, K., Goulding, N. J., Sorg, C., Droste, A., Stehling, M., Wallace, P. K., Morganelli, P. M., and Guyre, P. M. Human monocytes express cd163, which is upregulated by il-10 and identical to p155. *Cytokine*, 12(9):1312–1321, 2000.

Sun, J., Hoshino, H., Takaku, K., Nakajima, O., Muto, A., Suzuki, H., Tashiro, S., Takahashi, S., Shibahara, S., Alam, J., Taketo, M. M., Yamamoto, M., and Igarashi, K. Hemoprotein bach1 regulates enhancer availability of heme oxygenase-1 gene. *EMBO J*, 21(19):5216–24, 2002.

Sun, J., Brand, M., Zenke, Y., Tashiro, S., Groudine, M., and Igarashi, K. Heme regulates the dynamic exchange of bach1 and nf-e2-related factors in the maf transcription factor network. *Proc Natl Acad Sci USA*, 101(6):1461–6, 2004.

Sutherland, E. W. Studies on the mechanism of hormone action. *Science*, 177(47):401–8, 1972.

Suzuki, M., Youle, R. J., and Tjandra, N. Structure of bax: coregulation of dimer formation and intracellular localization. *Cell*, 103(4):645–54, 2000.

Svingen, P. A., Loegering, D., Rodriquez, J., Meng, X. W., Mesner, P. W. J., Holbeck, S., Monks, A., Krajewski, S., Scudiero, D. A., Sausville, E. A., Reed, J. C., Lazebnik, Y. A., and Kaufmann, S. H. Components of the cell death machine and drug sensitivity of the National Cancer Institute cell line panel. *Clin Cancer Res*, 10(20):6807–6820, 2004.

Takahashi, A. and Earnshaw, W. Ice-related proteases in apoptosis. *Curr Opin Genet Dev*, 6(1):50–55, 1996.

Takami, M. Catabolism of heme moiety of hemoglobin.haptoglobin in rat liver cells in vivo. *J Biol Chem*, 268(27):20335–20342, 1993.

Takaya, N., Yuan, C., Chu, B., Saam, T., Polissar, N. L., Jarvik, G. P., Isaac, C., McDonough, J., Natiello, C., Small, R., Ferguson, M. S., and Hatsukami, T. S. Presence of intraplaque hemorrhage stimulates progression of carotid atherosclerotic plaques: a high-resolution magnetic resonance imaging study. *Circulation*, 111(21):2768–75, 2005.

Takaya, N., Yuan, C., Chu, B., Saam, T., Underhill, H., Cai, J., Tran, N., Polissar, N. L., Isaac, C., Ferguson, M. S., Garden, G. A., Cramer, S. C., Maravilla, K. R., Hashimoto, B., and Hatsukami, T. S. Association between carotid plaque characteristics and subsequent ischemic cerebrovascular events: a prospective assessment with mri–initial results. *Stroke*, 37(3):818–823, 2006.

Tartaglia, L., Ayres, T., Wong, G., and Goeddel, D. A novel domain within the 55 kd tnf receptor signals cell death. *Cell*, 74:845–853, 1993.

Tenenbaum, M. and Pollard, H. *Ordinary Differential Equations*. Harper & Row, 1963.

Thompson, C. B. Apoptosis in the pathogenesis and treatment of disease. *Science*, 267 (5203):1456–1462, 1995.

Thornberry, N. and Lazebnik, Y. Caspases: enemies within. *Science*, 281(5381):1312–1316, 1998.

Toni, T. and Stumpf, M. P. H. Simulation-based model selection for dynamical systems in systems and population biology. *Bioinformatics*, 26(1):104–10, 2010.

Toni, T., Welch, D., Strelkowa, N., Ipsen, A., and Stumpf, M. P. H. Approximate bayesian computation scheme for parameter inference and model selection in dynamical systems. *J R Soc Interface*, 6(31):187–202, 2009.

Tsiftsoglou, A. S., Tsamadou, A. I., and Papadopoulou, L. C. Heme as key regulator of major mammalian cellular functions: molecular, cellular, and pharmacological aspects. *Pharmacol Ther*, 111(2):327–45, 2006.

Turányi, T. Sensitivity analysis of complex kinetic systems. tools and applications. *J Math Chem*, 5(3):203–248, 1990.

Turing, A. M. The chemical basis of morphogenesis. *Philos Trans R Soc Lond*, 237: 37–72, 1952.

Tyson, J., Chen, K., and Novak, B. Sniffers, buzzers, toggles and blinkers: dynamics of regulatory and signaling pathways in the cell. *Curr Opin. Cell Biol*, 15:221–231, 2003.

Ugocsai, P., Barlage, S., Dada, A., and Schmitz, G. Regulation of surface cd163 expression and cellular effects of receptor mediated hemoglobin-haptoglobin uptake on human monocytes and macrophages. *Cytometry. Part A : the journal of the International Society for Analytical Cytology*, 69(3):203–205, 2006.

Van den Heuvel, M. M., Tensen, C. P., van As, J. H., Van den Berg, T. K., Fluitsma, D. M., Dijkstra, C. D., Döpp, E. A., Droste, A., Van Gaalen, F. A., Sorg, C., Högger, P., and Beelen, R. H. Regulation of cd 163 on human macrophages: cross-linking of cd163 induces signaling and activation. *J Leukoc Biol*, 66(5):858–66, 1999.

Van Vlierberghe, H., Langlois, M., and Delanghe, J. Haptoglobin polymorphisms and iron homeostasis in health and in disease. *Clin Chim Acta*, 345(1-2):35–42, 2004.

Virmani, R., Kolodgie, F. D., Burke, A. P., Finn, A. V., Gold, H. K., Tulenko, T. N., Wrenn, S. P., and Narula, J. Atherosclerotic plaque progression and vulnerability to rupture: angiogenesis as a source of intraplaque hemorrhage. *Arterioscler Thromb Vasc Biol*, 25:2054–5061, 2005.

Watson, R. A. and Pollack, J. B. Modular interdependency in complex dynamical systems. *Artif Life*, 11(4):445–57, 2005.

Weber, C., Zernecke, A., and Libby, P. The multifaceted contributions of leukocyte subsets to atherosclerosis: lessons from mouse models. *Nat Rev Immunol*, 8(10):802–15, 2008.

Weiss, J. N. The hill equation revisited: uses and misuses. *FASEB J*, 11(11):835–41, 1997.

Weng, G., Bhalla, U. S., and Iyengar, R. Complexity in biological signaling systems. *Science*, 284(5411):92–6, 1999.

Werner, A., de Vries, E., Tait, S., Bontjer, I., and Borst, J. Trail receptor and cd95 signal to mitochondria via fadd, caspase-8/10, bid and bax but differentially regulate events downstream from truncated bid. *J Biol Chem*, 277(43):40760–20767, 2002a.

Werner, A., de Vries, E., Tait, S., Bontjer, I., and Borst, J. Bcl-2 family member bfl-1/a1 sequesters truncated bid to inhibit is collaboration with pro-apoptotic bak or bax. *J Biol Chem*, 277(25):22781–22788, 2002b.

Westermark, P. O., Hellgren-Kotaleski, J., and Lansner, A. Derivation of a reversible hill equation with modifiers affecting catalytic properties. *WSEAS Trans Biol Med*, 1 (91-98), 2004.

Williams, L., Jarai, G., Smith, A., and Finan, P. Il-10 expression profiling in human monocytes. *J Leukoc Biol*, 72(4):800–9, 2002.

Wright, K. M., Linhoff, M. W., Potts, P. R., and Deshmukh, M. Decreased apoptosome activity with neuronal differentiation sets the threshold for strict iap regulation of apoptosis. *J Cell Biol*, 167(2):303–313, 2004.

Xiong, W. and Ferrell, Jr, J. E. A positive-feedback-based bistable 'memory module' that governs a cell fate decision. *Nature*, 426(6965):460–465, 2003.

Xu, T.-R., Vyshemirsky, V., Gormand, A., von Kriegsheim, A., Girolami, M., Baillie, G. S., Ketley, D., Dunlop, A. J., Milligan, G., Houslay, M. D., and Kolch, W. Inferring signaling pathway topologies from multiple perturbation measurements of specific biochemical species. *Sci Signal*, 3(113):ra20, 2010.

Yakovlev, A. G., Ota, K., Wang, G., Movsesyan, V., Bao, W.-L., Yoshihara, K., and Faden, A. I. Differential Expression of Apoptotic Protease-Activating Factor-1 and Caspase-3 Genes and Susceptibility to Apoptosis during Brain Development and after Traumatic Brain Injury. *J Neurosci*, 21(19):7439–7446, 2001.

Yamada, S., Taketomi, T., and Yoshimura, A. Model analysis of difference between egf pathway and fgf pathway. *Biochem Biophys Res Commun*, 314(4):1113–1120, 2004.

Yates, A., Bergmann, C., Van Hemmen, J. L., Stark, J., and Callard, R. Cytokine-modulated regulation of helper t cell populations. *J Theor Biol*, 206(4):539–60, 2000.

Yates, A., Chan, C. C. W., Callard, R. E., George, A. J. T., and Stark, J. An approach to modelling in immunology. *Brief Bioinformatics*, 2(3):245–257, 2001.

Yates, A., Callard, R., and Stark, J. Combining cytokine signalling with t-bet and gata-3 regulation in th1 and th2 differentiation: a model for cellular decision-making. *J Theor Biol*, 231(2):181–196, 2004.

Yue, H., Brown, M., He, F., Jia, J., and Kell, D. Sensitivity analysis and robust experimental design of a signal transduction pathway. *Int J Chem Kinet*, 40(730-741), 2008.

Zheng, T. S. and Flavell, R. A. Death by numbers. *Nat Biotechnol*, 18(7):717–8, 2000.

Zheng, Y. and Rundell, A. Comparative study of parameter sensitivity analyses of the TCR-activated Erk-MAPK signalling pathway. *IEE Proc Syst Biol*, 153(4):201–211, 2006.

Zi, Z. and Sun, Z.-R. Robustness analysis of the IFN-γ induced JAK-STAT signaling pathway. *J Comput Sci Technol*, 20(4):491–495, 2005.

Zi, Z., Cho, K.-H., Sung, M.-H., Xia, X., Zheng, J., and Sun, Z. In silico identification of the key components and steps in IFN-γ induced JAK-STAT signaling pathway. *FEBS Lett*, 579(5):1101–1108, 2005.

Zi, Z., Zheng, Y., Rundell, A. E., and Klipp, E. SBML-SAT: a systems biology markup language (SBML) based sensitivity analysis tool. *BMC Bioinformatics*, 9(1):342, 2008.

Zimmermann, K., Bonzon, C., and Green, D. The machinery of programmed cell death. *Pharmacol Ther*, 92(1):57–70, 2001.

Zuzarte-Luis, V. and Hurle, J. M. Programmed cell death in the developing limb. *Int J Dev Biol*, 46(7):871–6, 2002.